Max-Planck-Institut für Astrophysik

Multi-dimensional simulations of core-collapse supernovae with a variable Eddington factor technique for energy-dependent neutrino transport

Robert Buras

Vollständiger Abdruck der von der Fakultät für Physik der Technischen Universität München zur Erlangung des akademischen Grades eines

Doktors der Naturwissenschaften (Dr. rer. nat.)

genehmigten Dissertation.

Vorsitzender: Univ.-Prof. Dr. Franz von Feilitzsch

Prüfer der Dissertation:

1. Priv.-Doz. Dr. Hans-Thomas Janka
2. Univ.-Prof. Dr. Manfred Lindner

Die Dissertation wurde am 21.12.2004 bei der Technischen Universität München eingereicht und durch die Fakultät für Physik am 17.6.2005 angenommen.

Mehrdimensionale Simulationen von Kernkollaps-Supernovae mit einer variablen Eddingtonfaktormethode für den energieabhängigen Neutrinotranport

Kernkollaps-Supernovae sind extrem interessante und spektakuläre Phänomene, zum Einen wegen ihres Beitrags zur Nukleosynthese schwerer Elemente, zum anderen wegen der Erzeugung messbarer Neutrino- und Gravitationswellensignale. Numerische Simulationen sind zum Verständnis der extrem komplexen Vorgänge in Supernovae unerlässlich. Die vorliegende Arbeit präsentiert die weltweit ersten Supernovarechnungen in denen zwei für den Explosionsmechanismus wichtige Effekte in bisher unerreichter Genauigkeit berücksichtigt werden konnten: Der Transport von Neutrinos und ihre Wechselwirkung mit dem Medium des Sterns, sowie hydrodynamische Instabilitäten. Ein neuer Typ von Instabilität konnte identifiziert werden, der in unseren Simulationen Explosionen begünstigt und wichtige Konsequenzen für den Explosionsmechanismus hat. Weitere Rechnungen sind notwendig um diese Aussage zu verifizieren.

Contents

1 Introduction

Ever since Arnett published the first simulations of stellar core-collapses which failed to show the expected supernova explosions in 1967 people have been speculating on what might be the right recipe to seduce the dying star into exploding. This unremitting cooking contest which has now gone on for almost fourty years has resulted in a variety of promising proposals. One of the first, and most important, ingredients originated from Colgate & White (1966): In their world-wide first core-collapse simulations they showed that the neutrinos emitted from the collapsed core of a star could actually be the source of the energy necessary to induce a supernova explosion in the stellar envelope. However, their inclusion of neutrino effects in the hydrodynamic simulation was too simplistic while the simulations of Arnett (1967) were the first to consistently calculate the transport of neutrinos and their interaction with the stellar medium.

Of course, the 37 years which have passed since these poineering works were published have changed completely the view we have of core-collapse supernovae. For one, many physical aspects of significant importance for supernovae have been revealed, e.g. the existence of weak neutral current interactions (Tubbs & Schramm 1975). Also, the limited computational power has always enforced strong simplifications of this very complex problem so that several important effects were found only after an increase in computational power allowed for more sophisticated simulations.

Although there still exist physical uncertainties such as for the properties of the nuclear equation of state and neutrino interaction rates at high densities, and the computers are still not fast enough to allow for simulations which would satisfy all the requirements of the theorists, the basic picture of stellar core collapse is quite well established nowadays. This picture has moreover been confirmed by the detection of the neutrinos which were produced by the Supernova 1987A. But the exact nature of the explosion mechanism is still unclear.

We know that core-collapse supernovae—not to be confused with the “standard candle” supernovae, which are the results of accretion-induced thermo-nuclear explosions of white dwarfs—are produced by massive stars with more than eight solar masses. These stars generally evolve a core which consists of iron-like nuclei and is stabilized against gravitational collapse mainly by the pressure of the degenerate electron gas. The slow contraction of the iron core due to the emission of neutrinos which carry away lepton number leads to a rise of the temperature. This evolution speeds up significantly when the photons in the medium become energetic enough to dissociate the nuclei. Together with the increasing neutrino emission rate the endothermic photo-dissociation destabilizes the core.

When the collapsing matter reaches densities above $10^{12}\,\mathrm{g\,cm^{-3}}$ coherent scattering of neutrinos on nuclei becomes so frequent that the neutrinos are trapped inside the core on dynamical

timescales. The neutrino-matter interactions come into equilibrium while the energy loss by neutrino diffusion is negligible. Still, the collapse is only halted when the matter reaches nuclear densities at about $3 \cdot 10^{14} \mathrm{g\,cm^{-3}}$ where the nuclei transform to a homogeneous phase of non-relativistic free nucleons and the pressure and the "stiffness" of the equation of state increase strongly due to repulsive nuclear forces. The dynamic collapse causes the core to overshoot the nuclear density and to rebound. The outer parts of the core, however, are by now falling with supersonic velocities, and where the rebounding inner core collides with the infalling outer core a shock forms.

This energetic, outward-moving "prompt" shock, which reverses the infall of the matter it plows through, quickly loses its power: First, the iron-like nuclei in the matter falling through the shock are dissociated immediately at the high temperatures present behind the shock, a highly endothermic process. Second, when the shock has moved out to densities below $10^{11} \mathrm{g\,cm^{-3}}$ where the matter is no longer opaque to neutrinos the shocked hot matter radiates away large amounts of lepton number and energy in form of electron neutrinos. Even if the nuclear dissociation would not deprive the shock of its energy, this "neutrino burst" at "shock breakout" (i.e. when the shock passes the "neutrinosphere") does it for sure. The "post-shock" velocities (i.e. the velocities of the shocked material) change from positive (i.e. expansion) to negative: After only a few milliseconds, the prompt shock "fails" while the matter behind it continues to settle onto the compact remnant of the collapse, the so-called proto neutron star (Bruenn 1989a,b).

For quite a long time it was believed that the explosion would occur promptly, i.e. the hydrodynamic shock would make its way out through the star directly, but all suggested attempts to keep the prompt shock alive ultimately failed (see Bethe 1990). There remain only few uncertainties concerning how far the prompt shock may expand before it inevitably stalls, which depend on details of the neutrino processes during collapse (Bruenn & Mezzacappa 1997; Langanke et al. 2003) and on the still remaining ambiguity of the equation of state at nuclear densities (Marek 2003).

It was in 1982 that Wilson revolutionized the field by performing a numerical calculation made possible by the availability of computational power: A simulation which was allowed to follow the evolution after shock formation for as long as several hundred milliseconds yielded an explosion: The neutrinos emitted from the slowly cooling proto neutron star and from the hot, shocked material that is accreted onto the proto neutron star (Bethe & Wilson 1985) were found to deposit enough energy in the layers just below the stalled prompt shock to revive it.

Newer models with a more sophisticated treatment of neutrino transport than by Wilson (1982), however, have shown that this so-called "neutrino-driven delayed explosion mechanism" may not work: The energy deposition of the neutrinos below the shock, which is only a few percent of the total amount of energy emitted with neutrinos and therefore sensitive to details of the interaction processes and the treatment of the transport, might not be sufficient to drive the shock (Bruenn 1987, 1993).

For understanding why it is so hard to explain the explosion it is helpful to discuss the situation after the prompt shock has stalled: Energy is overabundant in the proto neutron star where it was stored as internal energy during gravitational infall; energy is needed just below the shock to drive it outwards. In between, two effects dominate the evolution: neutrino cooling, which is roughly proportional to the sixth order of the temperature, and neutrino heating, which is roughly proportional to the neutrino flux and the matter density. As a consequence of the

specific, close to hydrostatic, structure between the neutrinosphere and the shock there will always exist a region, the "cooling region", where cooling is stronger and above this a region, the "gain layer", where cooling is weaker than heating. The pivot of all this is that the border between these two regions, the so-called "gain radius" where cooling and heating balance each other, is not at all fixed. Matter in the cooling region contracts steadily due to the energy loss. As a consequence the matter in the lower region of the gain layer will move inward and thereby contract to adopt to the hydrodynamic contitions at the lower radius. This contraction increases the temperature, and therefore the neutrino emission, and the matter becomes part of the cooling region. Hence material in the gain layer has only a limited time to absorb energy from neutrinos before it is lost to the cooling region and reemits this energy. Therefore it needs rather high neutrino fluxes to reverse the contraction of the gain layer. Close to the shock where the energy would be needed the density and neutrino flux are much lower and heating is less efficient. The search for the explosion mechanism is therefore concentrated on finding out how the energy is efficiently brought to just below the shock.

Over the years it became clear that several multi-dimensional phenomena would appear in a supernova (for a review see Bethe 1990). Many of these processes enhance the transport of energy from the proto neutron star to just below the shock or are helpful for shock revival in some other way. However, hydrodynamic simulations testing these effects had to wait until the needed computational power became available in the 1990s.

Two effects which both power the shock by increasing the efficiency of the neutrino heating origin from the formation of two convectively unstable regions. For one, in the proto neutron star, which is optically thick for neutrinos, convection transports energy towards the neutrinosphere (Epstein 1979) and thus has the potential of increasing the neutrino fluxes, and thus heating, if the convective region is large enough (Burrows 1987). Wilson & Mayle (1993) assumed a special, neutrino diffusion driven type of convection, the so-called "neutron finger instability", to arise just below the neutrinosphere. They obtained explosions in one-dimensional simulations that imitated this convective energy transport mechanism originally proposed by Smarr et al. (1981). However, the appearance and exact mode of convective instability depends sensitively on properties of the equation of state as well as on the structure of the proto neutron star. The latter in turn depends on the neutrino processes and transport during collapse, bounce, and neutrino burst. Especially the conditions for convective instabilities which are driven by neutrino diffusion, such as the neutron finger instability, are very sensitive to the details of the neutrino transport and interaction processes (Bruenn et al. 1995, 2004). Both the equation of state used by Wilson & Mayle (1993) as well as their treatment of neutrinos are not generally accepted. Thus it is no wonder that two-dimensional simulations—with a different equation of state—do not find neutron finger instabilities (see e.g. Keil et al. 1996; Mezzacappa et al. 1998a). Nevertheless other types of convective modes may occur deeper inside the proto neutron star as shown in a two-dimensional proto neutron star simulation by Keil et al. (1996) and as predicted by analytic studies based on one-dimensional simulations (Burrows 1987; Pons et al. 1999; Bruenn et al. 2004). These energy transport mechanisms also affect the neutrino emission, in general however to a smaller extent than seen in the one-dimensional models of Wilson & Mayle (1993). The extent to which these energy transport mechanisms affect the neutrino emission depends on the size of the convectively stable layer between the convective region and the neutrinosphere, where the energy can be transported only by means of neutrino diffusion. Except for in the analysis of Bruenn et al. (2004), this layer is found to be much larger than in Wilson & Mayle (1993). The question whether the convection-induced increase of the

neutrino flux can change the supernova dynamics significantly can only be answered by fully multi-dimensional supernova simulations with an adequate treatment of the neutrino physics.

The other convective instability occurs far above the neutrinosphere in the gain layer. Here, the neutrino heating of the material, the strength of which decreases quickly with increasing distance from the gain radius, establishes a negative entropy profile which makes the region convectively unstable (Bethe 1990; Herant et al. 1992). This convection transports heated material from close to the gain radius to just below the shock. Thereby the material expands nearly adiabatically and thus no longer is prone to energy losses via neutrino reemission. The expansion also pushes the shock farther out. Simultaneously yet unheated matter from above can flow down past the uprising matter to be heated more efficiently. Again, the results of numerical simulations of this so-called "hot bubble" convection are controversial. While all simulations feature this neutrino-driven convective instability and numerical parameter studies confirm that it is helpful for shock revival (Janka & Müller 1996), only in some of the simulations this decides the explosion (Herant et al. 1992, 1994; Burrows et al. 1995; Fryer 1999; Fryer & Heger 2000; Fryer & Warren 2002, 2004), while others find this process to be too weak (Miller et al. 1993; Mezzacappa et al. 1998b).

While all the just mentioned simulations use for the description of the neutrino transport a diffusion scheme in which a flux limiter governs the transition from diffusion to free streaming, the class of exploding simulations assumes a thermal spectrum for the neutrinos and thus does not adequately account for the fact that the cross sections of neutrino interactions are very sensitive to the neutrino energy and the heating may thus be altered significantly for non-thermal spectra. Although Mezzacappa et al. (1998b) therefore uses the more elaborate multi-energy group treatment, the flux-limited diffusion scheme is known to lead to too large neutrino fluxes and therefore underestimates the neutrino density and thus heating in the gain layer (Messer et al. 1998; Yamada et al. 1999).

Other multi-dimensional effects which have been under suspicion of helping with the explosion since Leblanc & Wilson (1970) are rotation and magnetic fields: Strong rotation can deform the proto neutron star, affect convective processes significantly, alter the neutrino emission, and provides an energy reservoir in form of rotational energy. Due to the action of magnetic fields supernovae are further believed to be able to create jet-like outflow. Magnetic fields and rotation could probably even link the enigmatic gamma ray bursts with supernovae, see Postnov (2004) for a recent collection of scenarios with magnetic fields. However, it is still uncertain how fast rotation and how strong magnetic fields can become in the cores of evolved massive stars. Recent calculations suggest moderate rotation (Heger et al. 2004) which would hardly affect the stellar core collapse and supernova evolution. In addition, the observation of neutron stars which are not pulsars, in particular the compact remnant of Cas A, and thus either lack strong rotation or strong magnetic fields or both can be interpreted such that the explosion mechanism does not depend on rotation or magneto-hydrodynamic effects.

If we ignore all exotic effects which have been suggested to support the explosion of a supernova, such as photon–mirror photon mixing in a left-right symmetric gauge group (Foot & Silagadze 2004) or non-standard neutrino interaction rates (Rampp et al. 2002; Amanik et al. 2004), as well as rapid rotation and strong magnetic fields, we are left with a model for the explosion mechanism in which neutrinos, supported by convective instabilities in two regions above and below the neutrinosphere, revive the stalled shock on a timescale of several hundred milliseconds. No doubt the reader has noted that the main uncertainty in previous simulations

discussed above was always concerning the treatment of neutrino transport and neutrino interactions. This is a critical shortcoming because the neutrinos are the main means of energy transport between the proto neutron star and the gain layer. It is exactly in this region where approximations of the neutrino transport mostly fails because the neutrinos still interact too frequently with the medium to be treated as freely streaming but also are no longer trapped so that the diffusion limit does not hold. Further, the energy emitted in form of neutrinos is more than a factor of ten larger than the amount needed for shock revival. Thus, e.g. absorbing only one additional percent of the total neutrino flux can have a dramatic influence on the evolution of the shock.

With the development of numerical codes which solve the energy-dependent Boltzmann equations in spherical symmetry for neutrinos in the supernova environment (Mezzacappa & Bruenn 1993a; Burrows et al. 2000; Rampp & Janka 2002) a strongly improved and now very reliable treatment of neutrino transport has recently become possible. The computational power has now reached a level where these equations can be solved with sufficient resolution in a reasonable amount of time, which was not the case a few years ago, see e.g. Yamada et al. (1999). Further, neutrino interactions which play a role in the supernova environment have been calculated to better accuracy or have only recently been recognized in their importance (Hannestad & Raffelt 1998; Burrows & Sawyer 1998, 1999; Buras et al. 2003, and many more). These advancements allowed me to perform one-dimensional simulations for various progenitors with 11.2–25 solar masses, using the neutrino transport and hydrodynamics code VERTEX[1] of Rampp & Janka (2002) which was supplemented with an update of all relevant neutrino interaction rates. These simulations together with those presented by Mezzacappa et al. (2001), Liebendörfer et al. (2001), and Thompson et al. (2003) have finally proven that Wilsons delayed neutrino-driven mechanism definitely does not work in spherical symmetry.

The most important goal of this work, however, was the application of the improved energy-dependent treatment of neutrino transport in two-dimensional hydrodynamic supernova simulations, which take into account the effects of convection. The extension of the code VERTEX to two dimensions is called MuDBaTH[2] and features a reasonable approximation of the non-radial part of the neutrino transport which can be justified in the absence of a strong deformation of the proto neutron star from spherical symmetry due to rapid rotation. The current version of MuDBaTH does not allow for simulations in three dimensions. Although an extension to three dimensions is straightforward, it currently is not feasible due to the computational limitations. Yet two dimensions are already sufficient for a description of basic effects of convection. Therefore these runs, which have been performed for three different progenitor models with masses varying from 11.2 to 20 solar masses, represent the world-wide first simulations with both an accurate spectral treatment of the neutrino transport and the multi-dimensional feature of convection.

The implications of this new generation of models are manifold. They show a moderate sensitivity of the dynamical evolution of core collapse supernovae on the progenitor model in spherical symmetry. Comparison with simulations with previously used approximations of the neutrino interaction rates also reveal only moderate differences. The effects of convective processes are most significant. The two-dimensional models confirm the existence of convection both in the proto neutron star as well as in the gain layer, and show that convection can take the evolution

[1] An abbreviation of **V**ariable **E**ddington factor **R**adiative **T**ransfer for supernova **Ex**plosions.

[2] An abbreviation of **Mu**lti-**D**imensional **B**oltzm**a**nn **T**ransport and **H**ydro.

considerably closer to explosion. For one model indeed a weak explosion is obtained.

The simulations are also interesting in other aspects. They provide detailed and reliable information about the spectra and fluxes of the emitted neutrinos of all types (ν_e, $\bar{\nu}_e$, ν_μ, ...) which have been used in detection analyses of supernova neutrinos (Kachelriess et al. 2004). Further, by artificially inducing an explosion in a two-dimensional model the neutron-to-proton ratio in the supernova ejecta could be determined more reliably than before with less sophisticated neutrino treatments. This led to interesting results for the nuclear composition of these ejecta (Pruet et al. 2004).

This thesis is splitted in three parts. In Chapter 2 I describe and justify the technical details of how the one-dimensional code VERTEX (described in Rampp & Janka 2002) was extended to two dimensions, creating the code MuDBaTH. In Chapter 3 all models, i.e. one- and two-dimensional ones, are presented that used the "reference" progenitor model s15s7b2 of Woosley & Weaver (1995). Chapter 4 discusses simulations for nine different progenitor models in spherical symmetry. Two progenitor models were investigated by two-dimensional runs and were compared with the two-dimensional run for the progenitor s15s7b2. Finally, in Section 4.3.3 a simulation that produces a weak explosion is discussed. Although this model should be interpreted carefully, it supports my conclusions in Chapter 5 that the explosion mechanism is nearly understood.

2 Equations for the two-dimensional problem and their numerical implementation

A variable Eddington factor method was developed by Rampp (2000) and Rampp & Janka (2002) for tackling the Boltzmann equation of neutrino transport in spherically symmetric simulations of core-collapse supernovae. They also proposed a generalization of their method to multi-dimensional problems (see Rampp & Janka 2002, Sect. 3.8). Based on their suggestions, we have developed a two-dimensional version of their code, called MuDBaTH (MUlti-Dimensional BoltzmAnn Transport and Hydrodynamics).

We will elaborate on the equations to be solved in multidimensional problems, present a detailed discussion of the approximations we found necessary to achieve a tolerable computational speed, and point out possible limitations of our approach. We also describe a new treatment of the equation of state (EoS) in the sub-nuclear density regime and compare a dynamic model obtained with this EoS with the corresponding model that was computed with the EoS of Rampp & Janka (2002).

In order to be able to exploit symmetries of the problem we work in a system of spherical coordinates with radius r, latitudinal angle ϑ, and longitudinal angle φ. For all simulations performed so far we have assumed that azimuthal symmetry holds with respect to the polar axis, but a generalization of the presented method to three-dimensional situations is straightforward.

Like the one-dimensional version documented by Rampp & Janka (2002) the algorithm relies on an operator splitting approach which means that the coupled system of evolution equations is processed in two independent steps, a hydrodynamic step and a neutrino-transport/interaction step. In each timestep these two steps are solved subsequently.

2.1 Hydrodynamics

For an ideal fluid characterized by the mass density ρ, the radial, lateral, and azimuthal components of the velocity vector $(v_r, v_\vartheta, v_\varphi)$, specific energy $\varepsilon = e + \frac{1}{2}(v_r^2 + v_\vartheta^2 + v_\varphi^2)$ and gas pressure p, the Eulerian, nonrelativistic equations of hydrodynamics in spherical coordinates and azimuthal symmetry read:

$$\frac{\partial}{\partial t}\rho + \frac{1}{r^2}\frac{\partial}{\partial r}\left(r^2 \rho\, v_r\right) + \frac{1}{r\sin\vartheta}\frac{\partial}{\partial \vartheta}\left(\rho \sin\vartheta\, v_\vartheta\right) = 0\,, \tag{2.1}$$

$$\frac{\partial}{\partial t}(\rho v_r) + \frac{1}{r^2}\frac{\partial}{\partial r}\left(r^2 \rho v_r\, v_r\right) + \frac{1}{r\sin\vartheta}\frac{\partial}{\partial \vartheta}\left(\rho \sin\vartheta\, v_\vartheta\, v_r\right) + \frac{\partial p}{\partial r} = -\rho\frac{\partial \Phi}{\partial r} + Q_{\mathrm{M}r}\,, \tag{2.2}$$

$$\frac{\partial}{\partial t}(\rho v_\vartheta) + \frac{1}{r^2}\frac{\partial}{\partial r}\left(r^2 \rho v_r\, v_\vartheta\right) + \frac{1}{r\sin\vartheta}\frac{\partial}{\partial \vartheta}\left(\rho \sin\vartheta\, v_\vartheta\, v_\vartheta\right) + \frac{1}{r}\frac{\partial p}{\partial \vartheta} = -\frac{\rho}{r}\frac{\partial \Phi}{\partial \vartheta} + Q_{\mathrm{M}\vartheta}\,, \tag{2.3}$$

$$\frac{\partial}{\partial t}\left(\rho v_\varphi\right) + \frac{1}{r^2}\frac{\partial}{\partial r}\left(r^2 \rho v_r\, v_\varphi\right) + \frac{1}{r\sin\vartheta}\frac{\partial}{\partial \vartheta}\left(\rho \sin\vartheta\, v_\vartheta\, v_\varphi\right) = 0\,, \tag{2.4}$$

$$\frac{\partial}{\partial t}(\rho\varepsilon) + \frac{1}{r^2}\frac{\partial}{\partial r}\left(r^2\,(\rho\varepsilon + p)\; v_r\right) + \frac{1}{r\sin\vartheta}\frac{\partial}{\partial \vartheta}\Big(\,(\rho\varepsilon + p)\sin\vartheta\, v_\vartheta\Big) = -\rho\left(v_r\frac{\partial \Phi}{\partial r} + \frac{v_\vartheta}{r}\frac{\partial \Phi}{\partial \vartheta}\right) + Q_{\mathrm{E}}\,, \tag{2.5}$$

where Φ denotes the gravitational potential of the fluid, and $\vec{Q}_{\mathrm{M}} = (Q_{\mathrm{M}r}, Q_{\mathrm{M}\vartheta})$ and Q_{E} are the neutrino source terms for momentum transfer and energy exchange, respectively. Eqs. (2.1–2.5) are closed by the equation of state (EoS) which, in the case of nuclear statistical equilibrium

(NSE), yields the pressure p for given ρ, e, and electron fraction Y_e. To achieve latter variable the hydrodynamic equations are supplemented by the conservation equation

$$\frac{\partial}{\partial t}\left(\rho Y_\mathrm{e}\right) + \frac{1}{r^2}\frac{\partial}{\partial r}\left(r^2 \rho Y_\mathrm{e}\, v_r\right) + \frac{1}{r\sin\vartheta}\frac{\partial}{\partial \vartheta}\left(\sin\vartheta\, \rho Y_\mathrm{e}\, v_\vartheta\right) = Q_\mathrm{N}\,, \tag{2.6}$$

where the source term $Q_\mathrm{N}/m_\mathrm{B}$ is the rate of change of the net electron number density (i.e. the density of electrons minus that of positrons) due to emission and absorption of electron-flavour neutrinos and m_B is the baryon mass. In case the medium is not in the state of NSE, the EoS additionally needs the chemical composition of the plasma to determine p. Thus, an equation like Eq. (2.6) also has to be solved for the abundance of each nucleus k, $Y_k \equiv n_k/n_\mathrm{by}$, using

$$\frac{\partial}{\partial t}\left(\rho Y_k\right) + \frac{1}{r^2}\frac{\partial}{\partial r}\left(r^2 \rho Y_k\, v_r\right) + \frac{1}{r\sin\vartheta}\frac{\partial}{\partial \vartheta}\left(\sin\vartheta\, \rho Y_k\, v_\vartheta\right) = R_k\,, \tag{2.7}$$

where n_k and n_by are the number density of nucleus k and the baryon number density, respectively, and $R_k \equiv \rho\,\delta Y_k/\delta t$, where $\delta Y_k/\delta t$ is a source term that describes the rate of composition changes by nuclear reactions for species k.

For the numerical integration of Eqs. (2.1–2.7) we employ the Newtonian finite-volume code PROMETHEUS (Fryxell et al. 1989, 2000), which was supplemented by additional problem specific features (Keil 1997) and the improvements described in Kifonidis et al. (2003). PROMETHEUS is a direct Eulerian implementation of the Piecewise Parabolic Method (PPM) of Colella & Woodward (1984). As a time-explicit, third-order in space, second-order in time Godunov scheme with a Riemann solver it is particularly well suited for following discontinuities in the fluid flow like shocks, contact discontinuities, or boundaries between layers of different chemical composition. A notable advantage in the present context is its capability of solving multi-dimensional problems with high computational efficiency and numerical accuracy. Our code makes use of the "Consistent Multifluid Advection" (CMA) method (Plewa & Müller 1999) for ensuring an accurate advection of different chemical components of the fluid, and switches from the original PPM method to the HLLE solver of Einfeldt (1988) in the vicinity of strong shocks to avoid spurious oscillations (the so-called "odd-even decoupling", or "carbunkel", phenomenon) when such shocks are aligned with one of the coordinate lines in multidimensional simulations (Quirk 1994; Liou 2000; Kifonidis et al. 2003; Sutherland et al. 2003).

Although our hydrodynamic scheme is Newtonian, we have included effects of general relativistic (GR) gravity approximately in the following way: the gravitational potential used in our simulations can be symbolically written as $\Phi(r,\vartheta) = \Phi^\mathrm{Newt}_\mathrm{2D}(r,\vartheta) + \left(\Phi^\mathrm{GR}_\mathrm{1D}(r) - \Phi^\mathrm{Newt}_\mathrm{1D}(r)\right)$. We compute the Newtonian gravitational potential $\Phi^\mathrm{Newt}_\mathrm{2D}$ for the two-dimensional axisymmetric mass distribution by expanding the integral solution of the Poisson equation into a Legendre series, truncated at $l = 10$ (cf. Müller & Steinmetz 1995). General relativistic effects are approximately taken into account by the spherically symmetric correction term $\Phi^\mathrm{GR}_\mathrm{1D} - \Phi^\mathrm{Newt}_\mathrm{1D}$, where $\Phi^\mathrm{GR}_\mathrm{1D}$ denotes an effective general relativistic gravitational potential as employed for spherically symmetric simulations (see Rampp & Janka 2002, Eq. 53) and $\Phi^\mathrm{Newt}_\mathrm{1D}$ is its Newtonian counterpart. The general relativistic potential $\Phi^\mathrm{GR}_\mathrm{1D}$ is deduced from a comparison of the Newtonian and relativistic equations of motion in spherical symmetry and includes terms due to the pressure and energy of the stellar medium and neutrinos (see Rampp & Janka 2002). Both, $\Phi^\mathrm{GR}_\mathrm{1D}(r)$ and $\Phi^\mathrm{Newt}_\mathrm{1D}(r)$ are computed using angular averages of the evolved variables. In two-dimensional simulations which cover only a limited range of latitudes $0 < \vartheta_\mathrm{min} \le \vartheta \le \vartheta_\mathrm{max} < \pi$ around the equatorial plane we set $\Phi(r,\vartheta) = \Phi^\mathrm{GR}_\mathrm{1D}(r)$.

The source terms $Q_{\mathrm{M}r}$, $Q_{\mathrm{M}\vartheta}$, Q_{E}, and Q_{N} on the right-hand sides of Eqs. (2.2,2.3,2.5,2.6) are determined by the solution of the neutrino transport equations. The source terms R_k depend on changes of the composition according to nuclear burning. Unless stated otherwise, the EoS we apply is the same as described in detail in (Rampp & Janka 2002, App. B).

Note that PROMETHEUS only solves the left-hand sides of the hydrodynamic Eqs. (2.1–2.7) and that the EoS is not evaluated during this procedure. The terms on the right-hand sides, i.e the gravitational, neutrino, and burning effects, as well as the evaluation of the EoS and, if applicable, of the NSE composition, are applied in operator split steps.

2.2 Neutrino transport

Solving the full two-dimensional set of moments equations is definitely the most precise way of simulating supernovae in two dimensions. However, starting from a one-dimensional code such an extension would be a huge step. It would introduce several more degrees of freedom to the moments equations which would require one additional moments equation to be solved and five more closure relations to account for. Thus we restrain ourselves to a mimimal extension of the one-dimensional moments equations to two dimensions in which new degrees of freedom (including, in case of our azimuthal symmetry, the lateral flux and off-diagonal pressure tensor terms which account for neutrino viscosity) are set to zero, but the additional moments equations (in our case for the lateral flux) is taken into account. In the next section, we will justify why we believe this approximation is sufficient for simulating two-dimensional neutrino transport in the context of core-collapse supernovae, but also explain why further simplifications are not allowed.

The great advantage of our minimal 2D neutrino transport is that the neutrino moments of different spatial angle (except for some terms which can be accounted for explicitly in an operator split) decouple from each other. Therefore, for each "radial ray", i.e. all zones of same spatial angle, the moments equations can be solved independently. Up to some terms this problem is identical to the problem of solving the moments equations for a spherically symmetric star.

We further make following usual assumptions: first, we ignore any kind of neutrino oscillations. This is justified if one ignores the results of LSND; then the parameters for atmospheric and solar neutrino oscillations predict the resonant MSW effect to be at densities far below $10^5\mathrm{g/cm}^3$ so that this effect has no influence on the region of interest. Furthermore, non-resonant oscillations are strongly suppressed in the proto neutron star (PNS) due to first and second order refractive effects, see Hannestad et al. (2000). Second, as the medium, even in the PNS, hardly contains any muons and tauons, which implies small or vanishing chemical potential for the μ and τ type neutrinos, and the opacities are nearly equal for ν_μ, $\bar{\nu}_\mu$, ν_τ, and $\bar{\nu}_\tau$ we treat these four neutrino types identically and set $\mu_{\nu_\mu} \equiv \mu_{\nu_\tau} \equiv 0$. We will notate them collectively as "ν_{x}".

2.2.1 Moments equations

In a two-dimensional transport scheme assuming azimuthal symmetry, the specific intensity $\mathcal{I}(t, r, \vartheta, \varphi, \epsilon, \boldsymbol{n})$ does not depend on the azimuth φ. We describe the direction of propagation $\boldsymbol{n}$ by the angle cosine $\mu \equiv \boldsymbol{n} \cdot \boldsymbol{r}/|\boldsymbol{r}|$, measured with respect to the radius vector $\vec{r}$, and the

angle ω. Then azimuthal symmetry implies $\mathcal{I}(\ldots,\mu,\omega) = \mathcal{I}(\ldots,\mu,-\omega)$, see also Appendix B. Making the additional assumption that $\mathcal{I}$ is independent of ω, each of the angular moments of the specific intensity can be expressed by one scalar, namely

$$\{J,H,K,L,\ldots\}(t,r,\vartheta,\epsilon) \equiv \frac{1}{2}\int_{-1}^{+1} \mathrm{d}\mu\, \mu^{\{0,1,2,3,\ldots\}}\, \mathcal{I}(t,r,\vartheta,\epsilon,\mu)\,, \tag{2.8}$$

where we have used the Eqs. (B.9-B.12), which follow from our assumptions, to reduce the number of independent variables in the angular moments of the neutrino intensity as defined in Eqs. (B.3). As usual, ϵ labels the energy of the neutrinos. As a consequence of the afore mentioned assumptions the three-dimensional set of moments equations for describing the evolution of neutrino energy and flux in the comoving frame, given by Eqs. (B.4-B.7) in the Newtonian, $O(v/c)$ approximation, simplifies to

$$\begin{aligned}
&\left(\frac{1}{c}\frac{\partial}{\partial t} + \beta_r\frac{\partial}{\partial r} + \frac{\boldsymbol{\beta_\vartheta}}{\boldsymbol{r}}\frac{\boldsymbol{\partial}}{\boldsymbol{\partial\vartheta}}\right) J + J\left(\frac{1}{r^2}\frac{\partial(r^2\beta_r)}{\partial r} + \frac{\mathbf{1}}{\boldsymbol{r}\sin\boldsymbol{\vartheta}}\frac{\boldsymbol{\partial}(\sin\boldsymbol{\vartheta}\boldsymbol{\beta_\vartheta})}{\boldsymbol{\partial\vartheta}}\right) \\
&+ \frac{1}{r^2}\frac{\partial(r^2 H)}{\partial r} + \frac{\beta_r}{c}\frac{\partial H}{\partial t} \\
&- \frac{\partial}{\partial\epsilon}\left\{\epsilon\left[\frac{1}{c}\frac{\partial\beta_r}{\partial t}H + K\left(\frac{\partial\beta_r}{\partial r} - \frac{\beta_r}{r} - \frac{\mathbf{1}}{\boldsymbol{2r}\sin\boldsymbol{\vartheta}}\frac{\boldsymbol{\partial}(\sin\boldsymbol{\vartheta}\boldsymbol{\beta_\vartheta})}{\boldsymbol{\partial\vartheta}}\right) + J\left(\frac{\beta_r}{r} + \frac{\mathbf{1}}{\boldsymbol{2r}\sin\boldsymbol{\vartheta}}\frac{\boldsymbol{\partial}(\sin\boldsymbol{\vartheta}\boldsymbol{\beta_\vartheta})}{\boldsymbol{\partial\vartheta}}\right)\right]\right\} \\
&+ K\left(\frac{\partial\beta_r}{\partial r} - \frac{\beta_r}{r} - \frac{\mathbf{1}}{\boldsymbol{2r}\sin\boldsymbol{\vartheta}}\frac{\boldsymbol{\partial}(\sin\boldsymbol{\vartheta}\boldsymbol{\beta_\vartheta})}{\boldsymbol{\partial\vartheta}}\right) + J\left(\frac{\beta_r}{r} + \frac{\mathbf{1}}{\boldsymbol{2r}\sin\boldsymbol{\vartheta}}\frac{\boldsymbol{\partial}(\sin\boldsymbol{\vartheta}\boldsymbol{\beta_\vartheta})}{\boldsymbol{\partial\vartheta}}\right) + \frac{2}{c}\frac{\partial\beta_r}{\partial t}H = C^{(0)}\,,
\end{aligned} \tag{2.9}$$

$$\begin{aligned}
&\left(\frac{1}{c}\frac{\partial}{\partial t} + \beta_r\frac{\partial}{\partial r} + \frac{\boldsymbol{\beta_\vartheta}}{\boldsymbol{r}}\frac{\boldsymbol{\partial}}{\boldsymbol{\partial\vartheta}}\right) H + H\left(\frac{1}{r^2}\frac{\partial(r^2\beta_r)}{\partial r} + \frac{\mathbf{1}}{\boldsymbol{r}\sin\boldsymbol{\vartheta}}\frac{\boldsymbol{\partial}(\sin\boldsymbol{\vartheta}\boldsymbol{\beta_\vartheta})}{\boldsymbol{\partial\vartheta}}\right) \\
&+ \frac{\partial K}{\partial r} + \frac{3K - J}{r} + H\left(\frac{\partial\beta_r}{\partial r}\right) + \frac{\beta_r}{c}\frac{\partial K}{\partial t} \\
&- \frac{\partial}{\partial\epsilon}\left\{\epsilon\left[\frac{1}{c}\frac{\partial\beta_r}{\partial t}K + L\left(\frac{\partial\beta_r}{\partial r} - \frac{\beta_r}{r} - \frac{\mathbf{1}}{\boldsymbol{2r}\sin\boldsymbol{\vartheta}}\frac{\boldsymbol{\partial}(\sin\boldsymbol{\vartheta}\boldsymbol{\beta_\vartheta})}{\boldsymbol{\partial\vartheta}}\right) + H\left(\frac{\beta_r}{r} + \frac{\mathbf{1}}{\boldsymbol{2r}\sin\boldsymbol{\vartheta}}\frac{\boldsymbol{\partial}(\sin\boldsymbol{\vartheta}\boldsymbol{\beta_\vartheta})}{\boldsymbol{\partial\vartheta}}\right)\right]\right\} \\
&+ \frac{1}{c}\frac{\partial\beta_r}{\partial t}(J + K) = C_r^{(1)}\,,
\end{aligned} \tag{2.10}$$

where, $\beta_r = v_r/c$ and $\beta_\vartheta = v_\vartheta/c$. For the moment, Eqs. (B.6-B.7) can be ignored as the variables which evolution they describe, i.e. H_ϑ and H_φ, are strictly zero. The functional dependences $\beta_r = \beta_r(t,r,\vartheta)$, $J = J(t,r,\vartheta,\epsilon)$, $\ldots$, are suppressed in the notation. With $\mathcal{J} = J/\epsilon$, $\mathcal{H} = H/\epsilon$, $\mathcal{K} = K/\epsilon$, and $\mathcal{L} = L/\epsilon$, the moments equations describing the evolution of neutrino number

read

$$\left(\frac{1}{c}\frac{\partial}{\partial t}+\beta_r\frac{\partial}{\partial r}+\boldsymbol{\frac{\beta_\vartheta}{r}\frac{\partial}{\partial\vartheta}}\right)\mathcal{J}+\mathcal{J}\left(\frac{1}{r^2}\frac{\partial(r^2\beta_r)}{\partial r}+\boldsymbol{\frac{1}{r\sin\vartheta}\frac{\partial(\sin\vartheta\beta_\vartheta)}{\partial\vartheta}}\right) \tag{2.11}$$
$$+\frac{1}{r^2}\frac{\partial(r^2\mathcal{H})}{\partial r}+\frac{\beta_r}{c}\frac{\partial\mathcal{H}}{\partial t}$$
$$-\frac{\partial}{\partial\epsilon}\left\{\epsilon\left[\frac{1}{c}\frac{\partial\beta_r}{\partial t}\mathcal{H}+\mathcal{K}\left(\frac{\partial\beta_r}{\partial r}-\frac{\beta_r}{r}\boldsymbol{-\frac{1}{2r\sin\vartheta}\frac{\partial(\sin\vartheta\beta_\vartheta)}{\partial\vartheta}}\right)+\mathcal{J}\left(\frac{\beta_r}{r}\boldsymbol{+\frac{1}{2r\sin\vartheta}\frac{\partial(\sin\vartheta\beta_\vartheta)}{\partial\vartheta}}\right)\right]\right\}$$
$$+\frac{1}{c}\frac{\partial\beta_r}{\partial t}\mathcal{H}=C^{(0)}\,,$$

$$\left(\frac{1}{c}\frac{\partial}{\partial t}+\beta_r\frac{\partial}{\partial r}+\boldsymbol{\frac{\beta_\vartheta}{r}\frac{\partial}{\partial\vartheta}}\right)\mathcal{H}+\mathcal{H}\left(\frac{1}{r^2}\frac{\partial(r^2\beta_r)}{\partial r}+\boldsymbol{\frac{1}{r\sin\vartheta}\frac{\partial(\sin\vartheta\beta_\vartheta)}{\partial\vartheta}}\right) \tag{2.12}$$
$$+\frac{\partial\mathcal{K}}{\partial r}+\frac{3\mathcal{K}-\mathcal{J}}{r}+\mathcal{H}\left(\frac{\partial\beta_r}{\partial r}\right)+\frac{\beta_r}{c}\frac{\partial\mathcal{K}}{\partial t}$$
$$-\frac{\partial}{\partial\epsilon}\left\{\epsilon\left[\frac{1}{c}\frac{\partial\beta_r}{\partial t}\mathcal{K}+\mathcal{L}\left(\frac{\partial\beta_r}{\partial r}-\frac{\beta_r}{r}\boldsymbol{-\frac{1}{2r\sin\vartheta}\frac{\partial(\sin\vartheta\beta_\vartheta)}{\partial\vartheta}}\right)+\mathcal{H}\left(\frac{\beta_r}{r}\boldsymbol{+\frac{1}{2r\sin\vartheta}\frac{\partial(\sin\vartheta\beta_\vartheta)}{\partial\vartheta}}\right)\right]\right\}$$
$$-\mathcal{L}\left(\frac{\partial\beta_r}{\partial r}-\frac{\beta_r}{r}\boldsymbol{-\frac{1}{2r\sin\vartheta}\frac{\partial(\sin\vartheta\beta_\vartheta)}{\partial\vartheta}}\right)-\mathcal{H}\left(\frac{\beta_r}{r}\boldsymbol{+\frac{1}{2r\sin\vartheta}\frac{\partial(\sin\vartheta\beta_\vartheta)}{\partial\vartheta}}\right)+\frac{1}{c}\frac{\partial\beta_r}{\partial t}\mathcal{J}=C_r^{(1)}\,.$$

This system of moments equations (2.9–2.12) is very similar to the Newtonian, $O(v/c)$ moments equations in spherical symmetry (see Rampp & Janka 2002, Eqs. 7,8,30,31), we have set the additional terms arising from our approximative generalization to two dimensions in boldface. Adding general relativistic (GR) effects in the spirit of Rampp & Janka (2002) to our approximative 2D transport proves not to alter the boldface terms, so that the corresponding equations are Eqs. (54–57) in the latter paper, which handle the GR effects for 1D transport, plus those terms in Eqs. (2.9–2.12) that are typeset in boldface. The equations are closed by substituting $K = f_K \cdot J$ and $L = f_L \cdot J$, where f_K and f_L are the variable Eddington factors.

In order to discretize Eqs. (2.9–2.12), the computational domain $[0, r_{\rm max}]\times[\vartheta_{\rm min}, \vartheta_{\rm max}]$ is covered by N_r radial and N_ϑ angular zones, where $\vartheta = 0, \pi$ correspond to the polar axis and $\vartheta = \pi/2$ to the equatorial plane of the spherical grid. All radiation variables are defined on the angular centres of the zones with the coordinate $\vartheta_{k+\frac{1}{2}} \equiv \frac{1}{2}(\vartheta_k + \vartheta_{k+1})$ being defined as the arithmetic mean of the corresponding interface values. The equations are solved in two operator splitted steps corresponding to a lateral and a radial sweep.

In a first step, we treat the boldface terms in the respectively first lines of Eqs. (2.9–2.12) which describe the lateral advection of the neutrinos with the stellar fluid, and thus couple the radiation moments of neighbouring angular zones. For this purpose we solve the equation

$$\frac{1}{c}\frac{\partial\Xi}{\partial t}+\frac{1}{r\sin\vartheta}\frac{\partial(\sin\vartheta\,\beta_\vartheta\,\Xi)}{\partial\vartheta}=0\,, \tag{2.13}$$

where Ξ represents one of the moments J, H, $\mathcal{J}$, or $\mathcal{H}$. After integration over the volume of a zone $(i+\frac{1}{2}, k+\frac{1}{2})$ the finite-differenced version of Eq. (2.13) reads:

$$\frac{\Xi^{n+1}_{i+\frac{1}{2},k+\frac{1}{2}}-\Xi^{n}_{i+\frac{1}{2},k+\frac{1}{2}}}{ct^{n+1}-ct^{n}}$$
$$+\frac{1}{\Delta V_{i+\frac{1}{2},k+\frac{1}{2}}}\left(\Delta A_{i+\frac{1}{2},k+1}\beta_{\vartheta\,i+\frac{1}{2},k+1}\Xi^{n}_{i+\frac{1}{2},\kappa_{i+1/2}(k+1)}-\Delta A_{i+\frac{1}{2},k}\beta_{\vartheta\,i+\frac{1}{2},k}\Xi^{n}_{i+\frac{1}{2},\kappa_{i+1/2}(k)}\right)=0\,, \tag{2.14}$$

with the volume element $\Delta V_{i+\frac{1}{2},k+\frac{1}{2}} = \frac{2\pi}{3}\,(r_{i+1}^3 - r_i^3)\,(\cos\vartheta_k - \cos\vartheta_{k+1})$ and the surface element $\Delta A_{i+\frac{1}{2},k} = \pi\,(r_{i+1}^2 - r_i^2)\sin\vartheta_k$. Note that additional indices of Ξ which label energy bins and the different types of neutrinos are suppressed for clarity. To guarantee monoticity, upwind values of the moments $\Xi^n_{i+\frac{1}{2},\kappa_{i+1/2}(k)}$, with

$$\kappa_{i+1/2}(k) \equiv \begin{cases} k - \frac{1}{2} & \text{for} \quad \beta_{\vartheta\, i+\frac{1}{2},k} > 0\,, \\ k + \frac{1}{2} & \text{else}\,, \end{cases} \tag{2.15}$$

are used for computing the lateral fluxes across the interfaces of the angular zones. The time-step limit enforced by the Courant-Friedrichs-Lewy (CFL) condition is

$$\Delta t_{\mathrm{CFL}} = \min_{i,k} \frac{\Delta x_{\vartheta;i+\frac{1}{2},k+\frac{1}{2}}}{\left|v_{\vartheta;i+\frac{1}{2},k+\frac{1}{2}}\right|}, \tag{2.16}$$

where Δx_ϑ is the zone width in lateral direction. It turns out that this condition is not restrictive in our simulations. In practice, the numerical time-step is always limited by other constraints.

Now, in the second step, the radial sweep for solving Eqs. (2.9–2.12) is performed. Considering a radial ray with given $\vartheta_{k+\frac{1}{2}}$, the radial discretization of the equations (and of their general relativistic counterparts) proceeds exactly as detailed in Rampp & Janka (2002). The terms in boldface not yet taken into account in the lateral sweep do not couple the radiation moments of neighbouring angular zones and thus can be included into the discretization scheme of the radial sweep in a straightforward way.

It should be noted that so far we have not included in our computer code the $\beta_r\,\partial/\partial t$-derivatives of the moments which appear at the end of the respective second lines of Eqs. (2.9–2.12), cf. Rampp & Janka (2002).

2.2.2 Eddington factors

In analogy to the treatment of the moments equations in the previous section the calculation of the variable Eddington factors could in principle also be done on (almost) decoupled radial rays. However, such a procedure would account for a sizeable amount of computer time. On the other hand, the Eddington factors are normalized moments of the neutrino phase space distribution and thus, in the absence of persistent global deformation of the star, should not show significant variation with the angular coordinate (cf. Rampp 2000; Rampp & Janka 2002). Therefore we have decided to determine the variable Eddington factors only once for an "angular averaged" radial ray instead of computing them for each radial ray separately. The corresponding reduction of the computational load can be up to a factor of 10 (Rampp & Janka 2002). We will discuss and try to estimate the possible errors associated with our approximate 2D transport treatment in Sect. 2.3.

Independent of, and in advance of, our two dimensional approximation of the moments equations, the code solves a time-step of the one-dimensional neutrino transport on a spherically symmetric image of the stellar background. The latter is defined as the angular averages of structure variables $\xi \in \{\rho, T, Y_\mathrm{e}, \beta_r, \dots\}$ according to $\xi(t,r) \equiv \frac{1}{b-a}\int_a^b d\cos\vartheta\;\xi(t,r,\vartheta)\;f(t,r,\vartheta)$, where $a = \cos(\vartheta_{\max})$ and $b = \cos(\vartheta_{\min})$ and f is a weighting function which can be either ρ or 1

depending on which choice is more sensible. The computation of the 1D transport step proceeds exactly as described for the spherically symmetric version of the code, i.e. the coupled set of the 1D moments equations and a 1D model Boltzmann equation are iterated to convergence to obtain solutions for the variable Eddington factors f_{K} and f_{L} (see Rampp & Janka 2002). These variable Eddington factors are used for all latitudes ϑ of the multidimensional transport grid when solving the two-dimensional moments equations.

2.2.3 Coupling to the hydrodynamics

The system of neutrino transport equations (2.9–2.12) is coupled with the equations of hydrodynamics (2.1–2.6) by virtue of the source terms

$$Q_{\mathrm{N}} = \sum_{\nu} -4\pi\, m_{\mathrm{B}}\, \mathrm{sgn}(\nu) \int_0^\infty \mathrm{d}\epsilon\, \mathfrak{C}_\nu^{(0)}(\epsilon)\,, \tag{2.17}$$

$$Q_{\mathrm{E}} = \sum_{\nu} -4\pi \int_0^\infty \mathrm{d}\epsilon\, C_\nu^{(0)}(\epsilon)\,, \tag{2.18}$$

$$Q_{\mathrm{M}r} = \sum_{\nu} -\frac{4\pi}{c} \int_0^\infty \mathrm{d}\epsilon\, C_{r,\nu}^{(1)}(\epsilon)\,, \tag{2.19}$$

$$Q_{\mathrm{M}\vartheta} = \sum_{\nu} -\frac{4\pi}{c} \int_0^\infty \mathrm{d}\epsilon\, C_{\vartheta,\nu}^{(1)}(\epsilon)\,, \tag{2.20}$$

where m_{B} denotes the baryon mass, $\mathfrak{C}_\nu^{(0)}(\epsilon) \equiv \epsilon^{-1} C_\nu^{(0)}(\epsilon)$, and $C_\nu^{(0)}(t,r,\vartheta,\epsilon) \equiv (4\pi)^{-1} \int \mathrm{d}\Omega\, C_\nu(t,r,\vartheta,\epsilon,\vec{n})$ and $\boldsymbol{C}_\nu^{(1)}(t,r,\vartheta,\epsilon) = \left(C_{r,\nu}^{(1)}, C_{\vartheta,\nu}^{(1)}\right) = (4\pi)^{-1} \int \mathrm{d}\Omega\, \boldsymbol{n}\, C_\nu(t,r,\vartheta,\epsilon,\vec{n})$ are angular moments of the collision integral of the Boltzmann equation, C_ν. Note that in Eqs. (2.17–2.20) the moments of the collision integral are summed over all neutrino types $\nu \in \{\nu_{\mathrm{e}}, \bar{\nu}_{\mathrm{e}}, \nu_\mu, \bar{\nu}_\mu, \nu_\tau, \bar{\nu}_\tau\}$, and $\mathrm{sgn}(\nu) = +1$ for neutrinos and -1 for antineutrinos. Remember that we treat ν_μ, $\bar{\nu}_\mu$, ν_τ and $\bar{\nu}_\tau$ identically because their matter interactions are nearly equal. They do not transport electron lepton number and therefore do not contribute to Q_{N}. In the following we suppress the index ν.

Our simplification of the neutrino transport equations enforces a *radial* flux vector, i.e. the angular flux component $H_\vartheta \equiv 0$. However, as we shall demonstrate below, the corresponding lateral component of the momentum transfer from neutrinos to the stellar medium, described by the source term $Q_{\mathrm{M}\vartheta}$, can not be neglected in the Euler equation of the stellar fluid (2.3) when the neutrinos are tightly coupled to the medium. This implies that we should solve the moments equation for the lateral transport of neutrino momentum (B.6) which, using the assumptions Eqs. (B.9-B.12), simplifies to

$$\begin{aligned} C_\vartheta^{(1)}(\epsilon) = {} & \left(\frac{\partial\beta_\vartheta}{\partial r} - \frac{\beta_\vartheta}{r}\right) H + \frac{1}{2r}\frac{\partial(J-K)}{\partial\vartheta} + \frac{1}{2c}\frac{\partial\beta_\vartheta}{\partial t}(3J-K) + \frac{\beta_\vartheta}{2c}\frac{\partial(J-K)}{\partial t} \\ & - \frac{\partial}{\partial\epsilon}\left\{\epsilon\left[\frac{1}{2c}\frac{\partial\beta_\vartheta}{\partial t}(J-K) + \frac{1}{2}\left(\frac{\partial\beta_\vartheta}{\partial r} + \frac{1}{r}\frac{\partial\beta_r}{\partial\vartheta} - \frac{\beta_\vartheta}{r}\right)(H-L)\right]\right\}. \end{aligned} \tag{2.21}$$

On the other hand, under the conditions present in the optically thick PNS diffusion is a good approximation (i.e. $J \equiv 3K$) and the above equation simplifies considerably to (assuming also stationary and static conditions, $\partial/\partial t \equiv 0$ and $\vec{\beta} \equiv 0$)

$$C_\vartheta^{(1)}(\epsilon) = \frac{1}{2r}\frac{\partial(J-K)}{\partial\vartheta} = \frac{1}{3r}\frac{\partial J}{\partial\vartheta}\,. \tag{2.22}$$

Given $J(r, \vartheta)$ as the solution of the moments equations (2.9, 2.10), Eq. (2.22) together with the definition Eq. (2.20) allows us to compute an approximation for the momentum exchange rate, $Q_{\mathrm{M}\vartheta}$, between neutrinos and the stellar fluid. Applying this procedure in supernova simulations turned out to give satisfactory results (see Sect. 2.3.2).

Finally, Eq. (B.7) would result in a momentum transfer from the neutrinos to the medium in azimuthal direction, $C_\varphi^{(1)}$, in the presence of rotation, $\beta_\varphi \neq 0$. Using our usual assumptions Eqs. (B.9-B.12) we obtain for Eq. (B.7)

$$\begin{aligned} C_\varphi^{(1)}(\epsilon) &= \left(\frac{\partial\beta_\varphi}{\partial r} - \frac{\beta_\varphi}{r}\right) H + \frac{1}{2c}\frac{\partial\beta_\varphi}{\partial t}(3J - K) + \frac{\beta_\varphi}{2c}\frac{\partial(J-K)}{\partial t} \\ &\quad - \frac{\partial}{\partial\epsilon}\left\{\epsilon\left[\frac{1}{2c}\frac{\partial\beta_\varphi}{\partial t}(J-K) + \frac{1}{2}\left(\frac{\partial\beta_\varphi}{\partial r} - \frac{\beta_\varphi}{r}\right)(H-L)\right]\right\} \end{aligned} \tag{2.23}$$

However, again assuming diffusion, stationary and static conditions, this term vanishes completely.

The numerical discretization of Eq. (2.22) reads

$$C^{(1)}_{\vartheta\ i+\frac{1}{2},k+\frac{1}{2}} = \frac{J_{i+\frac{1}{2},k+\frac{3}{2}} - J_{i+\frac{1}{2},k-\frac{1}{2}}}{3\, r_{i+\frac{1}{2}}(\vartheta_{k+\frac{3}{2}} - \vartheta_{k-\frac{1}{2}})}. \tag{2.24}$$

Since Eq. (2.22) is only valid in the limit of an optically thick medium we set $C^{(1)}_{\vartheta\ i+\frac{1}{2},k+\frac{1}{2}} = 0$ if the density $\rho_{i+\frac{1}{2},k+\frac{1}{2}}$ in a zone drops below 10^{12} g cm^{-3}. The chosen cut-off value is obviously specific to the core-collapse supernova problem where outside of this density the neutrino pressure gradients, in particular in the lateral direction, turn out to be negligibly small.

2.3 Discussion and tests of the numerical scheme

In the last section we described our implementation of an approximative neutrino transport scheme for two-dimensional geometry with spherical coordinates and azimuthal symmetry.

Besides adopting the approximations of general relativistic effects from the spherically symmetric VERTEX code of Rampp & Janka (2002) we made two major approximations of the transport equations. First, the dependence of the specific intensity on the direction of propagation $\vec{n}$ is replaced by a dependence on only one angle cosine μ. Secondly and closely related to the first approximation, we use scalar variable Eddington factors. These are obtained from the solution of the one-dimensional transport equations on a spherically symmetric image of the stellar background. Note, however, that our treatment described here is considerably less approximative than the simpler ray-by-ray transport scheme suggested in Rampp & Janka (2002, Sect. 3.8).

In the following we point out limitations of our approach and try to critically assess their influence on the results obtained with our method.

2.3.1 Treatment of general relativity

The radial neutrino transport contains gravitational redshift and time dilation, but ignores the distinction between coordinate radius and proper radius. This simplification is necessary for coupling the transport code to our basically Newtonian hydrodynamics. Of course, one would ultimately have to work in a genuinely multi-dimensional GR framework which, among other complications (see e.g. Cardall & Mezzacappa 2003), entails abandoning the use of the Lindquist metric.

Tests showed that in spherically symmetric simulations our approximations seem to work satisfactorily well (Liebendörfer et al. 2003), at least as long as there are only moderate (~10–20%) deviations of the metric coefficients from unity and the infall velocities do not reach more than 10–20% of the speed of light in decisive phases of the evolution. Unless very extreme conditions are considered (e.g. very rapid rotation or a very compact collapsed stellar core) gravity effects in the supernovae are dominated by radial gradients. We therefore expect that new effects from multi-dimensional GR are small and are likely to be dwarfed by the other approximations made in the multi-dimensional treatment of the transport.

2.3.2 Lateral advection and neutrino pressure gradients

A ray-by-ray non-equilibrium transport scheme which completely neglects lateral gradients in the moments equations (as e.g. suggested by Rampp & Janka 2002) is not suitable for multi-dimensional core-collapse supernova simulations. Performing numerical experiments we found empirically that disregarding terms in the neutrino moments equations that assure lateral coupling of the radial rays gives rise to unphysical fluid instabilities that grow from small perturbations in regions of the proto neutron star which are not expected to become unstable.

There are two reasons which we made out for this effect. First, in optically thick regions where neutrinos are tightly coupled to the stellar fluid, neutrinos must be allowed to be carried along with laterally moving fluid elements. This assures the conservation of the total lepton number ($Y_{\mathrm{lep}} = Y_{\mathrm{e}} + Y_{\nu}$) in these fluid elements in the absence of neutrino transport relative to the medium. If this conservation is violated, e.g. by omitting the terms describing lateral advection in the neutrino moments equations, fluctuations in the lepton number are artificially induced which grow and trigger macroscopic fluid motions. Secondly, when neutrinos yield a significant contribution to the pressure (as is the case in the dense interior of the hot, nascent neutron star) the inclusion of lateral neutrino pressure gradients is again important to prevent artificial acceleration of the fluid by gradients of the gas pressure.

In contrast, the omission of angular flux components ($H_{\vartheta} = 0$) means the disregard of "active propagation" of neutrinos relative to the stellar fluid. This is unlikely to lead to fundamental inconsistencies, because it is the correct physical limit for situations where the opacity is very high. In the same spirit also off-diagional terms of the neutrino pressure tensor (P_{ij} with $i \neq j$) can be dropped, implying that effects of neutrino viscosity are ignored.

We point out here that another inconsistency is imported into our treatment of 2D transport. The omission of angular flux components causes the problem that the correct limit at large radii and small optical depth may not be accurately reproduced since the neutrino density and flux are still advected laterally in accordance with fluid elements as though they would be strongly coupled

to the medium. Fortunately, here the specifics of the supernova problem help us justifying our approach: at large radii and low optical depth the lateral component v_ϑ of the fluid velocity is usually small so that all terms scaling with $\beta_\vartheta = v_\vartheta/c$ become of minor importance.

We performed three test calculations which were started by imposing random seed perturbations in the density with a maximum amplitude of ±2.5% on an early post-bounce model which was taken from a spherically symmetric simulation. The perturbed model was then evolved for a few milliseconds (corresponding to a multiple of the relevant dynamical timescale) in order to test different variants of the 2D transport code described above.

The time of the model was chosen such that the Ledoux criterion, evaluated for laterally averaged conditions,

$$C_\mathrm{L} \equiv \frac{ds}{dr}\left(\frac{\partial\rho}{\partial s}\right)_{Y_\mathrm{lep},P} + \frac{dY_\mathrm{lep}}{dr}\left(\frac{\partial\rho}{\partial Y_\mathrm{lep}}\right)_{s,P} \tag{2.25}$$

predicts stability everywhere inside the PNS, i.e. $C_\mathrm{L} < 0$. In Fig. 2.1b we show the corresponding Brunt-Väisälä frequency

$$\omega_\mathrm{BV} \equiv \mathrm{sign}(C_\mathrm{L})\sqrt{-\frac{g}{\rho}C_\mathrm{L}} \tag{2.26}$$

which is closely related to C_L and denotes the growth rate of fluctuations if positive (unstable) and the negative oscillation frequency for stable modes if negative.

Applying the Ledoux criterion here means that we assume that fluid elements do not exchange lepton number or heat with their environment. In the presence of neutrino diffusion this is not exactly true as was shown lately by Bruenn et al. (2004) where so-called "response functions" account for effective lepton number and entropy transport via diffusion induced by gradients of the same. Latter paper showed that including diffusive neutrino transport can affect the stability criteria significantly and can even be responsible for new types of convective instabilities. Unfortunately, latter paper did not present detailed information on the values of these response functions in the different regions of the proto neutron star. Since also the calculation of these response functions is not trivial, we restrained ourselves to use the Ledoux criterion as a measure for stability. We justify this simplification by the fact that this criterion actually predicts the stable and unstable regions in our 2D simulations fairly well, see Sect. 3.2.1 for a more elaborate discussion.

Figure 2.1a shows the standard deviation of density fluctuations in lateral direction

$$\sigma_\rho(r) \equiv \sqrt{\frac{1}{N}\sum_k \Delta\mathrm{c}\vartheta_k \cdot \left[\frac{\rho_k(r) - \langle\rho(r)\rangle_\vartheta}{\langle\rho(r)\rangle_\vartheta}\right]^2}, \tag{2.27}$$

where $\Delta\mathrm{c}\vartheta_k \equiv \cos(\vartheta_{k-\frac{1}{2}}) - \cos(\vartheta_{k+\frac{1}{2}})$, $N \equiv \sum_{k'} \Delta\mathrm{c}\vartheta_{k'}$, and $\langle\rho(r)\rangle_\vartheta \equiv \frac{1}{N}\sum_{k'}\rho_{k'}(r)\Delta\mathrm{c}\vartheta_{k'}$, as a function of radius after 3.6 ms of 2D evolution. The quantity σ_ρ serves as a convenient measure to specify the magnitude of the density fluctuations. Employing the full implementation of our neutrino treatment, which takes into account both lateral advection in the neutrino moments equations as well as lateral gradients of the neutrino pressure in the fluid equations, the initial perturbations do not grow to instabilities anywhere inside the PNS, which is in accordance with the prediction by the Ledoux criterion. We consider the residual fluctuations which can be

discerned at radii between 15km and 27km to be of physical origin since the Ledoux criterion predicts only marginal stability there.

When switching off the effects of neutrino pressure gradients we notice a strong amplification of the initial perturbations in a region where the damping should be strongest. This is clearly unacceptable. A naive ray-by-ray scheme, which in addition to the neutrino pressure gradients also disregards lateral advection of neutrinos, produces spurious convective activity in a broad region between 15 km and 25 km. Latter convection could easily could be misinterpreted as proto neutron star Ledoux convection but transports lepton number and entropy in the wrong direction. A lateral fluid motion which has been induced to flatten a lateral density gradient of the stellar fluid will, in the absence of lateral neutrino density advection, build up an artificial lepton number gradient. Apparently, and not surprisingly, this gradient generation creates an instability.

We have not attempted to perform a very detailed analysis of all effects of lateral advection and pressure gradients of neutrinos to extend our understanding beyond the more qualitative insights described above. However, we interprete our tests as a demonstration that approximations of multi-dimensional transport schemes must be tested carefully for the possibility of producing spurious convective activity (or suppression of convection) in the newborn neutron star, where neutrinos contribute significantly to the total pressure and total lepton number density.

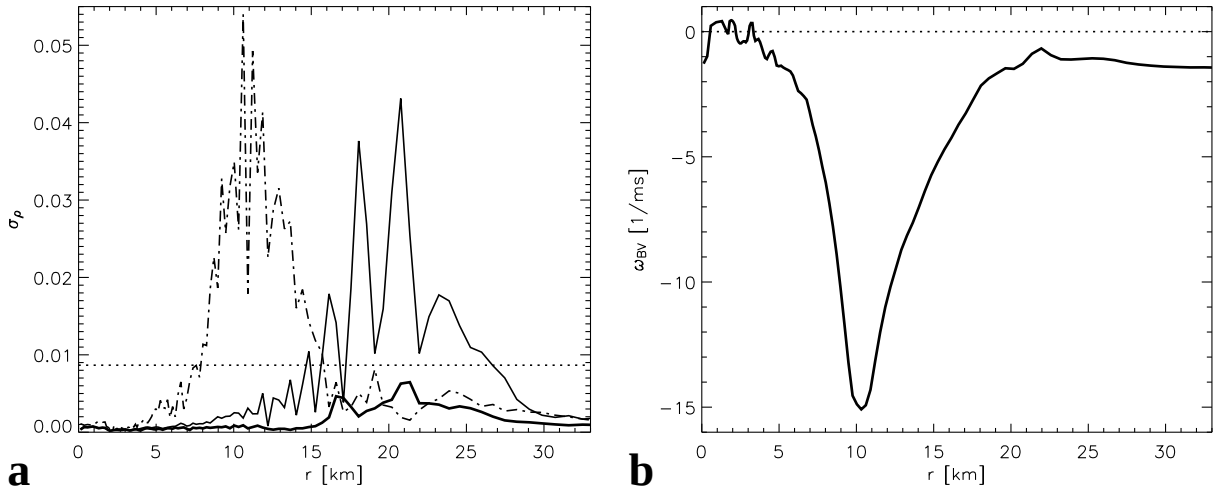

Figure 2.1: **a** Standard deviation of the density σ_ρ (see Eq. 2.27) indicating convective activity inside the neutron star. The 1D Model s15Gio_1d.b was mapped to 2D (16 zones with a resolution of 2.7°) at $t_{\rm PB}$ = 27ms and the density distribution ρ was perturbed. The plot shows the situation after 3.6ms of dynamic evolution computed with different implementations of the 2D transport equations. The dotted line is the initial deviation, the thick solid line shows the standard deviation σ_ρ when we include the lateral terms in our scheme as described in Sects. 2.2.1 and 2.2.3. For comparison, the thin solid line shows σ_ρ when running with pure ray-by-ray transport, and the dash-dotted line corresponds to a simulation where we included the lateral terms of Sects. 2.2.1 but not the momentum transfer to the fluid discussed in Sect. 2.2.3.

b Brunt-Väisälä frequency for the same model, derived from the Ledoux criterion. Negative $\omega_{\rm BV}$ indicates convectively stable regions.

2.3.3 Lateral propagation of neutrinos

A number of our two-dimensional supernova simulations, in particular those which produced lively hot-bubble convection, showed transient neutrino-bursts when narrow downflows of accreted stellar gas entered the cooling region and penetrated down to the vicinity of the neutrinosphere. In our simulations such bursts occured roughly every 20 ms, typically persisting for a few ms. The neutrinos of such bursts, which are the result of locally enhanced neutrino emission, would naturally propagate in all directions in a fully multi-dimensional treatment and would therefore illuminate the surroundings in all directions. Our code ignores the lateral propagation of neutrinos, thus the burst is only propagated outward radially and its width is essentially constrained to the layers above the hot, radiating area. Here we shall argue that although locally and transiently the neutrino heating rates can be incorrect by up to a factor of two due to the disregard of lateral neutrino propagation, the transfer of energy between neutrinos and stellar gas is not significantly changed on larger spatial and time scales, and therefore the global dynamics of our supernova simulations is not likely to be affected significantly.

Basically, our simplified neutrino transport overestimates the heating in the radial rays that contain a "hot spot", while adjacent rays experience less heating than in a 2D neutrino transport which includes lateral neutrino fluxes. Truely two-dimensional transport tends to redistribute neutrinos in lateral direction, in particular in the semi-transparent and transparent regimes where the mean free path becomes large. This can lead to a more uniform spatial distribution of neutrinos exterior to the neutrinosphere than in case of our ray-by-ray treatment, in particular in the presence of local hot spots (see also the discussion in Livne et al. 2004).

To test the implications of lateral neutrino redistribution for the neutrino heating behind the shock, we performed a post-processing analysis in which we angle-averaged the frequency-dependent neutrino densities at a given radius and time and used it to recalculate the local net heating rates. Then we compared the recalculated heating rate with the actual heating rate of the simulation, each integrated over the respective gain layer, for different times. Here the gain layer was defined as the region between the shock and, for each radial ray separately, the innermost radial point at which the net heating is not yet negative (gain radius). For this purpose, the position of the gain radius was also redetermined for the recalculated heating rates.

We have carried out this analysis for an $11.2 M_\odot$ progenitor (s11.2, Woosley et al. 2002) computed with 32 angular zones during its post-bounce evolution (Model s112_32, which will be discussed in Sect. 4.3), a model which showed lively hot bubble convection. The evaluation was started at $t_{\rm pb} = 100$ms; before that time hot bubble convection is weak and no strong local bursts of accretion luminosity do occur. We find that the angular averaging of the neutrino densities hardly changes the total net heating rate in the gain layer, $\delta_t E_{\rm gl}$, see Fig. (2.2, upper panel). Merely at a handful of evaluation times do we find a significant increase in $\delta_t E_{\rm gl}$ by at most 30%. In the temporal average this difference is reduced to only a few percent. For the average net heating per baryon in the gain layer (Fig. 2.2, middle panel), which, concerning global supernova dynamics, we consider to be the more decisive quantity (Janka 2001), the values for the two heating rates are almost indistinguishable.

Interestingly, the differences are somewhat larger if we separately analyze downflows of cold material and hot bubbles in the gain layer; a zone of the numerical grid is attributed to a downflow if the negative velocities are more than 1.5 times the angle-averaged (negative) velocity $\langle v \rangle_\vartheta$ at given radius r, otherwise we define the zone to belong to a high-entropy bubble. For

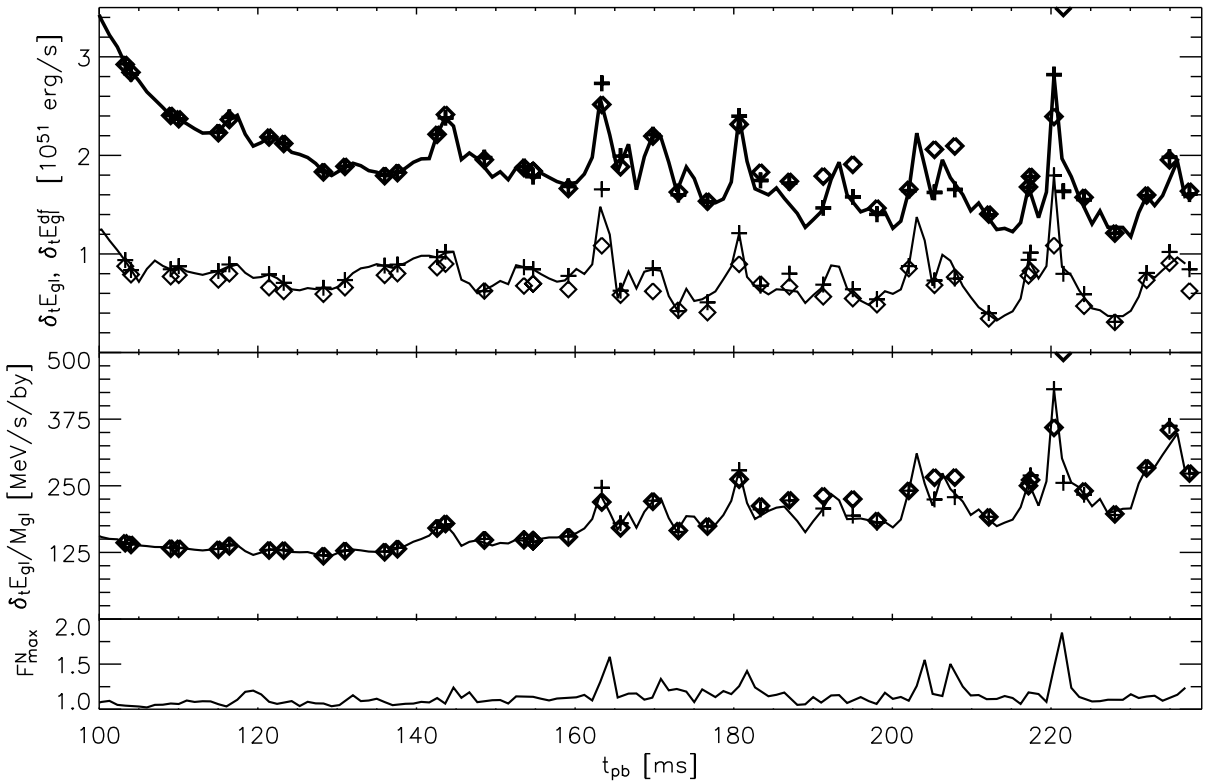

Figure 2.2: The upper panel compares total (volume integrated) neutrino heating rates in the gain layer $\delta_t E_{\rm gl}$. The bold upper solid line shows the evolution of $\delta_t E_{\rm gl}$ for the $11.2 M_\odot$ supernova Model s112_32 to be discussed in Sect. 4.3. The post-processed heating rate obtained by averaging the neutrino densities over all latitudes is represented by diamond-like symbols. For a consistency check crosses are drawn for the post-processed neutrino heating rate without using the lateral averages of the specific neutrino density. Ideally the latter post-processed results should be equal to the values returned from the model run. Remaining differences result from the fact that the post-processing may yield a gain radius shifted by one radial zone. The symbols trace the original values taken from the simulation. For drawing the second curve (thin solid line) and the corresponding symbols the analysis was restricted to downflows in the gain layer, i.e. for regions with velocity $v < 1.5\,\langle v\rangle_\vartheta < 0$. The middle panel shows the average net heating rate per baryon (symbols have the same meaning as in the upper panel), i.e. the total neutrino heating rate in the gain layer divided by the total mass $M_{\rm gl}$ contained in this region. The lower panel shows the maximum neutrino flux as measured slightly above the gain radius normalized to the flux average over all latitudes at the same radius, $F^{\rm N}_{\rm max} = \max_\vartheta(F)\,/\,\langle F\rangle_\vartheta$. The values indicate the relative strength of localized luminosity outbursts.

the downflows (see also Fig. 2.2, upper panel, lower curve), the time-averaged total net heating decreases by 14% for the angle-averaged neutrino density. On the other hand it increases by 12% for the high-entropy bubbles.

The results from this analysis should be read carefully: it does not take into account the dynamical influence of the altered heating rates. Also, the angle-averaging of the neutrino density overestimates the spreading of the flux bursts to other rays, especially close to the gain radius, where we obtain by far most of the heating. The modest sensitivity of the integral quantities to the described averaging of the neutrino distribution, however, gives us confidence that our approximation of the moments equations is a reasonable step towards fully consistent multidimensional simulations.

Even more difficult to assess quantitatively is the effect of replacing the Eddington tensors by scalar variable Eddington factors which are calculated from a solution of the one-dimensional transport equations using a spherically symmetric image of the star. We have to rely on the fact that these variables are normalized moments of the neutrino phase space distribution and thus, in the absence of persistent global deformation of the star, should not show significant variation with the angular coordinate (cf. Rampp 2000; Rampp & Janka 2002). Anyway, as we have seen, ignoring the lateral propagation of neutrinos does not seem to largely affect the neutrino-matter coupling in the semi-transparent region. We hope that the transport also shows sufficient insensitivity to our approximation concerning the variable Eddington factors. Final answers can only be expected from simulations employing a fully multidimensional treatment of the neutrino transport.

2.4 Equation of state

All calculations presented in this paper were run with the equation of state (EoS) described in detail in Rampp & Janka (2002, App. B). The EoS of Lattimer & Swesty (1991) (LS EoS) is employed to treat matter at densities above 6×10^7g/cm^3. Recently it became clear that this EoS underestimates the fraction of alpha particles (due to an error in the definition of the alpha particle rest mass; J. Lattimer, personal communication) and concerns were expressed that improvements of the EoS in the density regime between 10^8g/cm^3 and 10^{11}g/cm^3 could favor an explosion which we fail to achieve with the LS EoS (C. Fryer, personal communication).

In order to test this we have implemented a new EoS in our code. This EoS is similar to the low-density EoS (Janka 1999) described by Rampp & Janka (2002, App. B), but the very approximate description of nuclear dissociation and recombination in nuclear statistical equilibrium (NSE) in that EoS is replaced by a composition table in the (ρ, T, Y_e)-space. This table was computed assuming matter to be in NSE and solving the equations of Saha equilibrium for a mixture of free neutrons and protons, ^{4}He, and ^{54}Mn as a representative heavy nucleus (Janka 1991). We use the table for $T > 5 \times 10^9$K, where NSE is a reasonably good assumption. Given the nuclear composition, variables such as pressure and entropy can be calculated from the EoS of Janka (1999).

A comparison of this simple NSE table with a sophisticated NSE solver that takes into account 32 different species of heavy nuclei showed excellent agreement in entropy, pressure, and helium composition for typical conditions met in the post-shock layer. Note that this table

overestimates the fraction of free nucleons in parameter regions where heavy nuclei dominate the composition and Y_e is far from $25/54 \simeq 0.463$ (e.g. for $T = 1$MeV, $Y_e = 0.3$ this is the case at $\rho > 3 \times 10^{10}$g/cm^3, see Fig. 2.3). This problem originates from the restriction to one representative heavy nucleus and the necessity to fulfill charge neutrality. However, NSE in the post-shock layer of a supernova is not characterized by a significant mass fraction of heavy nuclei.

Comparing our composition table with data from the LS EoS (Fig. 2.3) we indeed observe a significantly larger helium mass fraction for certain combinations of density and temperature. Moreover, the region where helium contributes significantly to the composition is larger. This also affects the pressure and entropy, especially at low temperatures and entropies (Fig. 2.3).

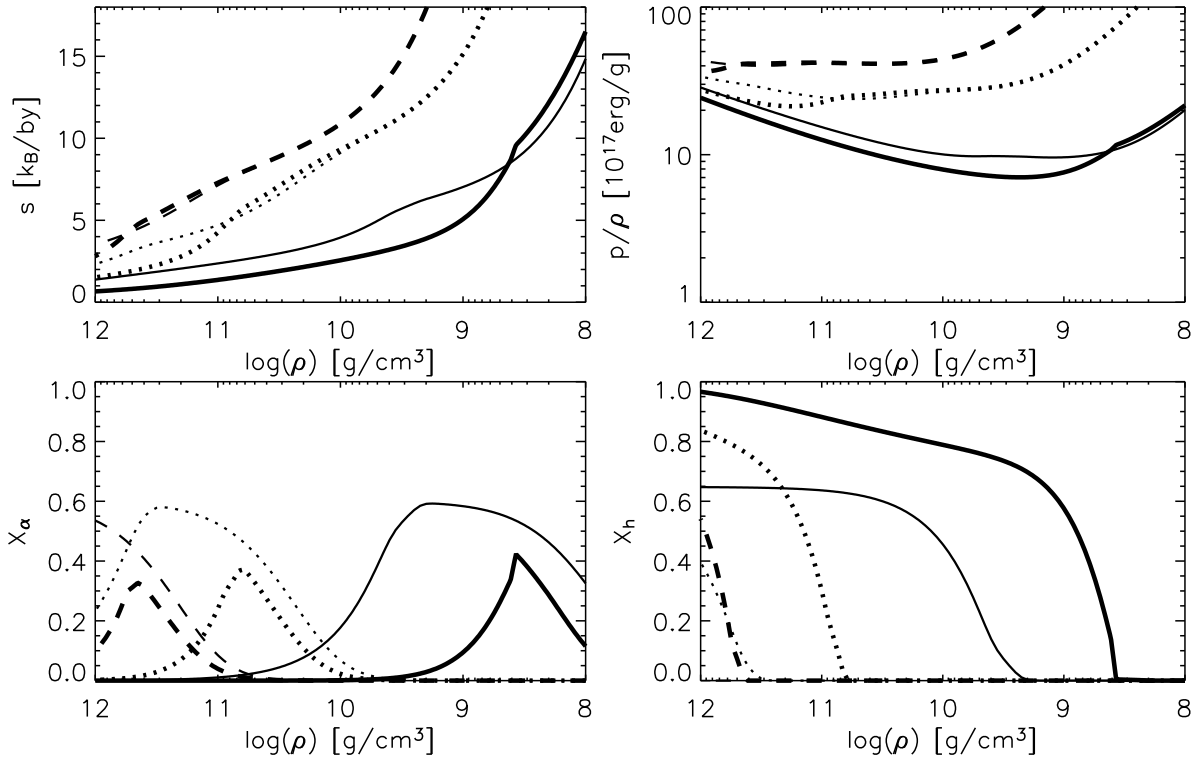

Figure 2.3: Comparison of the LS EoS (thick lines) with the four-species NSE table introduced here (thin lines), for $Y_e = 0.3$ and $T = 1$ (solid), 2 (dotted), and 3 (dashed) MeV.

To test whether the sizeable differences between the EoS using our table and the LS EoS have an influence on supernova simulations we reran the spherical symmetric $11.2M_\odot$ model (Model s11.2, which will be decribed in Sect. 4.2) with the LS EoS replaced by our NSE table at densities below 10^{11}g/cm^3. This comparison directly tests the influence of the different EoS implementations on the dynamical evolution of the supernova.

Surprisingly, both runs showed virtually no difference in the post-bounce history of the supernova (Fig. 2.4) and only small difference in the post-shock structure (Figs. 2.5 and 2.6) even though a post-processing analysis where profiles of T, ρ, Y_e were fed into the two variants of the EoS revealed differences in entropy and pressure of up to 15% and 10%, respectively, below the shock (Fig. 2.7). This phenomenon has a simple explanation: On the one hand the relatively high entropies behind the shock in our models imply that the influence of α-particles is not very important (Fig. 2.3). On the other hand the accretion layer behind the supernova shock can be

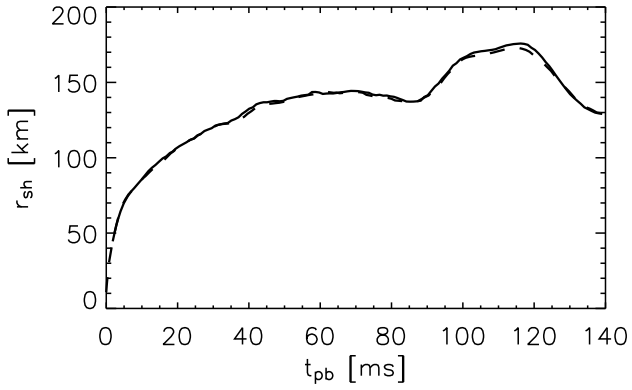

Figure 2.4: Shock positions for the two dynamical simulations of the post-bounce evolution of an $11.2M_{\odot}$ star with the LS EoS (dashed) and the four-species NSE table (solid) used in the density regime below 10^{11}g/cm^3.

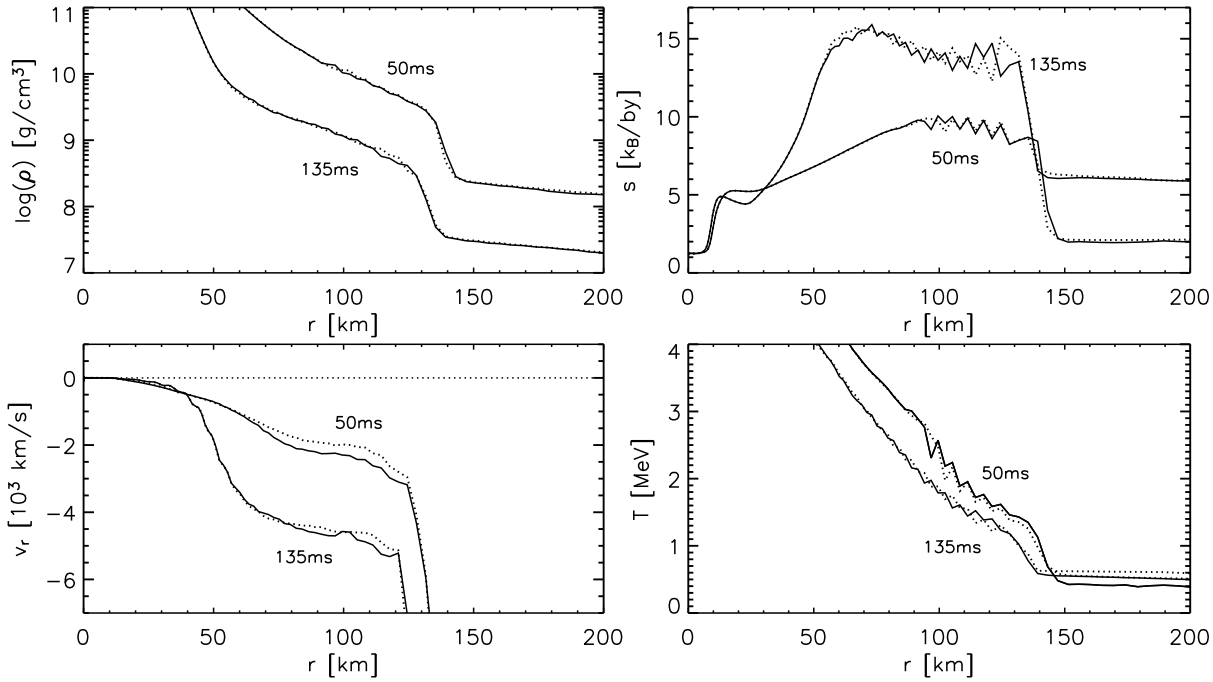

Figure 2.5: Comparison of the profi les for the two dynamical simulations of the post-bounce evolution of an $11.2M_{\odot}$ star with the LS EoS (dotted) and the four-species NSE table (solid) used in the density regime below 10^{11}g/cm^3 at selected times of the evolution.

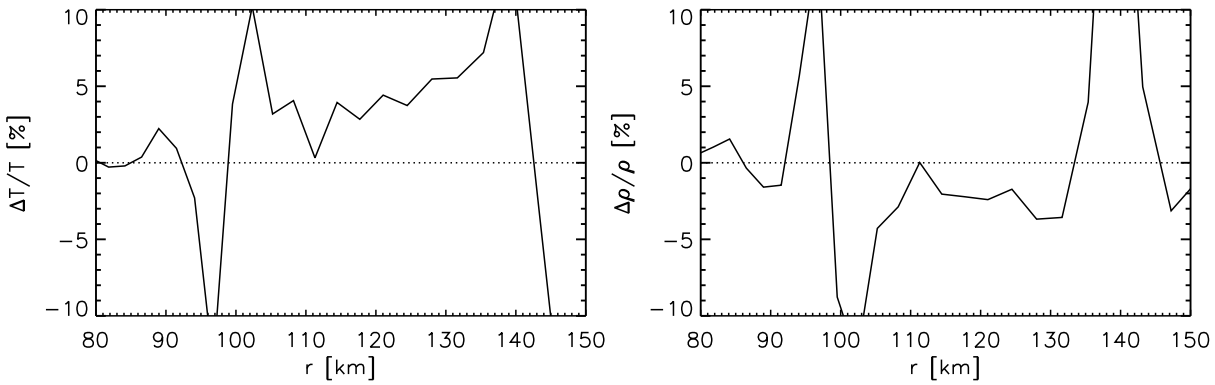

Figure 2.6: Relative difference of temperature and density between the simulations described in Fig. 2.5 at $t = 50$ms. $\Delta T > 0$ means higher T in the simulation with the four-species NSE table (solid) used in the density regime below 10^{11}g/cm^3, dito for $\Delta\rho$.

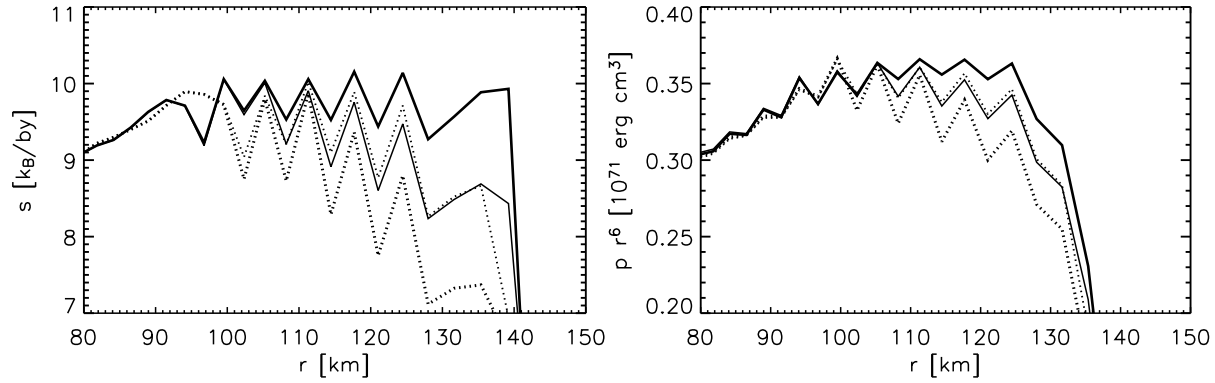

Figure 2.7: Enlarged comparison of the entropy and the pressure (renormalized with r^6) between the two simulations described in Fig. 2.5 at $t = 50$ms. The thin lines correspond to the actual values, the thick lines correspond to a post-processing analysis of the profiles using the other variant of the EoS.

considered as an approximately hydrostatic situation where velocities of the shocked medium and of the shock itself are much smaller than the sound speed c_s. In this case the stellar structure is then determined by the boundary conditions, i.e. the mass and radius of the proto neutron star (and therefore its gravitational field) on the one hand, and the mass accretion rate at the shock on the other (Janka 2001). Keeping in mind that the Rankine-Hugoniot conditions connect the flow in the infall region with the conditions in the post-shock layer, the pressure profile in the accretion layer is determined.

Thus, for a given pressure profile other variables, such as ρ and T, may vary for different EoSs (see Fig. 2.6) without changing the dynamical evolution of the supernova. Only if these variables have an effective influence on the evolution, e.g. by temperature-dependent neutrino emission, do we have to worry about the subtleties of the composition. Neutrino cooling, however, is unimportant in the gain layer while in the cooling region the composition differences between the EoSs can be neglected.

We conclude that, although the LS EoS might not be reliable for certain variables in the low density regime at supernova conditions we do not find a major effect on the dynamics of our simulations.

2.5 Entropy wiggles

All the models presented here feature a numerical problem, the origin of which we found only recently. In all profiles of 1D calculations, and also in part in 2D calculations, artificial wiggles appear below the shock. These wiggles are most pronounced in the entropy and pressure with amplitudes of up to 10%, see e.g. Fig. 2.7. The feature is connected to the polytropic index $\Gamma_e \equiv \frac{p}{e} + 1$ and the specific energy $\varepsilon = e + e_{\mathrm{kin}}$ which are needed for solving the hydrodynamic equations (2.1–2.7) with PROMETHEUS, see Sect. 2.1. By definition, the energy e should be equal to the internal energy e_{int}. However, analytically it is allowed to add certain terms to e thereby retaining the validity of Eqs. (2.1–2.7). In our code, we chose to use the definition

$$e = e_{\mathrm{int}} + e_{\mathrm{rm}} + e_0 \tag{2.28}$$

where e_{rm} is the specific baryon and electron rest mass energy and e_0 is a constant offset chosen to be in accordance with the energy definition in our high density EoS provided by Lattimer & Swesty (1991).

Although analytically correct, Γ_e is no longer the polytropic index $\Gamma_e = \frac{p}{e_{\mathrm{int}}} + 1$ as it should be physically. In particular, in regions with moderate internal energy and large $e_{\mathrm{rm}} + e_0$ (in case of our code where the material predominantly consists of free nucleons, e.g. below the shock), Γ_e can have values which are significantly below the physical minimal value of 4/3. Apparently, PROMETHEUS has problems finding a smooth solution of the hydrodynamic equations for these low values of Γ_e.

We have solved this problem by strongly reducing the additional terms $e_{\mathrm{rm}} + e_0$ in Eq. (2.28), the procedure is described in detail in App. C. We can not set $e = e_{\mathrm{int}}$ exactly since e_{int} is not known in the high density EoS of Lattimer & Swesty (1991). However, in a test calculation with the new implementation the wiggles turn out to disappear completely, see Fig. 2.8b.

As can also be seen from Fig. 2.8 the dynamic and global evolution of the simulations is

not at all affected by the wiggles which confirms that the hydrodynamic solutions given by PROMETHEUS are (on a larger scale) correct even if e from Eq. (2.28) and $e_{\rm int}$ deviate significantly from each other. Therefore the simulations presented in this paper can be believed in spite of the appearing wiggles. Of course, future calculations will be performed using the procedure in App. C.

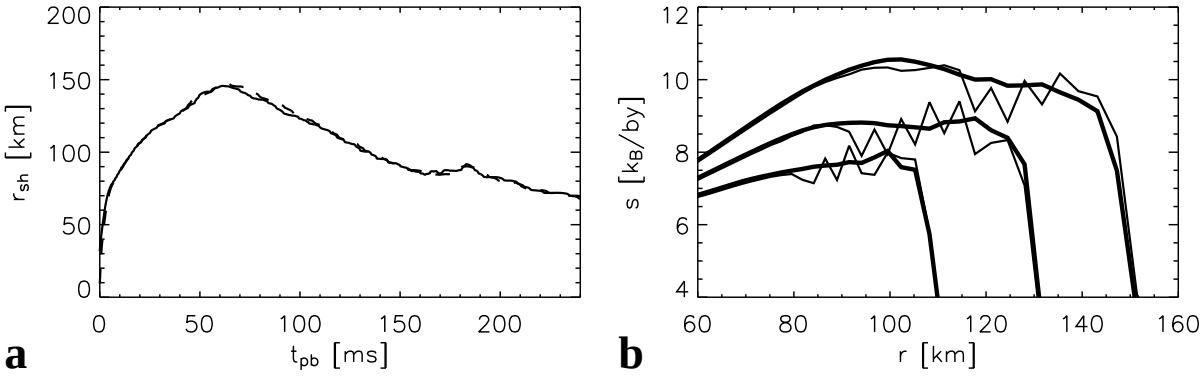

Figure 2.8: **a** Shock trajectories of the Model s15Gio_1d.b, described in Sect. 3.1.1 (solid), and a calculation with identical physics but with our new definition of the energy e (dashed). Note that the differences actually origin from a slightly different gravitational potential. **b** Entropy profiles for the Model s15Gio_1d.b (thin) and the simulation with our new definition of the energy e (thick) at the times 20ms, 40ms, and 60ms after bounce.

3 A fifteen solar mass star in one and two dimensions

We here present the first results from two-dimensional simulations with our "coupled ray-by-ray" approximation of spectral neutrino transport and an improved implementation of neutrino opacities with respect to Bruenn (1985). First, we will discuss the differences resulting from the extended opacities in the context of spherically symmetric (1D) models. We will also discuss the influence of general relativistic corrections on the core collapse and post-bounce evolution and will investigate the importance of velocity-dependent terms in the neutrino momentum equation, especially for a quantitatively correct description of neutrino heating and cooling between proto neutron star (PNS) and supernova shock. In this context we shall present an interesting 1D model which shows large-amplitude oscillations of the shock position and neutrino luminosities. Then we will elaborate on our first two-dimensional (2D) neutrino-hydrodynamical simulations with spectral neutrino transport. Finally, we present a 2D model that develops an explosion when the velocity dependent terms in the neutrino momentum equation are neglected.

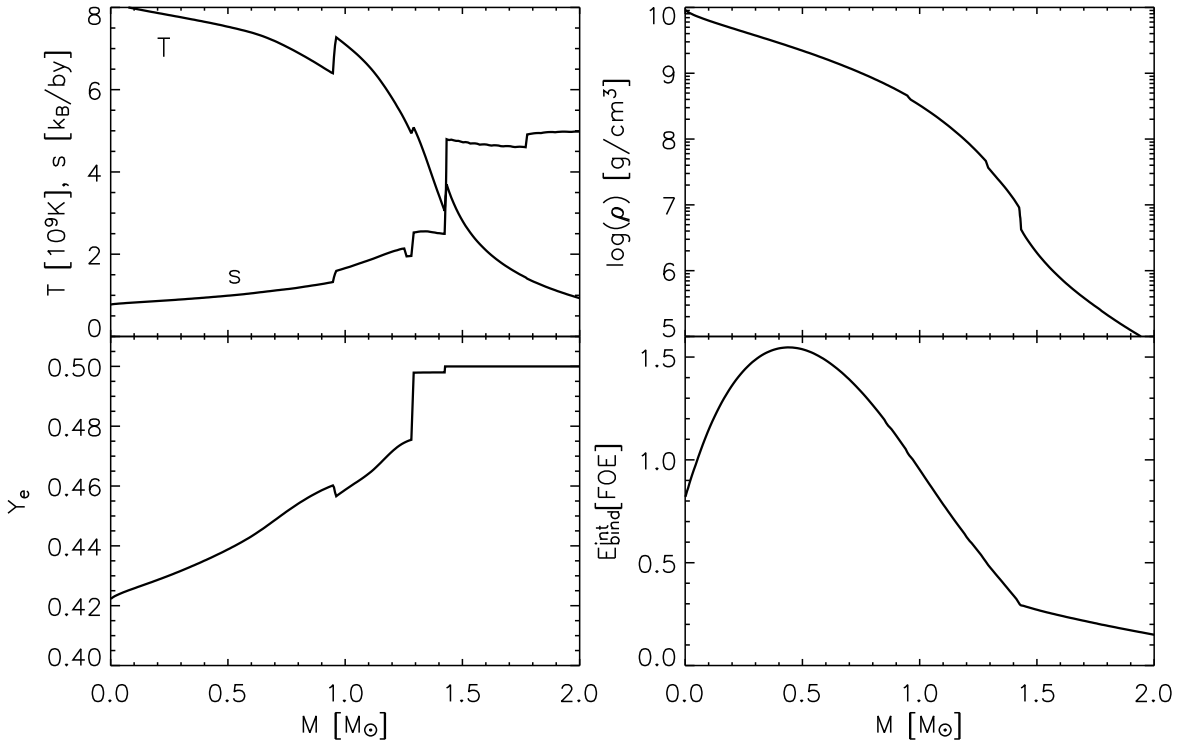

Figure 3.1: Progenitor structure. Temperature T, entropy per baryon s, electron fraction $Y_{\rm e}$, density ρ, and shell binding energy $E^{\rm shell}_{\rm bind}$, defined in Eq. (3.1), as functions of the enclosed mass. At 1.42 $M_\odot$ the interface between the pure silicon shell and the oxygen-enriched silicon shell is located.

Progenitor and model notation: The names of our models are chosen with the aim to provide information about the employed input physics. All models in this paper were started from the progenitor "s15s7b2", a star with a main-sequence mass of 15 $M_\odot$ kindly provided to us by S.Woosley (Woosley & Weaver 1995), see Fig. 3.1. Thus our model names start with "s15". The models were performed either with Newtonian ("N") or with our approximative implementation of general relativistic gravity ("G"). While most simulations included the most advanced description of neutrino interactions ("io"), we performed a few calculations with the standard

Bruenn opacities plus nucleon-nucleon bremsstrahlung ("so"). One-dimensional models are labelled with "_1d", the names of the two-dimensional models give away the number of lateral zones N_ϑ (in this paper only "_32"). Combining this with the chosen size of the angular wedge allows one to infer the equidistant angular zoning of the model. Finally, it is very important whether a model ran with our full implementations of the neutrino transport, case B (".b"), or whether the velocity dependent terms (except for the advection terms) in the neutrino momentum equation were omitted, case A (".a"). The presented models are listed in Table 3.1. The collapse phase was calculated Lagrangian, the post-bounce phase Eulerian, and the simulations were run with 400 radial hydro zones and 230 radial neutrino transport zones, both with geometric spacing. Inside of 400km, the hydro and transport zones were identical, outside of 400km only a few transport zones were added to correctly simulate the propagation till the outer boundary of the simulation at 10^4km. All models were run with 17 neutrino energy zones. When necessary, the radial grids were refined to encounter the increasing density gradient at the surface of the PNS.

Definitions: We define the shock radius $r_{\rm shock}$ as the radius where the radial velocity in the shock flank is half of its minimum value. The gain radius $r_{\rm gain}$ is the zone interface below the innermost zone for which the net energy transfer from neutrinos to the medium is not yet negative. Thus the gain layer is between $r_{\rm gain}$ and $r_{\rm shock}$ while the cooling region is below $r_{\rm gain}$ and includes the PNS. The total net energy transfer rates between neutrinos and medium, $\delta_t E_{\rm cool}$ and $\delta_t E_{\rm gl}$ in the cooling region and gain layer are defined as integrals over the respective region. An interesting quantity is the "shell binding energy" $E^{\rm shell}_{\rm bind}$, i.e. the energy needed to lift all material above a considered radius out of the gravitational potential of the mass enclosed by this radius and thus move the material to infinity. In the approximation with Newtonian 1D gravity its definition is

$$E^{\rm shell}_{\rm bind}(r) \equiv \frac{4\pi}{\cos\vartheta_{\rm max} - \cos\vartheta_{\rm min}} \int_r^\infty \int_{\cos\vartheta_{\rm min}}^{\cos\vartheta_{\rm max}} \varepsilon^{\rm shell}_{\rm bind}(r',\vartheta)\rho(r',\vartheta) r'^2 d\cos\vartheta dr' \,, \tag{3.1}$$

where $\varepsilon^{\rm shell}_{\rm bind}$ is our so-called local specific binding energy,

$$\varepsilon^{\rm shell}_{\rm bind}(r,\vartheta) \equiv e_{\rm int}(r,\vartheta) + (v_r^2 + v_\vartheta^2 + v_\varphi^2)(r,\vartheta) + \Phi^{\rm enclosed}_{\rm 1D}(r) \,. \tag{3.2}$$

The gravitational potential $\Phi^{\rm enclosed}_{\rm 1D}(r)$ is calculated taking into account only the mass inside of the radius r. These energies, as well as the neutrino luminosities, are generally given in the unit FOE, which is a short-cut for "ten to the fifty-one erg". Finally, the spectrally averaged transport optical depth is evaluated according to the formula (in analogy to Raffelt 2001)

$$\tau_\nu(r) \equiv \int_r^\infty \kappa_{{\rm T},\nu}(r')dr'; \quad \kappa_{{\rm T},\nu}(r') \equiv \int_0^\infty \kappa_{{\rm tr},\nu}(r',\varepsilon) H_\nu(r',\varepsilon) d\varepsilon \Big/ \int_0^\infty H_\nu(r',\varepsilon) d\varepsilon \tag{3.3}$$

where $\kappa_{{\rm tr},\nu}(r',\varepsilon,\nu)$ is the transport opacity for neutrino species ν, defined as

$$\kappa_{{\rm tr},\nu}(r',\varepsilon) = \int_{-1}^{+1} d\cos\theta\,(1-\cos\theta)\frac{d\sigma_\nu(r',\varepsilon,\theta)}{d\cos\theta} \tag{3.4}$$

and $d\sigma_\nu/d\cos\theta$ is the differential scattering cross section for neutrinos of energy ε and type ν including all neutrino-matter interactions. The neutrinosphere (radius) is defined by $\tau_\nu(r_\nu) = 1$. For radial profiles of quantities for 2D models the values are calculated by laterally averaging the 2D data, see Sect. 2.2.2 for the definition of this procedure. This also includes the definition of mass shells in 2D, i.e. a mass shell corresponds to the radius which encloses this mass.

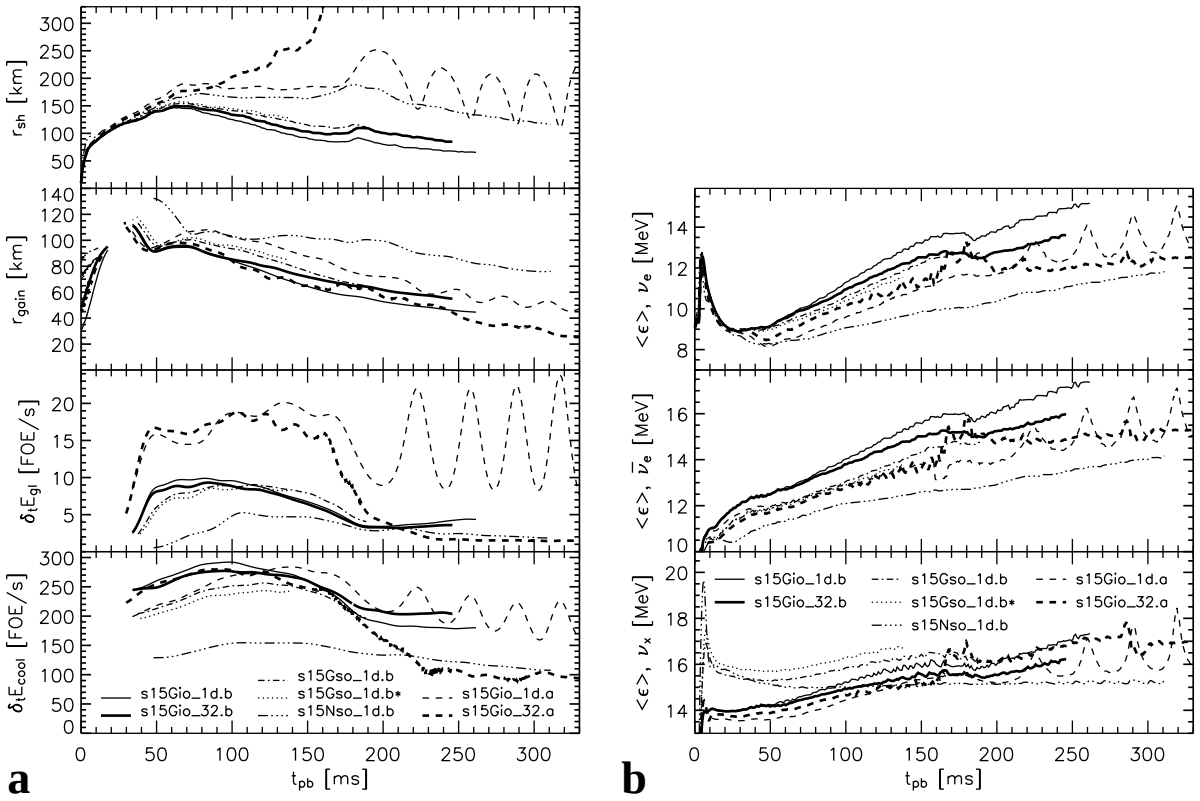

Figure 3.2: a The uppermost plot shows the shock positions versus time for all presented models. Thin lines are for 1D models, thick lines for 2D. The next plot shows the gain radius below which neutrino cooling dominates and above which neutrino heating is stronger. The third plot shows the total heating rate in the gain layer, i.e. between the gain radius and the shock. Finally, the plot at the bottom shows the total cooling rate below the gain radius. Note that the curves in the lower three plots were smoothed over intervals of 5ms. The evolution of Models s15Gio_1d.a and s15Gio_32.a was followed to later times. Their complete evolution can be seen in Figs. 3.15, 3.16, 3.28, and 3.34.

b The three plots show the average energies of the emitted ν_e (top), $\bar{\nu}_e$ (middle), and $\nu_{\mu,\tau}$ or $\bar{\nu}_{\mu,\tau}$ (bottom) as measured by an observer at rest at 400km.

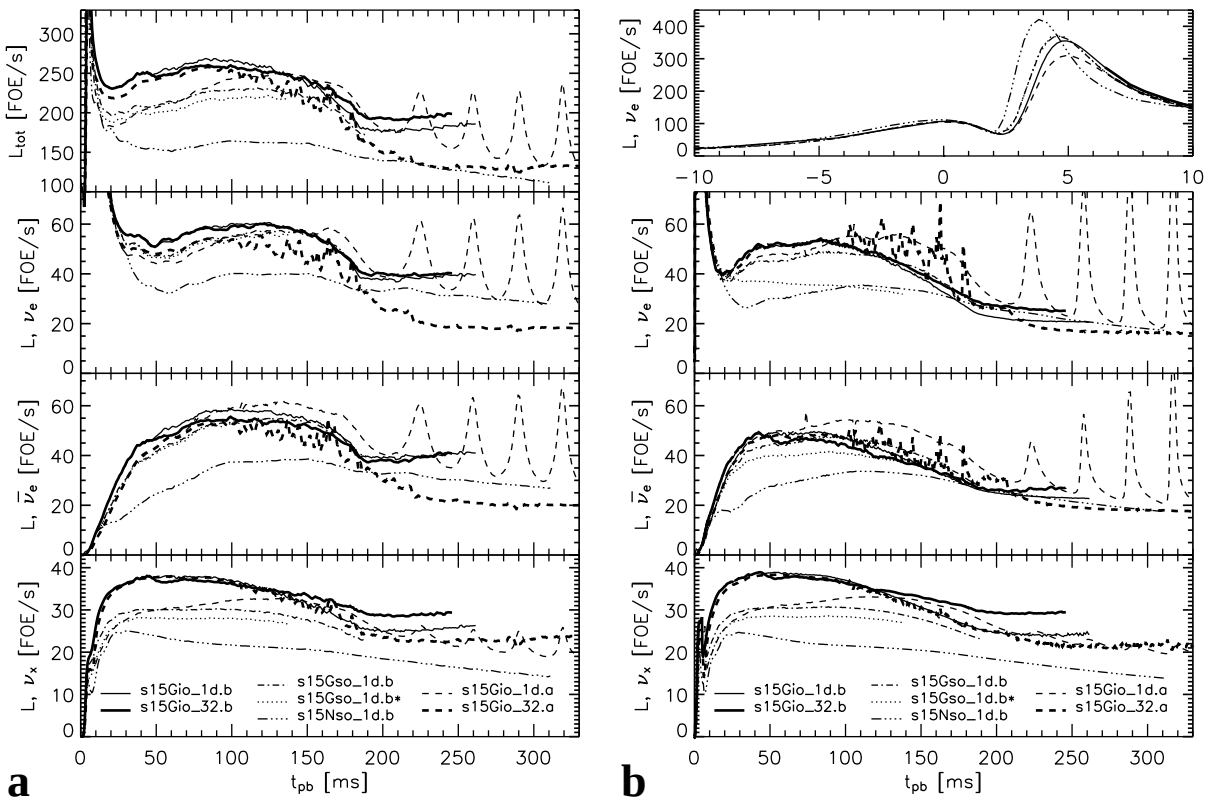

Figure 3.3: Comparison of neutrino luminosities for all models. **a** Luminosities for an observer at rest at 400km. The uppermost plot shows the total luminosity, the three lower ones those for the different ν types. The plot at the bottom gives the luminosity of ν_μ, $\bar{\nu}_\mu$, ν_τ, or $\bar{\nu}_\tau$, which are all assumed to be equal. **b** The uppermost plot shows the electron neutrino burst, again for an observer at rest at 400km. Note the different scale on the x-axis of this plot. The lower three plots display the neutrino luminosities of ν_e, $\bar{\nu}_e$, and heavy-lepton neutrinos individually, evaluated at their respective neutrinospheres (for a comoving observer).

Table 3.1: Input physics for our sample of computed models.

Model	*Dim.*	*Gravity*	*ν Reactions*	*Transport*	*Wedge*[a]	*ϑ-zones*
s15Nso_1d.b	1D	Newtonian	standard	Case B		
s15Gso_1d.b	1D	approx. GR	standard	Case B		
s15Gso_1d.b*	1D	approx. GR	standard[b]	Case B		
s15Gio_1d.a	1D	approx. GR	improved[c]	Case A		
s15Gio_32.a	2D	approx. GR	improved	Case A	±43.2°	32
s15Gio_1d.b	1D	approx. GR	improved	Case B		
s15Gio_32.b	2D	approx. GR	improved	Case B	±43.2°	32

[a] Angular wedge of the spherical coordinate grid around the equatorial plane.

[b] Calculation without neutrino-pair creation by nucleon-nucleon bremsstrahlung.

[c] Calculation without the neutrino-antineutrino processes of Buras et al. (2003).

3.1 Spherically symmetric models

3.1.1 The standard model

This one-dimensional model was run with the state-of-the-art description of neutrino opacities described in Appendix A and references therein. This treatment of neutrino-matter interactionsis improved compared to the standard rates by Bruenn (1985) by including effects of nucleon recoil and thermal motion, weak-magnetism corrections, and nucleon-nucleon correlations in neutrino-nucleon interactions. Moreover the reduction of the effective nucleon mass at nuclear densities and the quenching of the axial-vector coupling in nuclear matter was taken into account. In addition, we included nucleon-nucleon bremsstrahlung and purely neutrinic interactions which consist of scattering as well as pair creation processes between neutrinos of different flavors. The full list of included rates and their references can be found in Table A.1.

Further, we applied the approximation of general relativity described in Chapter 2. Finally, the simulation was done including the velocity dependent terms in the radiation momentum equation, i.e. the terms proportional to β_r in Eqs. (2.10,2.12). Despite of being formally small ($\beta_r \leq 0.1$) these terms turn out to be important when performing supernova simulations as we will elaborate in Section 3.1.3.

The evolution of this model can be seen in Fig. 3.5. The progenitor needs 174ms to reach core bounce. The central values of $Y_{\rm lep}$ and s evolving during collapse can be seen as a function of the central density in Fig. 3.4. The shock is then created at an enclosed mass of $M_{\rm sc} = 0.49 M_\odot$ and a radius of $r_{\rm sc} = 10.6$km. The prompt shock stalls around 1ms at r =32km, turning into an accretion shock. At first the high mass accretion rate through the shock leads to matter being accumulated between the PNS and the shock; the energy cooling via neutrinos is not quick enough to effectively compress this material so that the shock quickly expands. After 6ms, when the shock reaches 80km, this expansion is slowed down as the mass accretion rate drops and the neutrino cooling has become more effective, leading to an “equilibrium” between mass accreting through the shock and mass settling onto the PNS. The shock now slowly expands

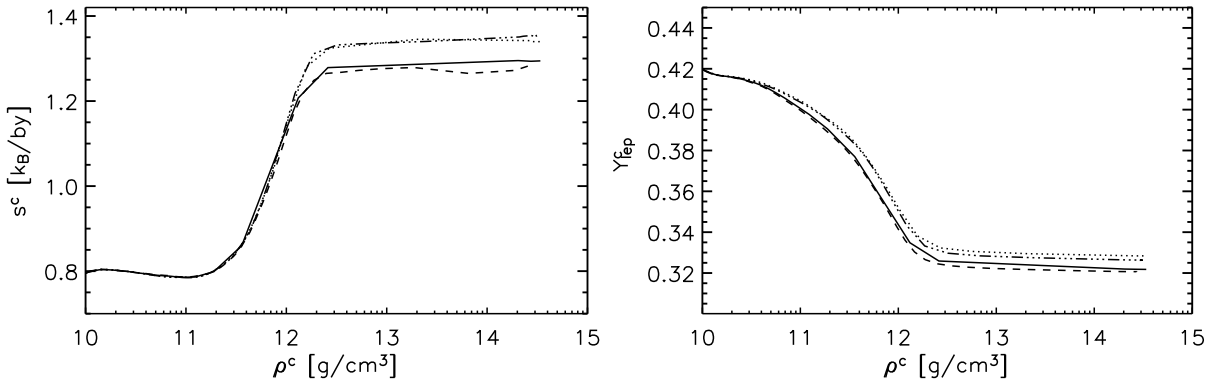

Figure 3.4: Evolution of the central values of the entropy and lepton number as functions of the central density during the collapse of Models s15Nso_1d.b (dash-triple-dotted), s15Gso_1d.b (dotted), s15Gio_1d.b (solid), and s15Gio_1d.a (dashed).

to 140km at 60ms. Then however, the shock slowly retreats as a consequence of the high ram pressure at these small radii, which can not be compensated by the weak neutrino heating in a relatively small gain layer (see also $\delta_t E_{\rm gl}$ in Fig. 3.2a). At 170ms, when the shock has reached a radius of less than 90km, we see a transient reexpansion of the shock setting in which is stopped after a few km. This feature results from a sudden drop of the density in the progenitor (see Fig. 3.1), and thus of the ram pressure, and is connected with the "interface" between the pure silicon shell and the oxygen-enriched silicon shell (i.e. Si-SiO interface, at $1.42 M_\odot$). This feature of transient shock expansion can be seen in all our models, with strongly differing consequences (even explosions, see Sect. 3.2.2). In Model s15Gio_1d.b the shock expands only by about 20km. Already while the expansion sets in, the neutrino luminosities decrease due to the drained accretion onto the PNS, and therefore the heating of the shocked material decreases. The shock finds a new equilibrium radius at only 90km to then follow the subsequent contraction of the nascent neutron star.

The neutrino emission reflects the different phases of the evolution. One distinguishes several phases: After the collapse phase, where only $\nu_{\rm e}$ are emitted in significant numbers, the prompt $\nu_{\rm e}$ burst is created few ms after bounce (in Fig. 3.3, note that the signal is delayed by approximately 1ms due to the time-of-flight). The burst lasts approximately 25ms, has a fwhm of 6ms, and reaches a peak luminosity of 350FOE/s (FOE = ten to the fifty-one erg), see Fig. 3.3b. Simultaneously, the newly created PNS starts emitting $\bar{\nu}_{\rm e}$ and $\nu_{\rm x}$. Their rise in luminosity takes 35ms and 15ms, respectively. In the following accretion phase, the emitted neutrinos come from two regions, a layer below the neutrinosphere of the cooling PNS as well as from the layer of newly accreted material between the PNS surface and the gain layer. The luminosity from the latter source depends sensitively on the mass accretion rate as can be seen in the drop of the luminosity when the Si-SiO interface enters the cooling region. Interestingly, the mean energies of $\bar{\nu}_{\rm e}$ and $\nu_{\rm x}$ become very similar in the later phases after 100ms, this feature has been discussed in detail in Keil et al. (2003).

We will discuss the differences of this simulation with its newly implemented improvements relative to a less sophisticated treatment of the physics in others of our models in the following section.

Looking more closely at our simulation, we find that its outcome is not very surprising. Fol-

lowing shock stagnation and during the whole subsequent evolution we see that the shock is unable to stop the infall of the accreted material: Behind the shock, the matter still has negative velocities of several 1000km/s, thus falling quickly through the narrow gain layer. As an example, at the time of maximal shock expansion at 72.5ms, the infall velocity behind the shock is still $4 \cdot 10^4$km/s (see Fig. 3.6), and the short distance between shock and gain radius of at most 50km corresponds to an advection timescale through the gain layer of less than 2ms. With a moderate neutrino heating rate of 300MeV/by/s only $\sim$ 0.6MeV per baryon can be deposited in these 2ms, an amount which is clearly insufficient to promote shock expansion: At the high entropies ($> 10 k_B$/by) behind the shock nuclei are nearly completely dissociated to nucleons. Only a small fraction of α-particles (less than 20%) survive the shock passage, and are quickly dissociated during infall. Thus, the shock loses 8–9MeV/by due to nuclear photo-dissociation.

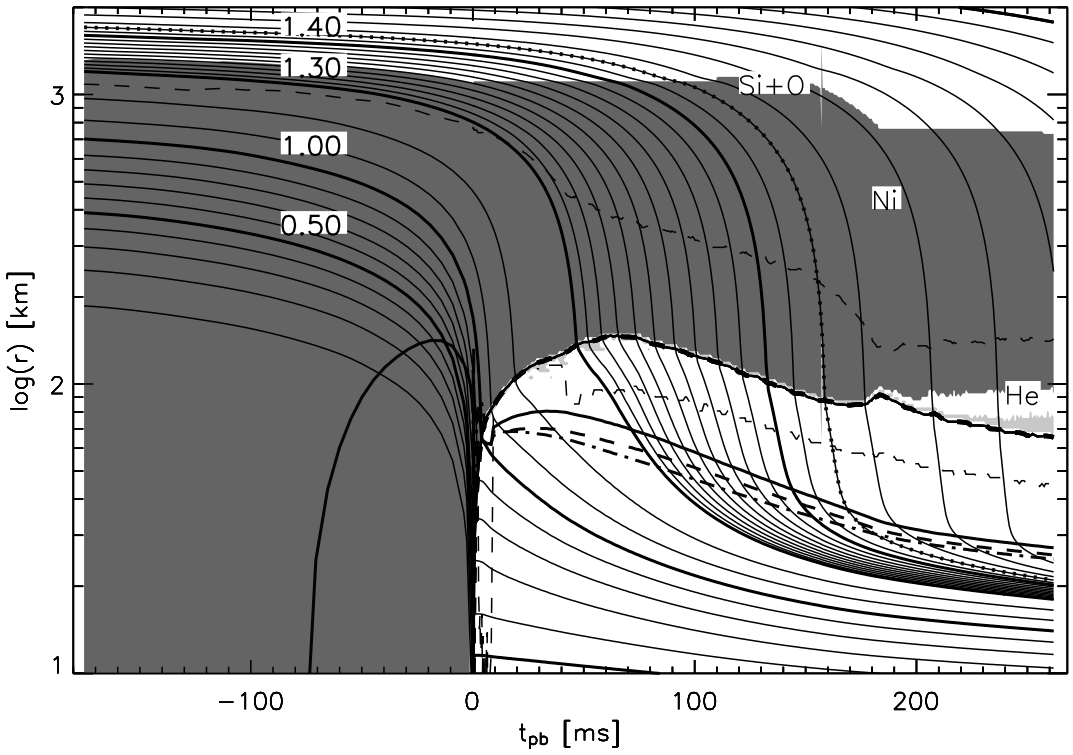

Figure 3.5: Mass shells for Model s15Gio_1d.b. The plot also shows the neutrinospheres for ν_e (thick solid line), $\bar{\nu}_e$ (thick dashed), and ν_x (thick dashed-dotted), the mass shell at which the silicon shell becomes oxygen-enriched (knotted solid line, at $1.42 M_\odot$), and the shock (thick solid line with superimposed dashes). Further we have marked the regions with a mass fraction of more than 60% in iron-group elements (dark shaded). Also shown are regions with a mass fraction between 30% and 60% in ^{4}He (light shaded). Finally the lower thin dashed line marks the gain radius, while the upper one marks the interface between our high-density and low-density EoSs (i.e. the thin dashed line corresponds to a density of $\rho = 6 \cdot 10^7$g/cm^3).

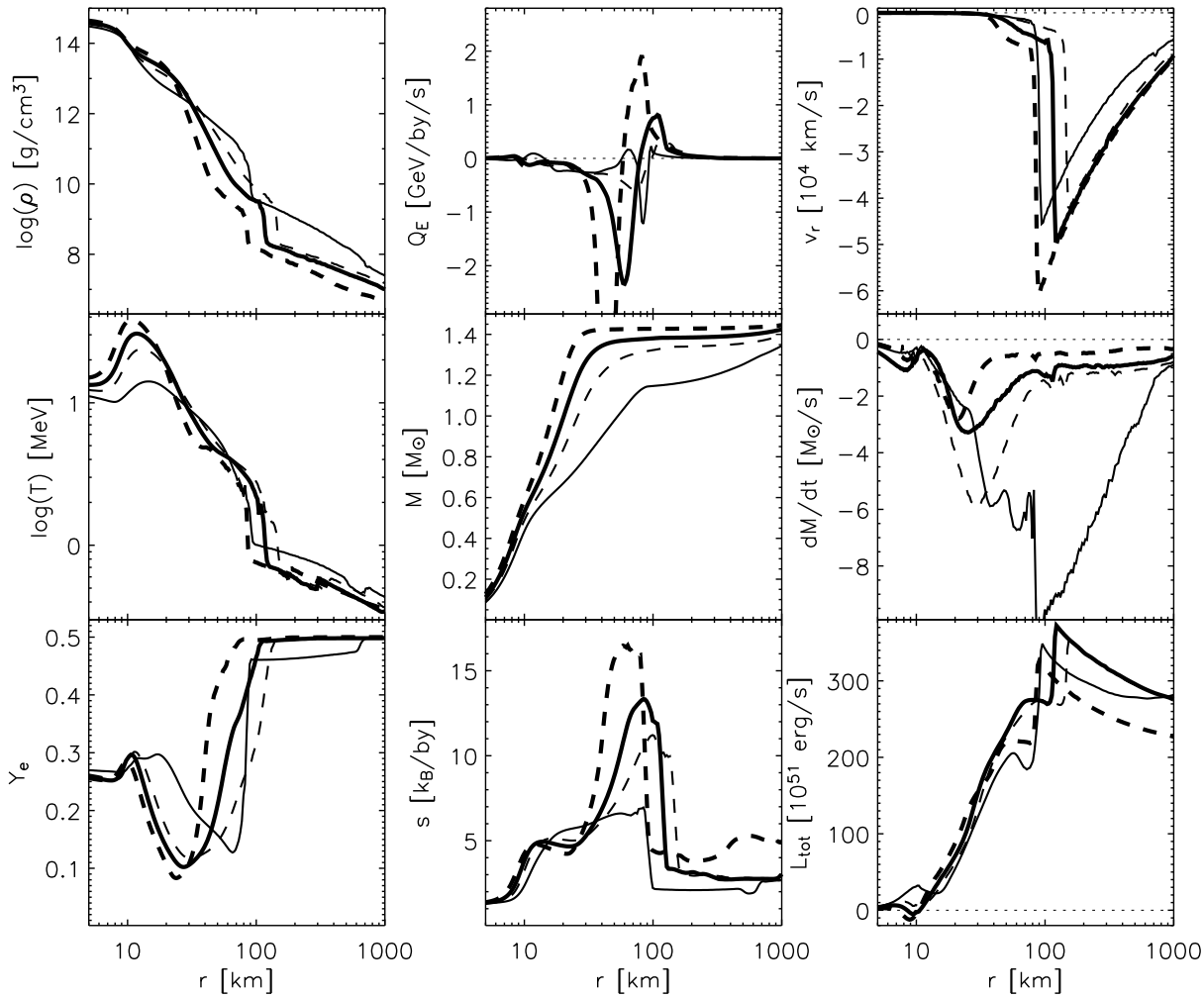

Figure 3.6: Stellar profi les of different quantities at post-bounce times 11.6ms (solid), 72.5ms (dashed), 113.7ms (thick solid), and 170.7ms (thick dashed) versus radius for our reference Model s15Gio_1d.b. For the latest time the cooling rate reaches a maximum value of $Q_{\rm E} = -10$GeV/by/s.

3.1.2 Variations of the input physics

"Standard" opacities vs. improved opacities We have performed most of our calculations either using a set of neutrino interactions which we call "standard opacities" (so) or our fully updated ("state-of-the-art") description of neutrino interactions which we call "improved opacities" (io)[1]. The treatment of neutrino interactions in case "io" is described in Appendix A. Case "so" uses the neutrino interactions found in Bruenn (1985) and Mezzacappa & Bruenn (1993a,b), implemented as described by Rampp & Janka (2002), but supplemented by neutrino pair creation and annihilation due to nucleon-nucleon bremsstrahlung.

The special properties of the different interaction rates can best be explained by comparing the corresponding opacities. In Figs. 3.7 and 3.8 we have plotted the opacities of all reactions included in Model s15Gio_1d.b for ν_e, $\bar{\nu}_e$, and heavy-lepton neutrinos (ν_x) for two different energies and times. For completeness, we also show the "standard" (approximate) rates for scattering and absorption on nucleons, i.e. the rates without effects from nucleon recoil and thermal motions, weak magnetism, effective nucleon masses, and nucleon-nucleon correlations. During the discussion, remember that absorption and emission fulfill detailed balance.

We have two types of charged-current absorption reactions. Absorption on nucleons is dominant after bounce, when the post-shock material is essentially fully dissociated. However, we can see that in the PNS core, the improved rate is reduced significantly compared to the standard rate, for ν_e by a factor of up to 30, for $\bar{\nu}_e$ even by up to 100. In the region around the neutrinosphere, including the gain layer, recoil and weak magnetism reduce the $\bar{\nu}_e$ absorption rate by 10–20%, while the effects nearly compensate each other in case of ν_e. Absorption on nuclei is small relative to nucleon absorption even in the pre-shock material. However, our rates for ν_e absorption by nuclei are still rather approximative, and $\bar{\nu}_e$ capture by nuclei is neglected. Improving this treatment is desirable.

Neutrino-antineutrino pairs can be produced or destroyed in different charged- and neutral-current reactions. One of these is nucleon-nucleon bremsstrahlung which contributes significantly to the emitted flux of heavy-lepton neutrinos ν_x (Keil et al. 2003; Thompson et al. 2003) because this process dominates the production of ν_x at high densities. Interestingly, bremsstrahlung is also the dominant production/absorption reaction for $\bar{\nu}_e$ in the PNS core, where the electron neutrino degeneracy is very high and therefore ν_e are orders of magnitudes more abundant than $\bar{\nu}_e$. The second pair process is the annihilation of $\nu\bar{\nu}$ pairs to e^+e^- pairs. It dominates bremsstrahlung in creating $\bar{\nu}_e$ at low densities and is also a very important process for the generation of ν_x. This rate, however, is surpassed by the rate of $\nu\bar{\nu}$ pair conversion between different flavors, which in most regimes is approximately a factor of two more important for producing $\nu_x\bar{\nu}_x$ pairs than e^+e^- annihilation. Both rates dominate the ν_x production around the neutrinosphere, thus being crucial in the spectrum formation process. For higher energies, the leptonic pair production rates become increasingly important relative to bremsstrahlung.

Finally, scattering processes contribute to the neutrino opacity. Scattering of neutrinos on nuclei dominates the scattering rates above the shock. Scattering on nucleons are the dominant rates in the NS core and postshock layer. Dense medium effects (see App. A), however, reduce the rate by a factor of 2–3 at high densities below the neutrinosphere. Again, weak magnetism and recoil produce a 10% difference for $\bar{\nu}_e$-nucleon scattering around the neutrinosphere, and

[1] The new treatment of electron captures on nuclei during core collapse with rates from Langanke et al. (2003), however, is not yet included in any of our models presented here.

a much smaller effect for ν_e (see App. A). For ν_x scattering off electrons and off ν_e, $\bar{\nu}_e$ are of similar importance.

At later times the temperature in the postshock layer increases and e^- degeneracy is reduced so that the e^+e^- pair process and $\nu e^\pm$ scattering become more important (see Fig. 3.7 compared with Fig. 3.8).

The influence of the neutrino interactions can be seen in dynamic simulations with different input physics (Figs. 3.2, 3.3). In addition to the above presented Model s15Gio_1d.b with the set of "improved" opacities, we have performed two dynamic simulations s15Gso_1d.b and s15Gso_1d.b*, which both were run with our the traditional approximations for the opacities. In the latter case bremsstrahlung was also ignored to make a direct comparison to simulations by other groups. The first 50ms are well fit for comparisons, here the structure of the PNS and the above lying layer where the neutrinospheres are situated are still very similar in all general relativistic models. Also, convection has not yet set in so that the 2D models can be considered as 1D. Even the simulations neglecting the β-terms can be used for comparison in a limited sense, the β-terms have no effect in the layers emitting the neutrinos (Note that the shock evolution *i*s influenced by the β-terms from the bounce on).

In a nutshell, the main difference between standard and improved opacities is produced by the purely neutrinic interactions. The improvements on neutrino-nucleon interactions and the quenching of the axial coupling, as well as bremsstrahlung, have a surprisingly weak effect on the dynamic evolution of the star. Merely the neutrino signal is affected by these improvements.

The collapse phase is hardly influenced by improving the neutrino interactions, since the only changes affect interactions with free nucleons, which during collapse are rare ($Y_n + Y_p \simeq 10^{-3}$). (Note that our collapse simulations ran without $\bar{\nu}_e$ and ν_x, both being irrelevant in this phase.) The improved opacities slightly increase the ν_e production rate, while the coherent scattering rate, which dominates the opacity during collapse, remains constant. Thus, more ν_e are emitted before the matter becomes optically thick. As a consequence, the simulation with standard opacities yields slightly higher entropies ($\Delta s \simeq 0.06$) and slightly increased Y_{lep} ($\Delta Y_{lep} \leq 0.01$) in the core with respect to the improved opacities simulation, see Fig. 3.4. Thus, the homologous core is slightly larger ($\Delta M_{sc} \simeq 0.02$) and the collapse time, too ($\Delta t_{coll} \simeq 2.3$ms).

Comparing s15Gso_1d.b* with s15Gio_1d.b, we obtain somewhat increased $\bar{\nu}_e$ energies and strongly reduced ν_x energies, but no changes in the ν_e energies. Bremsstrahlung (s15Gso_1d.b) has only a weak effect. The luminosities are affected similarly. Here we see some increase in the electron flavor neutrinos, and a strong increase for the other neutrinos. The effect of bremsstrahlung can be seen in an increased ν_x luminosity.

Taking the model s15Gio_1d.a into account, where purely neutrinic reactions were omitted, we see that the ν_x energies are similar to those in the Model s15Gio_1d.b, suggesting that the improved neutrino-nucleon interactions change their energies. However, the luminosities of Model s15Gio_1d.a resemble the Models s15Gso_1d.b and s15Gso_1d.b*, meaning that the change in luminosity is steered by the $\nu\nu$ scattering and absorption rates of Buras et al. (2003). The total change in the dynamic evolution is thus moderate and mainly contributed to by the process $\nu_e \bar{\nu}_e \leftrightarrow \nu_x \bar{\nu}_x$, which significantly fastens the cooling of the neutrinospheric region. The sum of improvements also alters the neutrino energies, so that the $\bar{\nu}_e$ and ν_x spectra become more similar.

These results are very well in agreement with the results by detailed Monte Carlo simulations

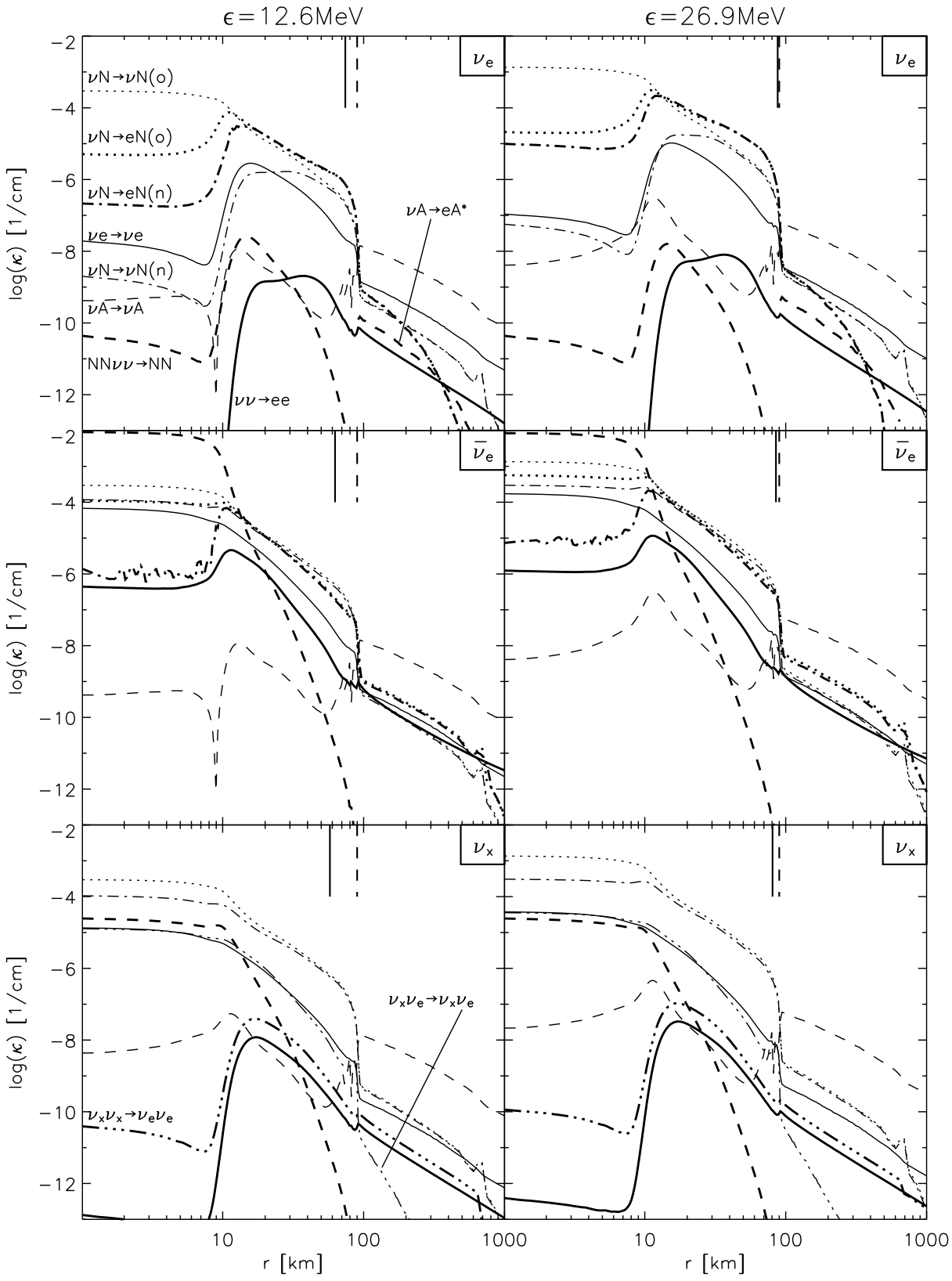

Figure 3.7: Opacities for the neutrino interactions taken into account in Model s15Gio_1d.b at t = 11.6ms post-bounce for two representative energies. Neutrino ("ν") reactions with electrons ("e", solid), nucleons ("N", dash-dotted), nuclei ("A", dashed), and electron-type neutrinos ("ν_e", dash-triple-dotted, for ν_x only) are shown. For comparison the "standard" opacities for the neutrino-nucleon interactions are also displayed (dotted). Thin lines represent scattering processes, thick lines correspond to absorption processes. Note that different from this convention nucleon-nucleon bremsstrahlung is also represented by thick dashed lines. (See also notes in Fig. 3.8).

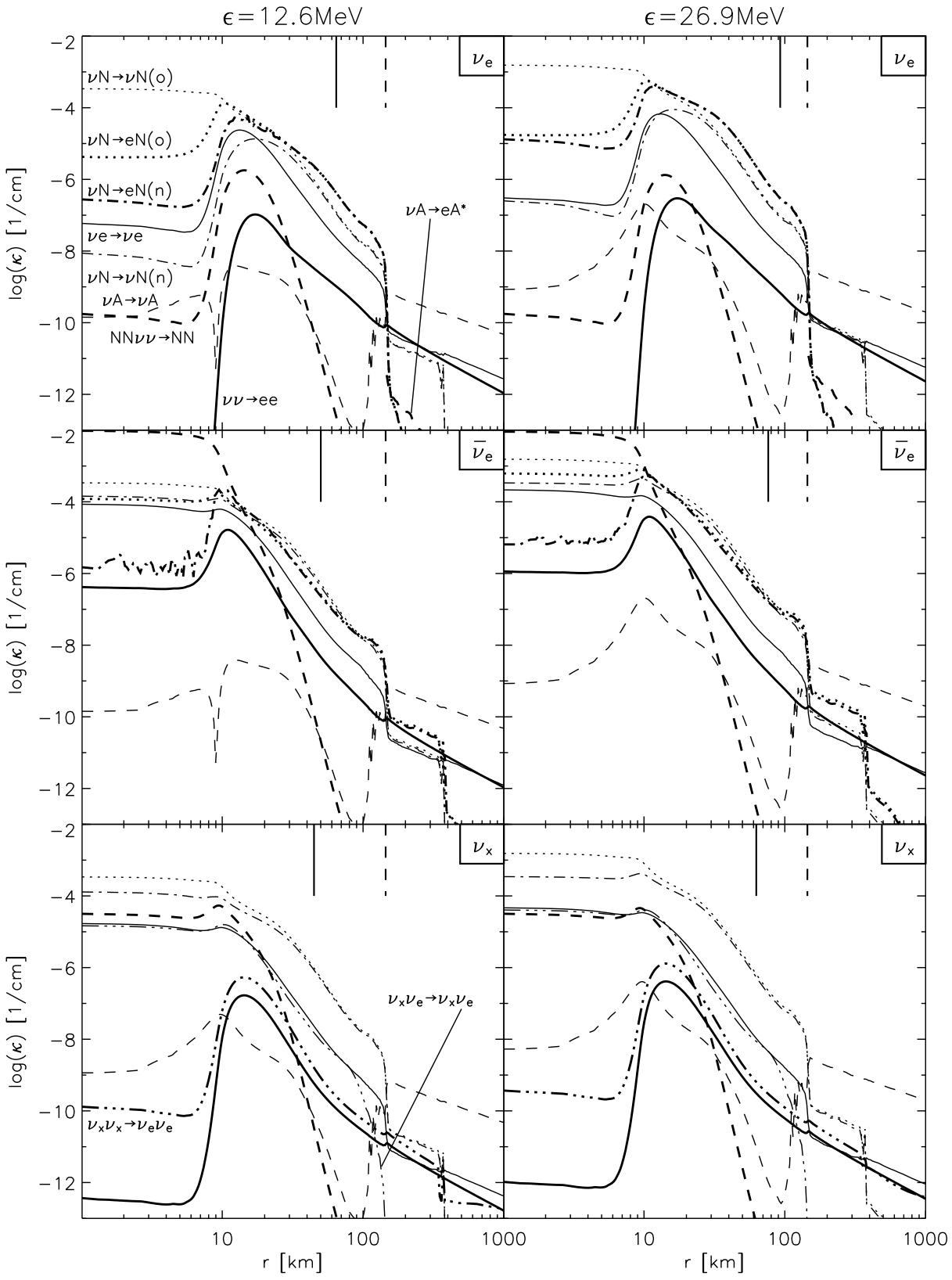

Figure 3.8: Same as Fig. 3.7, but for t = 73.4ms. The opacities include processes with all possible interaction partners, i.e. "N" stands for nucleons and can represent protons and/or neutrons, "e" can be electrons and/or positrons, "A" represents all nuclei, "ν" can be any type of neutrino or anti-neutrino, "ν_e" can be electron neutrinos and/or antineutrinos, and "ν_x" can be any type of heavy lepton neutrino or anti-neutrino. The opacities include all phase-space blocking factors. The short vertical lines on the top of the plots indicate the radii of the neutrinosphere (solid) and of the shock (dashed).

by Keil et al. (2003).

Note that recoil and weak magnetism do have an effect on Y_e in the gain layer, where the evolution of Y_e depends sensitively on the ratio of ν_e to $\bar{\nu}_e$ absorption.

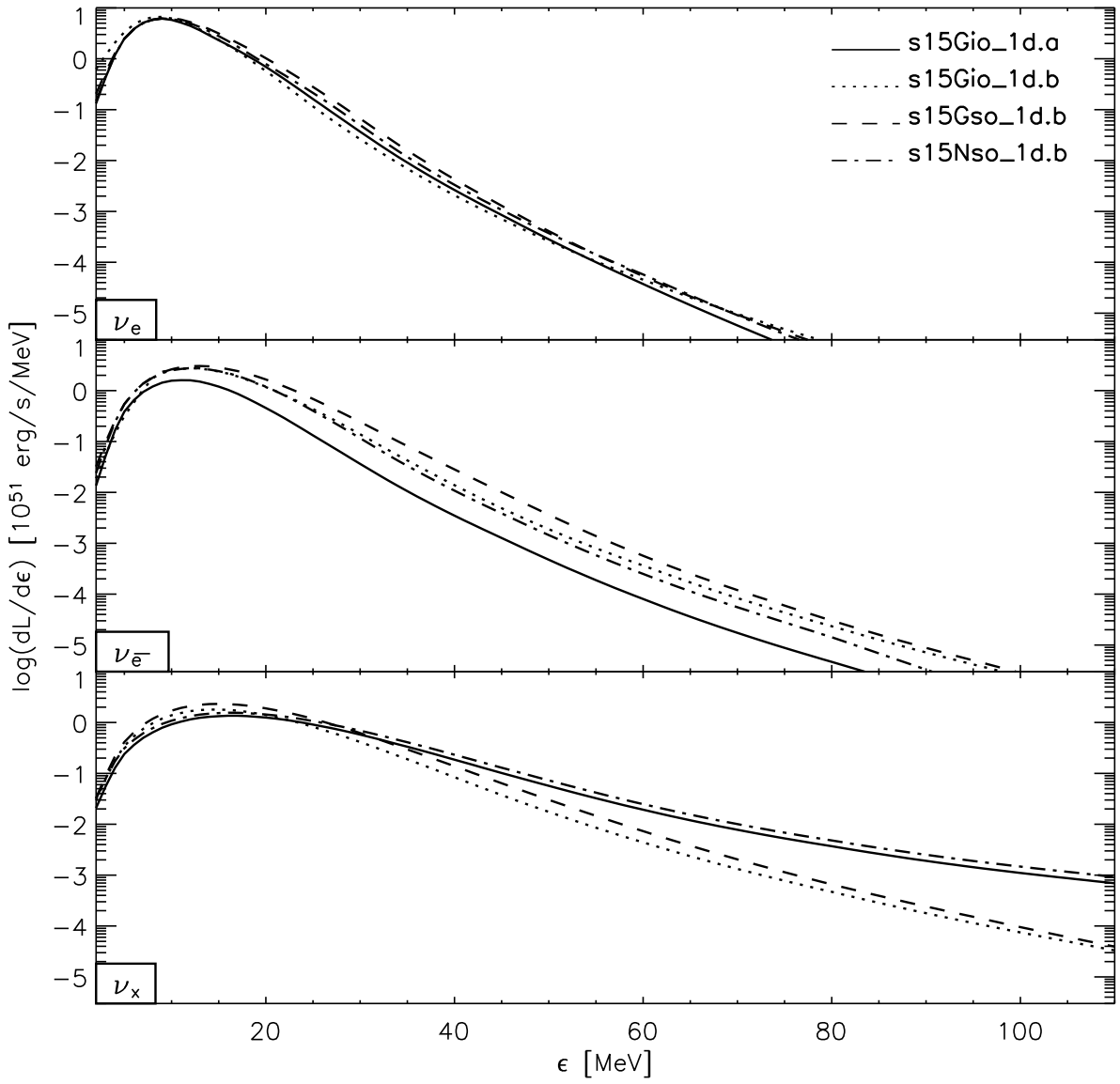

Figure 3.9: Spectra of the neutrino fluxes for four different models. The fluxes were evaluated for an observer at rest at 400km.

Newtonian vs. general relativistic simulations Finally we discuss the differences arising between general relativistic (GR) and Newtonian calculations by comparing s15Gso_1d.b with s15Nso_1d.b. In the Newtonian simulation, the gravitational force is of course smaller, therefore the star has to loose more leptons and energy to reduce the pressure to collapse. Hence the longer collapse time of 196.1ms and the lower central lepton fraction ($\Delta Y_{\rm lep} \simeq 0.02$), see Fig. 3.4. Although the smaller $Y_{\rm lep}$ would suggest a smaller homologous core, the smaller gravi-

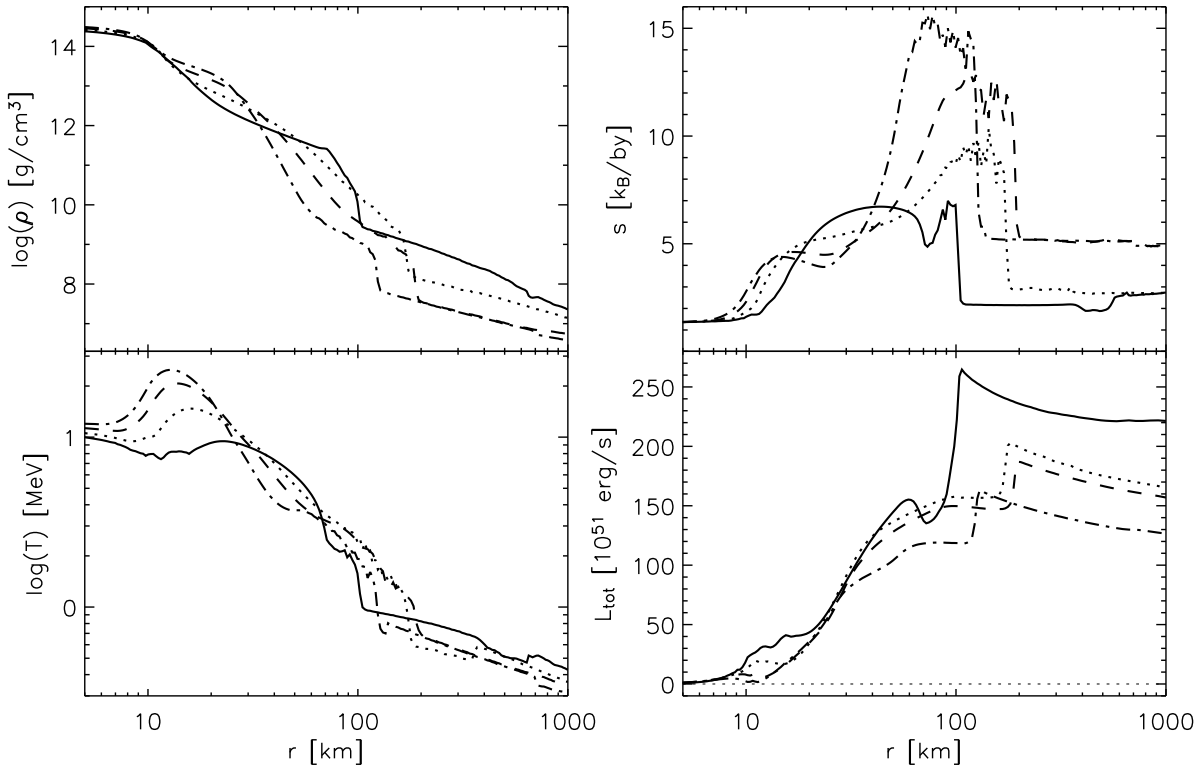

Figure 3.10: Various variables at the times 12.4ms (solid), 73.0ms (dashed), 177.7ms (thick), and 290.0ms (thick dashed) over radius for the Model s15Nso_1d.b.

tational force and infall velocities overcompensate this, and the shock creates at $M_{\rm sc} = 0.61 M_\odot$, which is $0.1 M_\odot$ further out of the core than in the GR simulation. Also, the shock creates at a larger radius $r_{\rm sc} = 12.5$km.

The less compact structure of the PNS strongly influences the post-bounce evolution: the standing accretion shock is at a larger radius, the increase of temperature and entropy in the gain layer is slower, and the neutrino luminosities are lower, see Figs. 3.10, 3.2, and 3.3.

3.1.3 Velocity terms in the first order moments equation

It is generally believed that the terms proportional to β in the radiation momentum equations (2.10,2.12) except for the $\beta\partial/\partial r$-terms in the first lines can be omitted (Mihalas & Mihalas (1984), see also the discussion in Rampp & Janka (2002)). Unfortunately, in the process of producing simulations, we found that this is not true at all. Our dynamic simulations show that these terms, which we will subsequently call β-terms, can contribute up to 20% of the LHS of the radiation momentum equation in the neutrino-heated region below the shock. Thus we find that the omission of these terms alters the dynamical evolution of our supernova simulations significantly and can trigger an artificial explosion (Sects. 3.1.4 and 3.2.2). If the β-terms can make the difference between explosion and failure, they must definitely be taken into account in supernova simulations.

We want to explain the problem on a snapshot of the Model s15Gio_1d.b at $t_{\rm pb} = 114$ms.

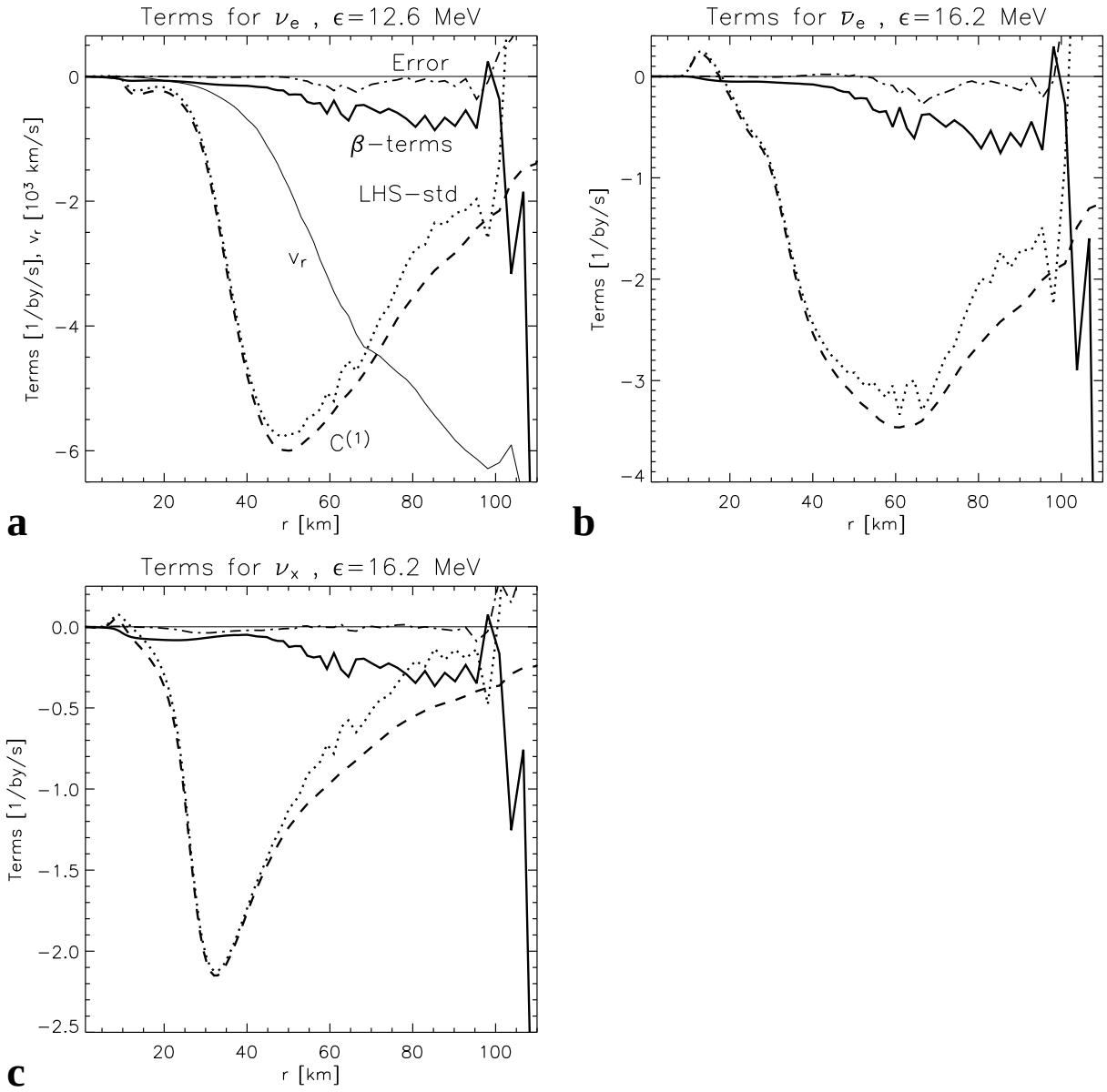

Figure 3.11: Comparison of the different terms in the radiation momentum equation (2.10) for the Model s15Gio_1d.b at t_{pb} = 114ms. The terms are collected in three lines: the β-terms (thick solid), the remaining terms on the LHS of Eq. (2.10) (dotted), and the source term on the RHS (dashed). We have also plotted the sum of all three (dashed-dotted), which should be zero, but is not due to our post-processing. All terms have been multiplied with m_B/ρ. Finally, the thin solid line depicts the velocity.

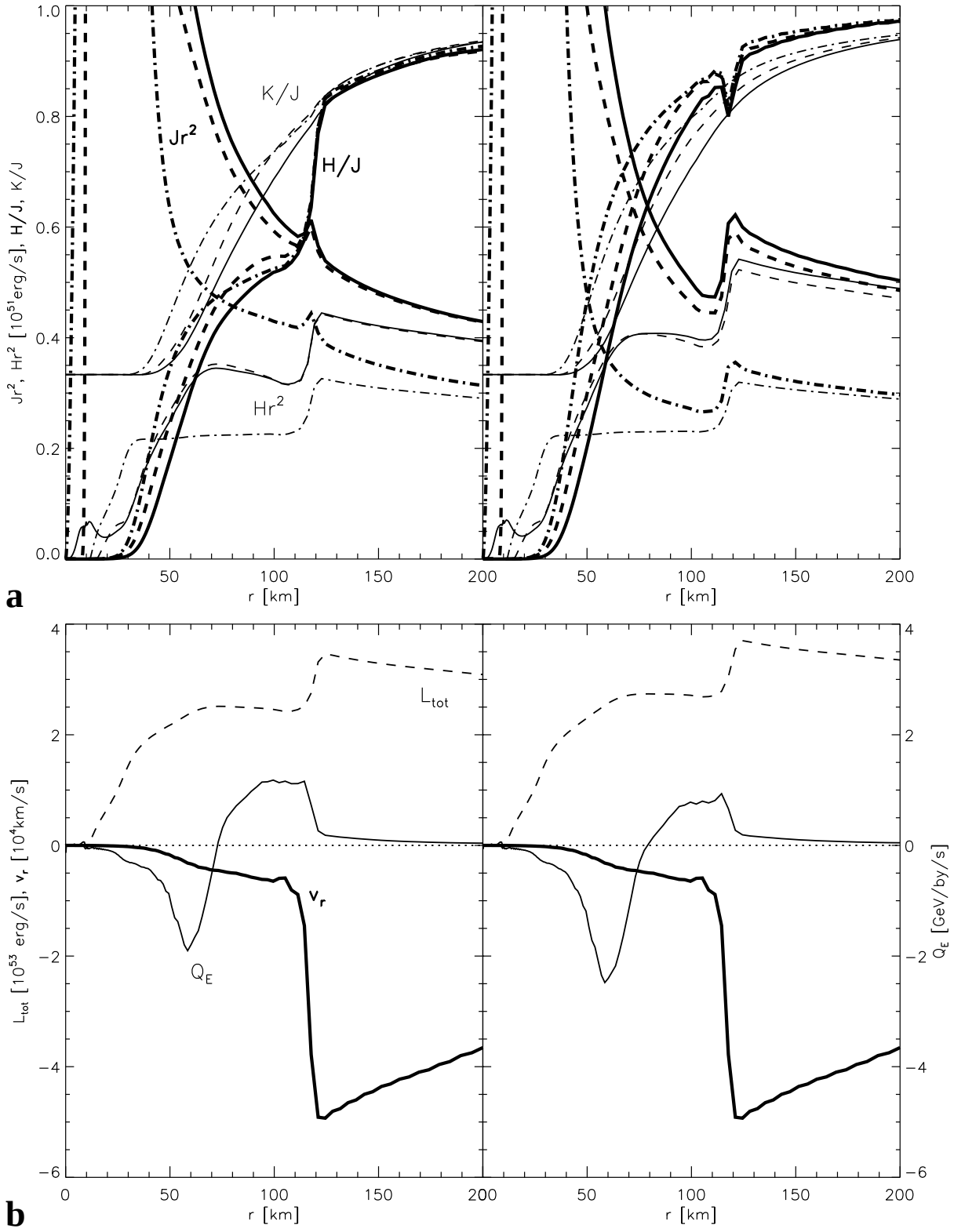

Figure 3.12: **a** Comparison of neutrino parameters for a stationary solution of the Model s15Gio_1d.b at t_{pb} = 114ms. The left panel shows the parameters for a solution where the β-terms have been dropped in the neutrino momentum equation, the right panel gives a solution consistent with the full neutrino momentum equation. We plot the neutrino energy density J, the flux factor $f_H = H/J$ (both thick), the neutrino energy flux H and the variable Eddington factor $f_{\mathrm{ed}} = K/J$ (both thin) for electron (solid), electron anti- (dashed) and muon neutrinos (dash-dotted).

b For the same situation as in (**a**), we show the velocity (thick), the total neutrino luminosity of all flavors (dashed) and the net source term (thin solid).

For this time we calculated the terms in the radiation momentum equation (2.10) for energies close to the spectral maxima (see Fig. 3.11). The β-terms contribute up to 20% of the LHS of Eq. (2.10) in the neutrino-heated region between 70-110km (see Fig. 3.12b); for the muon neutrinos, which do not heat significantly, the contribution can even dominate the LHS. If we interprete the β-terms as source terms, i.e. write them on the RHS, they have the effect of reducing the opacity. Thus, if we neglect the β-terms, the neutrinos stream less quickly, stay longer in the post-shock region, and thus the neutrino density is higher, leading to an increased heating above and below the gain radius. Note that for higher energies, the velocity terms become decreasingly important.

These statements are affirmed by Fig. 3.12, where we have calculated the stationary solutions for the above mentioned model and time both with and without the β-terms. The neutrino flux is larger in the solution with the β-terms, and consequently the neutrino density is smaller, which directly decreases the neutrino heating. From the plots, it can also be seen that the solution with the β-terms looks more consistent: the blue-shift (remember that the neutrino transport is solved in a comoving frame) of the neutrinos when they pass the shock leads to an increase in both luminosity and energy density, the shift in the energy density however can not be found in the solution without β-terms (the small peak designates the shock flank). Additionally, the flux factor of the solution with β-terms is consistent with other Boltzmann transport codes (see Liebendörfer et al. 2003). The variable Eddington factor $f_{\mathrm{ed}} = K/J$ is not very sensitive on the β-terms.

Dynamically, neglecting the β-terms can have dramatic effects. In Fig. 3.2a we see the evolution of the Models s15Gio_1d.a and s15Gio_1d.b, which merely differ in that only the Model “b” does include the β-terms. We see that the shock positions evolve increasingly different. Initially, the missing β-terms in Model “a” increase the heating. At later times, the increased heating has driven the shock further out, thus increasing the size and mass of the gain layer. The resulting positive back-reaction between increasing gain layer and thus increasing heating on the one hand and expanding shock radius on the other leads to a much larger shock radius than in Model “b”, where we obtain a negative back-reaction of decreasing gain layer and retreating shock.

A snapshot of the two models (Figs. 3.13, 3.14) confirms the static solution: in the consistent Model “.b”, the flux factor $f_H \equiv H/J$ increases much faster in the regions of effective cooling and heating than in Model “.a”, thus lowering the neutrino energy density and therefore decreasing the neutrino absorption rate significantly.

3.1.4 A model with marginal behaviour

Although the Model s15Gio_1d.a was not run with a consistent neutrino transport since the β-terms were neglected, its outcome is so fascinating that we decided to present it here. The oscillating shock behaviour, ending in an explosion, represents an, although hypothetical, nevertheless interesting riddle worth solving.

As discussed in the previous section, the omitted β-terms lead to an increased heating rate, thus driving the shock further out before it stalls into a standing accretion shock at 180km. Here, the shock remains until the oxygen-enriched silicon-shell passes through and leads to a sudden decrease of the ram pressure. The following cyclic behaviour is described as follows (see also

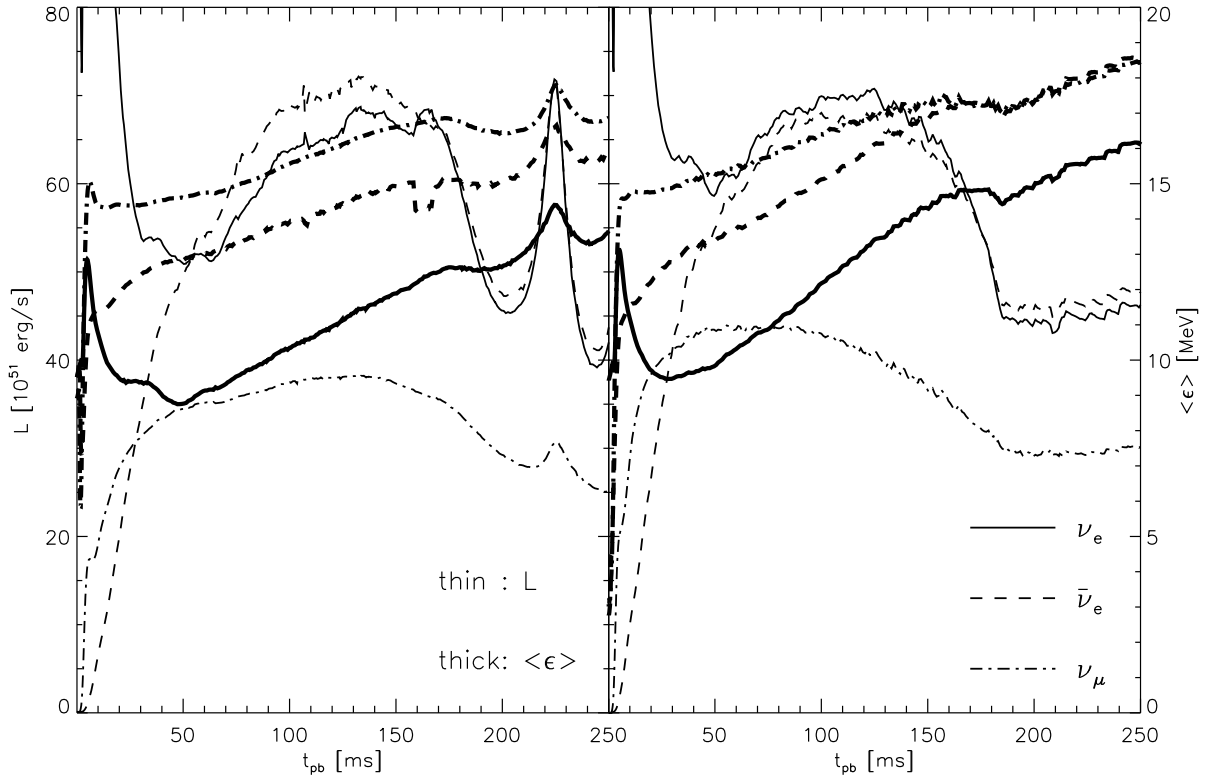

Figure 3.13: Comparison of the dynamical evolution of neutrino parameters for two models. The left panel shows the parameters for Model s15Gio_1d.a where the β-terms have been dropped, the right panel shows the Model s15Gio_1d.b, which is consistent with the full radation momentum equations. We show the luminosity (thin) and average energy (thick) over time for electron (solid), electron anti- (dashed) and muon neutrinos (dash-dotted), evaluated at a radius 400km for an observer at rest.

Fig. 3.15): the shock starts expanding, the matter passing is shocked more strongly and thus accreted slower into the cooling region. Slightly retarded, the neutrino luminosity drops as a consequence of the decreased mass accretion into the cooling region. As a consequence, the heating almost simultaneously drops due to the decreased luminosity, but also because the down-falling material has piled up close to the shock, where heating is inefficient. The shock is no longer resupplied with energy, but looses its strength because it has to cope with the ram pressure and the dissociation of nuclei. After propagation few tens of km, the shock has lost all its energy, and the material piled up just below it is not sufficiently supported by deeper layers. Both quickly fall inwards. The sudden accretion of matter into the cooling region increases the luminosities extremely, and the sudden increase of matter just above the gain radius, where heating is most efficient, drives the heating rate up to much more than 10% of the cooling rate. The shock bounces and is driven out with renewed energy. This cycle is repeated several times. Obviously, the backreaction of the cycle is positive, since the amplitudes increase with time and the cycle finally leads to an explosion.

However, it seems very difficult to pin down the reason why exactly this model features such an up and down, while no other of our models suffer this vertiginous fate. The fact that the β-terms are neglected surely increases the heating, especially during the sudden slump when negative velocities are high, which leads to even more efficient heating.

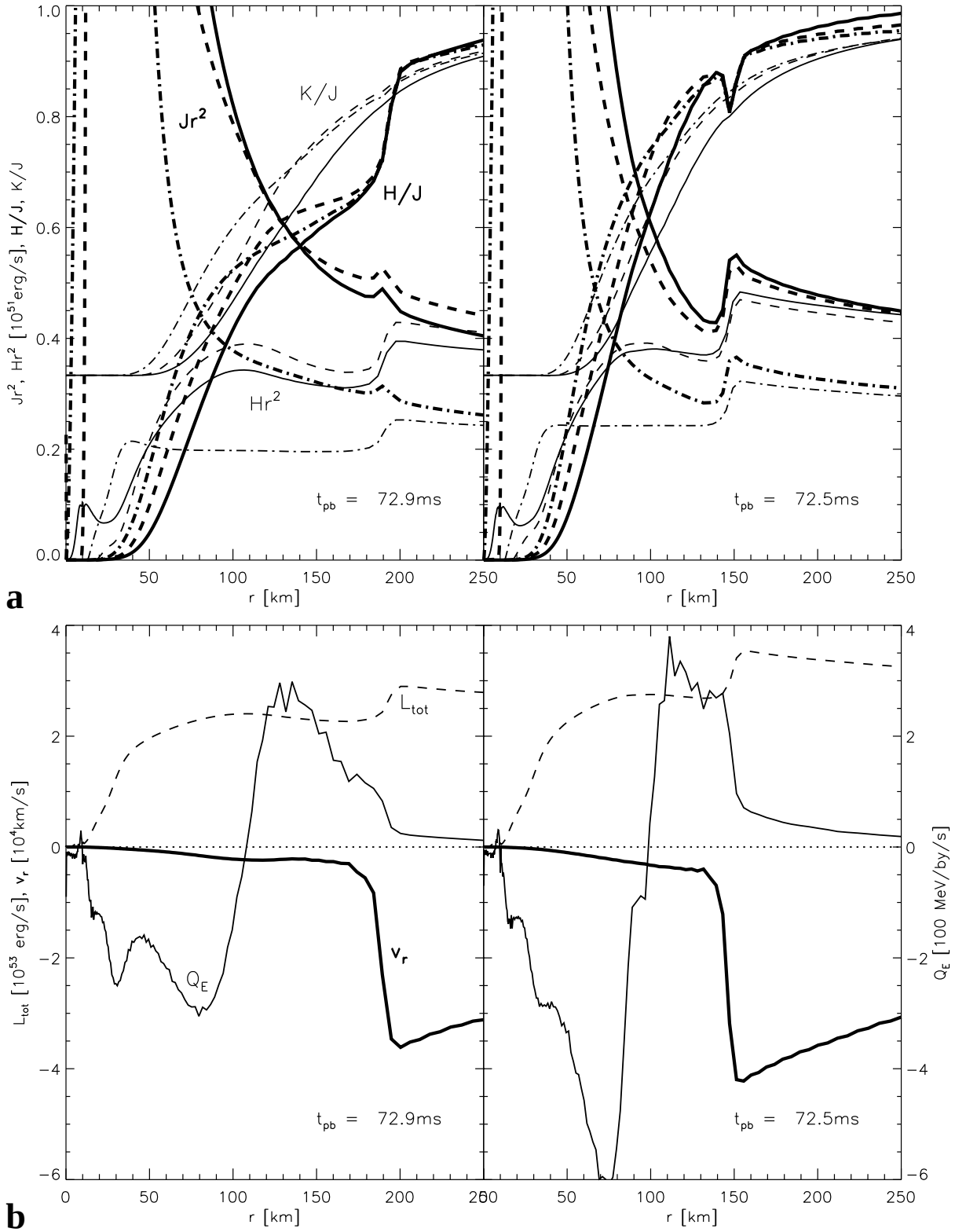

Figure 3.14: a Comparison of neutrino parameters for two models at t_{pb} = 73ms. The left panel shows the parameters for Model s15Gio_1d.a where the β-terms have been dropped, the right panel shows the Model s15Gio_1d.b, which is consistent with the full radation momentum equations. We plot the neutrino energy density J, the flux factor $f_H = H/J$ (both thick), the neutrino energy flux H and the variable Eddington factor $f_{ed} = K/J$ (both thin) for electron (solid), electron anti- (dashed) and muon neutrinos (dash-dotted).

b For the same situation as in (**b**), we show the velocity (thick), the total neutrino luminosity of all flavors (dashed) and the net source term (thin solid).

We see two possibilities for explaining the phenomenon, however make no effort to perform a detailed analysis of any of these. On the one hand the physical conditions which characterize the expansion and contraction phases resemble the conditions that allow for non-adiabatic vibrational instability (κ-mechanism) in stellar atmospheres where the outward-going heat flow is modulated by the rhythm of the pulsation and instability occurs if durng adiabatic compression the absorption coefficient increases (see, e.g. Kippenhahn & Weigert 1990, Chapter 39.1).

On the other hand, the model might reveal the action of the so-called acoustic-advective cycle proposed by Foglizzo & Tagger (2000) for adiabatic accretion flows to black holes. In this scenario, acoustic waves created at the PNS surface propagate to the shock and cause entropy fluctuations there. When these fluctuations are advected to the PNS surface by the accretion flow, they create new acoustic waves and so on. If the feedback is positive, an $l = 0$ mode can be built up, as seen in our model. A preliminary analysis by T. Foglizzo (2003, personal communication) revealed that our oscillating model has favorable conditions for developing an $l = 0$ instability by the advective acoustic cycle. However, in our model neutrino heating and cooling dominate and the accretion flow is not at all adiabatic. A more reliable analysis has to account for this fact and remains to be done.

3.2 Two-dimensional models

A look at the Ledoux criterion for the 1D models (Figs. 3.20b, 3.22, 3.30a) tells us that the gain layer as well as an extended region in the PNS are convectively unstable, so that multi-dimensional simulations become mandatory. Here, we present the first two-dimensional simulations run with a neutrino Boltzmann solver. The two Models s15Gio_32.a and s15Gio_32.b correspond to the one-dimensional Models s15Gio_1d.a and s15Gio_1d.b, respectively, presented in Sects. 3.1.1 and 3.1.4, i.e. they include state-of-the-art neutrino processes as described in (Rampp & Janka 2002) and Appendix A and an approximate, spherically symmetric treatment of general relativity (Sect. 2.1). Remember that Model "b" is the one with the correct treatment of neutrino transport, while Model "a" wrongly neglects the β-terms in radial direction (see Sect. 3.1.3). In the angular direction both models consist of 32 zones with a resolution of 2.7^{o}, thus covering a wedge around the equator from -43.2^{o} to $+43.2^{o}$. Both models were collapsed in one dimension and mapped to 2D around 7ms after the bounce. Simultaneously, lateral perturbations were seeded by randomly changing the radial velocity by up to $\pm 1\%$ in the entire star. The treatment of the lateral neutrino transport was carried out as described in Sect. 2.2. Note that in Model s15Gio_32.b the inner 2km were treated spherically symmetric to maintain a reasonable CFL time step. Model s15Gio_32.a did not include the lateral momentum transfer to the fluid, Eq. (2.22), and therefore had to be run spherically symmetric below 25km, thus inhibiting artificial, and unfortunately also physical, PNS convection (for a discussion see Sect. 2.3.2).

3.2.1 A model with full transport treatment

While Model s15Gio_32.b represents the present acme of supernova computation, it nevertheless fails to explode. In Fig. 3.18 we see the shock trajectory and mass shells of this model. After

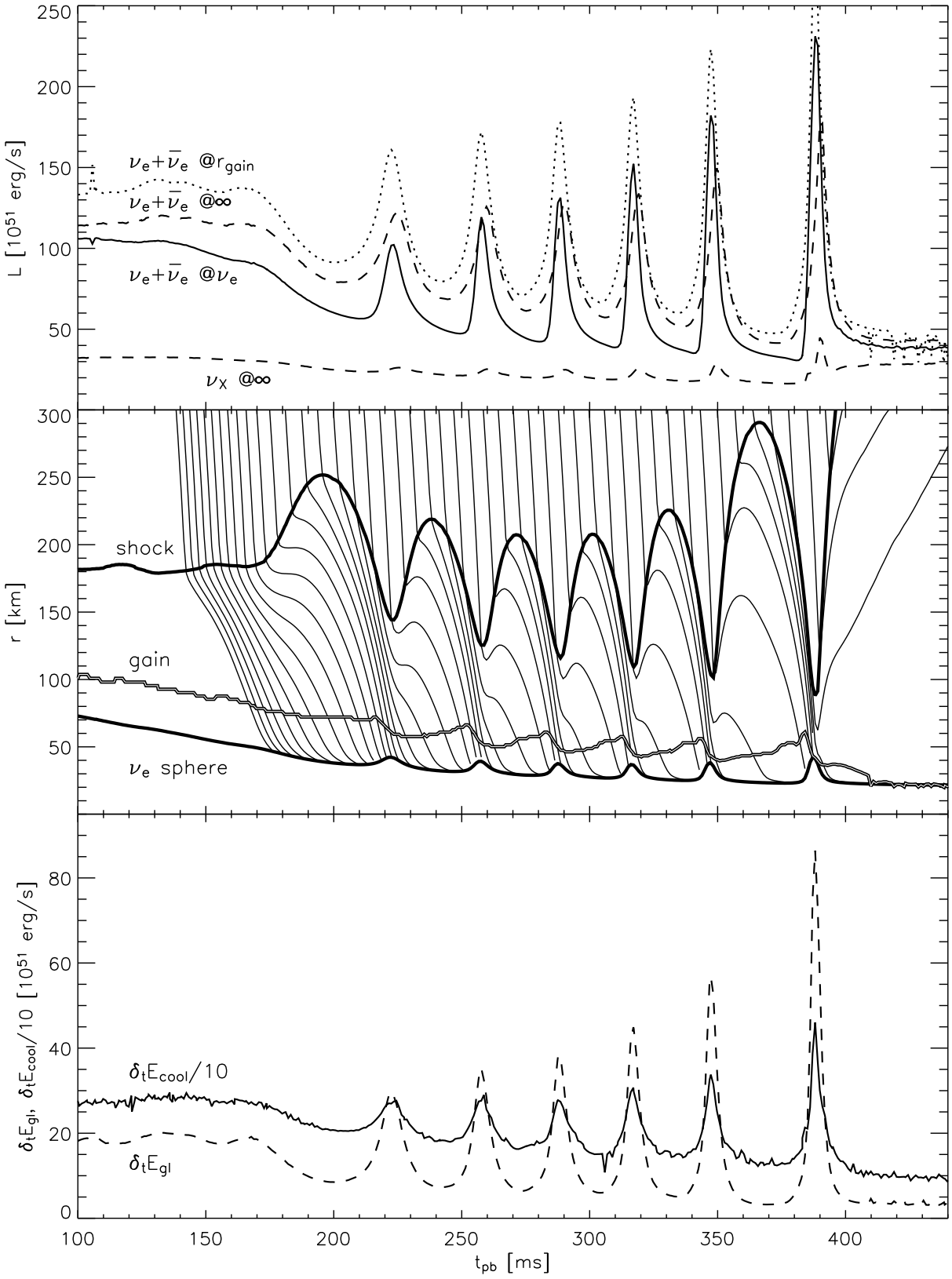

Figure 3.15: Detailed analysis of Model s15Gio_1d.a. The upper panel depicts the summed luminosity of electron type neutrinos at the neutrinosphere of the ν_e (solid), at the gain radius (dotted) and at 400km (dashed), latter for an observer at rest. The lower dashed line shows the luminosity for any one neutrino of type μ or τ, also for an observer at rest at 400km. The middle panel depicts the evolution of shock (upper thick), gain (striped) and ν_e-sphere (lower thick) radius. The thin lines stand for mass shells, starting at $M = 1.41 M_\odot$ and moving upwards in $0.002 M_\odot$ steps. The lines where cut off at the ν_e-sphere. The lower panel shows the total energy transfer into the neutrino sector in the cooling region (solid, divided by 10) related to the total net heating in the gain layer (dashed).

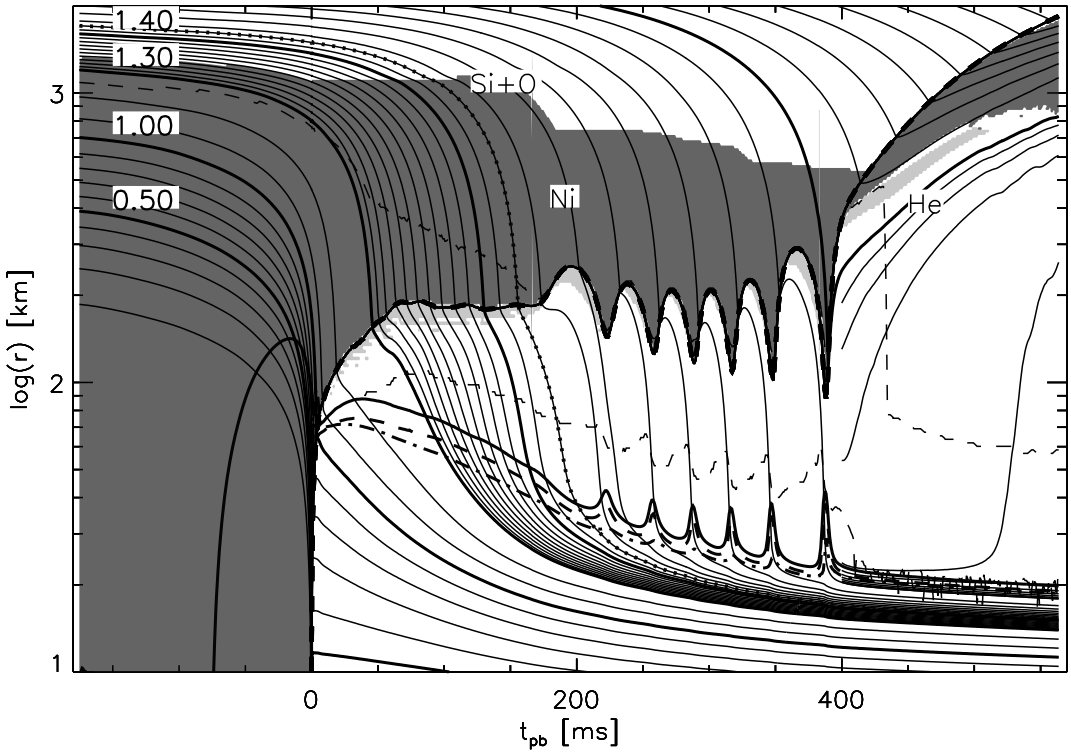

Figure 3.16: Mass shells for Model s15Gio_1d.a. We have supplemented the plot with the transport neutrinospheres for ν_e (thick solid), $\bar{\nu}_e$ (thick dashed) and ν_x (thick dashed-dotted), the mass shell at which the silicon shell becomes oxygen-enriched (knotted solid line, at $1.42 M_\odot$), and the shock (thick solid line with dashes). Further we have marked the regions which consist to more than 60% of nickel-like elements (dark shaded) and ^{4}He (shaded, not present). Also shown are regions which consist of more than 30% of ^{4}He (light shaded). Finally the lower thin dashed line marks the gain radius, while the upper one marks where we have the interface between our two EoS (i.e. at $\rho = 6 \cdot 10^7 \mathrm{g/cm}^3$).

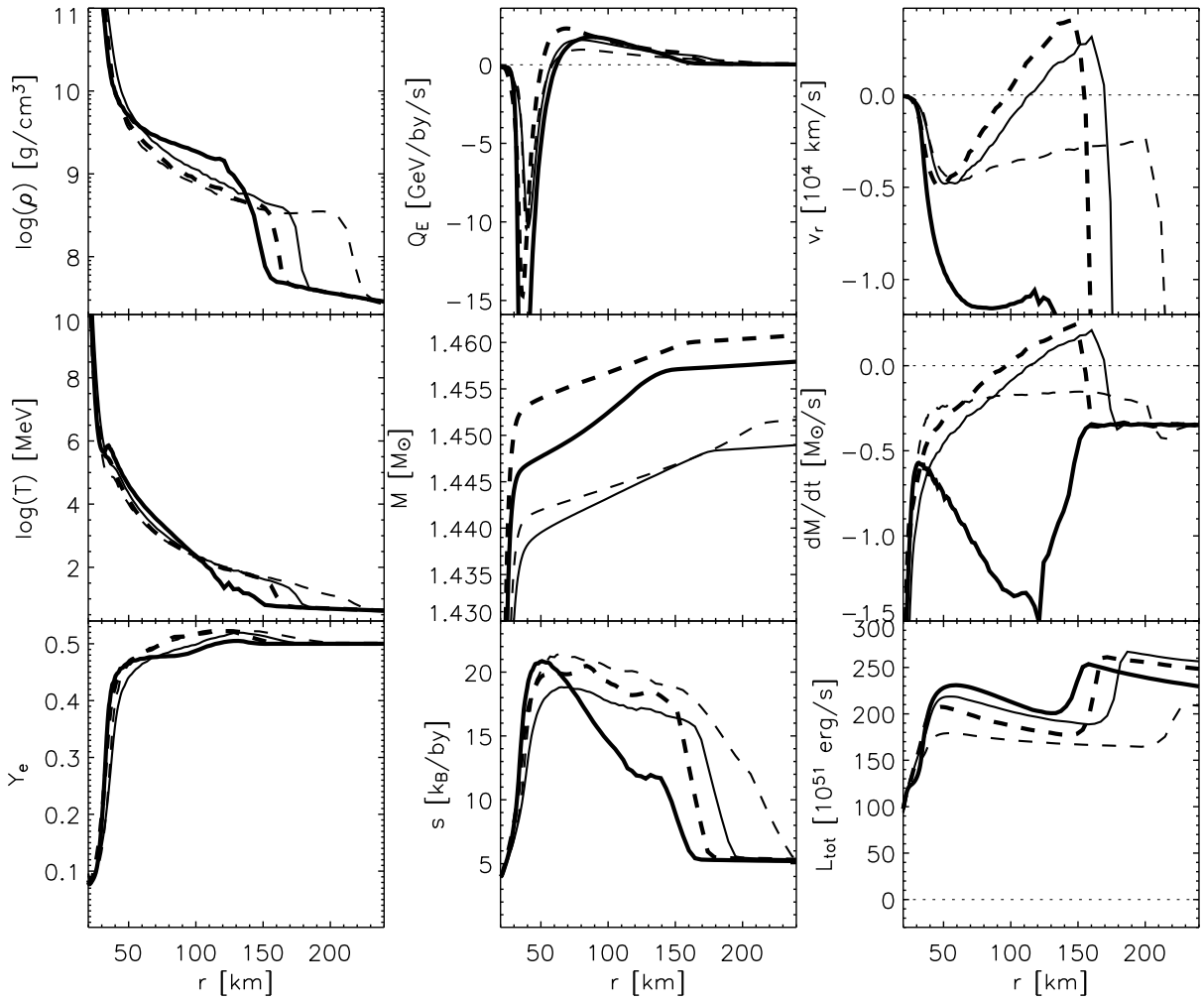

Figure 3.17: Various variables at the times 228.6ms (solid), 236.4ms (dashed), 254.4ms (thick), and 262.6ms (thick dashed) over radius for the Model s15Gio_1d.a. For the time 254ms the cooling extends down to $Q_{\mathrm{E}} = -30.1\mathrm{GeV/by/s}$.

the prompt shock expansion, the shock expands slowly to a maximal radius of 150km around 60ms, and then starts to retreat slowly. This is quite similar to the 1D case (c.f. Fig. 3.2a), 2D effects merely shift the shock position further out by some 10km.

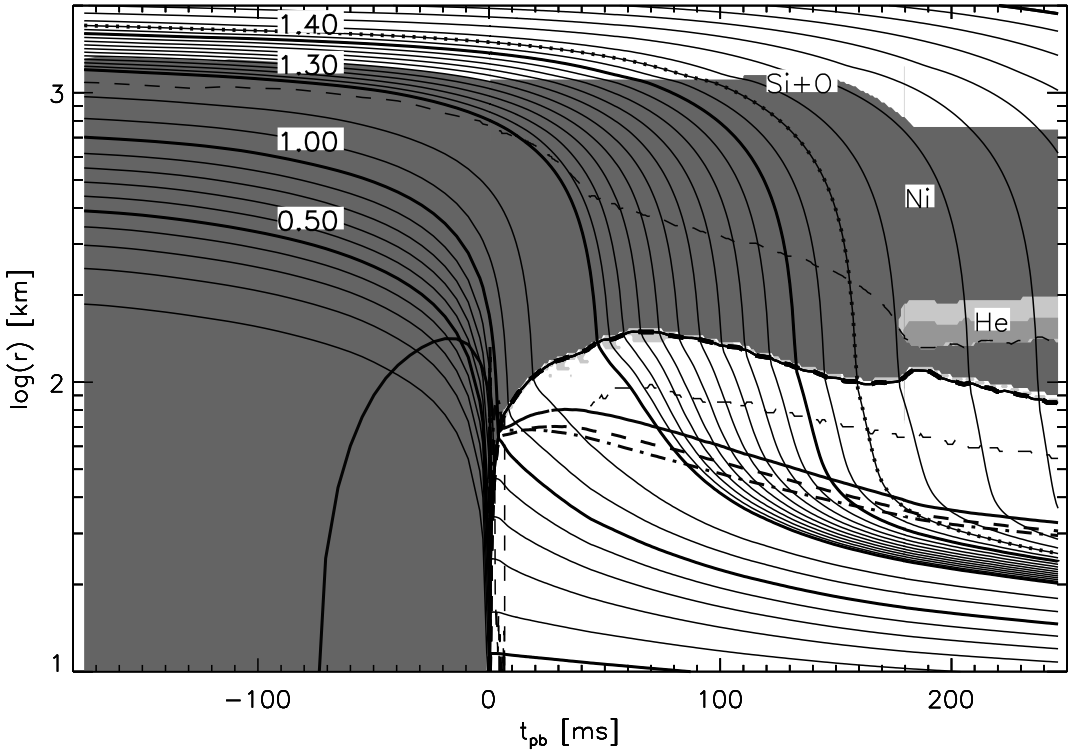

Figure 3.18: Angle-averaged mass shells for the failing Model s15Gio_32.b. We have supplemented the plot with the transport neutrinospheres for ν_e (thick solid), $\bar{\nu}_e$ (thick dashed) and ν_x (thick dashed-dotted), the mass shell at which the silicon shell becomes oxygen-enriched (knotted solid line, at $1.42 M_\odot$), and the shock (solid line with dashes). Further we have marked the regions which consist to more than 60% of nickel-like elements (dark shaded) and ^{4}He (shaded). Latter is surrounded by the regions which consist of more than 30% of ^{4}He (light shaded). Finally the lower thin dashed line marks the gain radius, while the upper one marks where we have the interface between our two EoS (i.e. at $\rho = 6 \cdot 10^7 \mathrm{g/cm}^3$).

The original hope in performing 2D calculations was that the hot bubble (HB) convection in the gain layer would strengthen the shock. This happens by means of a more effective neutrino energy deposition: strongly heated material close to the neutrino surface is brought up to the shock in bubbles by buoyant forces, at the same time narrow downflows passing besides the bubbles feed the region of effective neutrino heating with cool material. 2D calculations also get rid of one big disadvantage of 1D calculations: when the shock starts expanding in 1D calculations, the accretion of fresh material into the cooling region is drained, the sudden drop in luminosity and thus heating is fatal for the expanding shock.

In the current model, the convection has difficulties developing: starting to become distinct at 60ms, the HB convection (Fig. 3.20) has not yet formed large scale structures when the shock starts retreating, and thus does not yet push the shock significantly further out with respect to the 1D shock. Also in the subsequent phase the HB convection can not develop large, efficient

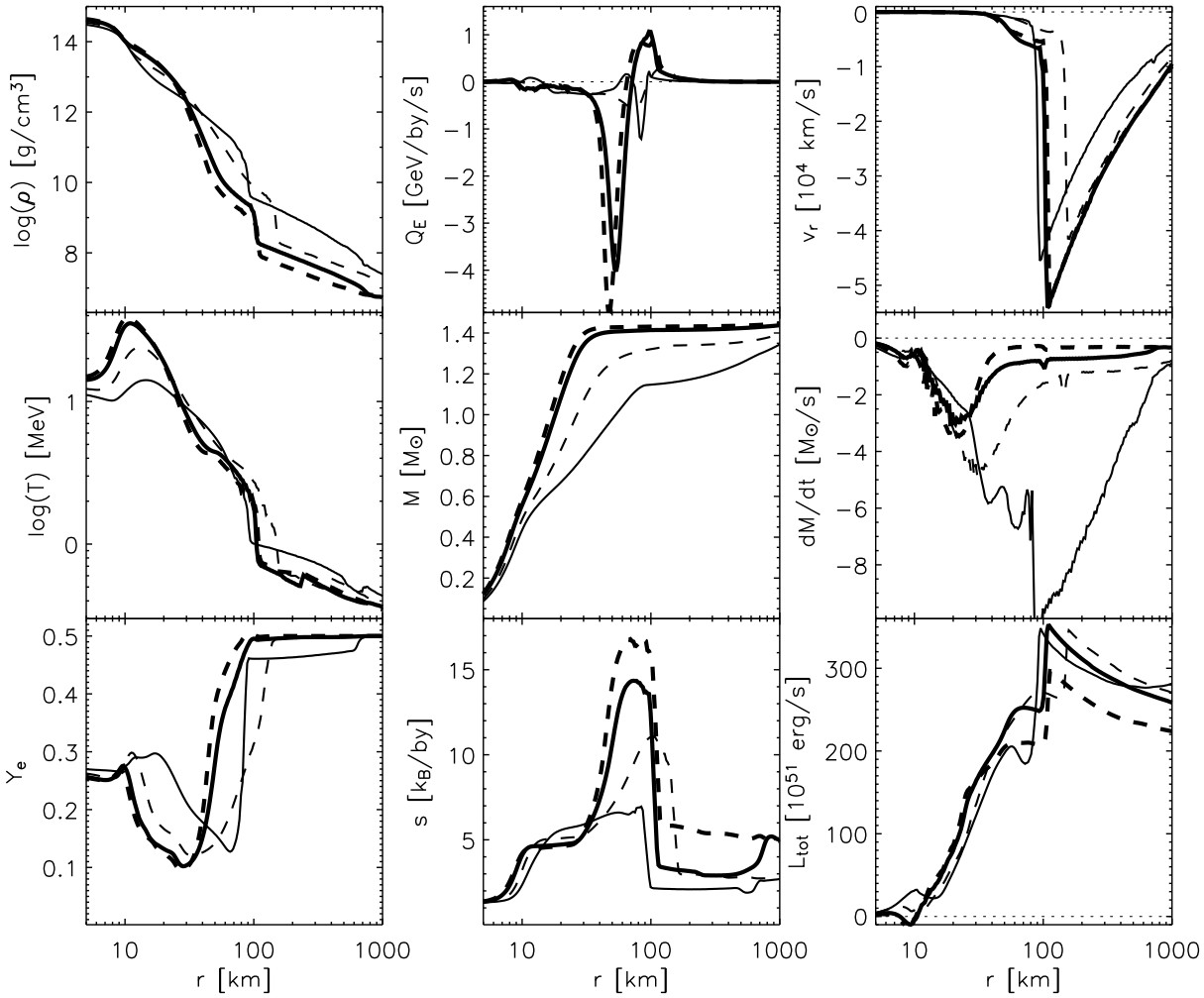

Figure 3.19: Various angle-averaged variables at the times 11.6ms (solid), 30.7ms (dashed), 72.3ms (thick), 150.7ms (thick dashed), and 181.4ms (dash-triple-dotted) over radius for the state-of-the-art Model s15Gio_32.b.

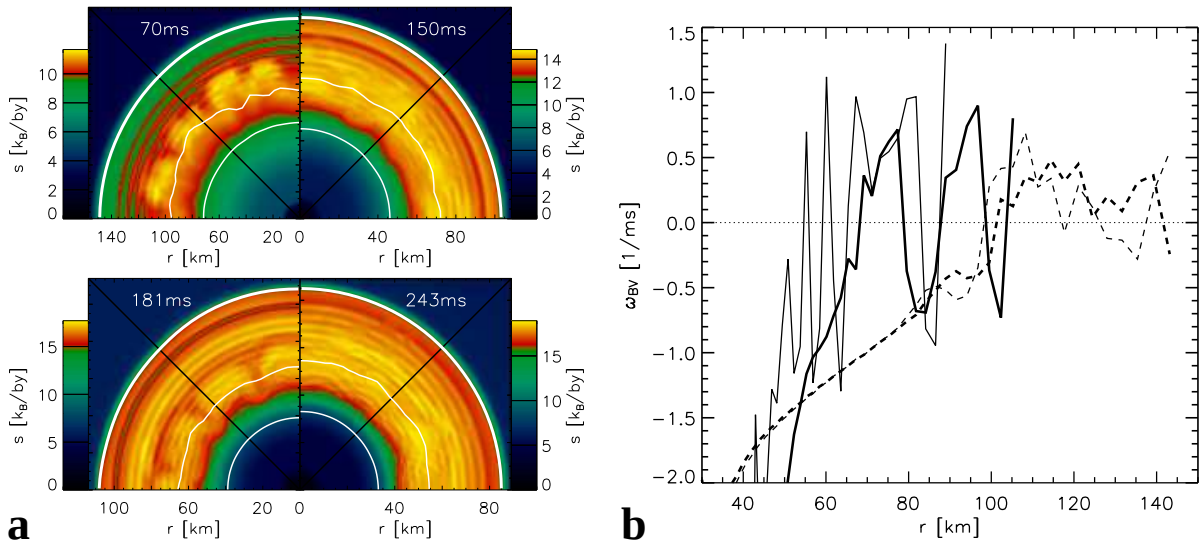

Figure 3.20: **a** Snapshots of the HB region of Model s15Gio_32.b. All panels show the entropy s, the lines mark the shock position (thick), the gain radius (upper thin), and the ν_e-sphere (lower thin). The solid black line denotes the equator.

b Brunt-Väisälä frequency for the times 72.3ms (dashed) and 181.4ms (solid) for the Model s15Gio_1d.b (thin) and s15Gio_32.b (thick). We only depict the lines below the shock.

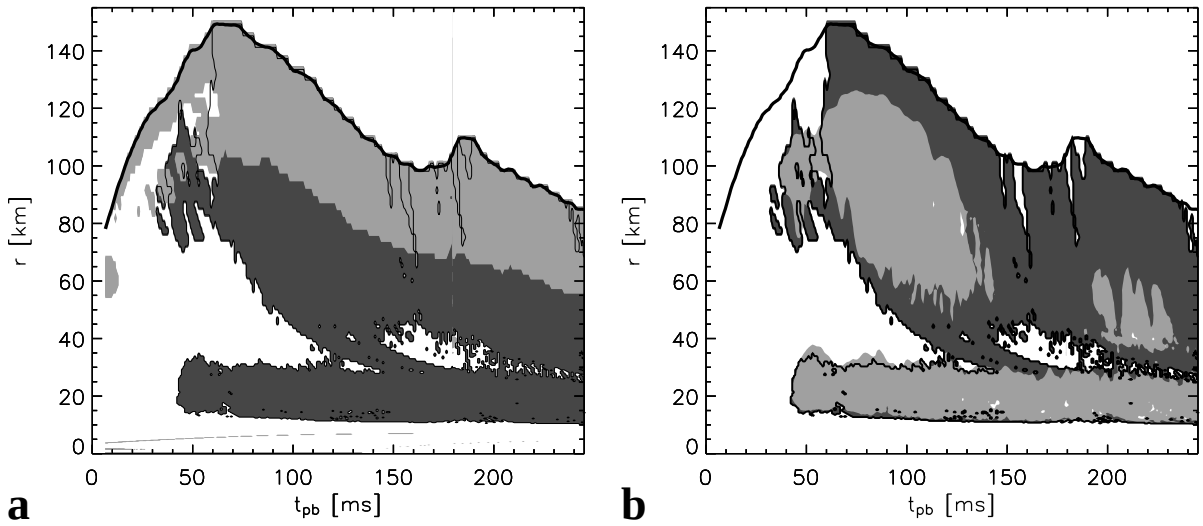

Figure 3.21: **a** Convective regions for Models s15Gio_32.b. The dark shaded region has lateral velocities above 700km/s, the light shaded region shows where the Ledoux criterion predicts instability ($C_L > 0$). The results were only evaluated below the shock (thick solid line).

b Same as **a** except that the light shaded region shows where the standard deviation of Y_e variations (defi ned in analogy to Eq. 2.27), $\sigma_{Y_e} > 0.03$.

modes: during the ms the advecting matter dwells in the gain layer, it can not establish strong buoyant forces; only small bubbles develop far below the shock, which shortly after are engulfed by the cooling region. The shock itself feels nothing of the convection and remains spherically symmetric throughout the run. The HB convection in this model remains a minor correction to the one-dimensional model.

Eventually, the transient shock expansion correlated with the sudden decrease of ram pressure when the oxygen-enriched silicon shell meets the shock revives the hot bubble convection, but by this time (180ms), the shock has already retreated to below 100km, and an explosion has become but a distant dream.

We should comment on the Helium visible in Fig. 3.18 at t>180ms and 150km<r<200km. This Helium is produced by the pseudo-NSE described in Rampp & Janka (2002, App. B), however, as soon as the material falls into the high-density EoS above $6 \times 10^7 \mathrm{g/cm^3}$, the Helium recombines again to heavy nuclei. This feature can be accounted for by the inadequate description of the composition by the pseudo-NSE. In this model, however, the evolution is not affected by this: the material is falling super-sonically, thus the transient dissociation and recombination of the material does not influence anything at all.

Proto neutron star convection This model represents a unique opportunity to examine proto neutron star (PNS) convection in a fully self-consistent simulation with neutrino Boltzmann transport. The model was run till 243ms post-bounce, thus presenting the early evolution of the PNS.

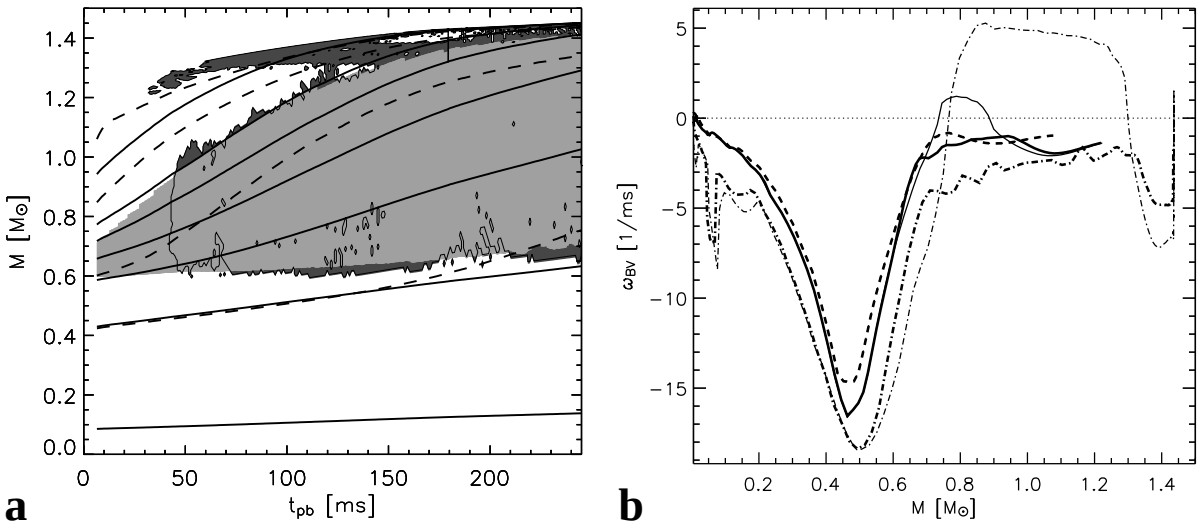

Figure 3.22: **a** Convective region in Model s15Gio_32.b. The dark shaded region has lateral velocities above 700km/s, the light shaded region fulfi lls the Ledoux-criterion for marginal stability, Eq. (3.5). The solid lines denote the radii up to 30km in 5km steps, and 50km, the dashed lines indicate density contour lines of 10^{14}, 10^{13}, 10^{12}, and $10^{11}\mathrm{g/cm^3}$.

b The Brunt-Väisälä frequency in Models s15Gio_1d.b (thin) and s15Gio_32.b (thick) at times 30ms (dashed), 62ms (solid), and 200ms (dash-dotted). For 30ms, the lines coincide. We cut off the lines above 50km.

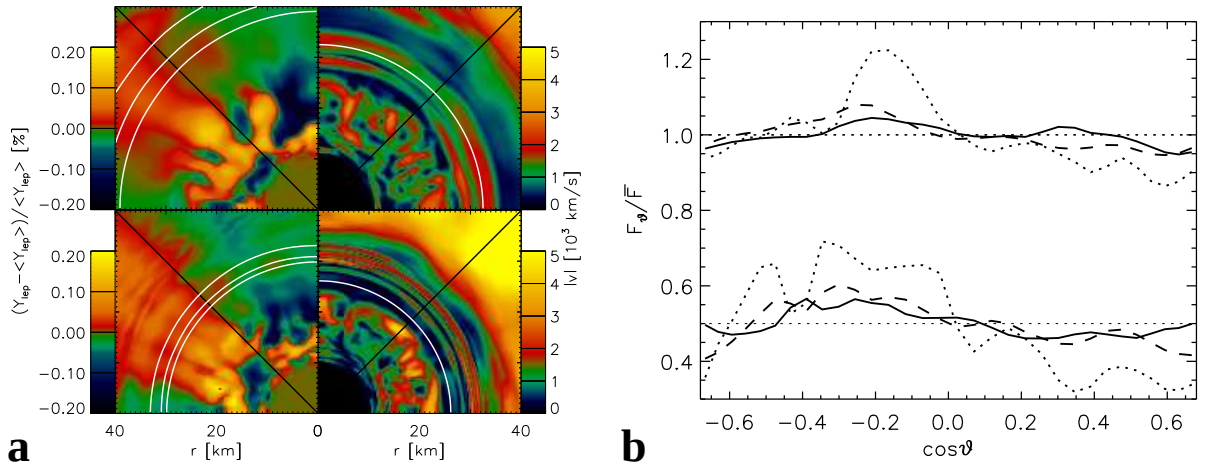

Figure 3.23: **a** Snapshots of the PNS of Model s15Gio_32.b. The upper panels depict the deviation in $Y_{\rm lep}$ (left) and the absolute velocity $|v| = \sqrt{v_r^2 + v_\vartheta^2}$ (right) for $t = 151$ms. Additionally, the neutrinosphere for the three types $\nu_{\rm e}$, $\bar{\nu}_{\rm e}$ and $\nu_{\rm x}$ are marked (solid white lines left), as well as the radius where the angle-averaged optical depth of the electron neutrinos $\tau = 15$ (solid white line right). The lower panels show the same for $t = 243$ms.

b Variation of the $\nu_{\rm e}$ fluxes F_ϑ at different radii, normalized over the average flux $\bar{F}$, for the same times as in **a**. The normalized flux is shown at the radius where the angle-averaged optical depth for $\nu_{\rm e}$ is $\tau = 15$ (dotted, at 32.5km and 26.1km), at the $\nu_{\rm e}$-sphere (dashed, at 46.1km and 33.1km), and at 380km (solid). For clarity, the lines for the later time have been shifted down by 0.5.

Convection appears in regions where the Ledoux criterion predicts instability or marginal stability. In analogy to Keil et al. (1996), our definition for marginal stability reads

$$C_{\rm L}(r) > a \cdot \min_r \left(C_{\rm L}(r)\right), \tag{3.5}$$

where $C_{\rm L}$ is defined in Eq. (2.25) and we chose $a = -0.05$. However, we only apply the criterion for marginal stability at densities above $3 \cdot 10^{12}$g/cm^3, at lower densities the coupling between the neutrinos and the medium is too weak so that neutrinos cannot alter the stability criterion. In Fig. 3.22a, we show how the region where the PNS is only marginally stable (light shaded) evolves. We see that PNS convection sets in around 40ms. Comparing with the Ledoux criterion at this time for the 1D model (Fig. 3.22b) this coincides with the time when the Ledoux-criterion first predicts true instability.

Lately, Bruenn et al. (2004) presented a more elaborate discussion of the stability analysis in the PNS which incorporates the influence of neutrino diffusion (an extension of the discussion in Bruenn & Dineva (1996)). They argue that local perturbations in the lepton number will show up in the neutrino phase space and thus cause a net neutrino diffusion which washes out the perturbation. Since neutrinos also carry entropy the same neutrino diffusion that smoothes the lepton number perturbation will create an entropy perturbation. Of course, entropy perturbations will analogously induce a net neutrino diffusion to smooth itself out. However, Bruenn et al. (2004) found in a numerical analysis that the neutrino diffusion would react much quicker on lepton number perturbations. Thus they found that for certain conditions which predict Ledoux stability the fact that neutrinos would *build up* entropy perturbations in order to wash

out lepton number perturbations would predict instability. They found two types of convection which should occur in the PNS: one where the buoyant rise of a perturbed fluid element, together with neutrino diffusion, will further increase the discrepancy between the entropy of the fluid element and its surroundings and thus drive the buoyant motion, and one where the neutrino diffusion creates an "overstable" situations, i.e. where the effect of neutrino diffusion will drive a perturbed fluid element back to its original position, but to such an extent that the fluid element overshoots and thus oscillates around its original position with increasing amplitude. Bruenn et al. (2004) call the convective types arising from these two instabilities "lepto-entropy finger" (LEF) convection and "lepto-entropy semi-convection" (LESC), respectively. They also distinguish Ledoux convection, however, Ledoux and LEF convection are closely connected (LEF is an extension of Ledoux convection) and we will treat them as one type of convection.

Their analysis of their stellar profiles show that Ledoux/LEF convection should appear in an extended region of the PNS from around 15km to the neutrinospheres while LESC should be visible below. We expect that our stellar profiles yield qualitatively similar results if one applies their analysis. Our two-dimensional simulations, however, do not reproduce these predictions. Our convection, which we interpret as Ledoux/LEF convection, appears between 10km and 25km but does not extend fully to the neutrinospheres. We suspect that their discussion is not fully correct in this regime. One of the assumptions which we believe is necessary for their discussion is that the size of the blobs which are perturbed is very much larger than the mean free path of the neutrinos. If this assumption does not hold, one can not speak of diffusion between the fluid element and its surroundings since the neutrinos can travel through the whole fluid element without interacting once. As a result, any fluctuations which could build up by their mechanism would be washed out. We find that the mean free path of the neutrinos becomes sizeable around the upper boundary of our PNS convective region, explaining why their predictions are not valid above this point.

Concerning the LESC convection that Bruenn et al. (2004) predicts far inside the PNS, we do not see this instability. We have not tried to understand the reason for this discrepancy between the prediction of Bruenn et al. (2004) and our numerical simulations, and argument that convection this far inside of the PNS should have even less influence on the shock dynamics than the PNS convection which we obtain. Therefore, with respect to the neutrino luminosities and the explosion mechanism, we are not very concerned about the absence of LESC convection in our simulations.

Over the time of the simulation, PNS convection appears above a mass around $0.5 M_{\odot}$. This inner boundary only changes little during the simulation. This evolution is somewhat different to that found by Keil et al. (1996), whos simulation showed PNS convection in an initially small region but with a constantly decreasing lower boundary. However, their model was run up to 1.3s, our model might also have shown a decreasing lower boundary at later times. The upper boundary of the convective region increases with time in mass, as matter is continuously advected onto the PNS.

The region with large lateral velocities (>700km/s, dark shaded in Fig. 3.22a) is larger than the region marked by marginal stability. This has two reasons: first, the PNS convection can over- and under-shoot the region which supports convection. Second, applying periodic boundary conditions, as was done in this model, allows rings of uniform, lateral velocities to appear; this numerical artefact is produced in this simulation by matter from the HB region settling onto the PNS. The rings are protuding in Figs. 3.22a and 3.21, where they can be seen as a bar

of high lateral velocity moving from the HB convective zone to the PNS convection region at t=110–150ms.

Looking at the 2D distribution of velocity, Fig. 3.23a, the rings can be identified around r=30km. From these plots it is also easy to see that the region with convective overturn is closely related to the region of marginal Ledoux-stability. E.g. for t=243ms the Ledoux criterion predicts convection between 10 and 23km (Fig. 3.22a), which coincides with the lower right panel of Fig. 3.23a (10–24km).

The effect of PNS convection can be seen comparing the profiles of the star after 243ms for the 1D and 2D simulations, Fig. 3.24. The PNS convection transports lepton number and energy from the lower region of the convective zone (0.6–1.0$M_\odot$) to the upper region (1.0–1.3$M_\odot$). The lower region already has nuclear densities and is thus marginally influenced in its structure. The upper region, however, is mainly held by the pressure from electron degeneracy, thus the structure changes significantly due to the larger Y_e and the density is lower than in the 1D model, which subsequently alters the structure of the matter above: the density of the 2D model drops slower in radius. Since the neutrinospheres tend to be at densities around 10^{12}g/cm^3, the neutrinos consequently are emitted at larger radii and thus lower temperature.

The lower temperature at the neutrinospheres displays in the lower mean energies of the neutrinos, see Fig. 3.2b. However, the effect of PNS convection on the luminosities is more subtle: following the rule $L \propto R_\nu^2 T^4(R_\nu)$ larger radii with lower T mean that the luminosity should not have changed strongly with PNS convection (e.g. Janka 1995). This is confirmed by the data (Fig. 3.3): from 50–150ms, the luminosities are very slightly decreased, after that, they are moderately increased with a stronger impact on ν_x. As an example, for t = 243ms (see Fig. 3.24), $T(R_\nu)$ in the 2D model is 4–7% lower than in the 1D model, while the neutrinosphere radius has increased by 15%, affirming a slight increase in luminosity.

The PNS convection also affects the neutrino luminosites through the increased lepton number in the outer regions of the PNS (around 25km). Although the PNS convection only reaches out to optical depths around 30, the quickly decreasing chemical potential of the ν_e leads to strong neutrino diffusion at the Fermi edge. This explains the strong deviations in lepton number outside the convective part of the PNS (Fig. 3.23). The diffusion partly reaches out to the neutrinosphere and increases the ν_e luminosity relative to the $\bar{\nu}_\mathrm{e}$ one.

The structural changes in the region between the neutrinosphere and the shock due to PNS convection are only moderate. I postpone the discussion of them to Sect. 4.3.

This analysis assumed that all discussed differences between 1D and 2D stem from the PNS convection. However, the HB convection in this model, although weak, could also have an impact on the evolution, especially of the ν luminosities and energies, since the material producing the main bulk of neutrino emission has to pass the HB region before cooling. The Model s15Gio_32.a, although without β-terms, gives us a hint on the effect of HB convection, since it was calculated with spherical symmetry below 25km, thus inhibiting PNS convection. Comparing it with its 1D companion, we see a quite similar evolution of the PNS before the onset of explosion where HB convection already is very lively. This suggests that the above discussed differences between s15Gio_32.b and s15Gio_1d.b mainly stem from PNS convection.

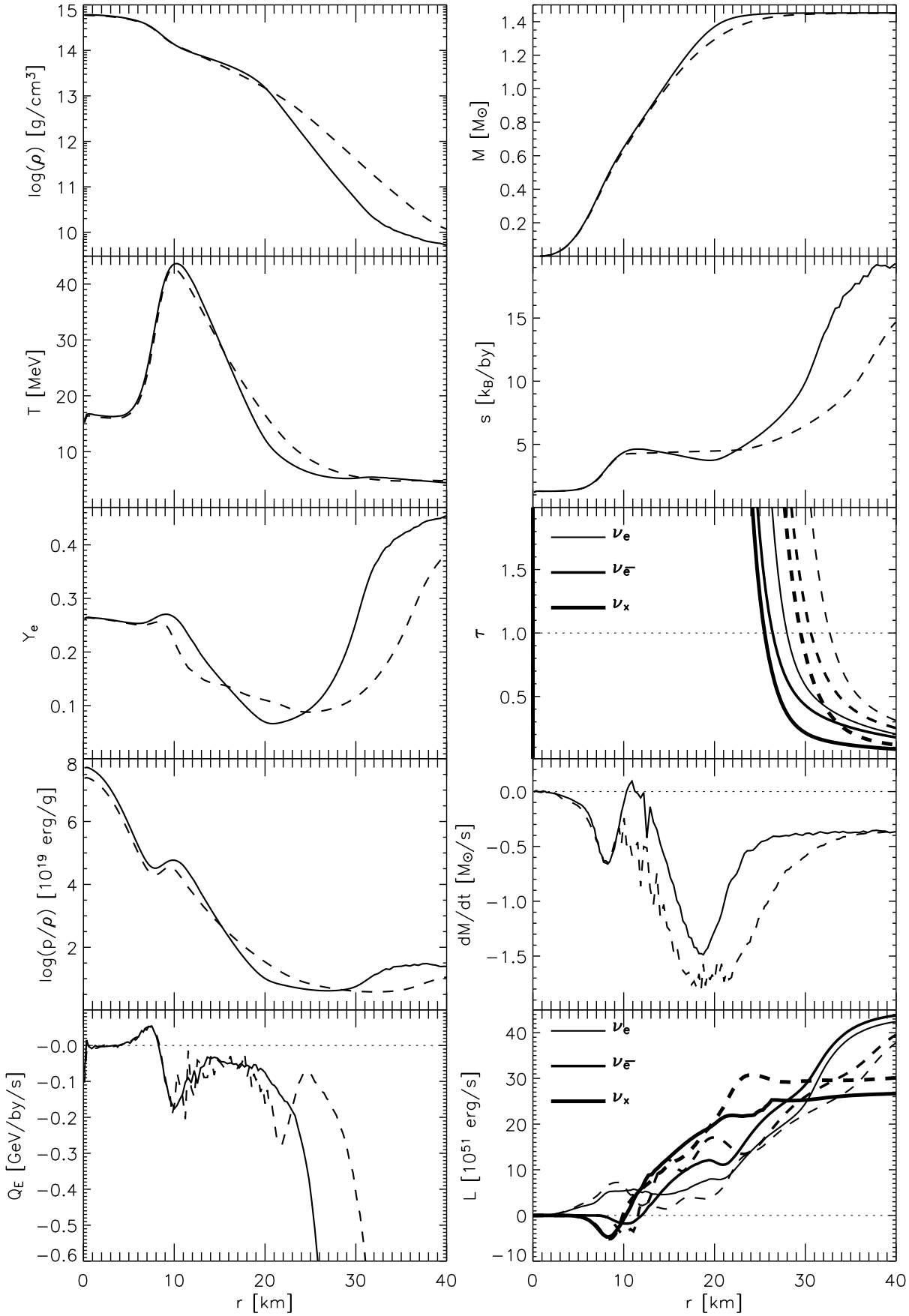

Figure 3.24: Comparison of the PNS of Models s15Gio_1d.b (solid) and s15Gio_32.b (dashed) at t = 243ms. For the 2D model we show 1D averaged values.

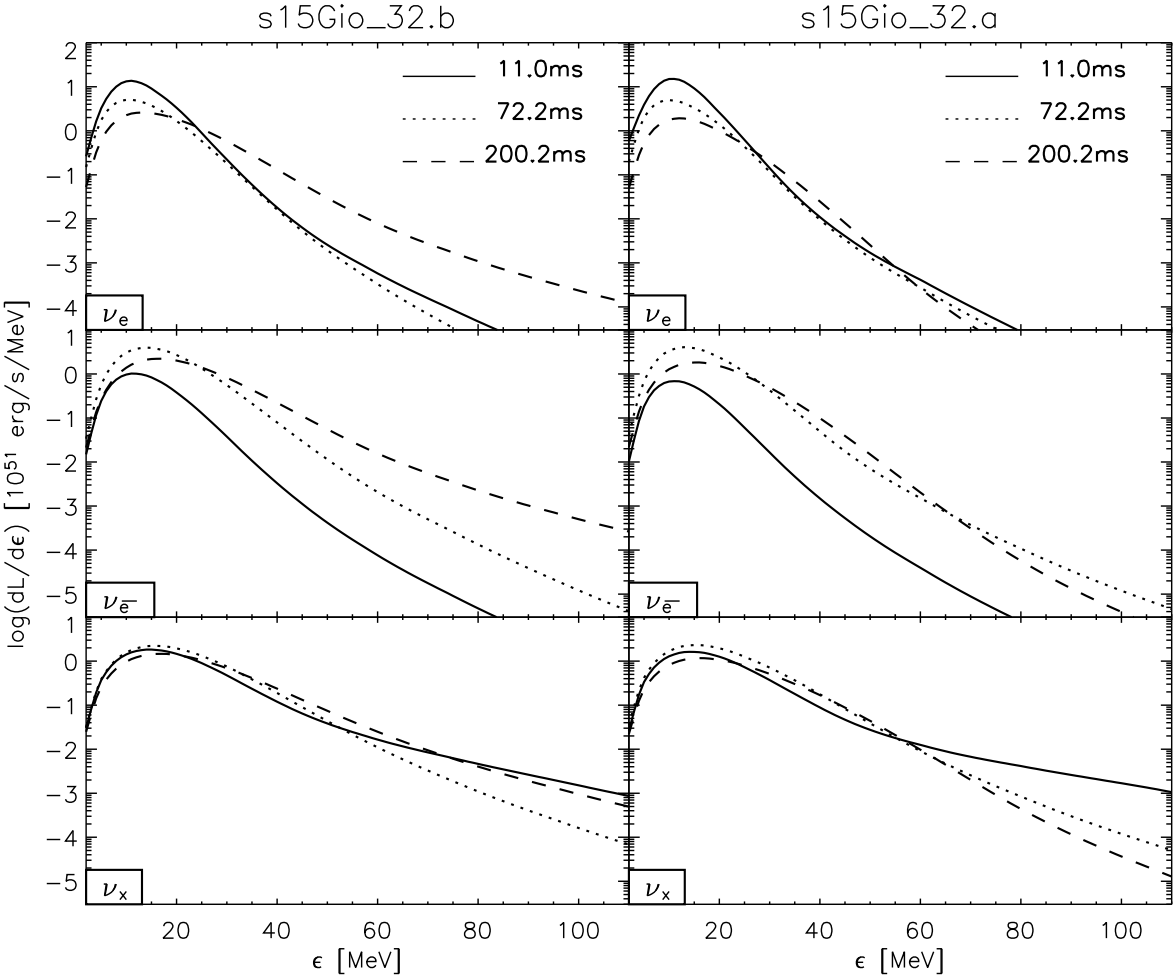

Figure 3.25: Spectra of the neutrino luminosities for the two Models s15Gio_32.a and s15Gio_32.b for a resting observer at ∞. The spectra are shown for an observer at rest (infinity) at three different times: during the ν_e burst at shock breakout, when the shock reaches its maximum for Model s15Gio_32.b and shortly after Model s15Gio_32.a has exploded. The lines depict the ν_e (solid), $\bar{\nu}_e$ (dotted) and ν_x (dashed) spectra.

3.2.2 A model with artificial explosion

We have produced one exploding model by omitting the velocity dependent terms (β-terms) in the radiation momentum equations (2.10,2.12). The model was actually simulated before we discovered the importance of the β-terms, however, its outcome is a unique opportunity to present results from an (almost) perfect exploding simulation.

As discussed in Sect. 3.1.3, the β-terms have the same effect as decreasing the opacity, so dropping them leads to an increase of opacity, especially in the gain layer. Note that we did not turn off the lateral velocity terms; however, what matters is the artificially increased opacity in **radial** direction.

Triggering the explosion was only possible by combining our state-of-the-art code, MuDBaTH, which features improved opacities, general relativity, and multi-dimensional convection, with an artificially increased heating by ignoring the velocity terms in the radiation momentum equations. From our other models, it can be seen that disregarding any of these improvements, or solving the full radiation momentum equations, would lead to a failure: the correct treatment of the radiation momentum equations in Model s15Gio_32.b stays far away from an explosion. The Model 2D s15Nso_20.a with standard opacities and newtonian gravity (see Janka et al. 2004) comes close to exploding but fails in the end. Only the 1D Model s15Gio_1d.a also succeeds to explode, but the result can not be taken serious, since the hot bubble convection predicted by the Ledoux criterion (see Fig. 3.30) is omitted.

Note that this model was calculated in spherical symmetry below a radius of 25km, thus inhibiting PNS convection. However, as can be seen from our state-of-the-art calculation (Sect. 3.2.1) where PNS convection occured we do not expect it to have a significant influence on the explosion mechanism; PNS convection becomes important on a much longer timescale of several 100ms.

To make it possible to calculate the late stages of the model in a finite time, we have mapped the 2D calculation to 1D at the time 468ms. At this time, the 2D effects no longer play a major role. The mapping made it necessary to set the lateral velocities to zero, the momentum and energy of this dimension were simply dropped. Along with this change we switched on the β-terms to obtain a more realistic evolution of the late proto neutron star, and switched to the more sophisticated treatment of nuclear recombination described in Sect. 2.4. Latter was necessary since the old description of NSE in the low density EoS (see Rampp & Janka (2002, App. B) for a detailed discussion) basically describes nuclear dissociation and recombination by first order phase transitions instead of correctly solving the Saha equations. This trifle caused numerical problems in the late phase of this model.

Note that the steepening of the PNS surface with time made it necessary to refine our eulerian grid in this region. Rezoning was done at 206ms, 468ms, and 759ms. We should also mention that the model did only run with Si burning, not yet with O, C, Mg, and Ne burning as described in Rampp & Janka (2002). A post-processing analysis however showed that oxygen burning would have contributed less than 0.011×10^{51}erg to the explosion energy, while the other burning processes would not have occurred, so we do not expect any dynamical changes.

Evolution The advantage of Model s15Gio_32.a is that strong convection can occur. Like in its brother s15Gio_32.b, convection in the gain layer starts developing around 60ms (see

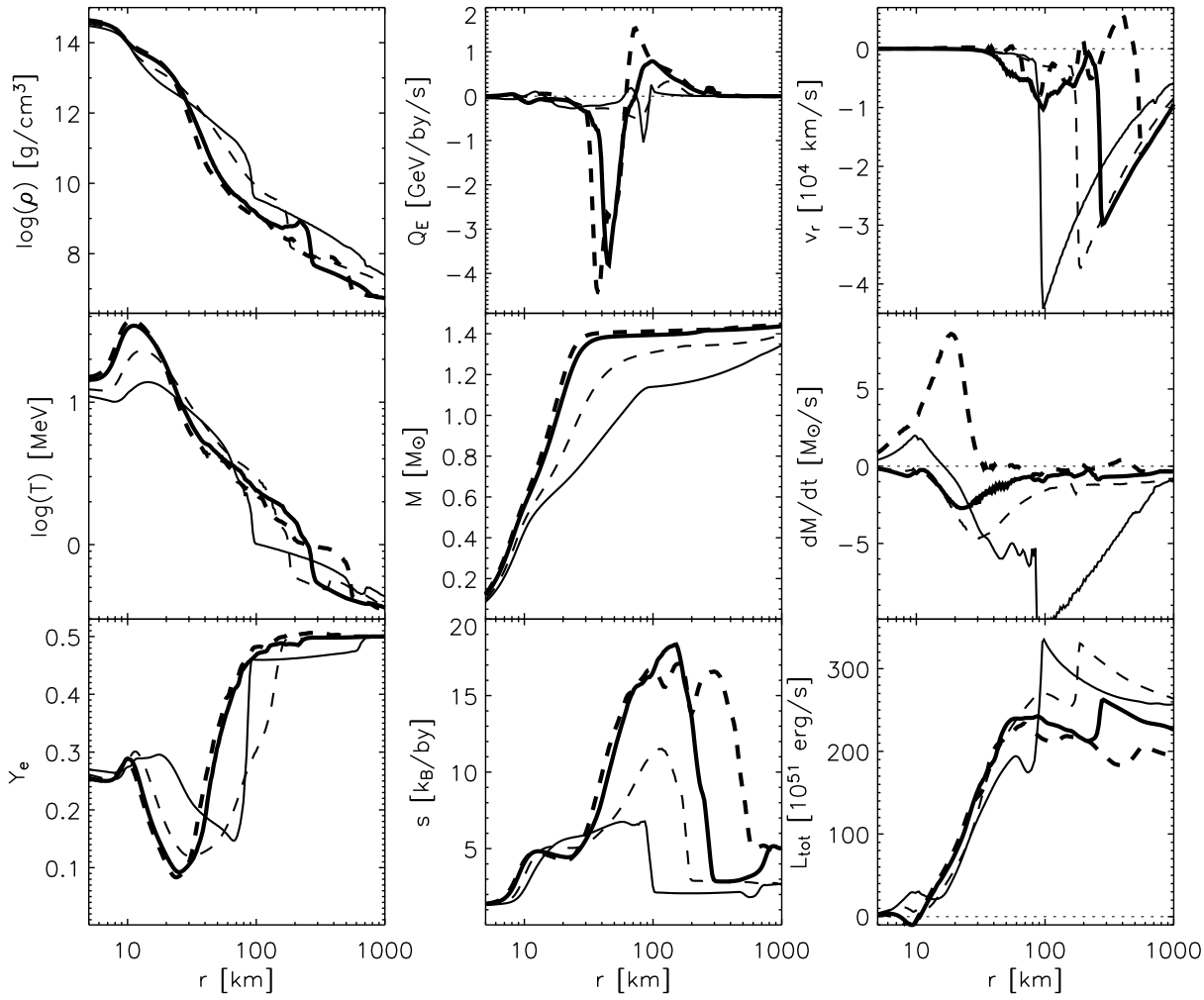

Figure 3.26: Various variables at the times 11.0ms (solid), 72.2ms (dashed), 150.1ms (thick), and 178.5ms (thick dashed) over radius for the exploding Model s15Gio_32.a.

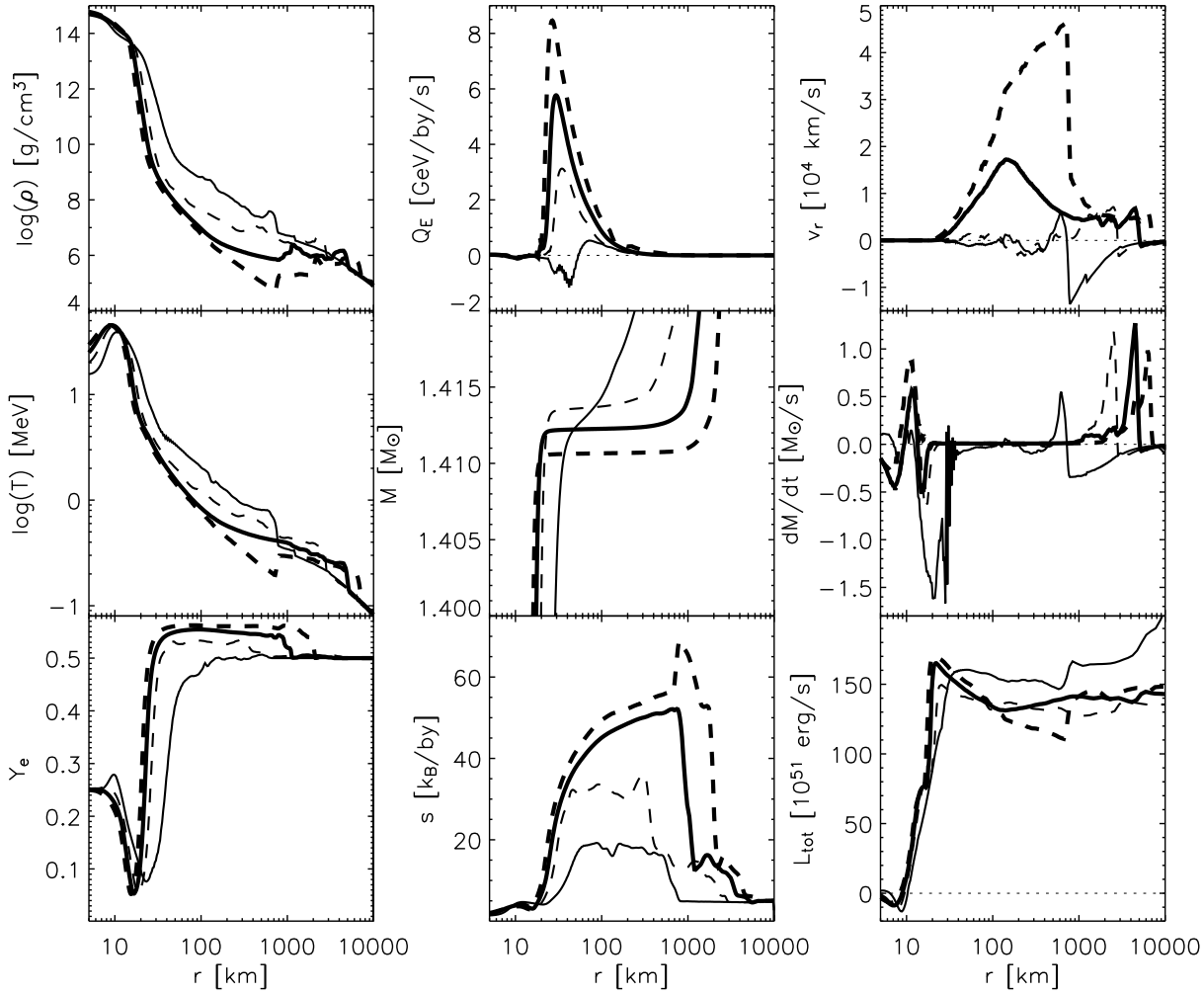

Figure 3.27: Various variables at the times 200.2ms (solid), 400.6ms (dashed), 600.5ms (thick), and 800.9ms (thick dashed) over radius for the exploding Model s15Gio_32.a. The thick lines in the lowest left panel indicate where $E^{\rm int}_{\rm bind}$ is negative, i.e. the material is unbound.

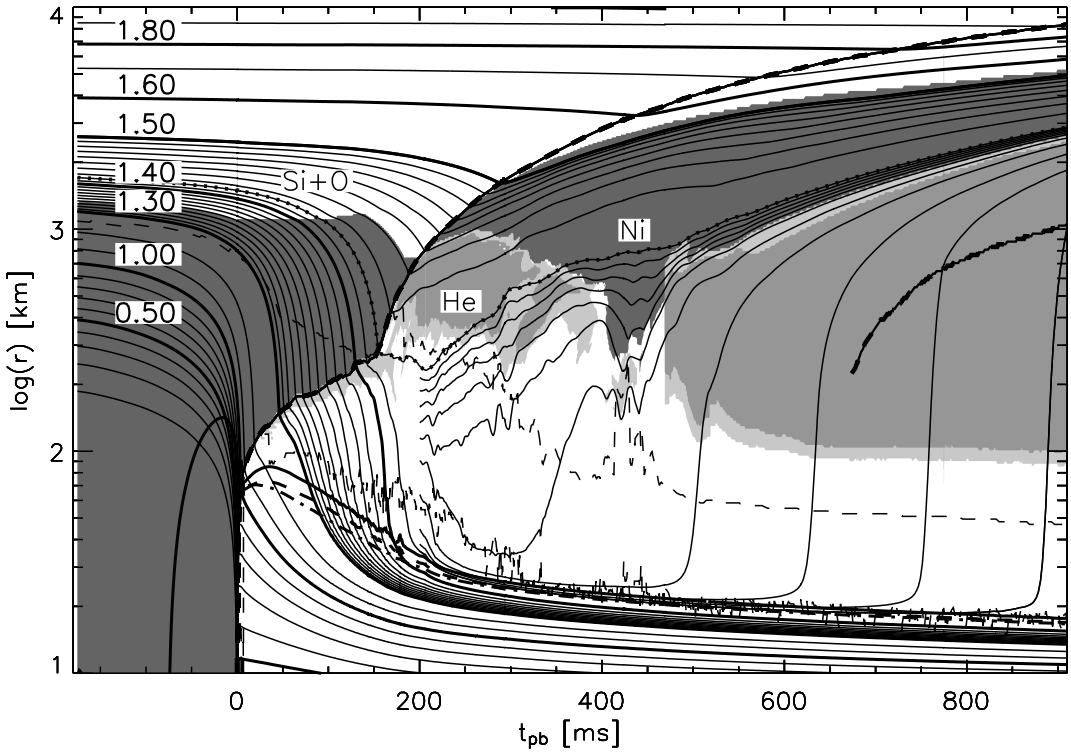

Figure 3.28: Angle-averaged mass shells for the exploding Model s15Gio_32.a. We have supplemented the plot with the transport neutrinospheres for ν_e (thick solid), $\bar{\nu}_e$ (thick dashed) and ν_x (thick dashed-dotted), the mass shell at which the silicon shell becomes oxygen-enriched (knotted solid line, at $1.42 M_\odot$), and the shock (thick solid line with dashes). Further we have marked the regions which consist to more than 60% of nickel-like elements (dark shaded) and ^{4}He (shaded). Latter is surrounded by the regions which consist of more than 30% of ^{4}He (light shaded). Finally the lower dashed line marks the gain radius, while the upper one marks where we have the interface between our two EoS (i.e. at $\rho = 6 \cdot 10^7 \mathrm{g/cm}^3$).

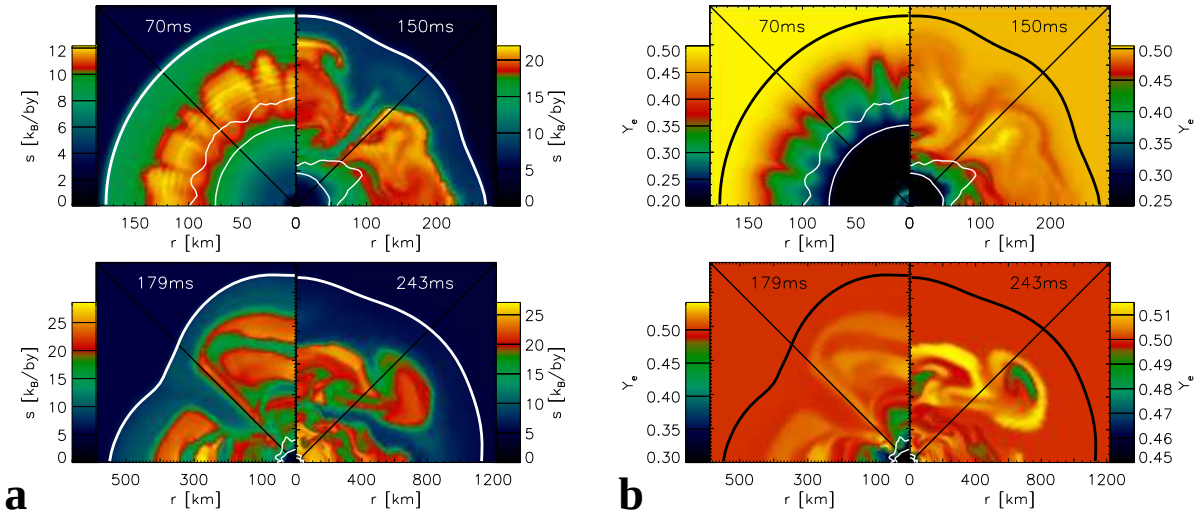

Figure 3.29: 2D snapshots of Model s15Gio_32.a for four different times. **a** shows the entropy s, **b** shows the electron fraction Y_e. The diagonal lines mark the equator, the horizontal border corresponds to $\cos(\vartheta) = -0.67$. The plots also contain the shock radius (thick line), and the gain radius and ν_e-sphere (thin lines).

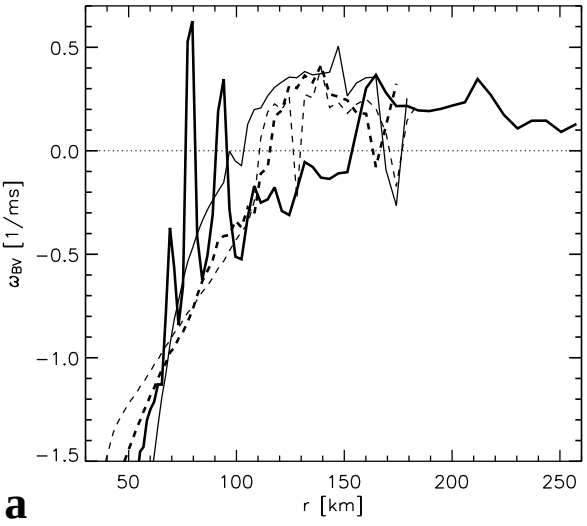

Figure 3.30: **a** Ledoux criterion for the times 72.2ms (dashed) and 150.1ms (solid) for the Models s15Gio_1d.a (thin) and s15Gio_32.a (thick). We only depict the lines below the shock. The missing data points in the thick solid line indicate that the angle-averaged variables are no longer consistent with the EoS and thus it is no longer possible to evaluate the Ledoux criterion.

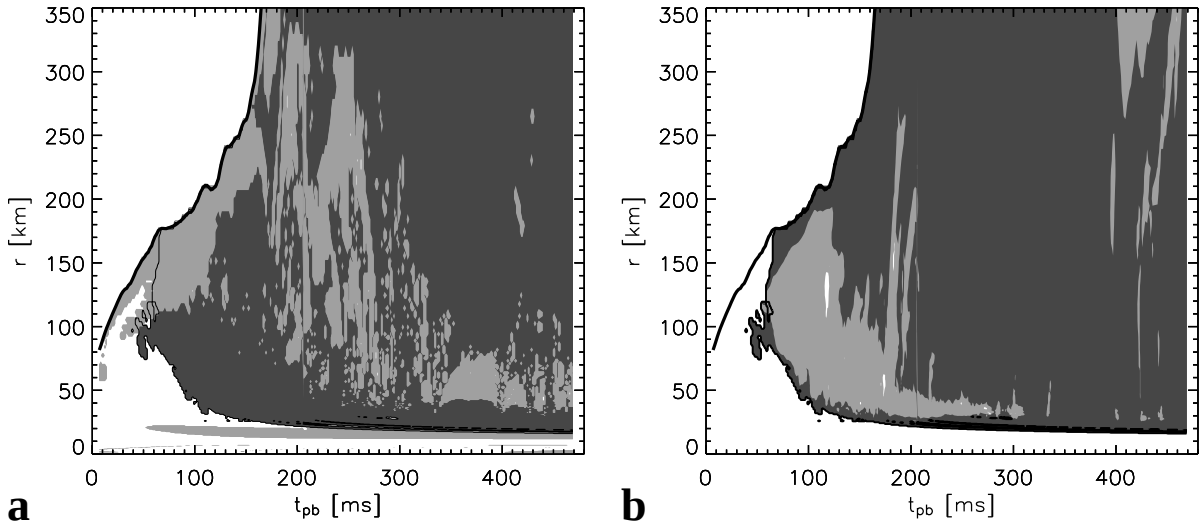

Figure 3.31: Same as Fig. 3.21, but for Model s15Gio_32.a.

Fig. 3.29). However, in this model the heating which is larger due to the omitted β-terms is strong enough to maintain a standing accretion shock at 70ms instead of a retreating one. As a consequence the convective region between gain radius and shock has the opportunity of developing large-scaled structures; these are favored by the convection. We end up in the largest possible scale of our calculation which with a grid covering the star in a wedge of $\pm 43.2^{\circ}$ around the equator roughly corresponds to an $l = 2$ mode (see Fig. 3.29). These huge structures (one bubble, one downflow) are also the most effective ones for efficient energy transport to the shock. This model develops these large structures around 100ms, the convection has now already become strong enough to push the shock further out; the gain layer, and thus the convective region, are slowly expanding outward (Fig. 3.2a).

The onstart of the explosion occurs when the oxygen-enriched silicon shell reaches down to the shock at 260km and 150ms. The interface between the pure Si-shell and the O-enriched one features an entropy step, the density drop is much steeper in the O-enriched layer. Consequently, this leads to a sudden decrease of the mass accretion rate, and thus of the ram pressure: the shock starts expanding. However, we might expect that Model s15Gio_32.a would also have experienced an explosion without the ram pressure drop since the shock was already in expanding motion, and the gain layer was gaining on mass and energy (see Figs. 3.28,3.32). Thus, in this model, the interface was probably not crucial for a successful explosion.

Explosion energy To calculate the explosion energy at a given time, we integrate the local specific binding (LSB) energy $\varepsilon_{\rm bind}^{\rm shell}$, defined in Eq. (3.2), over all zones between neutrinosphere and shock where the LSB energy and the radial velocity are positive:

$$E_{\rm expl} = \sum_{r,\vartheta,{\rm cond}} \varepsilon_{\rm bind}^{\rm shell}(r,\vartheta)\rho(r,\vartheta)\Delta V(r,\vartheta) \tag{3.6}$$

Note that the gravitational potential $\Phi_{\rm 1D}^{\rm Newt,\ enclosed}(r)$ used to calculate the LSB energy was calculated assuming a spherically symmetric mass distribution (2D effects play a minor role and were also ignored in the hydrodynamic simulation itself).

The change of explosion energy in time has several sources: first of all, the deposition of energy

by neutrinos is the main driving force in the initial stages of the explosion. Second, when the shock reaches around 400km, the post-shock matter has expanded sufficiently so that the neutrons and protons start recombining to ^{4}He, which releases 7.5MeV per baryon. Later on, the Helium further recombines to Iron-type elements, releasing another 1.3MeV per baryon. Third, when the shock reaches 800km (corresponding to a mass shell around 1.45–1.46$M_\odot$), the material hitting the shock is no longer dissociated, instead, the silicon is burned to ^{56}Ni, a process, however, which ends when the shock reaches 1700km (1.527$M_\odot$) and the shock does no longer heat the material for Si-burning. At late times, finally, the shock energy is only increased by the energy carried along with the neutrino-driven wind. The wind material initially also recombines, releasing nuclear binding energy, but later on the α particles become too sparse to recombine (α freeze-out).

On the other hand, the shock also looses energy by having to push outward the shocked material of the outer layers. Initially, before the shock reaches 800km, this material is even dissociated, but the energy lost hereby is regained when this material recombines. The time evolution of the composition is sketched by the shaded regions in Fig. 3.28.

The time evolution of the explosion energy can be seen in Fig. 3.32. Note that the explosion energy is already positive when the Si-O interface passes the shock at 150ms. We then recognize a steep increase after the onset of explosion powered by ν-heating, recombination and burning. At 300ms the burning ceases and the energy increase levels off somewhat. Finally, around 400ms, the ν-driven wind sets in, which only contributes little energy: the energy increases slowly. The transient jump in explosion energy at 468ms results in the mapping from 2D to 1D.

At the end of the calculation, the shock has reached the mass shell 1.9$M_\odot$, from Fig. 3.1 we can thus say that the shock will still loose 0.16FOE (FOE = ten to the fifty-one erg) energy by sweeping up the outer layers of the star. The end value of the explosion energy will also be altered by further input from the ν-driven wind, and fall-back of material onto the PNS. Anyway, the value 0.5–0.6FOE is a good estimate. Thus, our model creates an explosion which has an energy comparable to, e.g., SN1999br (see Hamuy 2003). Still, the explosion energy of our model should be called “weak”.

Mass and composition of ejecta Although a successful supernova simulation with a correct treatment of the β-terms and thus different heating rates might yield different results concerning the lepton number of the ejecta, it does no harm making an analysis here. The current model is especially interesting, since it is the first simulation including weak-magnetism and recoil effects of the neutrino interactions. They have the tendency of increasing Y_e in the neutrino-heated matter (see App. A.3).

Since our code unfortunately does not yet support marker particles, we had to calculate the Y_e distribution of the ejecta in a post-processing analysis: we integrate the outward advection of mass with given Y_e through a surface at a fixed radius r_0 over time, resulting in the function

$$M(Y_i < Y_\mathrm{e} < Y_{i+1}) = \frac{2}{\cos(\vartheta_\mathrm{min}) - \cos(\vartheta_\mathrm{max})} \sum_n \sum_{\vartheta,\mathrm{cond}} \Delta A(r_0,\vartheta)\cdot v_r(r_0,\vartheta,t_n)\cdot\rho(r_0,\vartheta,t_n)\cdot(t_{n+1}-t_n). \tag{3.7}$$

Here, the factor in front of the sum normalizes the result for wedges to the whole star and ΔA is the area through which the matter flows. The first sum accomplishes for the integration

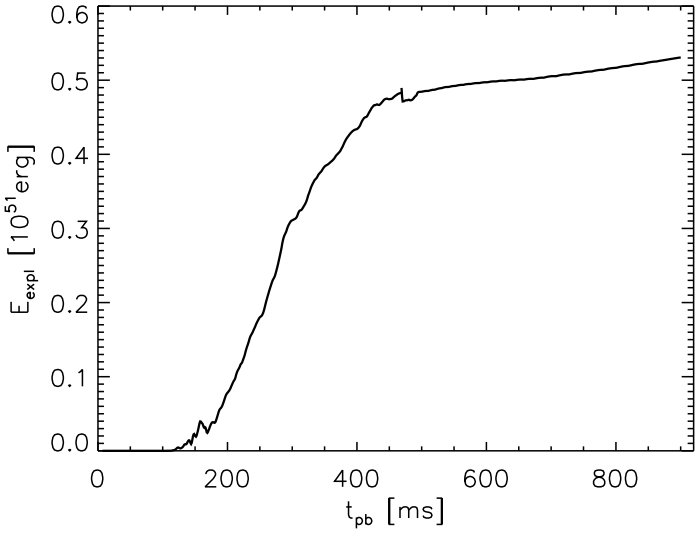

Figure 3.32: Explosion energy for Model s15Gio_32.a as defined in Eq. (3.6). The jump at $t_{pb} = 468$ms stems from the mapping of the model to one dimension.

over time, while the second sum means that only the angular bins are taken into account where following condition is fulfilled: $v_r(r_0, \vartheta, t_n) > 0 \ \wedge \ Y_i < Y_e(r_0, \vartheta, t_n) < Y_{i+1}$.

Choosing r_0 is not trivial: on the one hand, it should be as large as possible, so that the advected matter through the surface at r_0 is no longer influenced significantly by neutrino processes. On the other hand, the advection of material over our Eulerian grid washes out small patches with extreme values of Y_e, so we would like to choose r_0 as small as possible. The time resolution of the processed data lies between one and two ms, the processing ends at $t_{pb} = 468$ms.

The results are shown in Fig. 3.33, where we have used $r_0 = 350$km. To estimate the sensitivity of our processing, we show the difference when moving to $r_0 = 300$km (dark shaded) or $r_0 = 400$km (light shaded). In latter, the advection over zones has partly destroyed small patches of low Y_e, while in the first case we miss neutrino processing on the matter at larger radii, which would have the tendency of increasing Y_e. For information, the integrated mass of the three analyses with $r_0 = 350$, 300, and 400km are $M_{tot} = 0.0267$, 0.0273, and $0.0274 M_\odot$, respectively. The variation between the three r_0 can be interpreted as error bars.

Another problem is given by material falling back through the surface at r_0, and then re-emerging with different Y_e; this material is counted double in our analysis. As an example, in Fig. 3.28 we can see that between 400ms and 425ms, around $10^{-3} M_\odot$ of the material temporarily falls back below the radius 350km. Also, we do not know whether part of the material in the downflows was already processed by our analysis earlier. However, we do not expect the amount of double processed material to be large. Also note that the results are not final, since we only analyzed the explosion up to 468ms. In any case, the magnitudes of the results can be seen as good guess values, and for $Y_e < 0.5$ even as upper bounds at early times, since the subsequent ejecta have $Y_e > 0.5$ (although very late ejecta will have $Y_e < 0.5$ again).

A thorough analysis of the produced nuclei in neutrino-driven winds by Hoffman et al. (1996) demands that the ejected mass having $Y_e \lesssim 0.47$ must be at most $10^{-4} M_\odot$. A larger mass would lead to a rampant overproduction of closed neutron shell isotopes with $N = 50$, i.e. ^{88}Sr, ^{89}Y, and

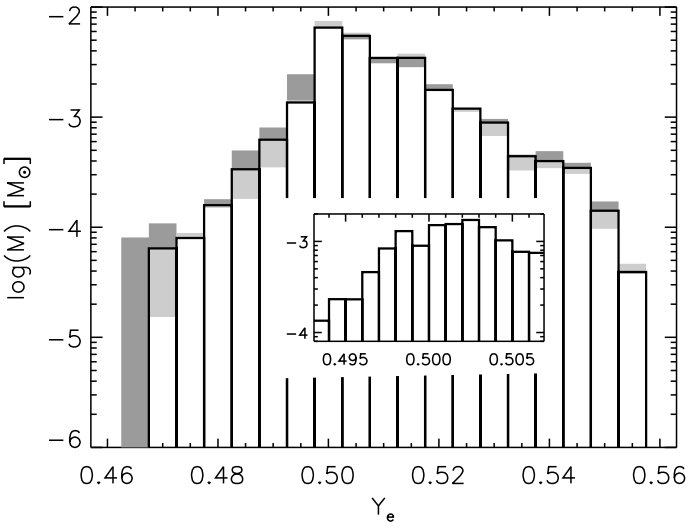

Figure 3.33: Mass of the neutrino-processed ejecta for Model s15Gio_32.a as a function of the local electron fraction Y_e. The function was calculated as defined by Eq. (3.7). The solid bars correspond to $r_0 = 350$km, while the dark and light shaded bars yield $r_0 = 300$km and $r_0 = 400$km, respectively. The central plot shows the masses for values of Y_e around 0.5 with improved resolution.

^{90}Zr. As can be seen from Fig. 3.33, our simulation really fulfills this constraint. At the time we stopped the calculation, the wind driven by the neutrinos contains material with $Y_e > 0.5$, so the constraint will not be violated at later times. This wonderful result can mainly be accounted for by the improved neutrino opacities. Although we do not have an exploding model with standard opacities, a comparison of the failing models yields that the improved opacities tend to increase Y_e (see Sect. 3.1.2). Therefore, the absence of weak magnetism and recoil effects in exploding models of other groups is probably the reason why they do not comply with the constraint by Hoffman et al. (1996).

Another interesting number is the amount of ^{56}Ni produced by the explosion. Since the simulation was run with strongly simplified pseudo-NSE and burning, and not with a consistent network, we can only make an estimate on the magnitude. Integrating the mass of all iron-like nuclei at the end of the simulation yield $M_{\rm heavy} = 0.12 M_\odot$. This value contains the ^{56}Ni produced by ^{28}Si burning, as well as the material ejected from the neutrino-processed region and recombined to iron-like nuclei. Adding the $0.009 M_\odot$ of ^{56}Ni that would have been produced additionally if we had turned on oxygen burning (derived from a post-processing analysis), we conclude that the amount of ^{56}Ni ejected in this simulation is lower than $0.13 M_\odot$.

Neutrino emission This model is unique, being the hitherto only fully self-consistent simulation which gives a neutrino signal for a successful explosion with a reasonable treatment of neutrino transport and interactions (with a small exception). The long-time evolution of the neutrino luminosities and mean energies is plotted in Fig. 3.34. We can distinguish four phases: the collapse phase, the neutrino burst, and the accretion phase are all known from the failing models, however, after the onset of the explosion we encounter a sudden drop of the luminosities. Here, the accretion of matter onto the PNS has ceased, so that the luminosity merely is powered

by cooling of the PNS. However, it would be wrong to already talk about Kevin-Helmholtz cooling, since the neutrino energies are still increasing; obviously, the PNS surface is still in a phase of relatively strong contraction. At later times, we expect this tendency to invert, our model is still on the calculator.

The lively hot bubble convection below the shock also affects the neutrino luminosities. When strong downflows hit the cooling region, the luminosities of the electron type neutrinos increase by up to 20%. Due to the locality of the downflows, these fluctuations also show up in lateral direction, see Fig. 3.35. Note that a fully implemented 2D transport would slightly wash out these deviations in lateral direction. Interestingly, large fluctuations even show up long after the onset of the explosion, e.g. at 307ms, triggered by some downflows which still manage to break through the shock.

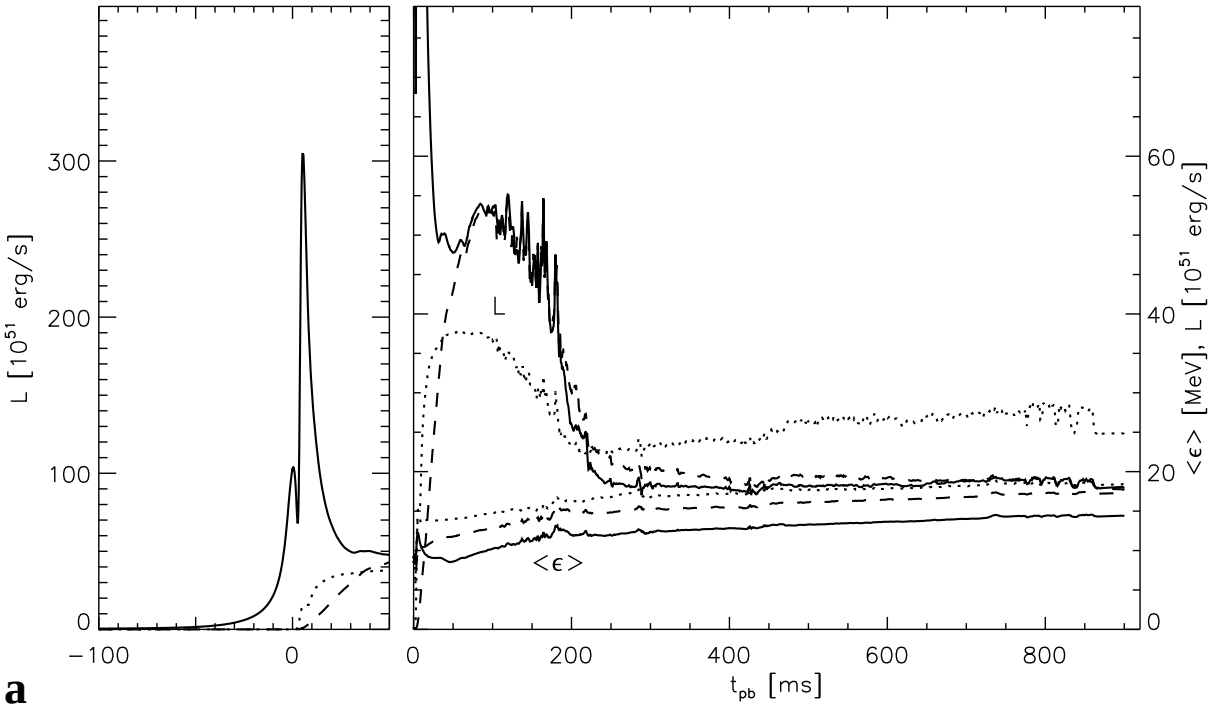

Figure 3.34: Evolution of the luminosities of Model s15Gio_32.a for ν_e (solid), $\bar{\nu}_e$ (dashed), and ν_x (dotted) around the bounce (left) and post-bounce (right) evaluated at radius 400km for an observer at rest. For the post-bounce phase, we also plot the average neutrino energies.

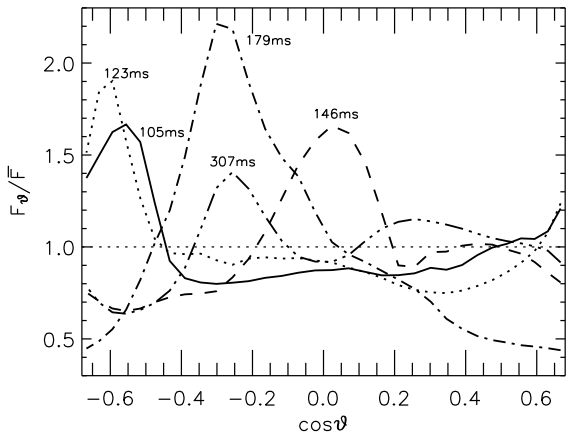

Figure 3.35: Snapshots of the normalized ν_e flux of Model s15Gio_32.a at radius 400km as a function of lateral angle for different post-bounce times. The times were chosen to show as large deviations as possible.

4 Progenitor variations

To evaluate the sensitivity of the structure of progenitor models on the evolution of core collapse supernovae we have chosen nine progenitors, presented in Section 4.1, for which we have simulated core collapse and the first 250ms after bounce in spherical symmetry, Section 4.2. In Section 4.3 we extend the variation of progenitors to two-dimensional simulations for three chosen progenitor models. We also perform test concerning the numerical resolution and the initialization of seed perturbations. In Section 4.3.3 we present a model where the chosen geometry allows for a special type of large scale mode instability which triggers an explosion. We discuss the validity of the model.

4.1 The progenitors

We have chosen a total of nine progenitors from different groups, listed in Table 4.1. These models cover a main sequence mass (MSM) range from 11 to 25 $M_\odot$ and represent various types of pre-collapse stellar structures. In Figs. 4.1 and 4.2 we compare the models at a core density of $\rho^c = 10^{11}\mathrm{g/cm}^3$, which was reached by evolving the models with our 1D Boltzmann transport code VERTEX. At this early stage of the collapse phase none of the models have changed significantly in structure or composition, the infall velocities are still sub-sonic, and the neutrinos are still streaming off almost unhindered. The original progenitor model data is shown in D.

Looking at Fig. 4.1, we see that the density structure of the inner $1.0M_\odot$ of the iron core is extremely similar in all progenitors. However, the electron fraction Y_e, entropy per baryon s, and velocity v show moderate differences: while Y_e varies only 5% between the progenitors, $|v|$ and s show differences of up to 40%. There is a general trend that $|v|$ and s increase with the MSM while Y_e decreases.

Above the core, we find larger differences in the progenitors, which are dictated by the composition interfaces. In particular, the Fe–Si and the Si–O interfaces are of interest for the early post-bounce evolution of the supernova shock. The enclosed mass shells at which the interfaces are situated vary strongly between the progenitors. Generally, the enclosed mass of an interface increases with MSM, see Table 4.1. Most interfaces are of discrete type, i.e. the composition changes discontinuously from the heavy to the lighter nucleus. However, some interfaces are merely positions above which e.g. the Fe shell becomes more and more enriched with Si. Both types of interfaces mark more or less strong entropy jumps in the progenitors. The stronger ones, which are underlined in Table 4.1, also show a strong jump in the density profile.

4.2 One-dimensional models

The one-dimensional simulations were performed with our 1D neutrino Boltzmann transport code VERTEX, using the physics described in Chapter 2. This includes state-of-the-art neutrino interactions and an approximative general relativistic treatment.

None of the simulations yield explosions. Thus, the evolution can be splitted into collapse, bounce, prompt shock, neutrino burst, accretion shock, and a possible transient shock expansion followed by a second accretion shock phase.

Table 4.1: List of progenitors used in the simulations. The notation (e) indicates that the particular interface merely means an enrichment of the lighter nucleus above this mass, while the heavier nucleus carries on to dominate the composition, e.g. these are actually Fe–FeSi and Si–SiO interfaces. Although several models feature both an enrichment interface as well as a composition jump, we only list the interfaces which feature entropy jumps. The underlined Fe–Si interfaces feature an entropy increase of more than $1k_B$ per baryon, the underlined Si–O interfaces an entropy increase of more than $2k_B$ per baryon.

Model	*MSM* [$M_\odot$]	*Reference*	$M_{\mathrm{Fe-Si}}$	$M_{\mathrm{Si-SiO}}$	*Notes*
s1b	>2.26	Woosley, personal comm.	1.34	1.38	Type Ib
s11.2	11.2	Woosley et al. (2002)	1.24	1.30(e)	from homepage
n13	13	Nomoto & Hashimoto (1988)	1.18?	1.50	
s15s7b2	15	Woosley & Weaver (1995)	1.28(e)	1.43(e)	
l15	15	Limongi et al. (2000)	1.16(e)	1.60	
s15a28	15	Heger et al. (2001)	1.42(e)	1.81	
s20.0	20.0	Woosley et al. (2002)	1.46	1.82	from homepage
l25	25	Limongi et al. (2000)	1.58	1.84(e)	
s25a28	25	Heger et al. (2001)	1.62	1.98(e)	

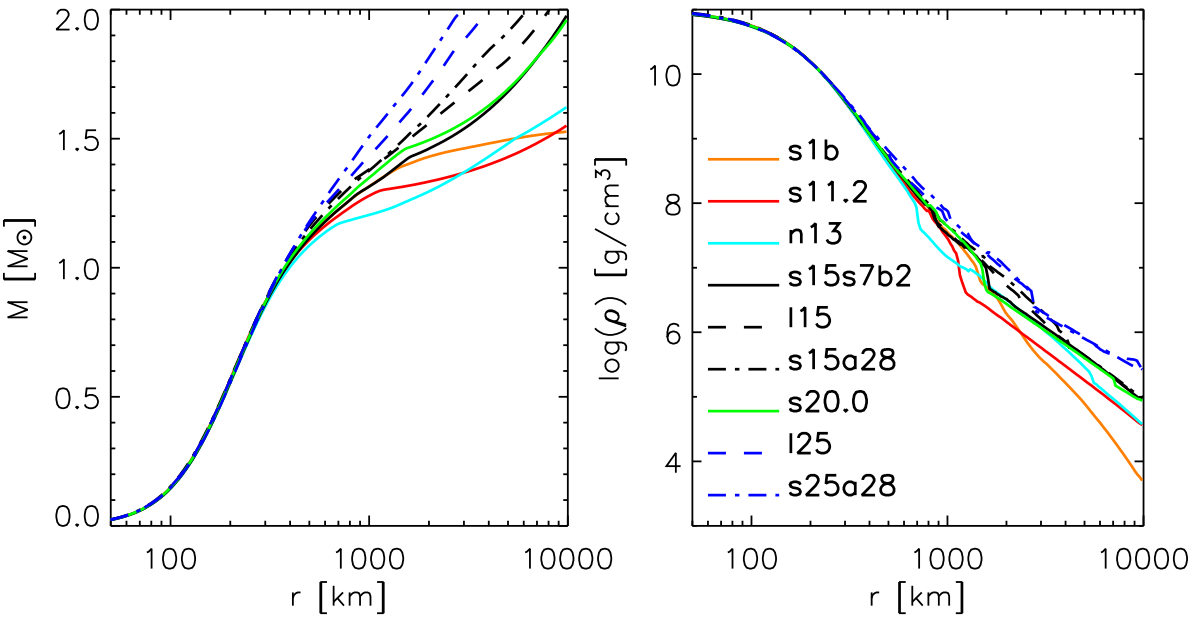

Figure 4.1: Snapshot of the collapse models at a central density $\rho^c = 10^{11}\mathrm{g/cm}^3$.

The collapse times, from a core density of $\rho^c = 10^{11}\mathrm{g/cm}^3$ till bounce, see Table 4.2, differ somewhat between the models, lying between 20 and 30ms (see Fig. 4.5 and Table 4.2). Initially, the models are differently strong deleptonized (Figs. 4.2, 4.3); thus the electron pressure

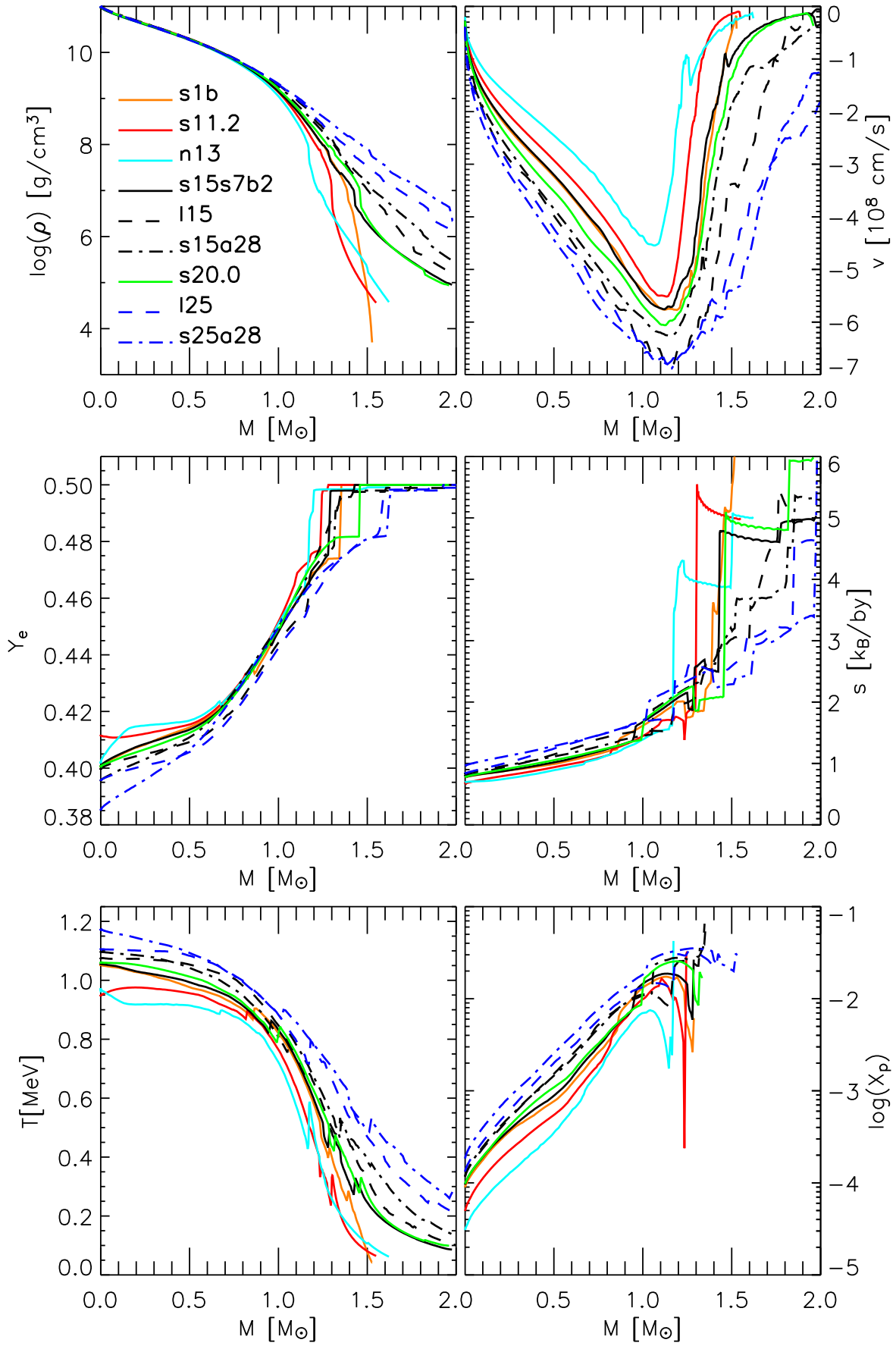

Figure 4.2: Snapshot of the collapse models at a central density $\rho^c = 10^{11}$g/cm^3. The data is only shown within the range of the simulations, i.e. for $r \leq 10000$km.

Table 4.2: Observables of the 1D models from the collapse, prompt shock, and neutrino burst phases. $t_{\rm coll}$ is the time passing from when the collapsing core reaches a density of 10^{11}g/cm^3 till shock creation, i.e. when the entropy in the core first reaches $3k_{\rm B}$/by. The shock creation radius $r_{\rm sc}$ and enclosed mass $M_{\rm sc}$ are defined at the same point. The energy loss via neutrinos during collapse $E^{\nu,\rm loss}_{\rm coll}$ is evaluated by integrating the neutrino luminosity (for an observer at rest at $r = 400$km) over the time from when the core reaches $\rho^{\rm c} = 10^{11}$g/cm^3 till the dip in the luminosity around 2.5ms after shock creation. We call the time when the velocities behind the shock drop below 10^7cm/s the end of the prompt shock, the time of it, $t_{\rm pse}$, is given relative to the time of shock creation. At the end of the prompt shock, the shock is at radius $r_{\rm pse}$ and enclosed mass $M_{\rm pse}$. Finally, the energy emission during the burst is defined as the time-integrated $\nu_{\rm e}$ luminosity of the FWHM of the burst, $E^{\nu}_{\rm burst}$. The energies are given in units of ten to the fifty-one erg (FOE).

Model	$t_{\rm coll}$ [ms]	$r_{\rm sc}$ [km]	$M_{\rm sc}$ [$M_\odot$]	$E^{\nu,\rm loss}_{\rm coll}$ [FOE]	$t_{\rm pse}$ [ms]	$r_{\rm pse}$ [km]	$M_{\rm pse}$ [$M_\odot$]	$E^{\nu}_{\rm burst}$ [FOE]
s1b	23.9	10.7	0.49	1.00	0.87	32	0.78	1.48
s11.2	25.2	10.7	0.50	1.00	0.87	32	0.78	1.38
n13	28.9	10.7	0.50	0.96	0.88	32	0.78	1.29
s15s7b2 †	23.9	10.7	0.49	1.01	0.91	32	0.78	1.47
l15	20.9	10.6	0.50	1.04	1.03	35	0.82	1.74
s15a28	21.6	10.7	0.49	1.03	0.95	33	0.79	1.60
s20.0	22.7	10.6	0.49	1.03	0.91	32	0.79	1.50
l25	20.0	10.7	0.49	1.06	1.15	37	0.83	1.82
s25a28	19.8	10.6	0.48	1.06	1.00	34	0.79	1.93

† This is the Model s15Gio_1d.b from Sect. 3.1.1.

is differently high. Models with large (small) electron fraction and pressure collapse slower (faster). As a consequence, they have more (less) time to deleptonize. So all in all, the electron fraction of the models converges during collapse (Fig. 4.4). Also, the central entropy converges in all models (Fig. 4.3) indicating that the hydrodynamics coupled with the neutrino interactions have a self-regulating character so that the entropy in the homologous core at bounce is almost independent of its original value. Merely the Model s25a28 initially has such high values for the entropy and low values for the electron fraction that it cannot converge with the other models. In this model the EoS yields much higher proton abundances which lead to a stronger deleptonization. Consistently with the similar collapse phase, all models lose approximately 1FOE of energy via neutrino emission during collapse.

As a consequence of the similar core structure and collapse history, all the shocks are created at mass $M_{\rm sc} \simeq 0.49 \pm 0.01 M_\odot$ and radius $r_{\rm sc} \simeq 10.7 \pm 0.1$km, where we define the shock creation (sc) time and space as the point where the entropy first reaches $3k_{\rm B}$ per baryon (Bruenn & Mezzacappa 1997). From now on all times are given with respect to the time of bounce, $t_{\rm cb}$.

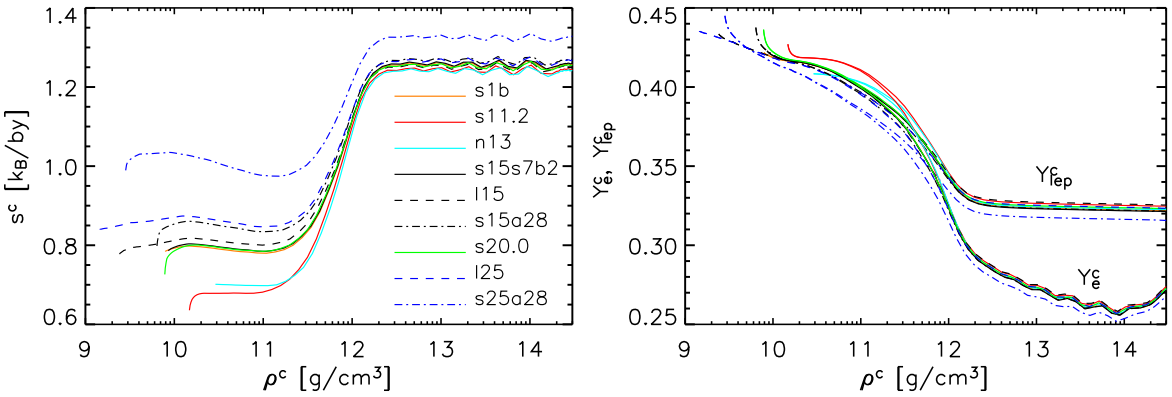

Figure 4.3: Left panel: Central entropy over central density during collapse. Right panel: Central electron and lepton fraction over central density during collapse.

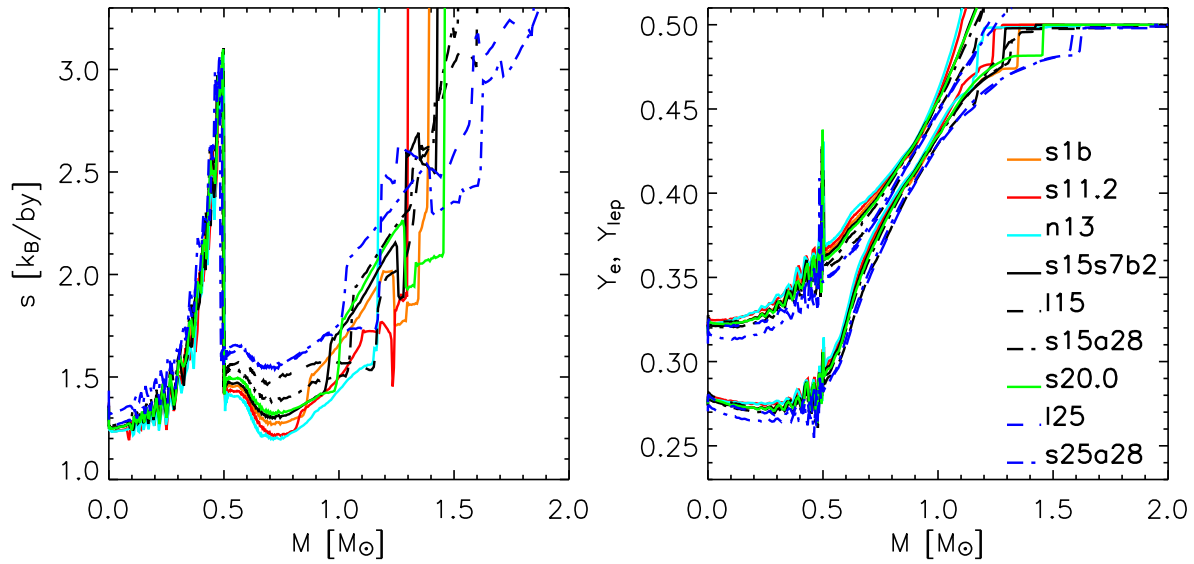

Figure 4.4: Left panel: Entropy over enclosed mass at bounce time. Right panel: Electron fraction over enclosed mass at bounce time.

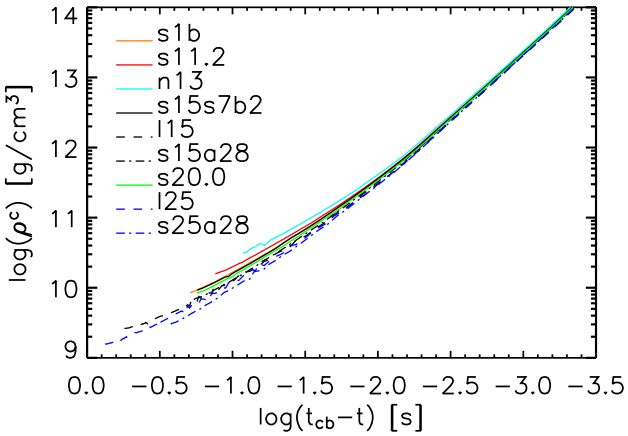

Figure 4.5: Central density over remaining time till bounce.

Also the prompt shock phases are quite similar. In most models, the velocities behind the shock become negative after 0.9ms at $M_{\rm pse} = 0.78 \pm 0.01 M_\odot$ and $r_{\rm pse} = 32 \pm 1$km (pse stands for "prompt shock ends"). Merely the progenitors from Limongi et al. (2000) manage to push their prompt shocks a bit further.

Although the prompt shock clearly fails, the radial expansion velocity of the shock remains large, see Fig. 4.6, upper left panel. When the shock reaches the neutrino sphere after 4ms at a radius of 70–80km, the strong energy and lepton number drain via neutrino emission releases some of the thermal and degenerate electron pressure of the accreting material, so that the shock expands more slowly. The strength of this neutrino burst is quite similar for all models, see Fig. 4.6, lower left panel.

Up to now we have seen little differences since the core structure is similar. At burst the shock has reached $\sim 1.0 M_\odot$ above which differences in the progenitor structure become important. Thus the mass infall rate through the shock differs between the models. Simultaneously, due to energy loss at the burst the shock becomes slow and the simulation enters the accreting shock phase. In this phase the shock evolution is governed by a complex system of coupled variables.

Recent analytic studies (Janka 2001; Arcones Segovia 2003) are able to find stationary solutions which represent standing accretion shocks. According to these studies, these solutions depend on a small set of independent variables only, e.g. the mass accretion rate through the shock, $\partial_t M_{\rm sh}$, the mass $M_{\rm PNS}$ and radius $r_{\rm PNS}$ of the proto neutron star (for simplicity, we set these equal to the enclosed mass and radius of the electron neutrino-sphere, $r_{\nu_{\rm e}}$) and the neutrino luminosity L_ν. These stationary solutions describe the numerical results fairly well provided that the model does not encounter sudden transients (e.g. sudden drops of $\partial_t M_{\rm sh}$) and as long as the model stays far from explosion (being a transient in itself).

Our models show that for such quasi-stationary phases even these four variables are coupled. The most important variable is the time dependent mass accretion rate through the shock, which is determined by the progenitor structure. Since this mass accretes further onto the PNS with a small time delay, the mass of the PNS is essentially the time integral of $\partial_t M_{\rm sh}$ plus an initial value. Starting at $t_{\rm pb} = 4$ms, this initial PNS mass is approximately $1.0 M_\odot$ for all models due to the similar core structure. Also the neutrino luminosity is closely related to $\partial_t M_{\rm sh}$: the accreted energy needs to be emitted if the shock is not to expand. Thus the total luminosity can be said to consist of a term proportional to $\partial_t M_{\rm sh}$ (again with a time delay since the material has to accrete from the shock to the cooling layer) plus a term from cooling of the settled core of the PNS (which cools on a timescale of 10s). Interestingly, also the neutrino sphere radii depend directly on $\partial_t M_{\rm sh}$. A larger accretion rate will lead to a stationary solution where more matter piles up before it can emit its energy in form of neutrinos. Thus, the cooling layer is more extended in radius, tendentially at higher optical depth, the matter emits its energy on a longer time scale and has higher densities due to the higher pressure induced by infalling material. This means a higher r_ν.

In summary, all these variables depend on the time evolution of $\partial_t M_{\rm sh}$: a higher $\partial_t M_{\rm sh}$ means, with a time delay of few tens of ms, larger r_ν and L_ν, and a faster increase of $M_{\rm PNS}$. Our simulations nicely confirm these rules. Looking e.g. at $t_{\rm pb} = 80$ms in Fig. 4.6 we see that $\partial_t M_{\rm sh}$ varies by a factor of five between the models, with n13 and s11.2 with 0.8 and $1.3 M_\odot$/s, respectively, at the low end, and l25 and s25a28 with 3–$4 M_\odot$/s at the high end of the spectrum. Consistently, the r_ν are only 60km for the light progenitors and 25% higher, i.e. ≈ 80km, for the heavy models. Also the luminosities differ by a factor of two, and PNS masses show 25%

differences.

Astonishingly, the effect on the shock radius seems to be negligible, at $t_{\rm pb} = 80$ms the shock radii of most models lie within a 5% margin (s20.0 within 10%, the exception of n13 will be discussed later). The above mentioned much larger differences of $\partial_t M_{\rm sh}$, $M_{\rm PNS}$, r_ν, and L_ν seem to cancel each other nicely in the determination of the shock radius. Higher $\partial_t M_{\rm sh}$ decreases $r_{\rm sh}$ due to the higher ram pressure, larger $M_{\rm PNS}$ increases the gravitational pull and thus also lowers $r_{\rm sh}$. But larger L_ν increases the heating and thus expands the heating region, which is supported by a large PNS if r_ν is larger.

Of course, the cancellation is not perfect, and as can be seen at later times, the shock radii can differ more strongly especially if $\partial_t M_{\rm sh}$ suffers a transient in between. However, the relatively weak depencence of $r_{\rm sh}$ on otherwise large differences between the models make its predictability rather safe in one-dimensional models.

Up to now we have ignored the aspect of neutrino heating. To discuss this topic we first define two timescales: the advection timescale

$$\tau_{\rm adv} = \int_{r_{\rm gain}(t)}^{r_{\rm sh}(t)} \frac{1}{v(r,t)} dr \tag{4.1}$$

where the gain radius $r_{\rm gain}$ is defined as the innermost point above which neutrino heating surpasses neutrino cooling, and $v(r,t)$ is the radial velocity, and the heating timescale

$$\tau_{\rm heat} = \frac{4\pi \int_{r_{\rm gain}(t)}^{r_{\rm sh}(t)} \varepsilon_{\rm bind}^{\rm shell}(r,t)\rho(r,t)r^2 dr}{N 4\pi \int_{r_{\rm gain}(t)}^{r_{\rm sh}(t)} Q(r,t)\rho(r,t)r^2 dr} \tag{4.2}$$

where Q is the local net heating rate in MeV/s, $N = 1\frac{\rm erg}{\rm MeV}\frac{1}{m_{\rm u}}$, and

$$\varepsilon_{\rm bind}^{\rm shell}(r) \equiv \varepsilon(r) + \Phi_{\rm 1D}^{\rm enclosed}(r), \tag{4.3}$$

is our so-called local specific binding energy already introduced in Sect. 3.2.2. Here, $\varepsilon = e + \frac{1}{2}v^2$ is the specific energy density, and e is the internal energy density. The gravitational potential $\Phi_{\rm 1D}^{\rm enclosed}(r)$ is calculated only taking into account the mass inside the radius r. Note that for two-dimensional models, this definition of the timescale is not applyable. Thus we there use following definition:

$$\begin{aligned} \tau_{\rm adv}^*(M_i) \equiv \tau_{\rm adv}^*(t_1) = t_2(M_i) - t_1(M_i)\,, \qquad & \text{where } M(r = r_{\rm gain}, t = t_2) = M_i \\ & \text{and } M(r = r_{\rm shock}, t = t_1) = M_i\,. \end{aligned} \tag{4.4}$$

This method is applied for a number of masses M_i. In case this definition of the advection timescale is used, we also apply it to the 1D models used for comparison.

While the advection timescale represents the time matter dwells in the gain layer (between shock and gain radius), the heating timescale tells us how long it takes to deposit enough energy into the material to make it unbound. Clearly, heating is of no importance as long as $\tau_{\rm adv} \ll \tau_{\rm heat}$. Thus, for obtaining a neutrino driven explosion, the condition $\tau_{\rm heat} \gtrsim \tau_{\rm adv}$ must hold over at least the time span $\tau_{\rm heat}$ (see also the discussion in Janka & Keil (1998)). Note that this condition does not necessarily lead to an explosion; in any case it will lead to a visible shock expansion.

A look at the timescales and their ratio (Figs. 4.7,4.8) immediately tells us that most models obtain too long heating timescales for an efficient neutrino heating. The ratio $\tau_{\rm adv}/\tau_{\rm heat}$ keeps a factor of two off the above mentioned minimal condition. Merely the two lightest models, s11.2 and n13, feature efficient neutrino heating over a small period of time.

This brings us to the most interesting feature obtained in our sample of models: the entropy-jump induced transient shock expansion. This phenomenon, which is best visible in Model n13 at $t_{\rm pb} = 30$ms and in Model s11.2 at $t_{\rm pb} = 90$ms, but also in a weaker form in the Models s1b, s20.0, and s15s7b2 at $t_{\rm pb} = 120$ms, 135ms, and 170ms, respectively, occurs whenever an entropy jump of the progenitor passes the shock. These jumps are correlated with composition interfaces as discussed in Sect. 4.1 and mark a change in the density profile of the infalling material. The consequence is always a more or less strong drop of the mass accretion rate. Consequently, the ram pressure drops and the freed shock can suddenly start expanding until it finds a new equilibrium position at larger radius (which is why the model n13 has a larger shock radius than the other models at $t_{\rm pb} = 80$ms, see above).

The drop of the ram pressure not only allows the shock to expand, also the material itself is forced less strongly into the direction of the proto neutron star surface. Thus, the advection timescale suddenly increases. This becomes interesting when $\tau_{\rm adv}$ becomes longer than $\tau_{\rm heat}$. Then the effective heating further strengthens the shock support: the shock can expand to even larger radii. This behaviour is obtained in the Model n13, and especially in Model s11.2, where $\tau_{\rm adv}/\tau_{\rm heat} \simeq 1$ over a time of $\tau_{\rm heat} \simeq 30$ms. Unforturnately, after 30ms the advection timescale drops again far below $\tau_{\rm heat}$. Now, the reduced mass accretion rate has reached the gain radius meaning that the mass of the material in the gain layer and thus also the support for the shock has dropped significantly. The shock quickly retreats and finds a new quasi-stationary solution where, however, heating proves to be ineffective again.

As for the Models s15, s20.0 and s1b, although the drop in $\dot{M}_{\rm sh}$ leads to a shock expansion, the transient is not strong enough to change $\tau_{\rm adv}$ significantly; also, in these models the entropy jump reaches the shock too late when it is already deep inside the gravitational potential well and the post-shock velocities are fairly high. Thus $\tau_{\rm adv}/\tau_{\rm heat}$ remains well below one.

Note that the sudden drop of $\partial_t M_{\rm sh}$ also nicely reveals the dependence of r_ν and L_ν on this variable: 10–20ms after such a drop both these variables decrease. Also, the total lepton number and energy loss via neutrino emission, see Fig. 4.10, depends strongly on $\partial_t M_{\rm sh}$ and thus the progenitor structure. This feature could be used to deduce the progenitor structure from a detected supernova neutrino signal.

Summarizing, we find that all our simulations evolve both qualitatively and quantitatively similar. Even at their maximum shock radii, around 130–150km, the simulations stay far from explosions. Merely in the two lightest progenitor models, s11.2 and n13, the drop in $\partial_t M_{\rm sh}$ at the composition interfaces is steep and large enough, and arrives early enough in time, to allow the shocks to reach 170km. Still, this is far from obtaining an explosion. Thus, the progenitor would have to have a significantly different structure than seen in stellar evolution models hitherto, if it were to bring the 1D supernova simulations closer to explosion. Note that one does find explosions for the low mass range of massive stars which are heavy enough to become gravitationally unstable, but have a degenerate NeMgO core at the onset of collapse, see Kitaura Joyanes (2003) and Nomoto (1984).

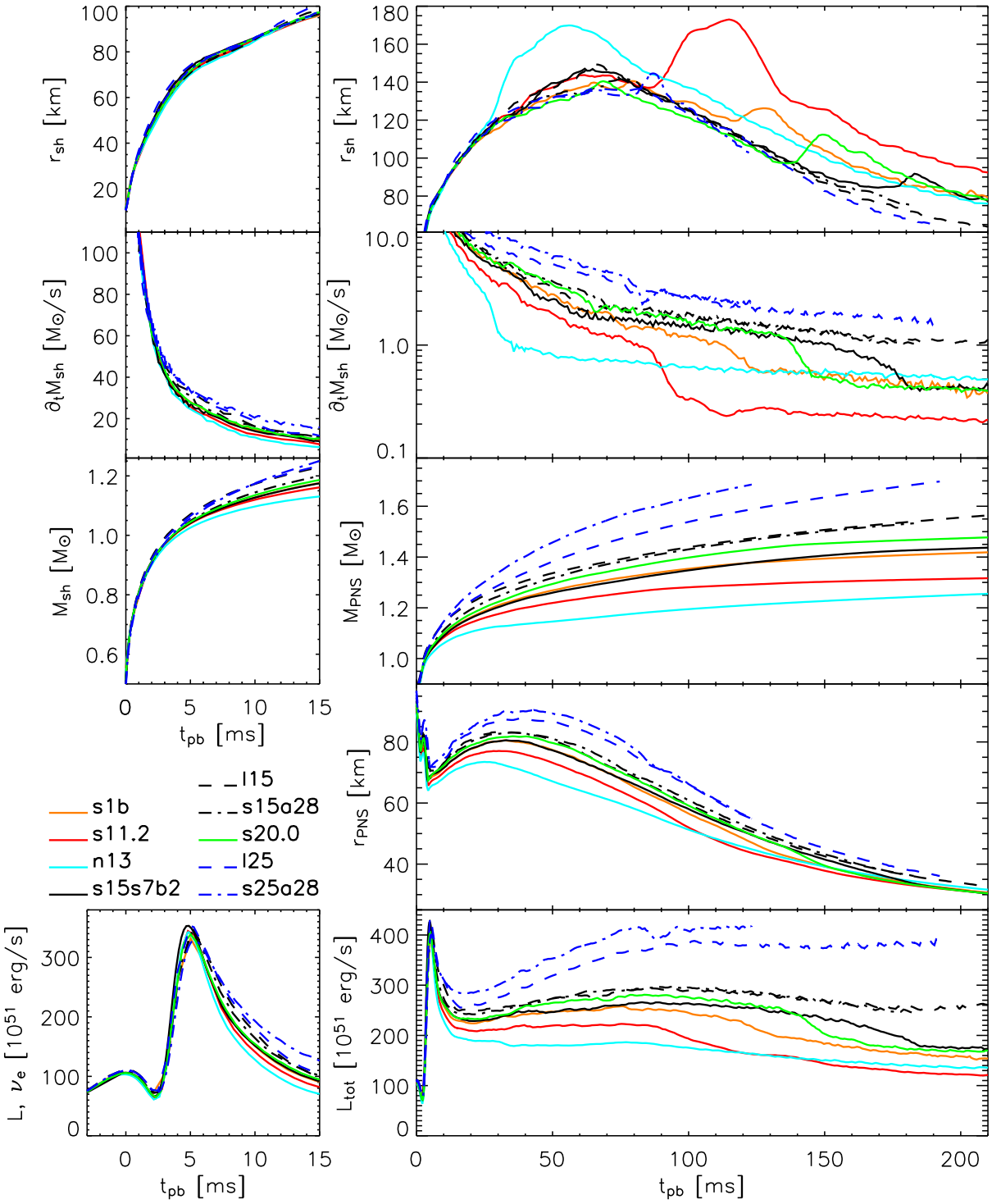

Figure 4.6: Post-bounce evolution of the models. The left panels show the prompt shock, neutrino burst, and early accretion shock evolution, the right panels depict the whole accretion shock phase. The panels show, from top to bottom, the shock radius, the mass accretion rate through the shock, the mass enclosed by the shock (left)/proto neutron star (right), the PNS radius, and the electron neutrino (left)/total (right) neutrino luminosity at r = 400km for an observer at rest. The PNS mass and radius were taken at the ν_e sphere for simplicity.

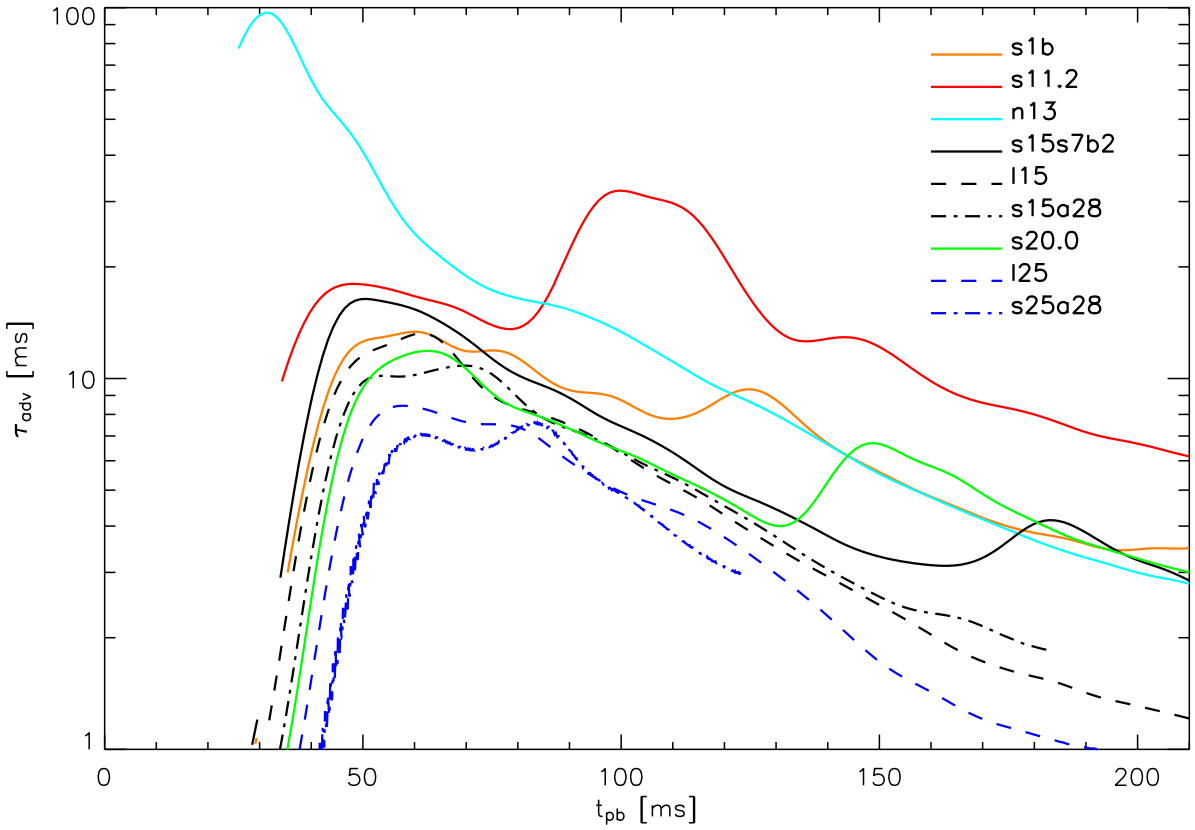

Figure 4.7: The advection timescales over time as defi ned in Eq. 4.1. The lines were smoothed over a time of 5ms.

4.3 Two-dimensional models

The one-dimensional models analyzed so far have one significant drawback: they do not allow for convective overturn of the material. Convection, especially the so-called hot bubble (HB) convection in the gain layer, is believed to strengthen the shock (see Introduction). We can analyze our 1D models in this aspect: approximately following Bruenn et al. (2004) we define a new observable,

$$n_{\mathrm{grow}}(t) = \max_{r_1<r_2}\left(\int_{r_1>r_{\mathrm{gain}}(t)}^{r_2<r_{\mathrm{shock}}(t)} \mathrm{sgn}\left(C_{\mathrm{L}}(r',t)\right)\sqrt{\left|\frac{C_{\mathrm{L}}(r',t)}{\rho(r',t)}\,\frac{d\phi(r',t)}{dr}\right|}\;\frac{dr'}{v_r(r',t)}\right) \tag{4.5}$$

where the Ledoux criterion is defined as

$$C_{\mathrm{L}} = \left(\frac{\partial\rho}{\partial s}\right)_{Y_{\mathrm{lep}},p}\frac{ds}{dr} + \left(\frac{\partial\rho}{\partial Y_{\mathrm{lep}}}\right)_{s,p}\frac{dY_{\mathrm{lep}}}{dr} \tag{4.6}$$

and predicts instability if $C_{\mathrm{L}} > 0$. This observable roughly gives us the number of e-folds a perturbation of the matter will grow between the shock and the gain radius from Ledoux instability. To obtain effective convection the perturbations must grow strongly in the gain layer, since the cooling layer is Ledoux stable. Looking at the growth number n_{grow} for our models (Fig. 4.9) we see that only few models will really be successful in achieving lively Ledoux convection.

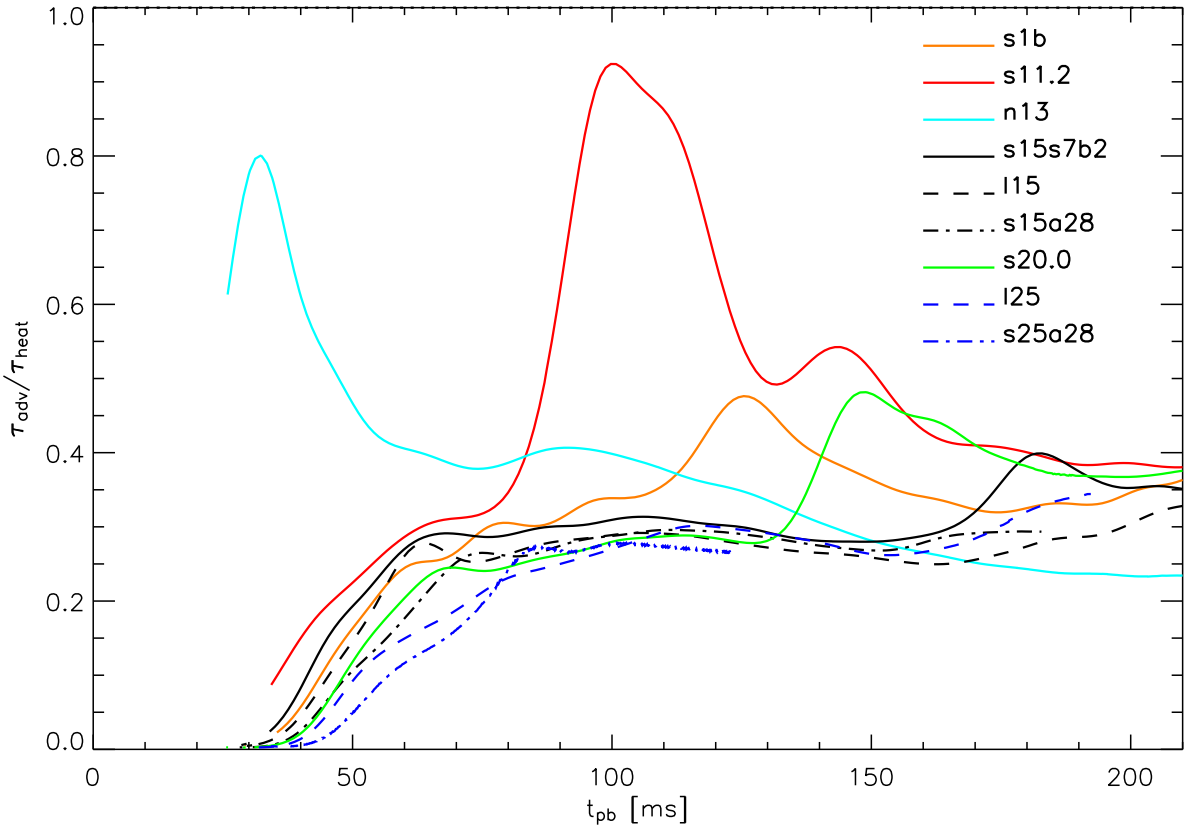

Figure 4.8: The heating efficiency, $\epsilon_{\rm heat} \equiv \tau_{\rm adv}/\tau_{\rm heat}$, as a function of time. The lines were smoothed over a time of 5ms.

For our two-dimensional studies we have chosen three representative progenitors, s11.2 which is expected to show strong Ledoux convection, as well as the two pessimistic progenitors s15s7b2 and s20.0. A total of seven models have been calculated in 2D, see Table 4.3. Most models were started from a 1D model at 7ms after bounce, thereby perturbing the radial velocity randomly with an amplitude of ±1%. For each progenitor we calculated a low angular resolution (2.7°) model covering a 86.4° wedge around the equator. Further we calculated high resolution (1.35°) versions for the two lighter progenitors s11.2 and s15s7b2, latter was started at the onset of collapse with an initial density perturbation of ±2%. One simulation was run covering the full star for the $11.2 M_\odot$ progenitor, s112_128_f, with a resolution of 1.41°.

The first subsection discusses PNS convection, starting with explaining what type of PNS convection we see, how it affects the evolution of the supernova and of the neutrino emission. We end by discussing resolution and perturbation effects and differences between simulations with different progenitors. The second subsection describes the HB convection. Again, we at first discuss differences compared to 1D models. Here, the resolution and size of the computated angular region play a much larger role and we need to elaborate on these subjects. Also the sensitivity of the onset of HB convection on perturbation seeds is discussed. Finally we elaborate on our calculation which covers a whole star, and signify the importance of the l=1 mode.

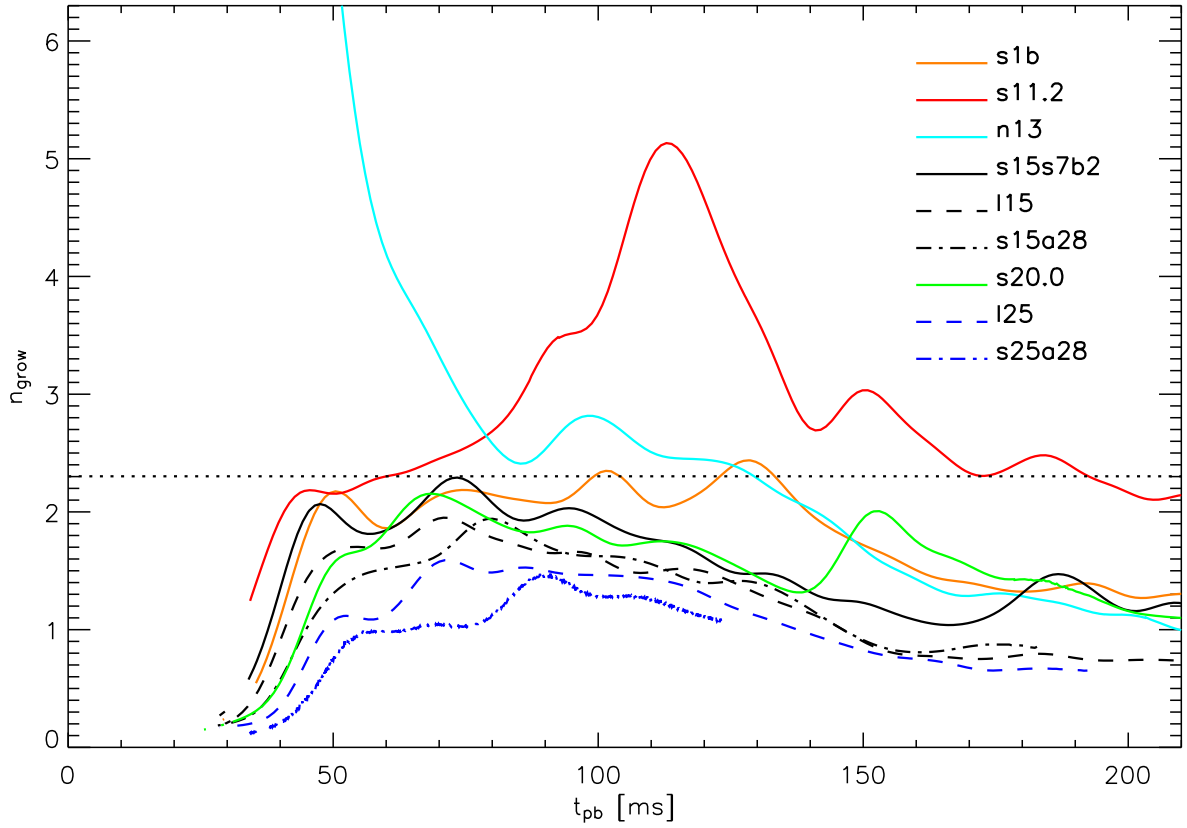

Figure 4.9: Number of e-folds that perturbations would increase in amplitude on their way from the shock to the gain radius. The lines were smoothed over a time of 5ms. For Model n13, n_{grow} starts at values of 20 at $t_{\mathrm{pb}} = 25$ms, and starts decreasing at $t_{\mathrm{pb}} = 35$ms.

4.3.1 Proto neutron star convection

The PNS can largely be studied independent of the HB convection (not vice versa!): Unless the gain layer changes its mass dramatically (e.g. at the onset of explosion), the mass accretion onto the PNS will be very similar to the mass accretion through the shock. Several of the discussed models show very weak HB convection (s15_32, s20_32, s15_64_p) and are thus perfectly suitable for this discussion.

An evaluation of the Ledoux criterion (Eq. 4.6) in Fig. 4.11 shows that the PNS becomes unstable around 40ms after bounce. This happens in a region which initially is stable due to a positive entropy gradient. As neutrino diffusion carries entropy away, this mechanism being more effective at larger radii where the opacity is lower, the entropy profile flattens and finally the entropy gradient becomes negative and the PNS gets Ledoux unstable. Similar to Keil (1997), we find that the structure of convective cycles initially is that of rings with angular sizes between 20° and 30° and lengths between 10 and 15km which persist for around 5ms and then reform at shifted locations, see Fig. 4.13. 200ms later, the contraction of the PNS has reduced the radial sizes of the convective cycles to 10km. The velocities in the rings are around $3 \cdot 10^8$cm/s with peaks of up to $5 \cdot 10^8$cm/s, at later times the velocities have values around $2 \cdot 10^8$cm/s.

The convection transports energy and lepton number from the inside of the PNS up to very close to the neutrino spheres, thereby flattening the entropy gradient, but also flattening the

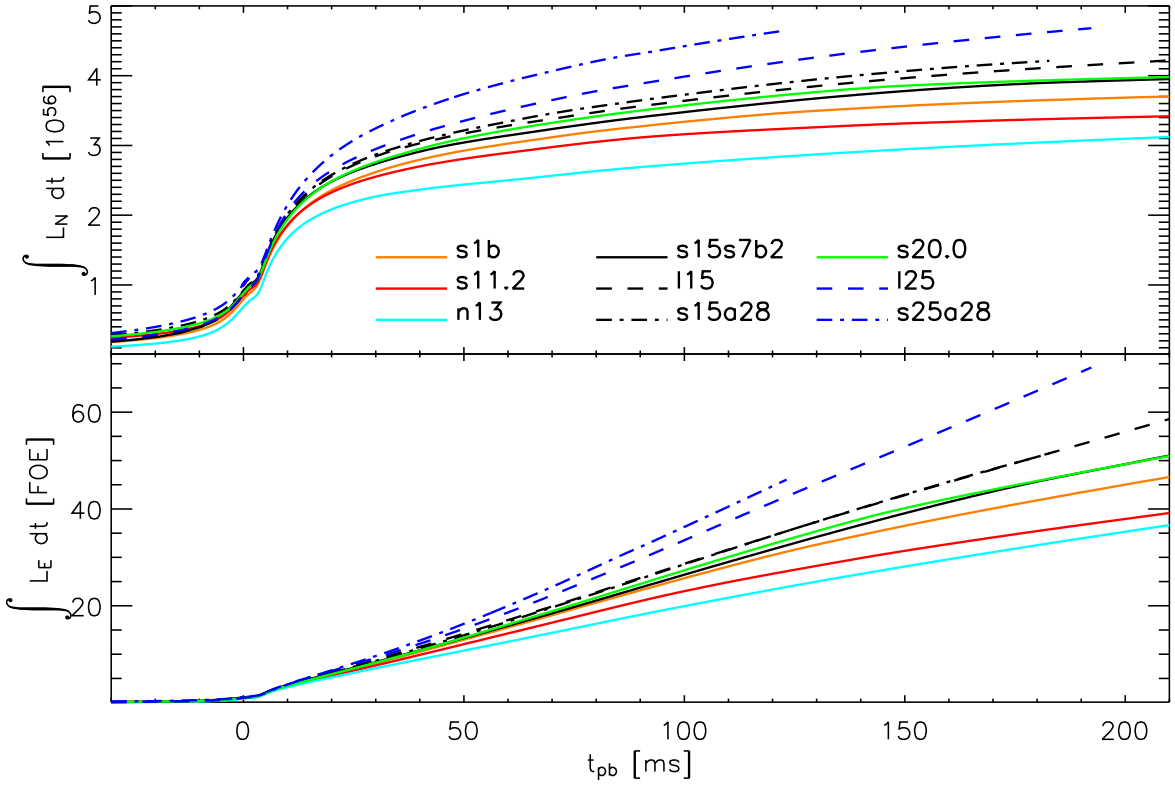

Figure 4.10: The lepton number and energy losses of the 1D models over time.

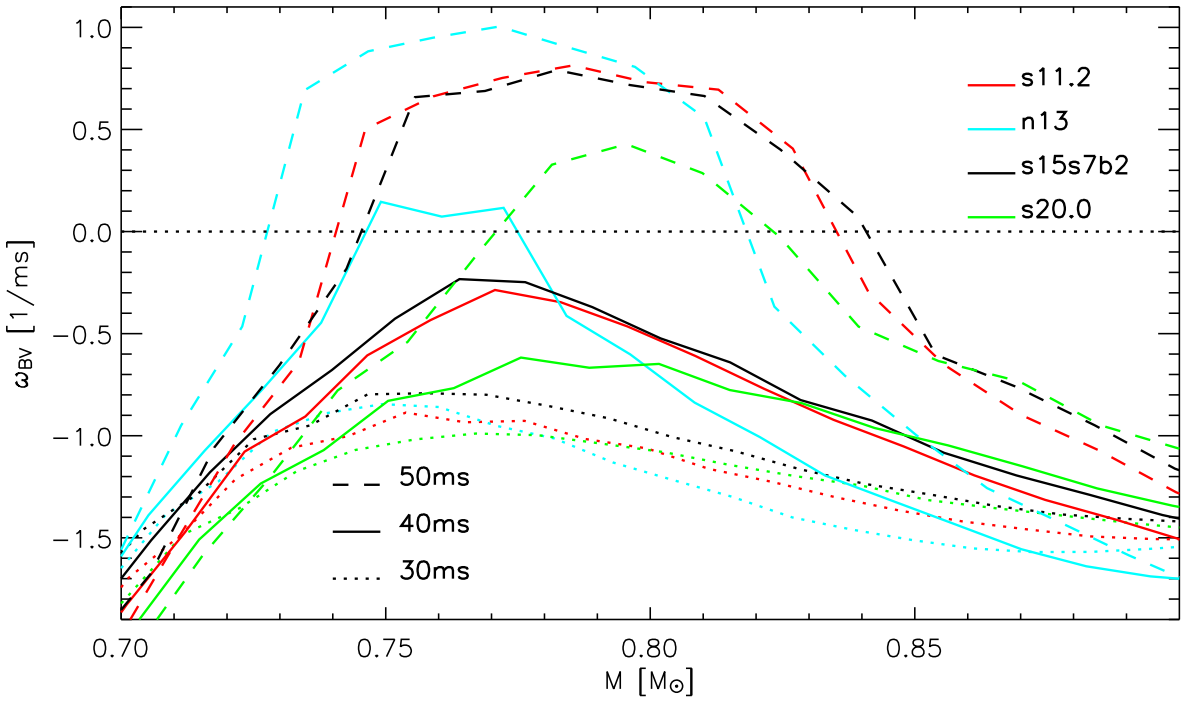

Figure 4.11: Ledoux criterion evaluated for different 1D models at 30, 40, and 50ms after bounce.

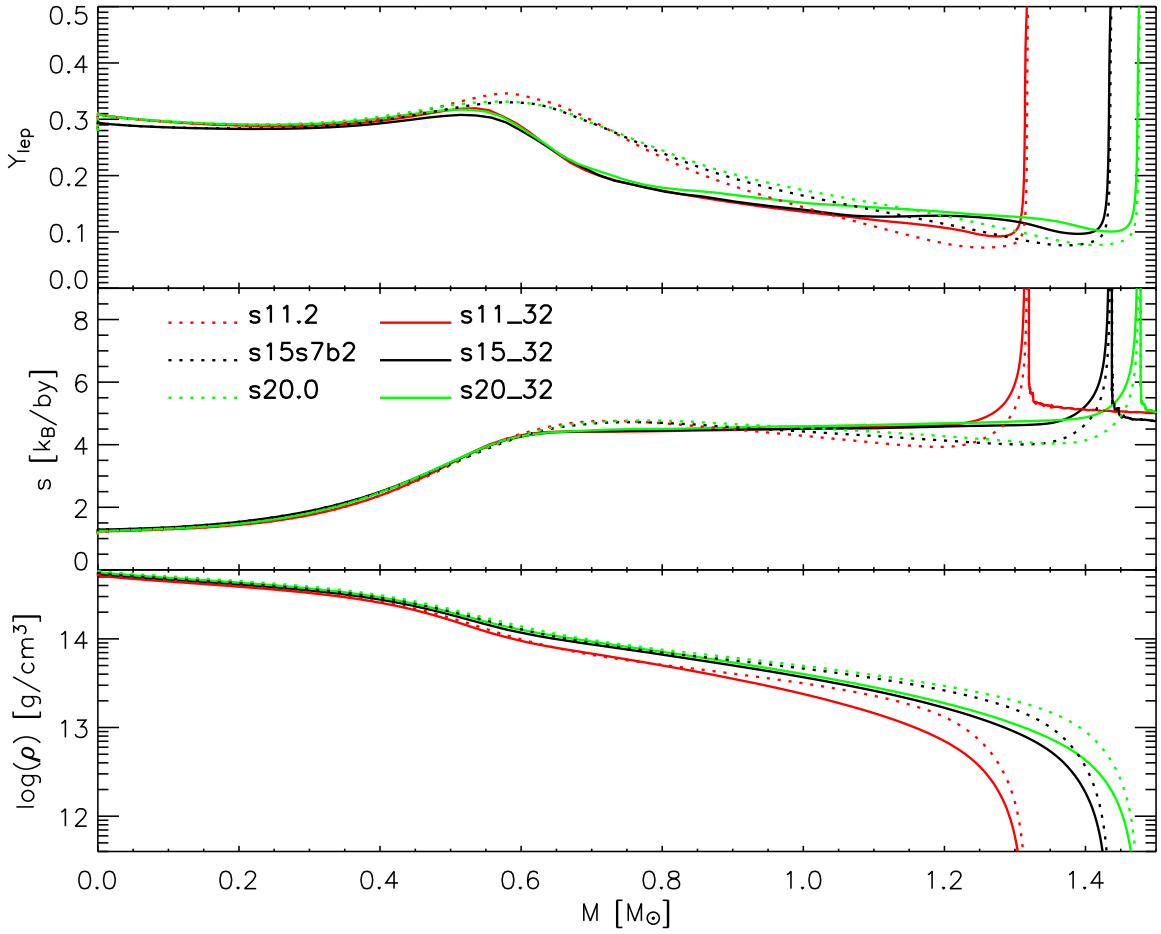

Figure 4.12: Lepton number, entropy, and density as a function of the enclosed mass for chosen models 200ms after bounce (i.e. approximately 160ms after the onset of PNS convection.)

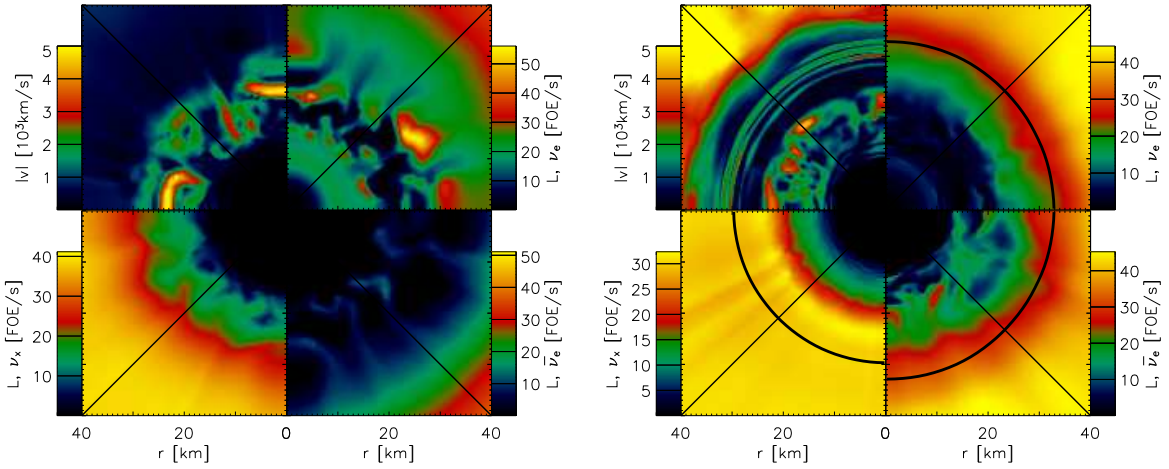

Figure 4.13: Snapshots of PNS convection in Model s15_32 for the times 48ms (left) and 243ms (right). The upper left panels depict the absolute matter velocity, the other three panels show the luminosities of the three neutrino types. For latter three panels, the upper range of the color bar corresponds to 110% of the luminosity at infinity. The thick black lines mark the respective neutrinospheres (which are larger than 60km for the time 48ms).

Table 4.3: Parameters of computed 2D models for progenitor stars with different masses. Ω_i is the angular velocity of the Fe-core prior to collapse, θ_0 and θ_1 are the polar angles of the lateral grid boundaries, and N_θ is the number of grid points in lateral direction.

Model	Progenitor	$[\theta_0, \theta_1]$ (degrees)	N_θ	Resol. (degrees)	Collapse in 2D	Pert. (%)	Boundary conditions
s11_32	s11.2	[46.8, 133.2]	32	2.70	–	$v, \pm 1$	periodic
s11_64	s11.2	[46.8, 133.2]	64	1.35	–	$v, \pm 1$	periodic
s11_128_f	s11.2	[0, 180]	128	1.41	–	$v, \pm 1$	reflective
s15_32 †	s15s7b2	[46.8, 133.2]	32	2.70	–	$v, \pm 1$	periodic
s15_64_p	s15s7b2	[46.8, 133.2]	64	1.35	+	$\rho, \pm 2$	periodic
s20_32	s20.0	[46.8, 133.2]	32	2.70	–	$v, \pm 1$	periodic

† This is the Model s15Gio_32.b from Sect. 3.2.1.

lepton number profile, see Fig. 4.12. However, at the end of the calculation the initially quite steep negative $Y_{\rm lep}$ gradient has not yet flattened out.

The redistribution of lepton number and energy slowly affects the structure of the PNS. The "drain" region where $Y_{\rm lep}$ and e drop has densities close to the nuclear density ($0.3–2\cdot10^{14}$g/cm^3) while the "dump" region where $Y_{\rm lep}$ and e are deposited has lower densities ($10^{12}–10^{13}$g/cm^3). The pressure in the "drain" region is less sensitive to changes in $Y_{\rm lep}$ and e than the pressure in the "dump" region. This can be seen in the EoS variable, $\left(\frac{\partial \ln p}{\partial \ln Y_{\rm lep}}\right)_{\rho,e}$, which for the Model s15s7b2 at times after 100ms post-bounce has values between −0.1 and −0.35 in the "drain" region and values between +0.1 and −0.15 in the "dump" region, while the EoS variable $\left(\frac{\partial \ln p}{\partial \ln e}\right)_{\rho,Y_{\rm lep}}$ lies in the range 1.05–1.40 in the "drain" region and in 1.35–1.90 in the "dump" region. Thus the decrease of pressure in the "drain" region due to PNS convection is overcompensated by the stronger increase of pressure in the "dump" region, leading to an expansion of the PNS. Consequently, also the neutrinosphere radii are larger than in the respective 1D "comparison" models, see Fig. 4.14.

All this has interesting consequences for the neutrino emission. Immediately after the onset of PNS convection the increase of $Y_{\rm lep}$ in some lateral zones at the upper end of the convective region leads to a higher electron chemical potential μ_e. Thus the $\bar{\nu}_e$ abundance decreases significantly in these zones. Although this happens in a region where the $\bar{\nu}_e$ luminosity has reached only 5–10% of its final value the decrease is enough to lower the total $\bar{\nu}_e$ luminosity immediately by several percent. When the PNS convection is running at full throttle, $L_{\bar{\nu}_e}$ can be lowered by up to 10% with respect to the 1D models, see Fig. 4.15.

The decreased $\bar{\nu}_e$ abundance also affects the ν_x luminosity via the process $\nu_e \bar{\nu}_e \rightarrow \nu_x \bar{\nu}_x$. Since this is the dominant ν_x production process and the decrease of $\bar{\nu}_e$ happens in a region where L_{ν_x} is 70% of its final value, the throttling of this process shows in L_{ν_x} which decreases by up to 5%.

On a timescale of 100ms these moderate effects are overridden by the structural change of the

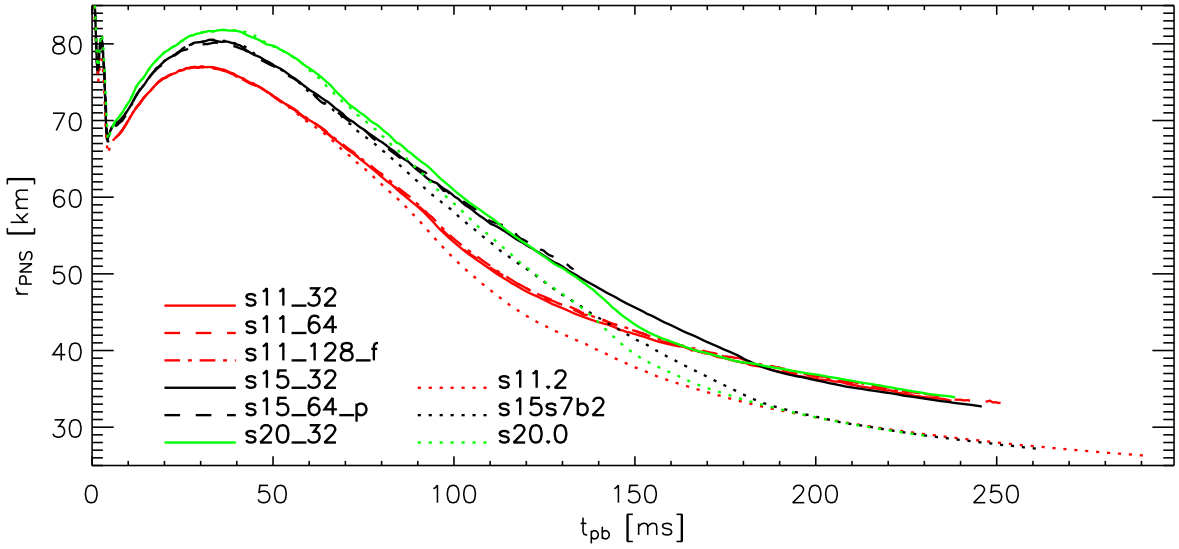

Figure 4.14: Proto neutron star radius for the 2D models and their comparison 1D models. For simplicity, the electron neutrinosphere radius was taken.

PNS as well as the persisting deposition of energy in the region below the ν_x sphere. The regions affected by PNS convection contribute 30%, 30%, and 90% to the ν_e, $\bar{\nu}_e$, and ν_x luminosities, respectively, at late times. The increase of the neutrino radii without the energy deposition would lead to lower luminosities, see Marek et al. (2005), because the expanded material would have lower temperatures at r_ν and this would overcompensate the r_ν factor in the relation $L \propto r_\nu^2 T_\nu^4$. However, in our 2D models the luminosities increase. We do find lower T_ν which result in lower neutrino energies $\langle \varepsilon_\nu \rangle$, see Fig. 4.16, by almost up to 10% after 200ms of PNS convection. But this decrease in T_ν is much weaker than it would be in case of pure adiabatic expansion. The energy deposition close to the neutrinospheres heats up the material strong enough to lead to a net increase of luminosity. The effect is strongest for the ν_x which decouple energetically from the medium already at the upper boundary of the convective region; after 200ms L_{ν_x} is almost 20% larger than in the 1D models, see Fig. 4.15. L_{ν_e} increases only by few %, while $L_{\bar{\nu}_e}$ is almost identical in 1D and 2D models, since the higher μ_e and the structural differences nearly compensate each other.

If we look at the total energy and net lepton number losses due to neutrino emission, comparing the 2D models with the 1D models, we find that after $\sim$ 100–140ms of reduced energy emission, the emission is stronger in 2D models. However, even 250ms after bounce, the total energy loss is only 2–4% higher with PNS convection. The deleptonization at that time is up to 10% larger with PNS convection.

Note that the luminosities in 2D models relative to 1D models are increased by 25%, 15%, and 25% for ν_e, $\bar{\nu}_e$, and ν_x at their respective neutrinospheres after 200ms, thus the effect of the PNS showing much stronger. These differences have been reduced when the neutrinos leave the star due to structural differences above the neutrinospheres; note also that the high energy end of the spectra decouple above the spectrum-averaged neutrinosphere.

We have run different simulations varying the resolution (2.7° and 1.35°/1.41°) and the size (wedge with 86.4° around the equator and a full star). The results show that these differences change little in the behaviour of the PNS convection. Thus, the resolution of 2.7° large angular

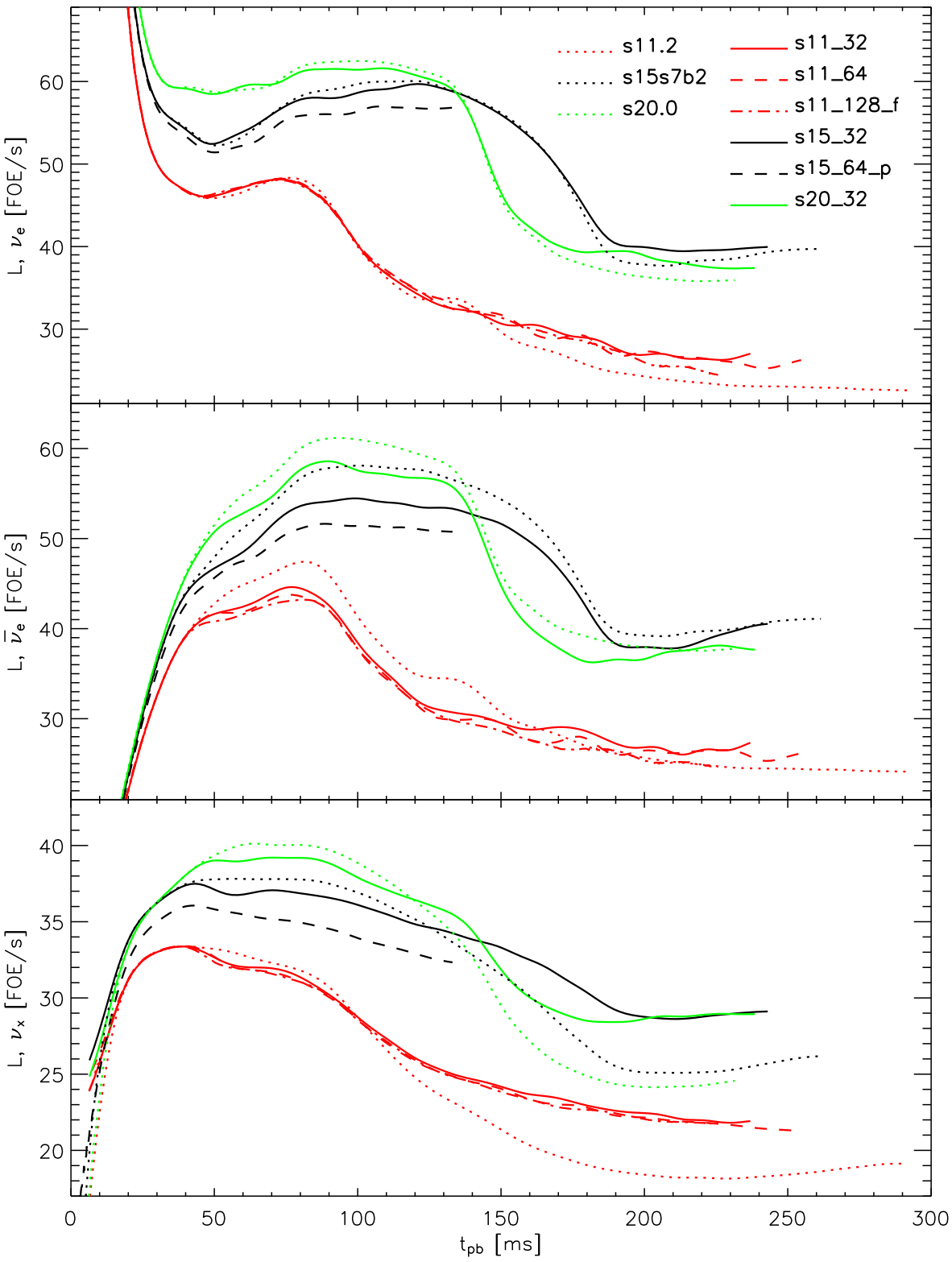

Figure 4.15: Neutrino luminosities for the 2D models and their comparison 1D models, evaluated at a radius of 400km for an observer at rest. The lines were smoothed over a time of 5ms.

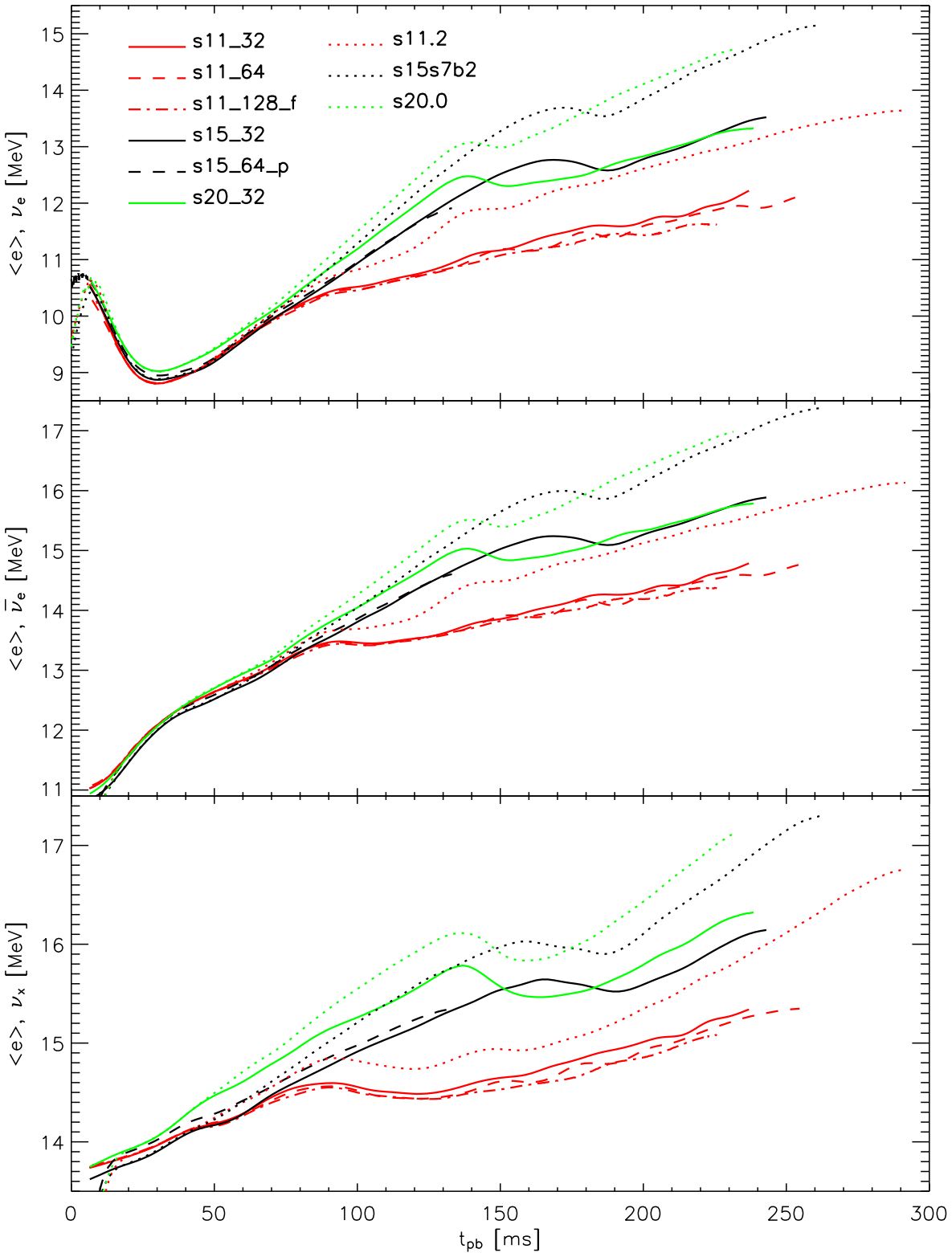

Figure 4.16: Neutrino average energies for the 2D models and their comparison 1D models, evaluated at a radius of 400km for an observer at rest. The lines were smoothed over a time of 5ms.

zones is sufficient to simulate PNS convection. As the convective rings only have a size of 20–30°, it is no surprise that the full star simulation s112_128_f does not differ in the PNS convection effect from the model s112_64.

The PNS convection also evolves similarly in simulations with different progenitors. The relative differences with respect to the 1D models is quite similar for all progenitors. The moderate differences, e.g. in $\int L^{2D} dt - \int L^{1D} dt$, see Fig. 4.17, are quite small with regard to the large differences in the mass accretion rates and the different evolution of HB convection.

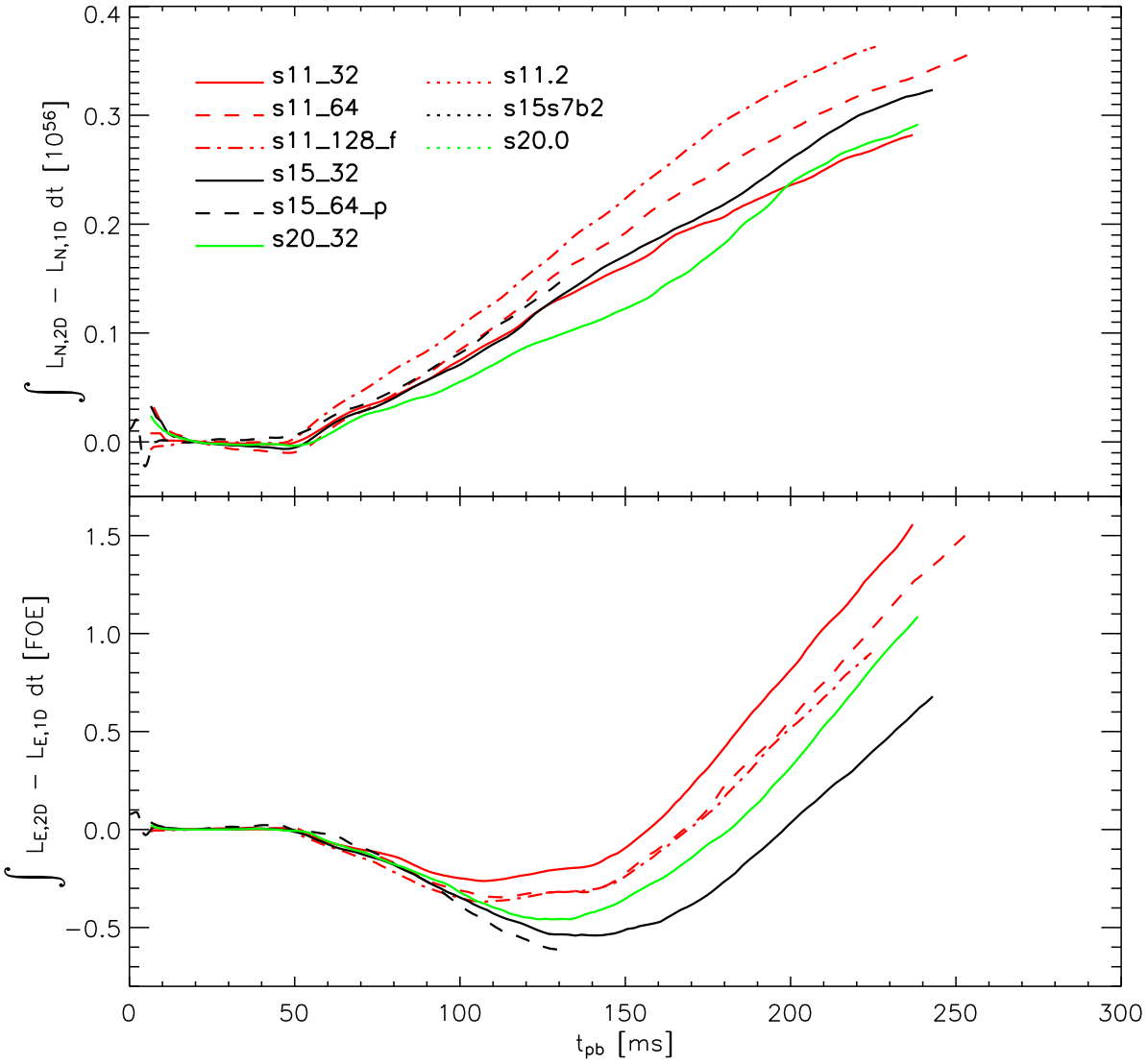

Figure 4.17: Difference between the lepton number and energy losses of the 2D models and their respective 1D models.

Even the influence of the choice of perturbation seeds has little effect on the evolution of the PNS. Large seeds like e.g. in Model s15_64_p merely lead to an earlier onset of PNS convection by 10–20ms. During this short period of time the PNS convection will hardly change anything.

In summary, the PNS convection amounts to two important consequences: first, the emitted neutrinos have lower energies than in 1D models (10% lower after 200ms), while the neutrino

luminosities increase, after 200ms of PNS convction by 20%, few %, and 20% for ν_e, $\bar{\nu}_e$, and ν_x, respectively. Second, the PNS convection affects the evolution of the gain layer and shock by a less compact PNS and by neutrinospheres at larger radii and with slightly lower temperatures, and thus significantly higher luminosities near the neutrinospheres. The less compact PNS of course implies a different structure between neutrinospheres and shock even without HB convection. However, looking at the models s15_32, s20_32, and s15_64_p, we see that the PNS convection only has a minor effect on the shock radius.

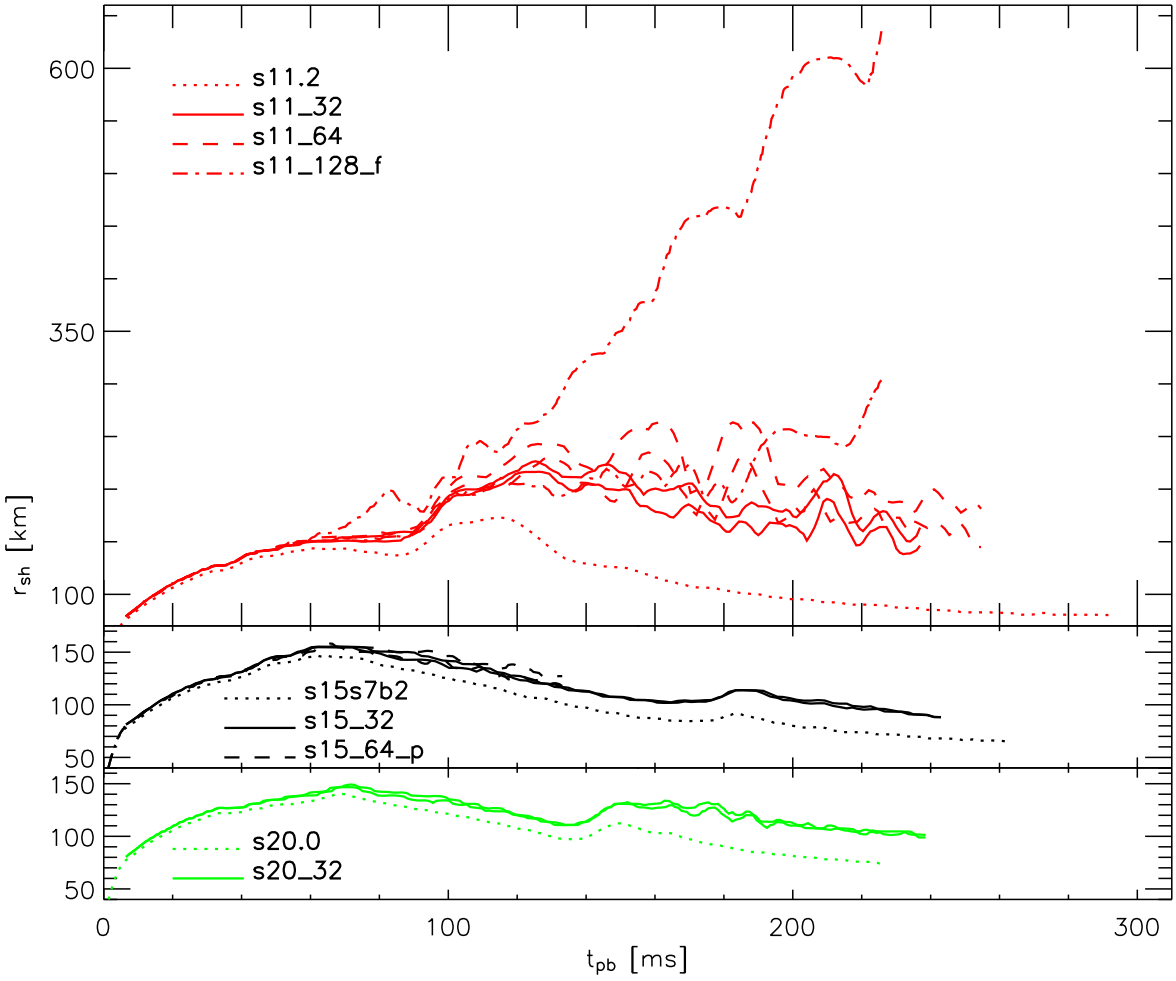

Figure 4.18: Shock radii for the 2D models of Table 4.3 and their 1D comparison models.

4.3.2 Hot bubble convection

We now turn to the discussion of the Ledoux-convection in the gain layer, the so-called hot bubble (HB) convection. As expected the Models s15_32 and s20_32 do not manage to develop significant overturn of material in the gain layer. This was explained with the small growth of perturbations between shock and gain radius, see Fig. 4.9. Although perturbations do show in the angular distribution of e.g. velocity and entropy (see e.g. Fig. 4.19), the radial structure is not influenced by this “weak” HB convection. Thus we can use these models to describe how the expansion of the PNS due to PNS convection alters the structure of the gain layer.

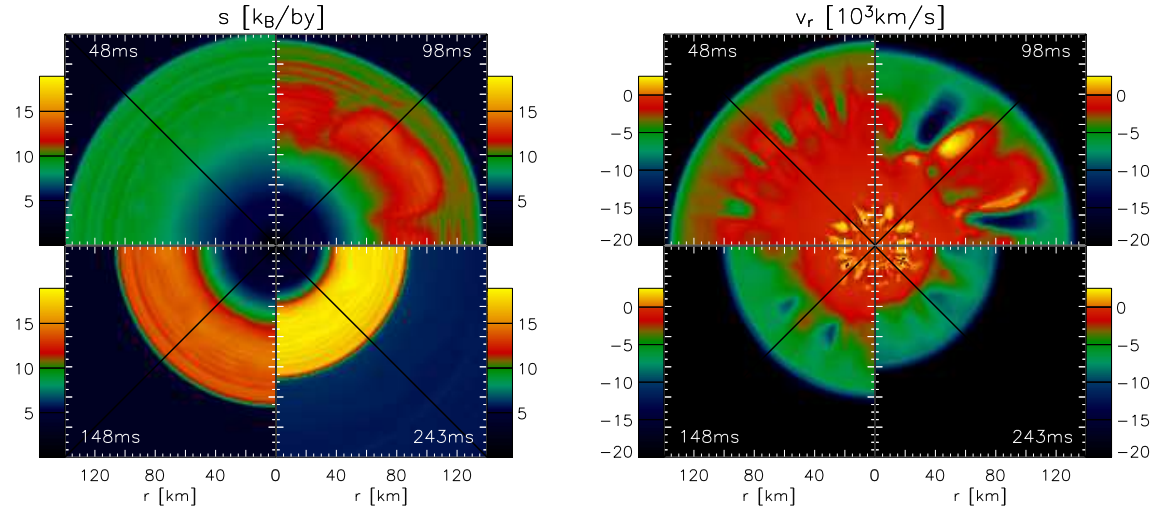

Figure 4.19: The left figure shows entropy snapshots of Model s15_32 for four times. The right figure shows the radial velocity for the same times. The upper range of the color bar corresponds to 2500km/s.

Remember that the radii of the neutrinospheres are larger than in 1D while the enclosed masses of the neutrinospheres are smaller due to the less compact PNS. For quite similar reasons this also applies for the gain radius and its enclosed mass. However, the mass which is enclosed by the shock is identical in 1D and 2D since the accretion rate merely depends on the gravitational mass of the PNS which is not different in 2D. Thus the mass in the gain layer has to be larger in 2D. Fig. 4.20 confirms this deduction, we find that the mass in the gain layer $M_{\rm gl}$ can be more than a factor of two larger than in 1D. Inevitably, the shock radius is also larger than in 1D, see Fig. 4.18. Since the density at given radius is higher in 2D (a structural consequence of the larger $\nu_{\rm e}$-sphere radius which is situated at $\rho \simeq 10^{11}$–10^{12}g/cm^3) and the mass accretion rate $\dot{M}(r)$ is approximately constant in radius above the gain radius (a feature of quasi-stationary solutions) and $\dot{M}(r)$ is equal in 1D and 2D (a consequence of the Rankine-Hugoniot conditions), the post-shock velocities are smaller in 2D. This implies a larger advection timescale, see Fig. 4.20, by up to a factor of two. What we find very surprising is that the total heating rate of the gain layer $\delta_t E_{\rm gl}$ is almost identical in 1D and 2D. The gain layer is situated at larger radii, the neutrino luminosities are higher while the neutrino energies and thus the interaction rates are lower, and the position of the actual gain radius depends sensitively on all these values as well as on the temperature and density profile. All this would suggest a different value for $\delta_t E_{\rm gl}$, so we suspect an underlying mechanism which controls this variable in the absence of HB convection.

As a consequence, $\tau_{\rm heat} \propto M_{\rm gl}/\delta_t E_{\rm gl}$ also increases. Again surprisingly, the heating efficiency $\epsilon_{\rm heat} = \tau_{\rm adv}/\tau_{\rm heat}$ does not increase although these two timescales seem to be independent of each other. Therefore we also suspect a correlation between $M_{\rm gl}$ and the velocity profile.

During the entropy-jump induced transient shock expansion the advection timescale becomes long enough to allow strong convection to develop. We will however discuss effective HB convection using the Model s112_64, since here the effects are much more pronounced.

As we can see from Fig. 4.9, the perturbation growth rate increases to values of five when the models with the s112 progenitor reach the time where the Si-SiO interface passes the shock 90ms after bounce. This leads to a quick expansion of the shock see Fig. 4.18. Although there is no real difference in the convective pattern before and right after the shock expansion (see

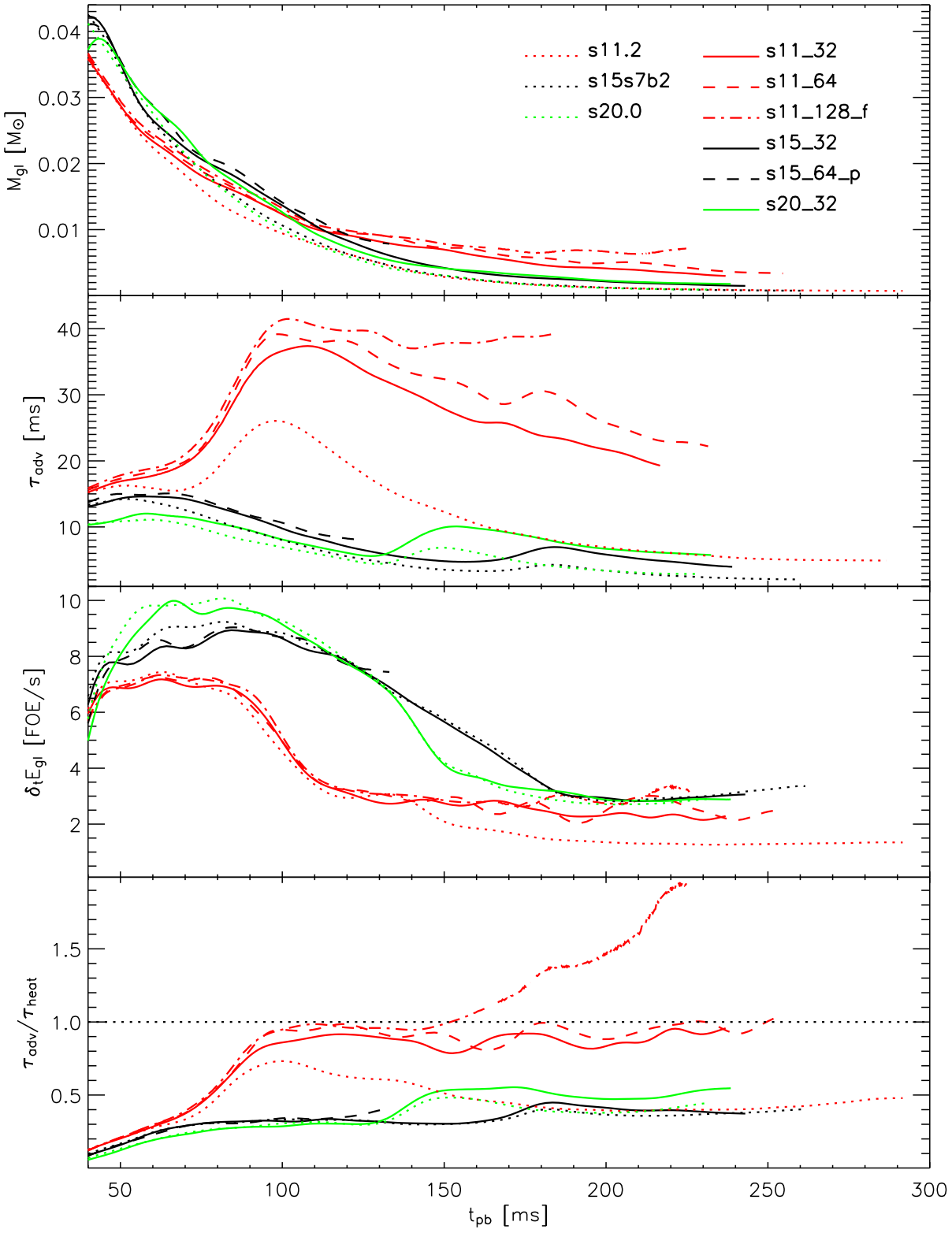

Figure 4.20: First panel: Mass of gain layer. Second panel: Advection time as defi ned by Eq. 4.4. Third panel: Total heating rate in gain layer. Fourth panel: Heating efficiency. All lines were smoothed over a time of 5ms.

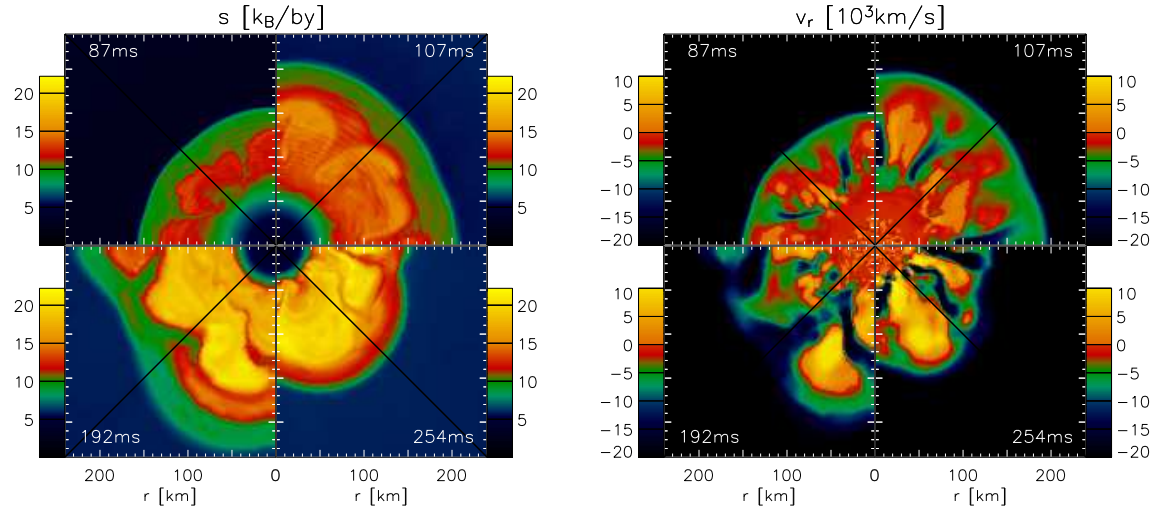

Figure 4.21: The left figure shows entropy snapshots of Model s112_64 for four times. The right figure shows the radial velocity for the same times. The velocities can reach up to 35000km/s (bright yellow).

Figs. 4.21a–b, upper left and right panel), the conditions for convection are much more favorable and convection is not suppressed as in the models with the heavier progenitors: The long advection timescale of 30–40ms (Fig. 4.20) leads to a higher heating efficiency of more than 0.8 (Fig. 4.20). This implies that the matter in the gain layer is less strongly bound (Fig. 4.22) so that the stationary solution would predict a larger shock radius due to the larger energy content which influences the pressure. The shock position is of course varying strongly due to the convective overturn in the gain layer.

We find that large scale modes which tend to be the most stable modes can develop in this environment. In Model s112_64 the number of hot (high-entropy) bubbles decreases from more than five at 40ms to only one at 110ms. All bubbles persist for about 20ms and then collapse. Also at 140ms and 170ms do large single bubbles appear which also collapse after 20ms. After the third large bubble has collapsed, the convection becomes weak again, i.e. small scale bubbles appear.

The three large scale bubbles are in fact correlated: As seen in 1D models, the shock and the region between shock and PNS surface can produce a back-reacting oscillatory behaviour, see Sect. 3.1.4. What we see here is in fact very similar to this 1D effect. The expansion of the dominant HB lowers the accretion rate through the gain layer, so that the neutrino luminosity descreases and thus the heating rate decreases. In short, the expanding HB cuts off its own energy supply. When it weakens and collapses, the mass of the former HB accumulates just above and below the gain radius and the reverse happens, the heating strongly increases and a new HB emerges. The crucial question is whether the performance of one such cycle increases the energy in the gain layer or whether it descreases it. In the first case we would end in an explosion such as in the simulation discussed in Sect. 3.1.4. However, in this case the cycle ends after three periods: the decisive quantity is the heating efficieny, which on a time average should be higher than one to obtain a cycle with positive energy balance. For Model s112_64 this does not happen. In short, although the Model s112_64 gets much closer to explosion than any of the other simulations due to the strong convection and the high heating efficiency of about one, the simulation fails to produce an explosion. To reach a heating efficiency above

one, some ingredient(s) is still missing.

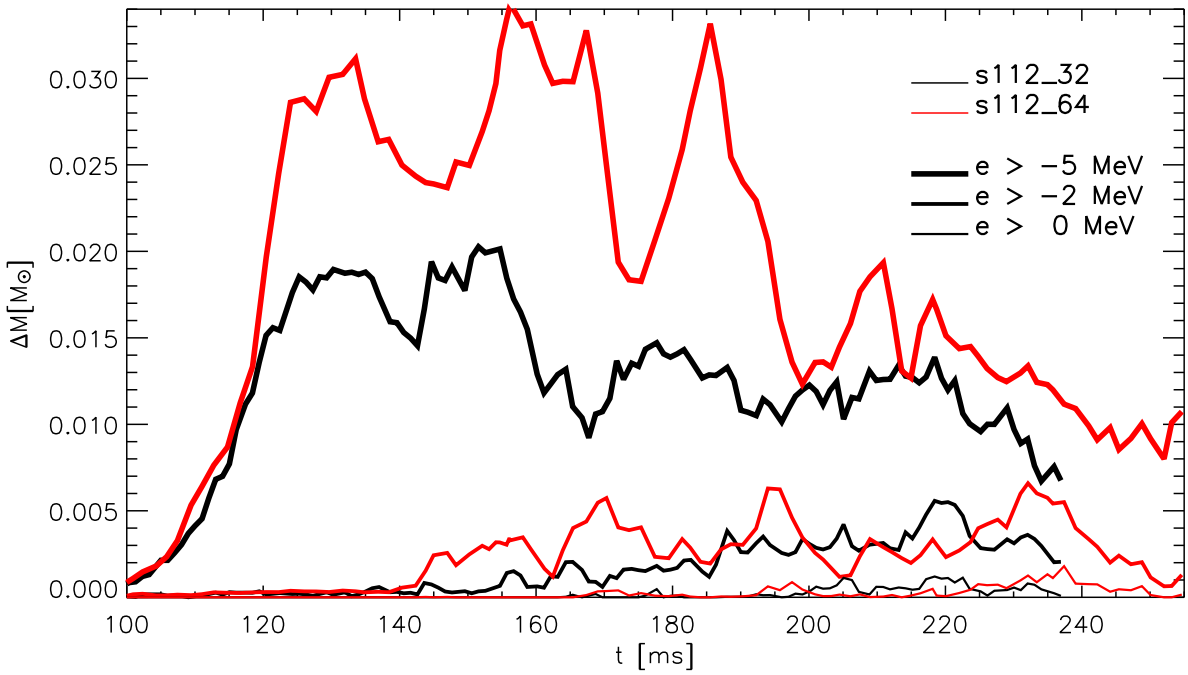

Figure 4.22: The lines show how much mass in the gain layer has a local specifi c binding energy above a certain value.

Turning to resolution studies, we can compare the Model s112_64 with the Model s112_32 which has only half the lateral resolution but is else identical in input of physics and in radial grid. Clearly, the shock does not reach as far as in the low resolution model and convection is not as pronounced, see Figs. 4.18. Although the large scale mode with one HB and one downflow also develops in this model, these overturns are weaker. One reason is that the downflow generally becomes very narrow and can not be dissolved in the low resolution model. Thus it is artificially wider than in reality.

Whether the resolution in Model s112_64 is sufficient is questionable, however, the decisive quantity for explosion, the heating efficiency, only increases slightly when increasing the lateral resolution from 2.7 degrees to 1.35 degrees. We doubt that further increasing the resolution can move the heating efficiency above 1 and so induce an explosion. Anyway, the resolution in Model s112_64 absolutely is the lowest we are allowed to use for realistic simulations. A resolution of 1 degree would be favorable (L. Scheck, private communication).

The choice of seed perturbations shows no significant influence on HB convection. Comparing the models s15_32 and s15_64_p we find that larger seeds (as in latter model) will lead to an earlier onset of convection by O(10ms). However, the timescales relevant for starting an explosion ($\tau_{\rm adv}$ and $\tau_{\rm heat}$) are much larger than 10ms.

4.3.3 A full star simulation

We now pay special attention to the Model s112_128_f. Clearly, the shock in this model manages to reach large radii of up to 600km (Fig. 4.18) and is expanding with a speed that is typical

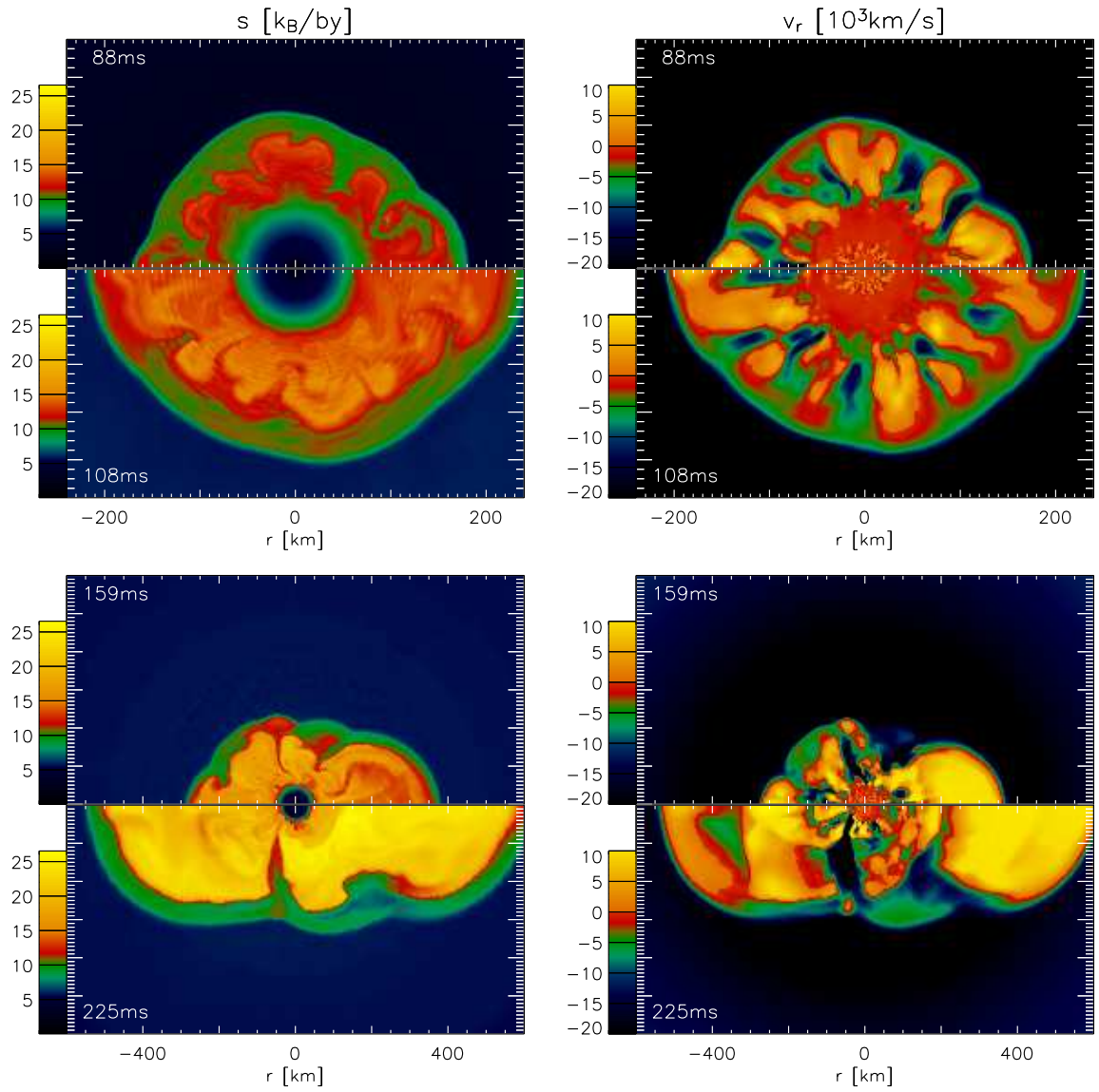

Figure 4.23: The left figures show entropy snapshots of Model s112_128_f for four times. The right figures show the radial velocity for the same times. The velocities can reach up to 47000km/s (bright yellow).

for shocks in exploding models (∼ 10000km/s). Although at the end of the simulation it was still too early to speak of an explosion the situation looks very favorable for explosion. Unfortunately, the simulation had to be stopped due to very small timesteps, as the equatorial downflow created strong local fluctuations in the medium below the neutrinospheres.

The model is different from Model s112_64 by two points. First, the complete star was simulated, from pole to pole, in Model s112_128_f, compared to a wedge around the equator which corresponds to ∼ 70% of the total volume in Model s112_64. This allows larger scale modes in Model s112_128_f. Second, while Model s112_64 used periodic lateral boundary conditions, the full star model necessarily had reflective boundary conditions at the poles. As we will show it is the latter difference that changes the behaviour of the simulation.

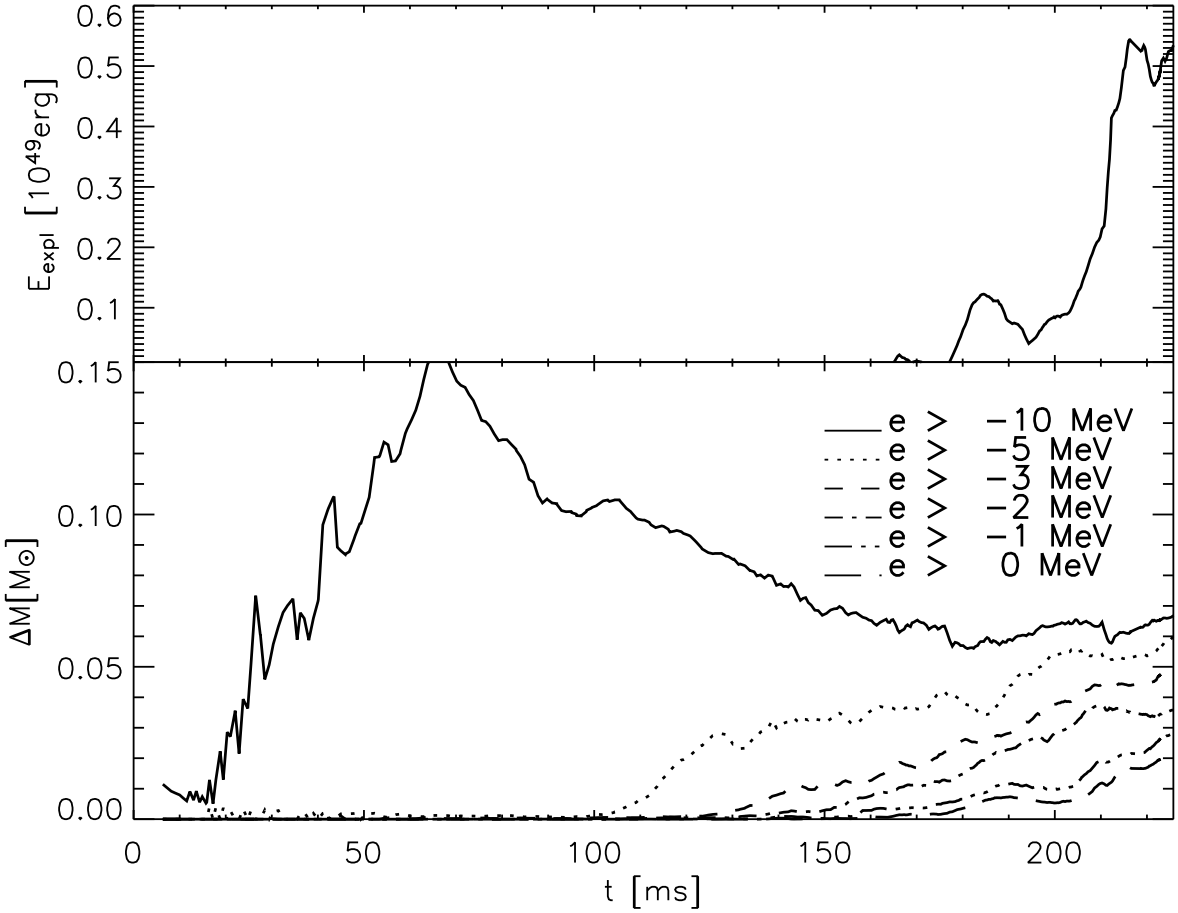

Figure 4.24: The upper panel shows the explosion energy of Model s112_128_f, defined in Eq. 3.6. The lines in the lower panel show how much mass in the gain layer has a local specific binding energy above a certain value.

Already early in the simulation of the full star do we see differences with respect to Model s112_64 (see Fig. 4.23, 88ms and Fig. 4.21, 87ms): Most of the convective structure resembles that of Model s112_64, but we find that the bubbles at the poles extend to larger radii. This is surely a numerical artefact connected to the geometry, in particular to the small volume of the zones near the poles. Therefore perturbations grow more quickly near the poles, see e.g. Kane et al. (2000). In the further development of the simulation the polar hot bubbles begin to dominate the convective structure of the gain layer as they become more and more prominent,

while the convective structure near the equatorial plane resembles very much the structure and size of hot bubbles and downflows seen in Model s112_64. Although the polar hot bubbles are weakened due to ram pressure and transient drops in heating they never really collapse and their starting infall is reversed by new waves of high-entropy, high-velocity matter streaming out along the pole. The snapshot at 225ms in Fig. 4.23 shows this when looking at the "left" pole: Above 400km the matter is expanding, but below it has started retreating due to *pdV* work applied from the matter falling through the shock. However, from below 300km a new hot bubble with very high velocities is already reviving the expansion of the matter betweeen 300km and 400km.

Eventually, 180ms after bounce, the gain layer is completely dominated by the two polar hot bubbles and one or two downflows near the polar axis, in latter case with a small transient hot bubble in between.

Interestingly, the reinforcement of the two hot bubbles occurs alternating, which is a consequence of the fact that the downflow flows alternately northward and southward into the cooling layer and thereby heats alternately the northern and southern hot bubble.

The capricious behaviour of the downflow has a simple explanation: Let us look at the situation where the downflow is turning northwards so that we have a strongly heated, strongly expanding, large, northern hot bubble, and a smaller, faltering, southern hot bobble. Roughly speaking the silhouettes of the hot bubbles describe axisymmetric surfaces which have their radial maximum at the poles and smoothly retreat in radius for increasing angle from the pole. The surface of the shock envelops the bubbles at slightly larger radii with cooler, dense shocked material in between. Now we consider an infalling fluid element in the northern hemisphere being halted by the shock. When this fluid element is shocked by the askew shock its velocity component vertical to the shock surface is strongly decreased while the velocity component parallel to the shock remains constant. Thus the fluid element will move with large lateral velocity (we find 10000km/s) towards the equatorial downflow. While moving towards the equator the fluid element will accelerate due to the gravitational pull and will therefore increase both its radial and lateral velocities (latter due to angular momenum conservation). When it reaches the downflow it has accelerated to high lateral velocity so that it has a tendency of ending up near the south pole cooling layer. Of couse, matter falling onto the south pole will experience the opposite lateral acceleration and meet the downflow material from the northern hemisphere at the equatorial downflow. However, as the northern bubble is larger, it extends over the equator. Thus, the matter falling through the askew shock at the equator will also be diverted southwards and the larger lateral momentum of the southward flowing material will win over that of the northward moving material so that the whole material will be pushed down to the neutrinosphere in the southern hemisphere. Later, when the southern hot bubble has expanded due to the strong heating while the northern bubble has stagnated or started retreating the southern bubble will push itself above the northern bubble at the equator and will thus redirect the equatorial infalling matter in the direction of the north pole: the downflow will turn northward.

This mechanism has also been seen in other 2D simulations and even in 3D simulations (L. Scheck, personal communications). This bi-polar instability seems sure to develop. However, it is questionable how strongly we *enforce* this mechanism to develop in our simulation. A true 3D simulation without angular boundary conditions might experience a slower development of this mechanism. By fixing the axis along which the mechanism shall develop we enhance its growth in this direction and completely suppress its growth in all other directions. It is possible that the

formation of these instabilities on different axes might interfere with each other and slow the development of one dominating direction. One argument which weakens this criticism is that even for very small rotation rates the polar axis obtains a physical meaning and the development of the bi-polar instability is likely to be enhanced on this axis and slightly suppressed in other directions. This question can of course only be answered with 3D calculations.

Therefore, we have to be careful with the results of this simulation. It yields a marginal explosion, so that details which could imply a weaker bi-polar instability might retard the time of explosion (and thus quantities such as the final proto neutron star mass and the explosion energy) or even change the explosion to a dud. Still, this model is much more realistic than the exploding model presented in Sec. 3.2.2, where the explosion resulted from an inconsistent treatment of the neutrino transport equations while here the explosion relies on a mechanism which is indeed physical, but whichs strength might be overestimated by the specific geometry of our simulation.

The choice of boundary conditions has proven to decide whether the bi-polar instability is suppressed completely (periodic boundary conditions) or allowed and probably enforced (reflecting boundary conditions). For the $11.2 M_\odot$ progenitor, this makes the difference between a model that marginally fails to explode (s112_64) and a model that barely manages to explode (s112_128_f). The bottomline is that we finally stand on the borderline between failure and success. But the effect which actually ensures successful explosions, i.e. the bi-polar instability (BPI), can only be simulated approximately in two-dimensional simulations, and thus we can not exclude that the success is a result of overestimating this effect. Therefore, to prove that the "delayed neutrino-, convection-, and BPI-driven explosion mechanism" works, we have to wait for three-dimensional calculations.

We turn to the discussion of the global quantities of Model s112_128_f. From Fig. 4.20 we see that the heating efficiency reaches values above 1 in this model. The advection timescale does no longer decrease, and after a time of $\sim \tau_{\mathrm{adv}}$ the heating efficiency starts increasing even more. This means that the neutrino heating, coupled with the bi-polar instability which is an even more efficient energy transport mechanism than the "standard" Ledoux convection, manages to heat material in the gain region sufficiently so that this matter can escape the star. This also can be seen in Fig. 4.24 which shows that the mass of matter with enough energy to escape the gravitational potential is increasing, and the mass of matter which is only weakly bound is increasing quickly. Thus, also the explosion energy is already increasing. In Fig. 4.15 we see that the neutrino luminosity is not yet decreasing, which implies that the mass accretion is not yet being throttled by the explosion. This is a good sign because then the neutrino heating/convective engine can still pump a significant amount of energy into the ejecta.

5 Conclusions

Core collapse supernovae are highly complex phenomena whose theoretical study requires the insight that can be gained by detailed numerical simulations. Even after almost fourty years the mechanism responsible for the explosion is not yet secured knowledge. The simulations made so far leave the impression that the revival of the stalled shock is sensitive to many details. It even seems possible that the conditions needed for explosions require fine-tuning. Or could it be that we are looking in the wrong direction, that we have completely missed a crucial point?

These thoughts of doubt naturally arise whenever success is not achieved for so many decades. However, the discouraged should not forget some important facts: For one, the explosion energy is only a small fraction—few percent—of the gravitational binding energy released during core-collapse. In this sense almost all observed core collapse supernova explosions could be called marginal, the explosion being only a weak side effect of the neutrino emission. If the energy transfer from neutrinos could easily revive the shock we would observe much larger explosion energies. Therefore it should be *expected* that obtaining the right amount of energy transfer is a difficult task.

Current supernova models, even the most sophisticated ones, have deficiencies associated with employed approximations which are known—or at least suspected—to underestimate effects which support shock revival. In other words, the reasons why these simulations do not yield explosions may be guessed. Therefore the obvious course of procedure is to patiently refine the simulations until one can ascertain that no important effects are under- or overestimated. The end of this path promises a deeper understanding of the explosion mechanism. And one should keep in mind that not necessarily all core-collapse events have to lead to explosions, but that a certain fraction of massive stars may well end their lives as black holes formed in a “silent” catastrophic collapse.

In course of this work significant progess has been made towards more realistic and more complete simulations of core collapse supernovae in one and two dimensions.

- With a detailed spectral treatment of neutrino-matter interactions and a reasonably good description of the two-dimensional transport—using a variable Eddington factor technique for describing the radial transport and an approximative handling of the lateral dimension—a new level of accuracy was reached in core collapse modeling.
- Neutrino-matter interactions were improved compared to previous, more schematic or approximative descriptions. Moreover, so far disregarded neutrino processes were included.
- A simple and computationally very efficient approximative treatment of general relativistic effects was developed which was tested to produce very good agreement with fully

relativistic simulations in spherical symmetry (Liebendörfer et al. 2003).

With these features implemented our newly developed neutrino-hydrodynamics code MuD-BaTH is an excellent and currently the most elaborate tool for simulating stellar core collapse in two dimensions.

Simulations were performed for a large variety of progenitors with 11–25 solar masses in spherical symmetry and for a number of these models in two dimensions to study the effects of convection. The results are manifold:

- The simulations confirm that a state-of-the-art treatment of the microphysics, i.e. of the neutrino interactions and of the nuclear equation of state, does not allow for successful explosions in spherical symmetry. This result is in agreement with recent results by other groups (Mezzacappa et al. 2001; Liebendörfer et al. 2001; Thompson et al. 2003), which employed numerically different treatments of the hydrodynamics and neutrino transport. This means that according to our present knowledge multi-dimensional processes are crucial for explaining the explosion of massive stars.

- The two-dimensional models with limited (90°) lateral wedge do not yield explosions and thus cannot confirm previous simulations (Herant et al. 1994; Burrows et al. 1995; Fryer 1999; Fryer & Heger 2000), which obtained explosions by the convectively supported neutrino-driven mechanism in two dimensions but used a much less sophisticated treatment of neutrino transport and neutrino-matter interactions by a grey, i.e. non-spectral, flux-limited diffusion method. Our simulations therefore demonstrate that simulations with such radical simplifications of the neutrino physics have to be taken with great caution. This is also true for the most recent three-dimensional models of Fryer & Warren (2002, 2004) where the same approximations of the transport physics were used.

- A first simulation with a full 180° grid produced a weak explosion, in contrast to the failure of the corresponding run with a 90° wedge. This simulation revealed an interesting phenomenon which could be a new twist in the explosion mechanism of massive stars. In addition to the "standard" Ledoux hot-bubble convection the gain layer developed a new mode of large-scale "bi-polar" instability. This allowed convection to become much stronger and more violent than in the wedge simulation where this large mode was suppressed by artificial (and unphysical) boundary conditions. This result is very encouraging and opens a new perspective for finally successful models of massive star explosions. Simulations for different progenitors are currently underway.

The models also provide information of so far unattained accuracy for the neutrino emission, nucleosynthesis conditions, and gravitational wave emission in core-collapse supernovae. Detailed spectral information of the neutrino signal produced by different progenitors was used to analyze, e.g., the detectability of the electron neutrino burst in a future generation of underground or underwater experiments, also with respect to the possibility of determining yet unknown neutrino properties, e.g. the yet unknown neutrino mixing angle ϑ_{13} (Kachelriess et al. 2004). An explosion model which was produced with a slight, artificial enhancement of the neutrino-energy transfer in the hot-bubble region showed that the matter which is ejected during the early phase of the explosion must be expected to be *proton-rich* and not neutron-rich as thought before. The interesting consequences for supernova nucleosynthesis were evaluated

in a recent paper by Pruet et al. (2004). The over-production problem of $N = 50$ closed neutron shell nuclei seen in previous supernova models is found to be solved. Finally, our models provided the so far most realistic model data for the gravitational wave emission from stellar core collapse events. This information is indispensible for detecting supernova signals in currently built or operative interferometer experiments (LIGO, VIRGO, and GEO600) and the detectability was analyzed in detail in recent papers by Müller et al. (2004) and Buonanno et al. (2004).

Of course this thesis is only one more step towards increasingly more refined, more detailed, and more accurate numerical simulations of core-collapse supernovae. A lot of work remains to be done, also for the exploration of the interesting new perspectives revealed by the presented models. It is clear from this work that an accurate treatment of the neutrino transport and neutrino-matter interactions is indispensable for reliable simulations of core-collapse supernovae and for reliable investigations of the explosion mechanism. A limited wedge in two dimensions constrains the convective modes which are allowed to develop, and the possibly crucial importance of low-mode convective instabilities indicated by our weakly exploding 11.2 solar mass model calls for future simulations in three dimensions.

Reaction			Implementation described in	References
$\nu e^{\pm}$	$\rightleftharpoons$	$\nu e^{\pm}$	Rampp & Janka (2002)	Mezzacappa & Bruenn (1993b); Cernohorsky (1994)
νA	$\rightleftharpoons$	νA	Rampp & Janka (2002)	Horowitz (1997); Bruenn & Mezzacappa (1997)
νN	$\rightleftharpoons$	νN	Sect. A.1	Burrows & Sawyer (1998)
ν_en	$\rightleftharpoons$	e^-p	Sect. A.1	Burrows & Sawyer (1999)
$\bar{\nu}_e$p	$\rightleftharpoons$	e^+n	Sect. A.1	Burrows & Sawyer (1999)
$\nu_e A'$	$\rightleftharpoons$	$e^- A$	Rampp & Janka (2002)	Bruenn (1985); Mezzacappa & Bruenn (1993c)
$\nu\bar{\nu}$	$\rightleftharpoons$	e^-e^+	Rampp & Janka (2002)	Bruenn (1985); Pons et al. (1998)
$\nu\bar{\nu}$NN	$\rightleftharpoons$	NN	Rampp & Janka (2002)	Hannestad & Raffelt (1998)
$\nu_{\mu,\tau}\bar{\nu}_{\mu,\tau}$	$\rightleftharpoons$	$\nu_e\bar{\nu}_e$	Buras et al. (2003)	see Buras et al. (2003)
$\overset{(-)}{\nu}_{\mu,\tau}\overset{(-)}{\nu}_e$	$\rightleftharpoons$	$\overset{(-)}{\nu}_{\mu,\tau}\overset{(-)}{\nu}_e$	Buras et al. (2003)	see Buras et al. (2003)

Table A.1: Overview of all neutrino-matter interactions currently implemented in the code. For each process we list the sections or point to references where the fundamental aspects of the calculation of the corresponding rate are summarized and details of its numerical implementation are given. The references in the third column point to papers where more information can be found about the physics and the approximations employed in the rate calculations. In the first column the symbol ν represents any of the neutrinos ν_e, $\bar{\nu}_e$, ν_μ, $\bar{\nu}_\mu$, ν_τ, $\bar{\nu}_\tau$, the symbols e^-, e^+, n, p, and A denote electrons, positrons, free neutrons and protons, and heavy nuclei, respectively, the symbol N means n or p.

A Neutrino opacities

Our set of so-called "standard" neutrino opacities closely follows the conventional description as introduced by Bruenn (1985) and Mezzacappa & Bruenn (1993a,b) with the only exception that we in addition take into account neutrino pair processes due to nucleon-nucleon bremsstrahlung. A complete list of reactions, corresponding pointers to the literature and details of the numerical implementation into our transport code can be found in the appendix of Rampp & Janka (2002).

The "improved description" of neutrino opacities that is used in our latest simulations is summarized in Table A.1. Specifically, the so-called iso-energetic or elastic approximation (cf. Bruenn 1985; Reddy et al. 1998), which the standard description for calculating rates of neutral-current neutrino scatterings off free nucleons and the corresponding charged-current absorption reactions relies on has been abandoned in order to take into account energy exchange due to recoil

and thermal motion of the nucleons as well as nucleon-nucleon correlations in the dense medium (Burrows & Sawyer 1998, 1999; Reddy et al. 1998, 1999). Modifications of the neutrino opacities which are due to the weak magnetism of the nucleon are also accounted for (cf. Horowitz 2002). We employ a density dependent effective mass of the nucleon which, at nuclear densities, is different from its free value and also take into account the effect of a possible quenching of the axial coupling in nuclear matter (Carter & Prakash 2002) on the neutrino opacities.

In the following we shall describe the numerical handling of these neutrino-matter interactions in some detail. Note that our list of considered interactions also contains the purely neutrinic reaction channels (last two lines of table A.1) which before have received only little attention from core-collapse supernova modellers. Their significance as well as their numerical implementation is discussed elsewhere (Buras et al. 2003).

A.1 Neutrino-nucleon interactions

A.1.1 Neutrino-nucleon scattering ($\nu\mathrm{N} \rightleftharpoons \nu\mathrm{N}$)

Differential rates for inelastic scattering of neutrinos off free nucleons are calculated according to Eq. (38) of Burrows & Sawyer (1998). For incorporating this type of neutrino-matter interactions into our transport code the formalism developed for inelastic scattering of neutrinos off electrons (NES) can be exploited (see Rampp & Janka 2002, Appendix A). Different from NES, however, the angular integration (let ω denote the cosine of the scattering angle) of the scattering kernels $R(\epsilon, \epsilon', \omega)$ to yield the coefficients $\phi_l(\epsilon, \epsilon')$ of the corresponding Legendre expansion (cf. Bruenn 1985, Appendix C) cannot be performed analytically in the case of neutrino-nucleon scattering. Moreover, the characteristic width of the kernels as a function of in and outgoing neutrino energies ϵ, ϵ' can be small (but finite) compared with the numerical resolution of the neutrino spectrum in the transport scheme, in which typically only about 20 energy bins with a resolution of $\Delta\epsilon/\epsilon \simeq 0.3$ can be afforded. Hence, in order to adequately sample the scattering kernels on such a coarse energy grid it is not sufficient to simply evaluate the functions $\phi_l(\epsilon, \epsilon')$ at each combination of energies $(\epsilon_{j+\frac{1}{2}}, \epsilon_{j'+\frac{1}{2}})$. Instead, we introduce for each energy bin $[\epsilon_j, \epsilon_{j+1}]$ a numerical subgrid of $N_{\epsilon j}$ neutrino energies $\epsilon_j \le \epsilon \le \epsilon_{j+1}$ and N_ω angle cosines $-1 \le \omega \le 1$ and compute $R(\epsilon, \epsilon', \omega)$ as given by Burrows & Sawyer (1998, Eq. 38) for all such combinations of ϵ, ϵ' and ω. For fixed values of ϵ and ϵ' we numerically integrate $R(\epsilon, \epsilon', \omega)$, appropriately weighted with the Legendre polynomials $P_l(\omega)$ over angles to yield $\phi_l(\epsilon, \epsilon')$. Averaging $\phi_l(\epsilon, \epsilon')$ over the energy bins $[\epsilon_j, \epsilon_{j+1}]$ and $[\epsilon_{j'}, \epsilon_{j'+1}]$ the final, binned Legendre coefficients $\phi_l(\epsilon_{j+\frac{1}{2}}, \epsilon_{j'+\frac{1}{2}})$ which are used in our neutrino transport scheme are obtained. In practice a six-point Gauss-quadrature scheme is used for the numerical integrations within each of the spectral and angular bins. In order to correctly reproduce the low-density limit, where only tiny energy transfers $\epsilon - \epsilon'$ between neutrino and nucleon occur and the coefficients ϕ_l become increasingly narrowly peaked functions of $\epsilon - \epsilon'$, we calculate ϕ_l according to the (analytically tractable) iso-energetic approximation (Bruenn 1985; Reddy et al. 1998) if the density drops below 10^8 g cm^{-3}. Note that evaluating Eq. (38) of Burrows & Sawyer (1998) requires the knowledge of nucleon-nucleon interaction potentials. Within the framework pursued by Burrows & Sawyer (1998) the latter can be expressed in terms of the Fermi-liquid parameters, which, in turn, are directly related to macroscopic observables such as the incompressibility K_s

or the symmetry energy S_v of bulk nuclear matter (see Reddy et al. 1999). Accordingly, we select values for the Fermi-liquid parameters which are consistent with the parameters chosen for the nuclear EoS we use for our simulations (Lattimer & Swesty 1991, with K_s = 180 MeV, S_v = 29.3 MeV).

Once the Legendre coefficients ϕ_0 and ϕ_1 are known the contribution of neutrino-nucleon scattering to the collision integral of the Boltzmann equation and its angular moments is calculated in exactly the same way as described for NES in Rampp & Janka (2002, Appendix A).

A.1.2 Absorption of electron-flavour neutrinos by free nucleons

($\nu_e n \rightleftharpoons e^- p$, $\bar{\nu}_e p \rightleftharpoons e^+ n$)

The calculation of the inverse mean free path $1/\lambda(\epsilon)$ for absorption of electron (anti)neutrinos by free neutrons (protons) is based on Eq. (2) of Burrows & Sawyer (1999). For the numerical implementation we employ the same techniques that we have already described for the neutral-current reactions in Sect. A.1.1. Different from neutrino-nucleon scattering, however, the outgoing lepton is a charged lepton, which, in our context is assumed to be in local thermodynamical equilibrium with the stellar medium. Hence no dependence of the scattering kernels on the energy ϵ' of the outgoing lepton needs to be retained and the averages over the energy bins $[\epsilon_{j'}, \epsilon_{j'+1}]$ are consequently replaced by an integral over the entire spectrum of energies ϵ' of the outgoing charged lepton. Given $1/\lambda(\epsilon)$, the absorption opacity corrected for stimulated absorption $\kappa^*(\epsilon)$ which enters our neutrino transport scheme can be calculated straightforwardly (cf. Rampp & Janka 2002, Appendix A).

A.1.3 Effective mass of the nucleons

Following Burrows & Sawyer (1999) we substitute an effective mass m^* for the nucleon mass m, wherever the latter appears explicitly in the formalism. Notably m^* is also used for inverting the particle density-chemical potential relation in order to compute the chemical potentials of protons and nucleons (including interaction potentials) for given number densities (cf. Burrows & Sawyer 1998, Eq. 11).

For the effective mass we adopt the density dependence (Reddy et al. 1999)

$$m^*(\rho) = \frac{m}{1 + \alpha \cdot \rho/\rho_{\rm nuc}}\,, \tag{A.1}$$

where the constant α is defined by the value of the effective mass at nuclear saturation density ($\rho_{\rm nuc}/m = 0.16\,{\rm fm}^{-3}$) being $m^*(\rho_{\rm nuc}) = 0.8\,m$.

A.1.4 Weak magnetism corrections

Correction factors for the iso-energetic cross-sections describing both weak magnetism and recoil effects of the nucleon are provided are provided by Horowitz (2002). Both effects appear at the level of $O(\epsilon/m)$ with ϵ being the neutrino energy and m the nucleon mass. For our

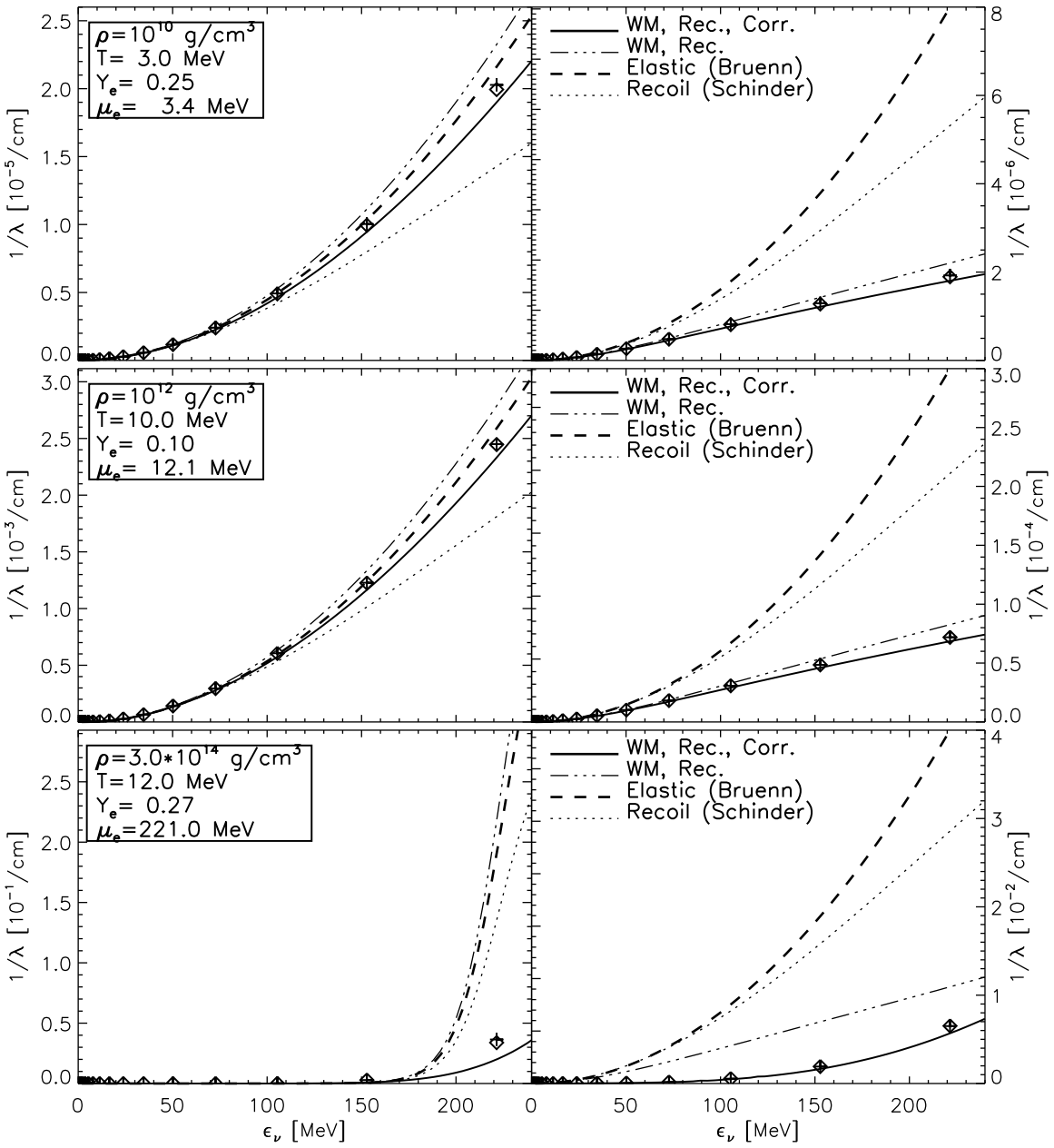

Figure A.1: Cross section as function of neutrino energy for absorption of ν_e (left column) and $\bar{\nu}_e$ (right column) by free nucleons. Note the different scale of the ordinates. The bold lines show the comparison between the "standard description" (dashed) and our "improved description". Thermodynamic conditions are given in the top left corners of the plots. For given density effective values for the nucleon mass m^* and the axial coupling g_A^* were calculated using Eq. (A.1) and Eq. (A.9), respectively. Thin dashed-dotted lines show the weak-magnetism plus recoil correction of Horowitz (2002) applied to the iso-energetic cross section of Bruenn (1985) which is drawn as a dashed line. The dotted lines correspond to the recoil and thermal motion approximation of Schinder (1990). In all cases neutrino phase-space was assumed to be empty. Lines connect values computed on an energy grid of 100 points which are linearly spaced between 0 and 380 MeV. For comparison, crosses show the improved rates on a geometrical energy grid with 17 bins and six-point Gauss-quadratures for the angular and spectral intergrations (relevant for the improved description; see text). This is the typical spectral resolution of our dynamical supernova simulations. Results obtained by using 30-point Gauss-quadratures instead are displayed by open diamonds.

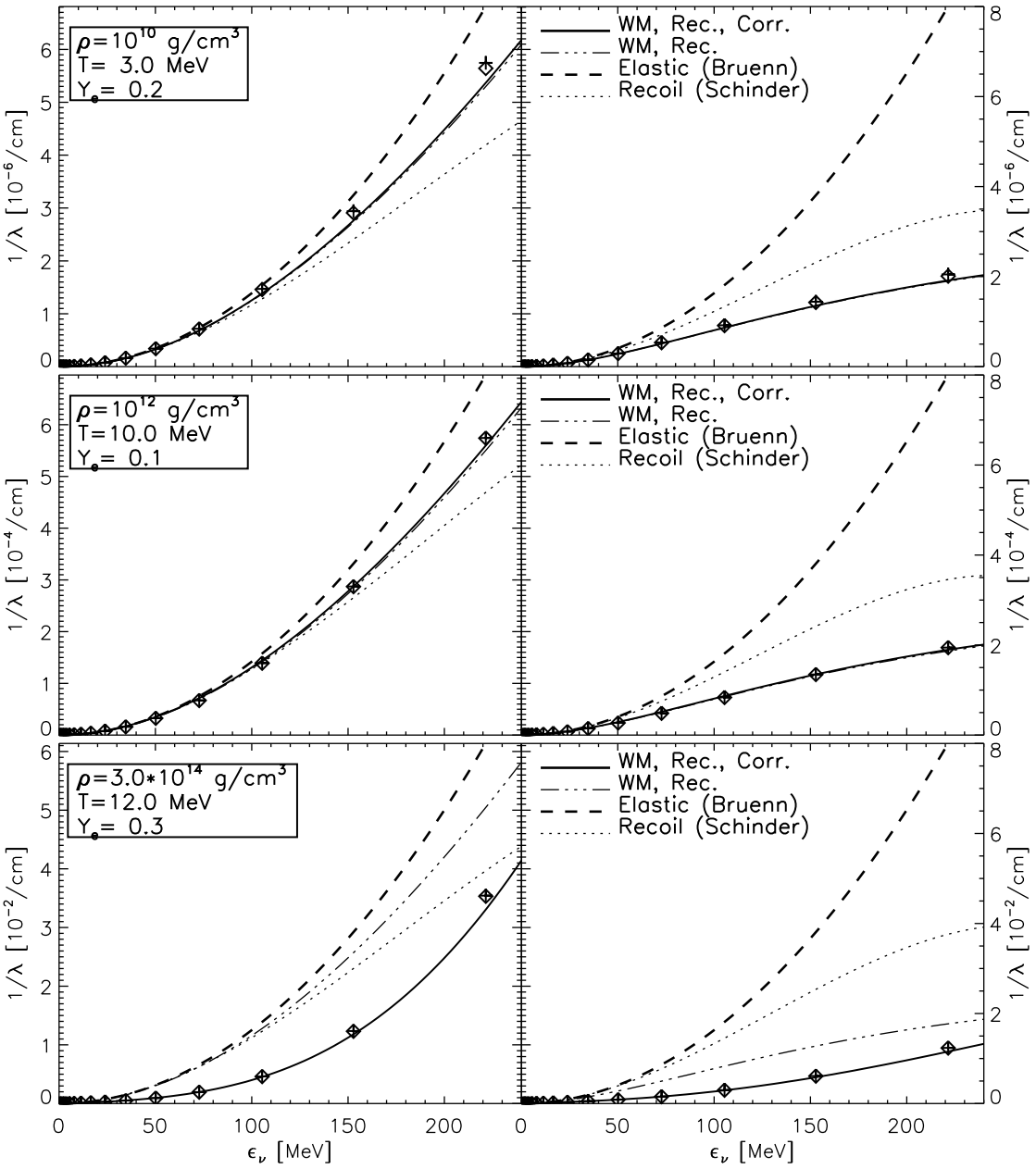

Figure A.2: Same as Figure A.1 but showing the corresponding neutral-current scattering cross sections of neutrinos (left column) and antineutrinos (right column). In order to obtain the quantity $1/\lambda(\epsilon)$ the differential scattering rate $R(\epsilon, \epsilon', \omega)$ was integrated over all angle cosines ω and final neutrino energies ϵ'.

purposes, however, we have to disentangle the contributions of both effects to the final rates in order to obtain a pure weak-magnetism correction for the formalism described above, which already includes recoil and also nucleon-nucleon correlations but unfortunately disregards weak magnetism. This is achieved by analytically averaging the differential rates which include weak magnetism as well as recoil and those for recoil alone over the scattering angle and using the resulting angle-independent ratio as the weak-magnetism correction to the rates of Burrows & Sawyer (1998, 1999). For the charged-current reactions the angular reduction is performed by simply integrating the differential rates over all angles between the momenta of the neutrino and the charged lepton while for the neutral current scatterings a $(1-\omega)$-weighting is used. The latter is motivated by the definition of the transport opacity (for details, see Horowitz 2002).

The Legendre coefficients for neutral-current scatterings as described in Sect. A.1.1 are finally modified according to $\phi_l^{\mathrm{out}}(\epsilon,\epsilon') \rightarrow \xi^{\mathrm{nc}}(\epsilon)\cdot\phi_l^{\mathrm{out}}(\epsilon,\epsilon')$, where

$$\xi^{\mathrm{nc}}(\epsilon) \equiv \frac{n_{\mathrm{n}}\cdot\mathcal{X}^{\mathrm{nc:n}}_{\mathrm{WM,Rec.}}(\epsilon) + n_{\mathrm{p}}\cdot\mathcal{X}^{\mathrm{nc:p}}_{\mathrm{WM,Rec.}}(\epsilon)}{n_{\mathrm{n}}\cdot\mathcal{X}^{\mathrm{nc:n}}_{\mathrm{Rec.}}(\epsilon) + n_{\mathrm{p}}\cdot\mathcal{X}^{\mathrm{nc:p}}_{\mathrm{Rec.}}(\epsilon)} \tag{A.2}$$

is the ratio of the full correction factor (Horowitz 2002, Eq. 32)

$$\begin{aligned}
&\mathcal{X}^{\mathrm{nc:n/p}}_{\mathrm{WM,Rec.}}(\epsilon) = \\
&= \left\{ C_{\mathrm{V}}^2\left[\frac{e-1}{2e^3}\ln\zeta + \frac{3+12e+9e^2-10e^3}{3e^2\,(\zeta)^3}\right] + C_{\mathrm{A}}^2\left[\frac{1+e}{2e^3}\ln\zeta - \frac{10e^3+27e^2+18e+3}{3e^2\zeta^3}\right]\right. \\
&\pm (C_{\mathrm{V}}+F_2)\,C_{\mathrm{A}}\left[\frac{1}{e^2}\ln(\zeta) - \frac{2+10e+\frac{28}{3}e^2}{e\zeta^3}\right] + C_{\mathrm{V}}F_2\left[\frac{1}{e^2}\ln\zeta - \frac{2}{3}\left(\frac{3+15e+22e^2}{e\zeta^3}\right)\right] \\
&\left. +F_2^2\left[\frac{1}{4e^2}\ln\zeta + \frac{8e^3-22e^2-15e-3}{6e\zeta^3}\right]\right\} \Bigg/ \left\{\frac{2}{3}\left(C_{\mathrm{V}}^2+5C_{\mathrm{A}}^2\right)\right\}\,,
\end{aligned} \tag{A.3}$$

and the correction factor for recoil alone

$$\mathcal{X}^{\mathrm{nc:n/p}}_{\mathrm{Rec.}} = \left\{ C_{\mathrm{V}}^2\left[\frac{e+1}{e^3}\ln\zeta - \frac{2}{e^2}\right] + C_{\mathrm{A}}^2\left[\frac{2e^2-1-e}{e^3}\ln\zeta + \frac{2}{e^2\zeta}\right]\right\} \Bigg/ \left\{\frac{2}{3}(C_{\mathrm{V}}^2+5C_{\mathrm{A}}^2)\right\}\,, \tag{A.4}$$

In Eqs. (A.3, A.4) we have used the abbreviations

$$e(\epsilon) \equiv \frac{\epsilon}{m\,c^2}, \qquad \text{and} \qquad \zeta(e) \equiv 1+2e\,. \tag{A.5}$$

Numerical values of the coupling constants C_{V}, C_{A} and F_2 can be found in Horowitz (2002, Table I). Since the values of C_{V}, C_{A} and F_2 are different for the reactions $\nu\mathrm{p} \rightleftharpoons \nu\mathrm{p}$ and $\nu\mathrm{n} \rightleftharpoons \nu\mathrm{n}$ the individual correction factors for protons $\mathcal{X}^{\mathrm{nc:p}}$ and neutrons $\mathcal{X}^{\mathrm{nc:n}}$ are weighted with the corresponding number densities n_{n} and n_{p}, respectively, to yield the final correction factor ξ^{nc} for neutral-current scatterings (Eq. A.2). Given $\phi_l^{\mathrm{out}}(\epsilon,\epsilon')$, detailed balance arguments (see Cernohorsky 1994) are exploited to compute the coefficient $\phi_l^{\mathrm{in}}(\epsilon,\epsilon')$ corresponding to the inverse reaction (for details, see Rampp & Janka 2002, Appendix A).

Analogously one modifies the inverse mean free path for charged-current reactions (see Sect. A.1.2) according to $1/\lambda(\epsilon) \rightarrow \xi^{\mathrm{cc}}(\epsilon)\cdot 1/\lambda(\epsilon)$, where

$$\xi^{\mathrm{cc}}(\epsilon) \equiv \frac{\mathcal{X}^{\mathrm{cc}}_{\mathrm{WM,Rec.}}(\epsilon)}{\mathcal{X}^{\mathrm{cc}}_{\mathrm{Rec.}}(\epsilon)}\,, \tag{A.6}$$

with

$$\chi^{\rm cc}_{\rm WM,Rec.}(\epsilon) = \left\{ C_{\rm V}^2 \left(1 + 4e + \frac{16}{3}e^2\right) + 3C_{\rm A}^2 \left(1 + \frac{4}{3}e\right)^2 \pm 4\,(C_{\rm V} + F_2)\,C_{\rm A} e \left(1 + \frac{4}{3}e\right) \right.$$
$$\left. + \frac{8}{3} C_{\rm V} F_2 e^2 + \frac{5}{3} e^2 \left(1 + \frac{2}{5}e\right) F_2^2 \right\} \Big/ \left\{ \left(C_{\rm V}^2 + 3C_{\rm A}^2\right)(1 + 2e)^3 \right\} , \qquad \text{(A.7)}$$

as given by Horowitz (2002, Eq. 22), and

$$\chi^{\rm cc}_{\rm Rec.}(\epsilon) = \left\{ C_{\rm V}^2 \left[\frac{1}{e} - \frac{1}{e^2} \ln\zeta \right] + C_{\rm A}^2 \left[\frac{4e^2 - 2e + \zeta \ln\zeta}{2e^2\zeta} \right] \right\} \Big/ \left\{ C_{\rm V}^2 + 3C_{\rm A}^2 \right\} . \qquad \text{(A.8)}$$

The ±-symbol in Eqs. (A.3, A.7) refers to a positive sign for neutrinos and a negative sign for antineutrinos, respectively. In our transport method, we presently do not discriminate between $\nu_{\mu,\tau}$ and the corresponding antiparticles. For these flavours we therefore take the particle/antiparticle average of Eqs. (A.3, A.7), respectively, which in effect means that all terms that are multiplied by the ±-symbol vanish for the heavy-lepton neutrinos.

Recall that we switch from the description of Burrows & Sawyer (1998, 1999) to the iso-energetic approximation (Bruenn 1985) if $\rho < 10^8$ g cm^{-3} (see Sect. A.1.1). Consequently, in order to take into account nucleon recoil and weak-magnetism also for these conditions the correction factors defined in Eqs. (A.2, A.6) are replaced by $\xi^{\rm nc} = (n_{\rm n} \cdot \chi^{\rm nc:n}_{\rm WM,Rec.} + n_{\rm p} \cdot \chi^{\rm nc:p}_{\rm WM,Rec.})/(n_{\rm n} + n_{\rm p})$, and $\xi^{\rm cc} = \chi^{\rm cc}_{\rm WM,Rec.}$, respectively, wherever the density falls short of 10^8 g cm^{-3}.

A.2 Quenching of the axial coupling

In the calculations of all neutrino-matter interactions we replace the axial coupling $g_{\rm A} = 1.254$ by an effective, "quenched" value $g_{\rm A}^*$ which depends on the baryon density and is given by Carter & Prakash (2002, Eq. 13):

$$g_{\rm A}^*(\rho) = g_{\rm A} \left(1 - \frac{\rho}{4.15\,(\rho_{\rm nuc} + \rho)}\right) . \qquad \text{(A.9)}$$

In effect, opacities are reduced by a factor $(g_{\rm A}^*/g_{\rm A})^2$ at densities $\rho \gtrsim \rho_{\rm nuc}$.

A.3 Discussion

In Figures A.1, A.2 opacities for neutrino-nucleon interactions computed with the procedures described above are compared with the iso-energetic approximation adopted by Bruenn (1985) and the description of Schinder (1990). The latter work approximately takes into account the reaction kinematics (recoil, thermal motions and final-state blocking of the nucleons) but disregards weak magnetism and nucleon-nucleon correlations. According to our core-collapse simulations for the 15 $M_\odot$ star the chosen combinations of values for the density ρ, temperature T, and electron fraction $Y_{\rm e}$ of the stellar medium are roughly characteristic for the conditions in

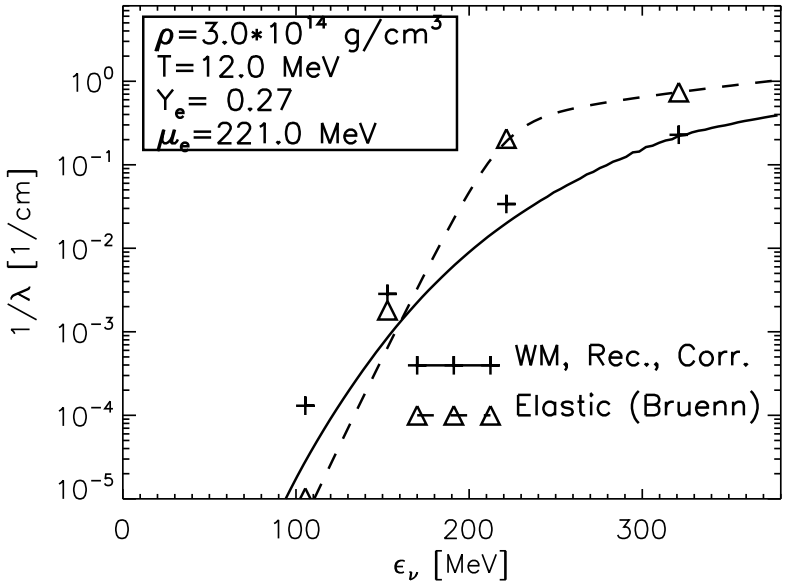

Figure A.3: Cross section for absorption of ν_e by free neutrons for the conditions given in the last row of Fig. A.1. The solid (improved description) and dashed (standard description) lines show reference solutions which were obtained with high spectral resolution (see Fig. A.1). The result of averaging the rates over the comparably coarse bins of the energy grid used in dynamical simulations results in rates shown by crosses (improved description) and open triangles (standard description).

the gain layer, where neutrino heating is strongest (top rows of Figs. A.1, A.2), the region where most of the neutrino luminosity is produced (middle rows), and the interior of the forming proto neutron star (bottom rows).

As discussed in detail by Horowitz (2002) the effects of weak-magnetism and recoil of the nucleons counterbalance each other for ν_e while in the case of $\bar{\nu}_e$ both add up leading to an appreciable net reduction of the standard opacities (computed according to Bruenn 1985). This can be seen in Figs. A.1, A.2 by comparing the bold, dashed lines with the thin, dashed-dotted lines. While the size of the weak-magnetism and recoil effects is independent of the density the additional reduction of both ν_e and $\bar{\nu}_e$ opacities due to nucleon-nucleon correlations shows up only at nuclear densities (see Burrows & Sawyer 1998, 1999; Reddy et al. 1998, 1999; Horowitz 2002, for a thorough discussion).

Employing the averaging procedure described in Sects. A.1.1, A.1.2 we calculated energy-averaged cross sections for a numerical energy grid with a resolution that is typically used in our dynamical supernova simulations. The results are shown by crosses drawn at the centres of the energy bins. Notable deviations from the reference solutions show up only in the vicinity of large opacity gradients which arise, e.g., due to final state blocking of the degenerate electron gas in the reaction $\nu_e + n \rightarrow e^- + n$ (see Fig. A.3). Note, however, that this phenomenon is not specific to our improved physical description (see the open triangles in Fig. A.3).

Increasing the number of quadrature weights for the numerical integrations within the spectral and angular bins by a factor of five each, i.e. employing 30-point Gauss-quadratures (open diamonds in Figs. A.1, A.2), we find good agreement with the standard six-point results (crosses

in Figs. A.1, A.2).

B Moments equations in three dimensions

To order $O(v/c)$ of the fluid velocities (the so-called Newtonian approximation) the full three-dimensional moments equations are given by (Kaneko et al. 1984, correcting a number of misprints):

$$\frac{\rho}{c}\frac{D}{Dt}\left(\frac{J}{\rho}\right)+\nabla\cdot\mathbf{H}+\frac{1}{c}\frac{\partial}{\partial t}(\boldsymbol{\beta}\cdot\mathbf{H})-\frac{\epsilon}{c}\frac{\partial\boldsymbol{\beta}}{\partial t}\cdot\frac{\partial\mathbf{H}}{\partial\epsilon}-\epsilon\nabla\boldsymbol{\beta}:\frac{\partial\mathbf{P}}{\partial\epsilon}=C^{(0)} \tag{B.1}$$

$$\frac{\rho}{c}\frac{D}{Dt}\left(\frac{\mathbf{H}}{\rho}\right)+\nabla\cdot\mathbf{P}+\mathbf{H}\cdot\nabla\boldsymbol{\beta}+\frac{1}{c}\frac{\partial}{\partial t}(\boldsymbol{\beta}\cdot\mathbf{P})+\frac{J}{c}\frac{\partial\boldsymbol{\beta}}{\partial t}-\frac{1}{c}\frac{\partial\boldsymbol{\beta}}{\partial t}\cdot\frac{\partial(\epsilon\mathbf{P})}{\partial\epsilon}-\nabla\boldsymbol{\beta}:\frac{\partial(\epsilon\mathbf{N})}{\partial\epsilon}=\mathbf{C}^{(1)}, \tag{B.2}$$

where $\boldsymbol{\beta}=\boldsymbol{v}/c$. In general spherical coordinates, the moments are defined by

$$J=\frac{1}{4\pi}\int\int I d\Omega,\ \mathbf{H}=\frac{1}{4\pi}\int\int I\mathbf{n}d\Omega,\ \mathbf{P}=\frac{1}{4\pi}\int\int I\mathbf{nn}d\Omega,\ \mathbf{N}=\frac{1}{4\pi}\int\int I\mathbf{nnn}d\Omega. \tag{B.3}$$

Here, $\mathbf{n}=(n_r,n_\vartheta,n_\varphi)=(\cos\Theta,\sin\Theta\cos\omega,\sin\Theta\sin\omega)$, $\mu=\cos\Theta$, and Θ and ω are the two angles defining the direction of propagation. The moments equations written in coordinate form are the following:

$$\begin{aligned}
&\frac{\rho}{c}\frac{D}{Dt}\left(\frac{J}{\rho}\right)+\frac{1}{r^2}\frac{\partial(r^2H_r)}{\partial r}+\frac{1}{r\sin\vartheta}\frac{\partial(\sin\vartheta H_\vartheta)}{\partial\vartheta}+\frac{1}{r\sin\vartheta}\frac{\partial H_\varphi}{\partial\varphi}+\frac{1}{c}\frac{\partial}{\partial t}\left(\beta_rH_r+\beta_\vartheta H_\vartheta+\beta_\varphi H_\varphi\right)\\
&-\frac{\epsilon}{c}\left(\frac{\partial\beta_r}{\partial t}\frac{\partial H_r}{\partial\epsilon}+\frac{\partial\beta_\vartheta}{\partial t}\frac{\partial H_\vartheta}{\partial\epsilon}+\frac{\partial\beta_\varphi}{\partial t}\frac{\partial H_\varphi}{\partial\epsilon}\right)\\
&-\epsilon\left\{\frac{\partial P_{rr}}{\partial\epsilon}\left(\frac{\partial\beta_r}{\partial r}\right)+\frac{\partial P_{\vartheta r}}{\partial\epsilon}\left(\frac{1}{r}\frac{\partial\beta_r}{\partial\vartheta}-\frac{\beta_\vartheta}{r}\right)+\frac{\partial P_{\varphi r}}{\partial\epsilon}\left(\frac{1}{r\sin\vartheta}\frac{\partial\beta_r}{\partial\varphi}-\frac{\beta_\varphi}{r}\right)\right.\\
&+\frac{\partial P_{r\vartheta}}{\partial\epsilon}\left(\frac{\partial\beta_\vartheta}{\partial r}\right)+\frac{\partial P_{\vartheta\vartheta}}{\partial\epsilon}\left(\frac{1}{r}\frac{\partial\beta_\vartheta}{\partial\vartheta}+\frac{\beta_r}{r}\right)+\frac{\partial P_{\varphi\vartheta}}{\partial\epsilon}\left(\frac{1}{r\sin\vartheta}\frac{\partial\beta_\vartheta}{\partial\varphi}-\frac{\beta_\varphi\cos\vartheta}{r\sin\vartheta}\right)\\
&\left.+\frac{\partial P_{r\varphi}}{\partial\epsilon}\left(\frac{\partial\beta_\varphi}{\partial r}\right)+\frac{\partial P_{\vartheta\varphi}}{\partial\epsilon}\left(\frac{1}{r}\frac{\partial\beta_\varphi}{\partial\vartheta}\right)+\frac{\partial P_{\varphi\varphi}}{\partial\epsilon}\left(\frac{1}{r\sin\vartheta}\frac{\partial\beta_\varphi}{\partial\varphi}+\frac{\beta_r}{r}+\frac{\beta_\vartheta\cos\vartheta}{r\sin\vartheta}\right)\right\}=C^{(0)},
\end{aligned} \tag{B.4}$$

$$\frac{\rho}{c}\frac{D}{Dt}\left(\frac{H_r}{\rho}\right)-\frac{H_\vartheta\beta_\vartheta}{r}-\frac{H_\varphi\beta_\varphi}{r}+\frac{2}{r}P_{rr}+\frac{\partial P_{rr}}{\partial r}+\frac{\cos\vartheta}{r\sin\vartheta}P_{\vartheta r}+\frac{1}{r}\frac{\partial P_{\vartheta r}}{\partial\vartheta}+\frac{1}{r\sin\vartheta}\frac{\partial P_{\varphi r}}{\partial\varphi}-\frac{P_{\vartheta\vartheta}+P_{\varphi\varphi}}{r}$$
$$+H_r\left(\frac{\partial\beta_r}{\partial r}\right)+H_\vartheta\left(\frac{1}{r}\frac{\partial\beta_r}{\partial\vartheta}-\frac{\beta_\vartheta}{r}\right)+H_\varphi\left(\frac{1}{r\sin\vartheta}\frac{\partial\beta_r}{\partial\varphi}-\frac{\beta_\varphi}{r}\right)$$
$$+\frac{1}{c}\frac{\partial}{\partial t}\left(\beta_rP_{rr}+\beta_\vartheta P_{\vartheta r}+\beta_\varphi P_{\varphi r}\right)+\frac{J}{c}\frac{\partial\beta_r}{\partial t}-\frac{1}{c}\frac{\partial\beta_r}{\partial t}\frac{\partial(\epsilon P_{rr})}{\partial\epsilon}-\frac{1}{c}\frac{\partial\beta_\vartheta}{\partial t}\frac{\partial(\epsilon P_{\vartheta r})}{\partial\epsilon}-\frac{1}{c}\frac{\partial\beta_\varphi}{\partial t}\frac{\partial(\epsilon P_{\varphi r})}{\partial\epsilon}$$
$$-\left\{\frac{\partial(\epsilon N_{rrr})}{\partial\epsilon}\left(\frac{\partial\beta_r}{\partial r}\right)+\frac{\partial(\epsilon N_{r\vartheta r})}{\partial\epsilon}\left(\frac{1}{r}\frac{\partial\beta_r}{\partial\vartheta}-\frac{\beta_\vartheta}{r}\right)+\frac{\partial(\epsilon N_{r\varphi r})}{\partial\epsilon}\left(\frac{1}{r\sin\vartheta}\frac{\partial\beta_r}{\partial\varphi}-\frac{\beta_\varphi}{r}\right)\right.$$
$$+\frac{\partial(\epsilon N_{\vartheta rr})}{\partial\epsilon}\left(\frac{\partial\beta_\vartheta}{\partial r}\right)+\frac{\partial(\epsilon N_{\vartheta\vartheta r})}{\partial\epsilon}\left(\frac{1}{r}\frac{\partial\beta_\vartheta}{\partial\vartheta}+\frac{\beta_r}{r}\right)+\frac{\partial(\epsilon N_{\vartheta\varphi r})}{\partial\epsilon}\left(\frac{1}{r\sin\vartheta}\frac{\partial\beta_\vartheta}{\partial\varphi}-\frac{\beta_\varphi\cos\vartheta}{r\sin\vartheta}\right)$$
$$\left.+\frac{\partial(\epsilon N_{\varphi rr})}{\partial\epsilon}\left(\frac{\partial\beta_\varphi}{\partial r}\right)+\frac{\partial(\epsilon N_{\varphi\vartheta r})}{\partial\epsilon}\left(\frac{1}{r}\frac{\partial\beta_\varphi}{\partial\vartheta}\right)+\frac{\partial(\epsilon N_{\varphi\varphi r})}{\partial\epsilon}\left(\frac{1}{r\sin\vartheta}\frac{\partial\beta_\varphi}{\partial\varphi}+\frac{\beta_r}{r}+\frac{\beta_\vartheta\cos\vartheta}{r\sin\vartheta}\right)\right\}=C_r^{(1)},\quad\text{(B.5)}$$

$$\frac{\rho}{c}\frac{D}{Dt}\left(\frac{H_\vartheta}{\rho}\right)-\frac{H_r\beta_\vartheta}{r}+\frac{H_\varphi\beta_\varphi\cos\vartheta}{r\sin\vartheta}+\frac{3}{r}P_{r\vartheta}+\frac{\partial P_{r\vartheta}}{\partial r}+\frac{\cos\vartheta}{r\sin\vartheta}P_{\vartheta\vartheta}+\frac{1}{r}\frac{\partial P_{\vartheta\vartheta}}{\partial\vartheta}+\frac{1}{r\sin\vartheta}\frac{\partial P_{\varphi\vartheta}}{\partial\varphi}$$
$$-\frac{P_{\varphi\varphi}\cos\vartheta}{r\sin\vartheta}$$
$$+H_r\left(\frac{\partial\beta_\vartheta}{\partial r}\right)+H_\vartheta\left(\frac{1}{r}\frac{\partial\beta_\vartheta}{\partial\vartheta}+\frac{\beta_r}{r}\right)+H_\varphi\left(\frac{1}{r\sin\vartheta}\frac{\partial\beta_\vartheta}{\partial\varphi}-\frac{\beta_\varphi\cos\vartheta}{r\sin\vartheta}\right)$$
$$+\frac{1}{c}\frac{\partial}{\partial t}\left(\beta_rP_{r\vartheta}+\beta_\vartheta P_{\vartheta\vartheta}+\beta_\varphi P_{\varphi\vartheta}\right)+\frac{J}{c}\frac{\partial\beta_\vartheta}{\partial t}-\frac{1}{c}\frac{\partial\beta_r}{\partial t}\frac{\partial(\epsilon P_{r\vartheta})}{\partial\epsilon}-\frac{1}{c}\frac{\partial\beta_\vartheta}{\partial t}\frac{\partial(\epsilon P_{\vartheta\vartheta})}{\partial\epsilon}-\frac{1}{c}\frac{\partial\beta_\varphi}{\partial t}\frac{\partial(\epsilon P_{\varphi\vartheta})}{\partial\epsilon}$$
$$-\left\{\frac{\partial(\epsilon N_{rr\vartheta})}{\partial\epsilon}\left(\frac{\partial\beta_r}{\partial r}\right)+\frac{\partial(\epsilon N_{r\vartheta\vartheta})}{\partial\epsilon}\left(\frac{1}{r}\frac{\partial\beta_r}{\partial\vartheta}-\frac{\beta_\vartheta}{r}\right)+\frac{\partial(\epsilon N_{r\varphi\vartheta})}{\partial\epsilon}\left(\frac{1}{r\sin\vartheta}\frac{\partial\beta_r}{\partial\varphi}-\frac{\beta_\varphi}{r}\right)\right.$$
$$+\frac{\partial(\epsilon N_{\vartheta r\vartheta})}{\partial\epsilon}\left(\frac{\partial\beta_\vartheta}{\partial r}\right)+\frac{\partial(\epsilon N_{\vartheta\vartheta\vartheta})}{\partial\epsilon}\left(\frac{1}{r}\frac{\partial\beta_\vartheta}{\partial\vartheta}+\frac{\beta_r}{r}\right)+\frac{\partial(\epsilon N_{\vartheta\varphi\vartheta})}{\partial\epsilon}\left(\frac{1}{r\sin\vartheta}\frac{\partial\beta_\vartheta}{\partial\varphi}-\frac{\beta_\varphi\cos\vartheta}{r\sin\vartheta}\right)$$
$$\left.+\frac{\partial(\epsilon N_{\varphi r\vartheta})}{\partial\epsilon}\left(\frac{\partial\beta_\varphi}{\partial r}\right)+\frac{\partial(\epsilon N_{\varphi\vartheta\vartheta})}{\partial\epsilon}\left(\frac{1}{r}\frac{\partial\beta_\varphi}{\partial\vartheta}\right)+\frac{\partial(\epsilon N_{\varphi\varphi\vartheta})}{\partial\epsilon}\left(\frac{1}{r\sin\vartheta}\frac{\partial\beta_\varphi}{\partial\varphi}+\frac{\beta_r}{r}+\frac{\beta_\vartheta\cos\vartheta}{r\sin\vartheta}\right)\right\}=C_\vartheta^{(1)},\text{(B.6)}$$

$$\frac{\rho}{c}\frac{D}{Dt}\left(\frac{H_\varphi}{\rho}\right)-\frac{H_r\beta_\varphi}{r}-\frac{H_\vartheta\beta_\varphi\cos\vartheta}{r\sin\vartheta}+\frac{3}{r}P_{r\varphi}+\frac{\partial P_{r\varphi}}{\partial r}+\frac{2\cos\vartheta}{r\sin\vartheta}P_{\vartheta\varphi}+\frac{1}{r}\frac{\partial P_{\vartheta\varphi}}{\partial\vartheta}+\frac{1}{r\sin\vartheta}\frac{\partial P_{\varphi\varphi}}{\partial\varphi}$$
$$+H_r\left(\frac{\partial\beta_\varphi}{\partial r}\right)+H_\vartheta\left(\frac{1}{r}\frac{\partial\beta_\varphi}{\partial\vartheta}\right)+H_\varphi\left(\frac{1}{r\sin\vartheta}\frac{\partial\beta_\varphi}{\partial\varphi}+\frac{\beta_r}{r}+\frac{\beta_\vartheta\cos\vartheta}{r\sin\vartheta}\right)$$
$$+\frac{1}{c}\frac{\partial}{\partial t}\left(\beta_rP_{r\varphi}+\beta_\vartheta P_{\vartheta\varphi}+\beta_\varphi P_{\varphi\varphi}\right)+\frac{J}{c}\frac{\partial\beta_\varphi}{\partial t}-\frac{1}{c}\frac{\partial\beta_r}{\partial t}\frac{\partial(\epsilon P_{r\varphi})}{\partial\epsilon}-\frac{1}{c}\frac{\partial\beta_\vartheta}{\partial t}\frac{\partial(\epsilon P_{\vartheta\varphi})}{\partial\epsilon}-\frac{1}{c}\frac{\partial\beta_\varphi}{\partial t}\frac{\partial(\epsilon P_{\varphi\varphi})}{\partial\epsilon}$$
$$-\left\{\frac{\partial(\epsilon N_{rr\varphi})}{\partial\epsilon}\left(\frac{\partial\beta_r}{\partial r}\right)+\frac{\partial(\epsilon N_{r\vartheta\varphi})}{\partial\epsilon}\left(\frac{1}{r}\frac{\partial\beta_r}{\partial\vartheta}-\frac{\beta_\vartheta}{r}\right)+\frac{\partial(\epsilon N_{r\varphi\varphi})}{\partial\epsilon}\left(\frac{1}{r\sin\vartheta}\frac{\partial\beta_r}{\partial\varphi}-\frac{\beta_\varphi}{r}\right)\right.$$
$$+\frac{\partial(\epsilon N_{\vartheta r\varphi})}{\partial\epsilon}\left(\frac{\partial\beta_\vartheta}{\partial r}\right)+\frac{\partial(\epsilon N_{\vartheta\vartheta\varphi})}{\partial\epsilon}\left(\frac{1}{r}\frac{\partial\beta_\vartheta}{\partial\vartheta}+\frac{\beta_r}{r}\right)+\frac{\partial(\epsilon N_{\vartheta\varphi\varphi})}{\partial\epsilon}\left(\frac{1}{r\sin\vartheta}\frac{\partial\beta_\vartheta}{\partial\varphi}-\frac{\beta_\varphi\cos\vartheta}{r\sin\vartheta}\right)$$
$$\left.+\frac{\partial(\epsilon N_{\varphi r\varphi})}{\partial\epsilon}\left(\frac{\partial\beta_\varphi}{\partial r}\right)+\frac{\partial(\epsilon N_{\varphi\vartheta\varphi})}{\partial\epsilon}\left(\frac{1}{r}\frac{\partial\beta_\varphi}{\partial\vartheta}\right)+\frac{\partial(\epsilon N_{\varphi\varphi\varphi})}{\partial\epsilon}\left(\frac{1}{r\sin\vartheta}\frac{\partial\beta_\varphi}{\partial\varphi}+\frac{\beta_r}{r}+\frac{\beta_\vartheta\cos\vartheta}{r\sin\vartheta}\right)\right\}=C_\varphi^{(1)}.\text{(B.7)}$$

Note that using the continuity equation yields

$$\begin{aligned}\frac{\rho}{c}\frac{D}{Dt}\left(\frac{X}{\rho}\right) &= \left(\frac{1}{c}\frac{\partial}{\partial t}+\boldsymbol{\beta}\cdot\nabla\right)X + X\nabla\cdot\boldsymbol{\beta} \\ &= \left(\frac{1}{c}\frac{\partial}{\partial t}+\beta_r\frac{\partial}{\partial r}+\frac{\beta_\vartheta}{r}\frac{\partial}{\partial\vartheta}+\frac{\beta_\varphi}{r}\frac{\partial}{\partial\varphi}\right)X \\ &\quad + X\left(\frac{1}{r^2}\frac{\partial(r^2\beta_r)}{\partial r}+\frac{1}{r\sin\vartheta}\frac{\partial(\sin\vartheta\beta_\vartheta)}{\partial\vartheta}+\frac{1}{r\sin\vartheta}\frac{\partial\beta_\varphi}{\partial\varphi}\right). \qquad \text{(B.8)}\end{aligned}$$

The different moments defined in Eqs. (B.3) are linked by the following relations, which are generally valid:

$$\begin{aligned}P_{rr}+P_{\vartheta\vartheta}+P_{\varphi\varphi} &= J\,, \\ N_{rrr}+N_{r\vartheta\vartheta}+N_{r\varphi\varphi} &= H_r\,, \\ N_{rr\vartheta}+N_{\vartheta\vartheta\vartheta}+N_{\vartheta\varphi\varphi} &= H_\vartheta\,, \\ N_{rr\varphi}+N_{\vartheta\vartheta\varphi}+N_{\varphi\varphi\varphi} &= H_\varphi\,. \qquad \text{(B.9)}\end{aligned}$$

Also note that **P** and **N** are completely symmetric tensors, i.e. the indices can be permutated arbitrarily. The number of independent variables therefore is $\#(J,H,P,N) = (1,3,5,7)$ after applying Eqs. B.9.

In two dimensions the symmetry relation $I(-\omega,\mu) = I(\omega,\mu)$ holds which leads to

$$H_\varphi = P_{r\varphi} = P_{\vartheta\varphi} = N_{rr\varphi} = N_{r\vartheta\varphi} = N_{\vartheta\vartheta\varphi} = N_{\varphi\varphi\varphi} \equiv 0 \qquad \text{(B.10)}$$

and therefore $\#(J,H,P,N) = (1,2,3,4)$; note that the last equation in (B.9) becomes redundant. In one dimension one has $I(\omega,\mu) = I(\mu)$ so that in addition

$$H_\vartheta = P_{r\vartheta} = N_{rr\vartheta} = N_{\vartheta\vartheta\vartheta} = N_{\vartheta\varphi\varphi} \equiv 0. \qquad \text{(B.11)}$$

This time, the third equation in (B.9) becomes redundant. Furthermore, one obtains two new equations from comparing the relations in Eqs. (B.3):

$$P_{\vartheta\vartheta} = P_{\varphi\varphi}, \quad N_{r\vartheta\vartheta} = N_{r\varphi\varphi}, \qquad \text{(B.12)}$$

which results in $\#(J,H,P,N) = (1,1,1,1)$. Now one can introduce the definitions $H \equiv H_r, K \equiv P_{rr}, L \equiv N_{rrr}$.

C Specific energy without offset

Here we describe our procedure for solving the Eulerian equations of hydrodynamics, Eqs. (2.1–2.7), together with a general EoS without the side effect of ugly fluctuations in the entropy and pressure as dependent variables.

As discussed in Sect. 2.5 the wiggles disappear if we feed the hydrodynamics solver PROMETHEUS with the total specific energy

$$\varepsilon = e_{\rm int} + e_{\rm kin}\,, \tag{C.1}$$

where $e_{\rm int}$ is the internal specific energy and $e_{\rm kin} = \frac{1}{2}(v_r^2 + v_\vartheta^2 + v_\varphi^2)$ is the kinetic energy per unit of mass. Then the polytropic index $\Gamma_{\rm e} \equiv \frac{p}{\varepsilon - e_{\rm kin}} + 1 = \frac{p}{e_{\rm int}} + 1$ yields physical values $\geq 4/3$, which deem necessary for PROMETHEUS to find smooth hydrodynamic solutions. On the other hand, our high density EoS, provided by Lattimer & Swesty (1991), yields an energy definition which contains the nucleic rest masses and the rest masses of the unpaired electrons, the so-called "relativistic" specific energy, plus a constant offset energy:

$$e_{\rm rel,0} = e_{\rm int} + e_{\rm rm} + e_0\,, \tag{C.2}$$

where the total specific rest mass energy is defined as

$$e_{\rm rm} = \sum_{k=1}^{n_Y} Y_k \cdot \frac{m_k}{m_{\rm B}} \cdot c^2 + Y_{\rm e} \cdot \frac{m_{\rm e}}{m_{\rm B}} \cdot c^2\,. \tag{C.3}$$

and the specific energy offset e_0 is a constant (equal to $-930.7731\mathrm{MeV} \times 1.602 \cdot 10^{-6} \frac{\rm erg}{\rm MeV}/m_{\rm B}$ in our case). This energy definition is also the one which was used in our hydrodynamics solver hitherto, i.e. $\varepsilon = e_{\rm rel,0} + e_{\rm kin}$. For reasons explained below, we still wish to retain the energy definition Eq. (C.2) when evaluating the EoS and at the same time use the new definition Eq. (C.1) when solving the hydrodynamics. This is possible using the following scheme.

The Eulerian equation for the total specific energy, Eq. (C.1), can be derived by subtracting the normalized sum over the Eqs. (2.7) and further subtracting Eq. (2.6), i.e. "(2.5) $-$ $\sum_k (2.7)_k m_k c^2/m_{\rm B} - (2.6) m_e c^2/m_{\rm B}$":

$$\frac{\partial}{\partial t}(\rho\varepsilon) + \frac{1}{r^2}\frac{\partial}{\partial r}\left(r^2\,(\rho\varepsilon + p)\;v_r\right) + \frac{1}{r\sin\vartheta}\frac{\partial}{\partial\vartheta}\Big(\,(\rho\varepsilon + p)\sin\vartheta\,v_\vartheta\Big) = -\rho\left(v_r\frac{\partial\Phi}{\partial r} + \frac{v_\vartheta}{r}\frac{\partial\Phi}{\partial\vartheta}\right) + Q_{\rm E} + Q_{\rm nuc}\,, \tag{C.4}$$

where the nuclear sourcterm is

$$Q_{\rm nuc} = -\sum_{k=1}^{n_Y}\frac{m_k}{m_{\rm B}}c^2 R_k - \frac{m_{\rm e}}{m_{\rm B}}c^2 Q_{\rm N}\,. \tag{C.5}$$

The abundance of each species k is evolved according to Eq. (2.7):

$$\frac{\partial}{\partial t}(\rho Y_k) + \frac{1}{r^2}\frac{\partial}{\partial r}\left(r^2 \rho Y_k v_r\right) + \frac{1}{r\sin\vartheta}\frac{\partial}{\partial \vartheta}(\sin\vartheta\, \rho Y_k v_\vartheta) = R_k \tag{C.6}$$

and the electron fraction according to Eq. (2.6):

$$\frac{\partial}{\partial t}(\rho Y_\mathrm{e}) + \frac{1}{r^2}\frac{\partial}{\partial r}\left(r^2 \rho Y_\mathrm{e} v_r\right) + \frac{1}{r\sin\vartheta}\frac{\partial}{\partial \vartheta}(\sin\vartheta\, \rho Y_\mathrm{e} v_\vartheta) = Q_\mathrm{N}\,. \tag{C.7}$$

Starting at time step n, we calculate a hydrodynamic time step with PROMETHEUS using the initial total specific energy of this time, ε^n, as defined in Eq. (C.1). Remember that PROMETHEUS only solves the LHS of the hydrodynamic equations (in this implementation Eqs. 2.1–2.4,C.4,C.6,C.7), i.e. the source terms and gravitational effects on the RHS of the equations are ignored for the present. Also note that the EoS is *not* solved in PROMETHEUS so that for instance composition changes, even in regions with NSE, origin *solely* from advection, Eqs. (C.6)!

The solution of the evolution equations, after applying the gravitational effects and all source terms except for Q_nuc, Q_N, and R_k yields ε^* as well as the advected nuclear abundances Y_k^* and the electron fraction Y_e^*. The asterisk denotes that the nuclear reaction effects and the neutrinic source term Q_N of time step $n+1$ have not yet been taken into account.

Next, we transform the energy to

$$e_\mathrm{rel,0}^* = \varepsilon^* - e_\mathrm{kin}^{n+1} + \sum_{k=1}^{n_Y} Y_k^* \cdot \frac{m_k}{m_\mathrm{B}} \cdot c^2 + Y_\mathrm{e}^* \cdot \frac{m_\mathrm{e}}{m_\mathrm{B}} \cdot c^2 + e_0\,, \tag{C.8}$$

where e_kin^{n+1} is the specific kinetic energy after the hydrodynamics step.

This energy transformation analytically transforms Eq. (C.4) back to its form Eq. (2.5) while the other hydrodynamic equations are invariant to this transformation. In the context of this energy definition we can now apply the remaining source terms to the hydrodynamic variables as well as update the EoS and NSE composition *exactly* in the same way as we did in our former version of the code since Q_nuc has disappeared from the energy equation. This results in the new composition Y_k^{n+1} and electron fraction Y_e^{n+1}.

We now transform the energy back to

$$\varepsilon^{n+1} = e_\mathrm{EoS}^{n+1} + e_\mathrm{kin}^{n+1} - \sum_{k=1}^{n_Y} Y_k^{n+1} \cdot \frac{m_k}{m_\mathrm{B}} \cdot c^2 - Y_\mathrm{e}^{n+1} \cdot \frac{m_\mathrm{e}}{m_\mathrm{B}} \cdot c^2 - e_0\,, \tag{C.9}$$

where we use $e_\mathrm{rel,0}^{n+1} = e_\mathrm{rel,0}^*$. By this trivial treatment, we have indirectly taken into account the nuclear source term Q_nuc since

$$\varepsilon^{n+1} - \varepsilon^* = -\sum_{k=1}^{n_Y} (Y_k^{n+1} - Y_k^*) \cdot \frac{m_k}{m_\mathrm{B}} \cdot c^2 - (Y_\mathrm{e}^{n+1} - Y_\mathrm{e}^*) \cdot \frac{m_e}{m_\mathrm{B}} \cdot c^2 = Q_\mathrm{nuc} \Delta t^n\,, \tag{C.10}$$

where Δt^n is the size of the time step n.

In other words, because we apply effects which transform mass into internal energy and vice versa, i.e. composition changes due to nuclear transmutation and transmutation of electrons

to massless neutrinos, at a stage where the energy is defined including the rest masses of the particles which change abundance, Eq. (C.2), this energy is not affected by the transmutations and does not change. The shift of energy from $e_{\rm int}$ to $e_{\rm rm}$ or back is not visible in their sum, $e_{\rm rel} = e_{\rm int} + e_{\rm rm}$. Note that, in order to achieve the abundances Y_k^* which are needed in Eq. (C.8) the advection of abundances Eqs. (C.6) has to be solved even in regions for which NSE applies!

This procedure of changing the energy definition during computation seems at first sight to origin from the laziness of the programmer to fix his scheme. However, it features several advantages: first, we do not need to calculate any nuclear source terms. This includes the NSE regime, where the nuclear composition and temperature are well defined functions of ρ, $Y_{\rm e}$, and $e_{\rm rel,0}$ so that an iteration between T, $e_{\rm int}$, and the composition becomes unnessecary if we have saved the NSE EoS in a table. Also in a regime where a burning procedure applies, the conservation of $e_{\rm rel,0}$ ensures strict energy conservation in accordance whith the philosophy of PROMETHEUS. Second, at high densities the nucleon masses are not equal to their masses in vacuum because of nucleon-nucleon interactions. The problems which arise from this physical effect is avoided by our implementation. For the energy transformations, Eqs. (C.8,C.9), we use the vacuum rest masses, while we demand that $e_{\rm rel,0}$ must be exact, as the correctness of this variable is needed to derive correct temperatures, composition, and especially the gravitational potential (via the gravitational mass, which is proportional to $e_{\rm rel} = e_{\rm int} + e_{\rm rm}$ in general relativity). The arising uncertainty in ε of course brings us back to the initial problem, that $\Gamma_{\rm e} = \frac{p}{\varepsilon - e_{\rm kin}} + 1 \neq \frac{p}{e_{\rm int}} + 1$. However, this discrepancy now takes place in the PNS, which tends to have $\Gamma_{\rm e} \gg 4/3$ and has high temperature and electron degeneracy which are likely to be larger than the remaining discrepancy between $e_{\rm int}$ and $\varepsilon - e_{\rm kin}$. Finally, our test runs with this new procedure show that the profiles remain smooth, even in the PNS.

D Progenitor data

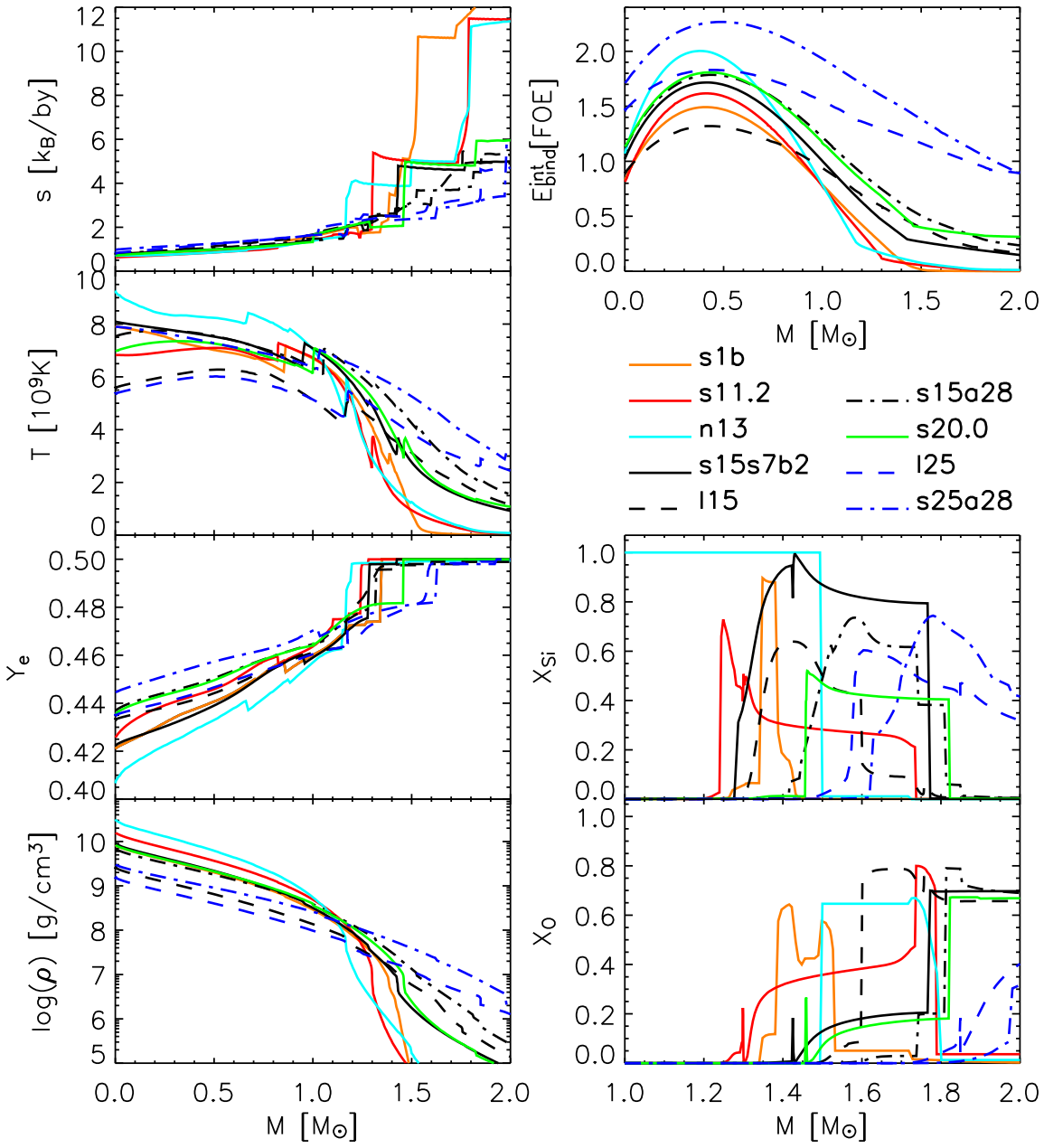

Figure D.1: The progenitor data as provided by the originators (see Table 4.1 for references.

Bibliography

Amanik, P. S., Fuller, G. M., & Grinstein, B. 2004, Flavor Changing Supersymmetry Interactions in a Supernova, preprint astro-ph/0407130

Arcones Segovia, A. 2003, Diploma thesis, Technische Universität München

Arnett, W. D. 1967, Canadian Journal of Physics, 45, 1621

Bethe, H. A. 1990, Reviews of Modern Physics, 62, 801

Bethe, H. A. & Wilson, J. R. 1985, ApJ, 295, 14

Bruenn, S. W. 1985, ApJS, 58, 771

Bruenn, S. W. 1987, Physical Review Letters, 59, 938

Bruenn, S. W. 1989a, ApJ, 340, 955

Bruenn, S. W. 1989b, ApJ, 341, 385

Bruenn, S. W. 1993, in Nuclear Physics in the Universe, ed. M. Guidry & M. Strayer, First Symposium on Nuclear Physics in the Universe (Oak Ridge, Tennessee, USA: Institute of Physics Publishing, Bristol and Philadelphia), 31–50

Bruenn, S. W. & Dineva, T. 1996, ApJ, 458, L71

Bruenn, S. W. & Mezzacappa, A. 1997, Phys. Rev. D, 56, 7529

Bruenn, S. W., Mezzacappa, A., & Dineva, T. 1995, Phys. Rep., 256, 69

Bruenn, S. W., Raley, E. A., & Mezzacappa, A. 2004, Fluid Stability Below the Neutrinospheres of Supernova Progenitors and the Dominant Role of Lepto-Entropy Fingers, preprint astro-ph/0404099

Buonanno, A., Sigl, G., Raffelt, G. G., Janka, H.-T., & Mueller, E. 2004, Stochastic Gravitational Wave Background from Cosmological Supernovae, preprint astro-ph/0412277

Buras, R., Janka, H.-T., Keil, M.-T., Raffelt, G., & Rampp, M. 2003, ApJ, 587, 320

Burrows, A. 1987, ApJ, 318, L57

Burrows, A., Hayes, J., & Fryxell, B. A. 1995, ApJ, 450, 830

Burrows, A. & Sawyer, R. F. 1998, Phys. Rev. C, 58, 554

Burrows, A. & Sawyer, R. F. 1999, Phys. Rev. C, 59, 510

Burrows, A., Young, T., Pinto, P., Eastman, R., & Thompson, T. 2000, ApJ, 539, 865

Cardall, C. & Mezzacappa, A. 2003, Phys. Rev. D, 68, 023006

Carter, G. W. & Prakash, M. 2002, Physics Letters B, 525, 249

Cernohorsky, J. 1994, ApJ, 433, 247

Colella, P. & Woodward, P. 1984, J. Comp. Phys., 54, 174

Colgate, S. A. & White, R. H. 1966, ApJ, 143, 626

Einfeldt, B. 1988, SIAM Jour. Numer. Anal., 25, 294

Epstein, R. I. 1979, MNRAS, 188, 305

Foglizzo, T. & Tagger, M. 2000, A&A, 363, 174

Foot, R. & Silagadze, Z. K. 2004, Supernova explosions, 511 keV photons, gamma ray bursts and mirror matter, preprint astro-ph/0404515

Fryer, C. L. 1999, ApJ, 522, 413

Fryer, C. L. & Heger, A. 2000, ApJ, 541, 1033

Fryer, C. L. & Warren, M. S. 2002, ApJ, 574, L65

Fryer, C. L. & Warren, M. S. 2004, ApJ, 601, 391

Fryxell, B., Müller, E., & Arnett, W. 1989, Hydrodynamics and Nuclear Burning, preprint MPA-449, Max Planck Institut für Astrophysik, Garching

Fryxell, B., Olson, K., Ricker, P., et al. 2000, ApJS, 131, 273

Hamuy, M. 2003, ApJ, 582, 905

Hannestad, S., Janka, H.-T., Sigl, G., & Raffelt, G. 2000, Phys. Rev. D, 62, 093021

Hannestad, S. & Raffelt, G. 1998, ApJ, 507, 339

Heger, A., Langanke, K., Martínez-Pinedo, G., & Woosley, S. E. 2001, Physical Review Letters, 86, 1678

Heger, A., Woosley, S. E., & Spruit, H. C. 2004, Presupernova Evolution of Differentially Rotating Massive Stars Including Magnetic Fields, preprint astro-ph/0409422

Herant, M., Benz, W., & Colgate, S. 1992, ApJ, 395, 642

Herant, M., Benz, W., Hix, W. R., Fryer, C. L., & Colgate, S. A. 1994, ApJ, 435, 339

Hoffman, R. D., Woosley, S. E., Fuller, G. M., & Meyer, B. S. 1996, ApJ, 460, 478

Horowitz, C. 1997, Phys. Rev. D, 55, 4577

Horowitz, C. J. 2002, Phys. Rev. D, 65, 043001

Janka, H.-T. 1991, PhD thesis, Technische Universität München, preprint MPA-587

Janka, H.-T. 1995, Astropart. Physics, 3, 377

Janka, H.-T. 1999, unpublished

Janka, H.-T. 2001, A&A, 368, 527

Janka, H.-T., Buras, R., Kifonidis, K., Plewa, T., & Rampp, M. 2004, in Stellar Collapse, ed. C. Fryer No. MPA1510 (Dordrecht, The Netherlands: Kluwer Academic Publishers), 65–97

Janka, H.-T. & Keil, W. 1998, in Supernovae and Cosmology, ed. L. Labhardt, B. Binggeli, & R. Buse (Astronomisches Institut, Universität Basel), 7

Janka, H.-T. & Müller, E. 1996, A&A, 306, 167

Kachelriess, M., Tomas, R., Buras, R., et al. 2004, Exploiting the neutronization burst of a galactic supernova, preprint astro-ph/0412082

Kane, J., Arnett, D., Remington, B. A., et al. 2000, ApJ, 528, 989

Kaneko, N., Morita, K., & Maekawa, M. 1984, Ap&SS, 107, 333

Keil, M.-T., Raffelt, G., & Janka, H.-T. 2003, ApJ, 590, 971

Keil, W. 1997, PhD thesis, Technische Universität München

Keil, W., Janka, H.-T., & Müller, E. 1996, ApJ, 473, L111

Kifonidis, K., Plewa, T., Janka, H.-T., & Müller, E. 2003, A&A, 408, 621

Kippenhahn, R. & Weigert, A. 1990, Stellar Structure and Evolution, Astronomy and Astrophysics Library (Berlin: Springer)

Kitaura Joyanes, F. S. 2003, Diploma thesis, Technische Universität München

Langanke, K., Martínez-Pinedo, G., Sampaio, J. M., et al. 2003, Physical Review Letters, 90, 241102

Lattimer, J. & Swesty, F. 1991, Nucl. Phys. A, 535, 331

Leblanc, J. M. & Wilson, J. R. 1970, ApJ, 161, 541

Liebendörfer, M., Mezzacappa, A., Thielemann, F., et al. 2001, Phys. Rev. D, 63, 3004

Liebendörfer, M., Rampp, M., Janka, H.-T., & Mezzacappa, A. 2003, A comparison of two Boltzmann neutrino transport codes for core-collapse supernova simulations: Discrete ordinates vs. variable Eddington factor method, preprint astro-ph/0310662

Limongi, M., Straniero, O., & Chieffi, A. 2000, ApJS, 129, 625

Liou, M. 2000, Journal of Computational Physics, 160, 623

Livne, E., Burrows, A., Walder, R., Lichtenstadt, I., & Thompson, T. A. 2004, ApJ, 609, 277

Müller, E., Rampp, M., Buras, R., Janka, H.-T., & Shoemaker, D. H. 2004, ApJ, 603, 221

Marek, A. 2003, Diploma thesis, Technische Universität München

Marek, A., Buras, R., Janka, H.-T., & Rampp, M. 2005, ApJ

Messer, O. E. B., Mezzacappa, A., Bruenn, S. W., & Guidry, M. W. 1998, ApJ, 507, 353

Mezzacappa, A. & Bruenn, S. W. 1993a, ApJ, 405, 669

Mezzacappa, A. & Bruenn, S. W. 1993b, ApJ, 410, 740

Mezzacappa, A. & Bruenn, S. W. 1993c, ApJ, 405, 637

Mezzacappa, A., Calder, A. C., Bruenn, S. W., et al. 1998a, ApJ, 493, 848

Mezzacappa, A., Calder, A. C., Bruenn, S. W., et al. 1998b, ApJ, 495, 911

Mezzacappa, A., Liebendörfer, M., Messer, O., et al. 2001, Phys. Rev. Lett., 86, 1935

Mihalas, D. & Mihalas, B. 1984, Foundations of Radiation Hydrodynamics (Oxford University Press)

Miller, D. S., Wilson, J. R., & Mayle, R. W. 1993, ApJ, 415, 278

Müller, E. & Steinmetz, M. 1995, Comp. Phys. Comm., 89, 45

Nomoto, K. 1984, ApJ, 277, 791

Nomoto, K. & Hashimoto, M. 1988, Phys. Rep.

Plewa, T. & Müller, E. 1999, A&A, 342, 179

Pons, J. A., Miralles, J. A., & Ibanez, J. M. A. 1998, A&AS, 129, 343

Pons, J. A., Reddy, S., Prakash, M., Lattimer, J. M., & Miralles, J. A. 1999, ApJ, 513, 780

Postnov, K. 2004, Stellar explosions: from supernovae to gamma-ray bursts, preprint astro-ph/0410349

Pruet, J., Woosley, S. E., Buras, R., Janka, H.-T., & Hoffman, R. D. 2004, Nucleosynthesis in the Hot Convective Bubble in Core-Collapse Supernovae, preprint astro-ph/0409446

Quirk, J. J. 1994, Int. J. Num. Meth. Fluids, 18, 555

Raffelt, G. G. 2001, ApJ, 561, 890

Rampp, M. 2000, PhD thesis, Technische Universität München

Rampp, M., Buras, R., Janka, H.-T., & Raffelt, G. 2002, in Proceedings of the 11th Workshop on Nuclear Astrophysics, ed. E. Müller & W. Hillebrandt, 119–125, preprint astro-ph/0203493

Rampp, M. & Janka, H.-T. 2002, A&A, 396, 361

Reddy, S., Prakash, M., & Lattimer, J. M. 1998, Phys. Rev. D, 58, 3009

Reddy, S., Prakash, M., Lattimer, J. M., & Pons, J. 1999, Phys. Rev. C, 59, 2888

Schinder, P. J. 1990, ApJS, 74, 249

Smarr, L., Wilson, J. R., Barton, R. T., & Bowers, R. L. 1981, ApJ, 246, 515

Sutherland, R. S., Bisset, D. K., & Bicknell, G. V. 2003, ApJS, 147, 187

Thompson, T. A., Burrows, A., & Pinto, P. A. 2003, ApJ, 592, 434

Tubbs, D. & Schramm, D. 1975, ApJ, 201, 467

Wilson, J. R. 1982, in Proc. Univ. Illinois, Meeting on Numerical Astrophysics

Wilson, J. R. & Mayle, R. 1993, Phys. Rep., 227, 97

Woosley, S. E., Heger, A., & Weaver, T. A. 2002, Reviews of Modern Physics, 74, 1015

Woosley, S. E. & Weaver, T. A. 1995, ApJS, 101, 181+

Yamada, S., Janka, H.-T., & Suzuki, H. 1999, A&A, 344, 533

Danksagung

Fast jeder Doktorand schließt irgendwann seine Doktorarbeit ab, selbst wenn sein Thema Teil der “Unendlichen Geschichte der Supernovasimulationen” ist. Ohne Hilfe und Unterstützung hätte ich jedoch mit Sicherheit nicht zu dieser Mehrheit gehört. Daß ich diesen Lebensabschnitt bewältigt habe verdanke ich zuallererst meinem Betreuer, Doktorvater und Mentor Thomas Janka, dessen unnachgiebige Geduld und Unterstützung mich vor Verzweiflung und Widrigkeiten retteten. Mit seinem Wissen und Ideenreichtum wirkte er stets richtungsweisend sodaß ich niemals Gefahr lief mich in den Niederungen der Physik zu verirren. Nur Dank seines ansteckenden Enthusiasmus konnte ich soviel erreichen.

Ohne Zweifel steht “Untergruppenoberleiter” Markus Rampp an nächster Stelle der Danksagung. In den ersten zwei Jahren meiner Zeit als Doktorand führte er mich in **DEN CODE** ein, brachte mir vieles über den Umgang mit einem komplexen Code bei. In den fast täglichen Gesprächen bekam ich zudem einen tieferen Einblick in die Zusammenhänge der Numerik und Physik.

Um meinen weiteren Kollegen zu danken, bräuchte ich noch etliche Seiten mehr, deshalb greife ich auf die tabellarische Form zurück:

	Diskussion	Zus.arbeit	Unterstützung	Büroklima	Bildung
Wolfgang Hillebrandt			x		x
Ewald Müller		x	x		x
Georg Raffelt	x	x	x		x
Francisco “Paco” Kitaura	x	x	x	x	
Almudena Arcones	x		x	x	
Andreas Marek	x	x	x		
Leonhard Scheck	x				
Konstantinos Kifonidis	x	x			
Harald Dimmelmeier	x				
Corina Vogts			x	x	
Manfred Kitzbichler				x	
Mathias Keil	x	x		x	
Ricard Tomas		x			
Michael Kachelrieß		x			

Trozdem möchte ich noch ein paar Worte ausholen um auszudrücken, was die Tabelle nicht vermag: Georg Raffelt, dem Betreuer meiner Diplomarbeit, verdanke ich es, daß ich überhaupt erst in die Supernovabranche eingestiegen bin, anstatt aus der Physik auszusteigen. Paco und Andreas möchte ich dafür danken, daß ich erfahren durfte wie es ist Betreuer zu sein. Dadurch wurde mir klar daß ich doch etwas weiss, und es war eine Freude mein Wissen weiterzugeben. Andreas möchte ich zusätzlich für die vielen Testrechnungen und Codeimplementierungen danken, die er vor allem gegen Ende meiner Doktorandenzeit für mich durchführte. Weiterhin bedanke ich mich bei Leonhard für die fruchtbaren Diskussionen zum Schwipp-Schwapp-Mechanismus (engl. mezzo-mixing). Erwähnung finden müssen auch Ewald und Wolfgang, durch deren interessante Vorlesungen ich meinen Erstkontakt zur Astrophysik bekam — und wohl nicht mehr davon loskommen werde. Und schließlich, lang ist’s her, erinnere ich micht

mit Freude an die vielen Entdeckungsfahrten ins dunkle Reich der Physik, die Mathias und ich stets aufs neue wagten.

Natürlich darf ich nicht vergessen, meine Physikerfreunde zu danken, die meine Freizeit und mein Leben so gestalteten, daß ich die teils erschöpfende Arbeit trotzdem vollbringen konnte. Almudena und vor allem Paco haben auch hier wieder Erwähnung zu finden (und Paco, danke fürs heimfahren). Benedikt und Martin danke ich für die lange Freundschaft, die mich mit ihnen bindet, und insbesondere für Basketball, Billard, Kneipentouren, Schafkopfen, Schlafstätte, undundund. Und nicht zu vergessen, **Die Band** (Cyrille Barbot, Christoph Bobeth, Sebastian Jäger, Martin Gorbahn): wir hatten zwar nur einen Auftritt, aber dabei sein ist alles. Schließlich bleibt nur noch Mona zu danken für die vielen tiefgehenden Gespräche, und vor allem dafür, daß sie mir den Rettungsring zuwarf, als ich dabei war unterzugehen. Ohne ihren Zuspruch und ihre aufbauenden Worte wäre ich jetzt ein arbeitsloser Computerspezialist.

Ach ja, beinahe hätte ich es vergessen: Dank an “himiko”, “spa” und “psi”, ohne sie hätte ich die Simulationen nie durchführen können; und natürlich danke ich auch den Betreuern dieser Hochleistungsrechner, der Computercrew vom Rechenzentrum Garching. Weiterhin Dank an meine Geldgeber, das sind der Sonderforschungsbereich Astroteilchenphysik, und mit ihm die Technische Universität München, sowie die Max-Planck-Institute für Physik und für Astrophysik.

Nun zu zwei besonderen Danksagungen: “Präsident” G.W. Bush danke ich dafür daß er wenigstens **eine** gute Tat während seines Regimes vollbrachte (… was war es nochmal?). Und dank Ussama bin Ladin öffnete sich mein Geist und ließ die Welt hinein. Selbst die schrecklichsten Ereignisse sollten zumindest **eine** positive Konsequenz haben.

Ich darf nicht vergessen, Dr. Kurt Müller zu erwähnen, er hat mein Leben gerettet.

Wer jetzt denkt, ich würde nur Physiker kennen: danke an all meine Nichtphysikerfreunde, hier wäre selbst ein Diagramm zu aufwendig. Besonderen Dank verdienen meine WG-Mitbewohner der letzten eineinhalb Jahre, allen voran Alt-Mitglied Anja Burkel, ich vermisse unsere gemeinsamen Mittagessen. Ohne Nicole Legrands Hilfe hätte ich die letzten drei Monate nicht durchgehalten, aber ich sehe das nur als weiteren Beweis unserer festen Freundschaft. Und, Annette, danke.

Zuletzt, meine Familie. Ihr verdanke ich so viel, wenn ich anfangen würde es aufzuzählen würde ich bestimmt die Hälfte vergessen, also lass ich’s ganz.

Und, selbstverständlich, zuallerallerletzt danke ich mir selber, dafür, daß ich nicht aufgegeben habe, daß ich der Beste bin, daß ich meiner Treu geblieben bin, daß ich .....